อุทกพลศาสตร์ของฟลูอิไดเซชันของอนุภาคเอฟซีซีและอนุภาคระดับนาโน

นางสาว วีรยา จิรดิลก

สถาบันวิทยบริการ
จุฬาลงกรณ์มหาวิทยาลัย

วิทยานิพนธ์นี้เป็นส่วนหนึ่งของการศึกษาตามหลักสูตรปริญญาวิทยาศาสตรดุษฎีบัณฑิต

สาขาวิชาเคมีเทคนิค ภาควิชาเคมีเทคนิค

คณะวิทยาศาสตร์ จุฬาลงกรณ์มหาวิทยาลัย

ปีการศึกษา 2548

ISBN 974-53-24119-1

ลิขสิทธิ์ของจุฬาลงกรณ์มหาวิทยาลัย

HYDRODYNAMICS OF FLUIDIZATION OF FCC PARTICLES AND NANOPARTICLE

Miss Veeraya Jiradilok

A Dissertation Submitted in Partial Fulfillment of Requirements
For the Degree of Doctor of Philosophy in Chemical Technology
Department of Chemical Technology
Faculty of Science
Chulalongkorn University
Academic year 2005

ISBN 974-53-24119-1

Thesis Title	HYDRODYNAMICS OF FLUIDIZATION OF FCC PARTICLES AND NANOPARTICLES
By	Veeraya Jiradilok
Filed of study	Chemical Technology
Thesis Advisor	Professor Somsak Damronglerd, Dr.Ing.
Thesis Co-advisor	Distinguished Professor Dimitri Gidaspow, Ph.D.
Thesis Co-advisor	Assistant Professor Suchaya Nitivattananon, Ph.D.

Accepted by the Faculty of Science, Chulalongkorn University in Partial Fulfillment of the Requirements for the Doctor's Degree

.....Dean of the Faculty of Science

(Professor Piamsak Menasveta, Ph.D.)

THESIS COMMITTEE

.....Chairman

(Professor Pattarapan Prasassarakich, Ph.D.)

.....Thesis Advisor

(Professor Somsak Damronglerd, Dr.Ing.)

.....Thesis Co-advisor

(Distinguished University Professor Dimitri Gidaspow, Ph.D.)

.....Thesis Co-advisor

(Assistant Professor Suchaya Nitivattananon, Ph.D.)

.....Member

(Associate Professor Lursuang Mekasut, Dr.Ing.)

.....Member

(Associate Professor Pornpote Piumsomboon, Ph.D.)

.....Member

(Kanokrot Phalakronkul, Ph.D.)

วีรยา จิรดิลก : อุทกพลศาสตร์ของฟลูอิไดเซชันของอนุภาคเอฟซีซีและอนุภาคระดับนาโน (HYDRODYNAMICS OF FLUIDIZATION OF FCC PARTICLES AND NANOPARTICLES) อ. ที่ปรึกษา : ศ.ดร.สมศักดิ์ ดำรงค์เลิศ, อ.ที่ปรึกษาร่วม : Distinguished Prof. Dimitri Gidaspow, ผศ.ดร.สุชญา นิติวัฒนานนท์, 346 หน้า. ISBN 974-53-2419-1.

งานวิจัยนี้อธิบายแบบจำลองทางคอมพิวเตอร์ของการไหลแบบไม่คงที่ ได้แก่ อุทกพลศาสตร์ของฟลูอิไดเซชันของอนุภาคเอฟซีซีในช่วงการไหลแบบปั่นป่วน, การแพร่กระจายของอนุภาคซิลิกา 10 นาโน เนื่องจากการระเบิด และ อุทกพลศาสตร์ของฟลูอิไดเซชันของอนุภาคซิลิกา 10 นาโนในเครื่องปฏิกรณ์แบบ 2 มิติ นอกจากนั้นการทดลองคุณสมบัติการไหลของ อนุภาคซิลิกา 10 นาโนทำการศึกษาในเครื่องปฏิกรณ์ฟลูอิไดเซชันแบบหมุนเวียน และ ทำการศึกษาฟลูอิไดเซชันของอนุภาคซิลิการะดับนาโนที่แตกต่างกัน 3 ชนิดในเครื่องปฏิกรณ์คล้าย 2 มิติ แบบจำลองทางคอมพิวเตอร์ของการไหลแบบไม่คงที่เป็นเครื่องมือใหม่ที่ใช้เพื่อศึกษาอุทกพลศาสตร์ของการไหลของของผสมหลายสถานะ ก่อนที่เครื่องมือชนิดนี้จะมีประโยชน์สำหรับการออกแบบเครื่องปฏิกรณ์นั้น เราต้องเข้าใจปัญหาทางทฤษฎีอย่างถ่องแท้ โดยงานวิจัยนี้ได้อธิบายอุทกพลศาสตร์ของฟลูอิไดเซชันของอนุภาคเอฟซีซีและอนุภาคระดับนาโน

ภาควิชา เคมีเทคนิค	ลายมือชื่อนิสิต.....
สาขาวิชา เคมีเทคนิค	ลายมือชื่ออาจารย์ที่ปรึกษา.....
ปีการศึกษา 2548	ลายมือชื่ออาจารย์ที่ปรึกษาร่วม.....
	ลายมือชื่ออาจารย์ที่ปรึกษาร่วม.....

4573837623 : MAJOR CHEMICAL TECHNOLOGY

KEY WORD: GAS-PARTICLE FLOW / FLUIDIZATION / COMPUATIOPNAL FLUID DYNAMICS / FCC PARTICLES / NANOPARTICLES

VEERAYA JIRADILOK : HYDRODYNAMICS OF FLUIDIZATION OF FCC PARTICLES AND NANOPARTICLES. THESIS ADVISOR : PROF. SOMSAK DAMRONGLERD, THESIS COADVISORS : DISTINGUISHED PROF. DIMITRI GIDASPOW, ASST. PROF. SUCHAYA NITIVATTANANON, 346 pp. ISBN 974-53-2419 -1.

This dissertation describes computational fluid dynamics simulations of the flow of FCC particles in the turbulent fluidization regime, explosive dissemination of 10 nm silica particles and the flow of 10 nm silica particles in a 2-dimensional fluidized bed. In an experimental study flow properties of 10 nm silica particles were determined in a two-story circulating fluidized bed riser. Fluidization of three kinds of silica nanoparticles were also investigated in a 2-dimensional fluidized bed. Computational fluid dynamics (CFD) is a new tool for acquiring the understanding of the hydrodynamics of multiphase flow. However, before this a tool becomes useful for the design purpose, a number of theoretical questions must be answered. This thesis is an attempt to answer some of the unresolved issues.

Department CHEMICAL TECHNOLOGY Student's signature Veeraya Jiradilok

Field of study CHEMICAL TECHNOLOGY Advisor's signature

Academic year 2005 Co-advisor's signature Dimitri Gidaspow

Co-advisor's signature Suchaya N.

ACKNOWLEDGEMENTS

First and foremost, I would like to express my sincere appreciation to my thesis advisors, Professor Somsak Damronglerd and Distinguished Professor Dimitri Gidaspow, for their guidance and encouragement. I further acknowledge the help to my co-advisor, Associate Professor Suchaya Nittivantananon. I would like to thank Professor Alex Nikolov for useful discussions and many help.

Thanks are due to my colleagues, especially Dr. Jungwong Jung, with whom I had many useful discussions. My other colleagues, Mr. Jalesh Karla, Ms. Viju N Vasishta, Mr Michael C Driscoll, Ms. Jing Huang, and Mr. Mayank Kashyap are sincerely appreciated.

Furthermore, my thanks are extended to the staff of the department of Chemical Technology, Chulalongkorn University and the department of Chemical and Environmental Engineering, Illinois Institute of Technology, Chicago for many help.

For providing me with financial support, my thanks are extended to the Thailand Research Fund through the Royal Golden Jubilee Ph.D. Program (Grant No. PHD/0124/2545). Reza Mostofi and William J. Koves at UOP were thanked for partially support during the second year at USA.

Specially, I would like to thank my friend, Mr. Varasit In-Ieam. Finally and most importantly, I come to my family. My greatest appreciation goes to my mother Buarin, my father Paisan and my sister Suchada. They were a constant source of support, encouragement and inspiration.

TABLE OF CONTENTS

LIST OF TABLES

สถาบันวิทยบริการ
จุฬาลงกรณ์มหาวิทยาลัย

LIST OF FIGURES

สถาบันวิทยบริการ
จุฬาลงกรณ์มหาวิทยาลัย

LIST OF SYMBOLS

Abbreviation	Term
A	Coefficient matrix
Ar	Archimedes number
B	Coefficient matrix
D	Diffusivity
C_d	Drag coefficient
$\langle C \rangle$	Mean speed
c_k	Heat capacity of phase “k”
c_g	Heat capacity of gas
d_k	Particle diameter
$\vec{E}$	Electric filed strength
e_k	Restitution coefficient of phase “k”
e_w	Restitution coefficient at wall
F_e	Electric force
F_g	Forces acting on gas phase
F_k	Forces acting on phase “k”
F_i	Drag force acting on a single or cluster
FCC	Fluid Catalytic Cracking
G_s	Solids modulus
g	Gravitational acceleration
g_o	Radial distribution function
H_g	Enthalpy of gas phase
H_k	Enthalpy of phase “k”

h_{vk}	Heat transfer coefficient of gas & phase “k”
k	Boltzmann constant
K_g	Gas phase heat transfer
K_k	Particulate phase heat transfer
k_g	thermal conductivity of gas phase
k_k	thermal conductivity of phase “k”
Nu	Nusselt Number
m	mass
M_i	Number of particles or clusters per unit volume
P	Continuous phase pressure
P_k	Dispersed (particulate) phase pressure
Pr	Prandtl number
q_e	Mass charge density (coulomb per mass)
r	Particle radius
R	riser radius
$\tilde{R}$	Gas constant
Re	Reynolds number
T	Temperature
TNT	Trinitrotoluene
t	Time
$\vec{u}$	Velocity in x direction
U_o	Superficial gas velcoty
U_{mf}	Minimum fluidization velocity
U_t	Terminal velocity
U_c	Velocity at which amplitude of pressure fluctuations peak

U_k	Velocity at which amplitude of pressure fluctuations level off
U_{tr}	Transport velocity
$\vec{v}$	Velocity in y direction
v_i	Hydrodynamic velocity in i direction
$\overline{v_i}$	Mean particle velocity in i direction
$\overline{v_i' v_j'}$	Reynolds stress (i = j nornal Reynolds stress; i $\neq$ j shear Reynolds stress)
W_s	solid feed flux

Greek Letters

β_{gk}	Gas-solid drag coefficients
β_{kl}	Particle-particle drag coefficients
ε_k	Volume fraction of phase “k”
ε_g	Volume fraction of gas phase
ϕ	Specularity coefficient
γ_s	Energy dissipation due to inelastic particle collision
κ_s	Granular conductivity
λ_κ	Bulk viscosity of phase k
μ_k	Shear viscosity of phase k
θ	Granular temperature
ρ_k	Density of phase k
τ_k	Stress of phase k
τ_{ck}	Cohesive force

$\hat{\sigma}$	Volume charge density (coulomb per volume)
$\in_r$	Dielectric constant of the gas-solid mixture
$\in_0$	Permittivity of free space
Ψ	Electric potential

Subscripts

g	gas phase
s	solid phase
i	cell in x direction
j	cell in y direction

สถาบันวิทยบริการ
จุฬาลงกรณ์มหาวิทยาลัย

CHAPTER I

INTRODUCTION

Multiphase flows occur in almost all aspects of chemical engineering. Fluidization is used industrially very widely due to its good heat and mass transfer characteristics. Then characteristics are partially due to missing caused by bubbles or clusters and by the random oscillations of particles. Such applications as catalytic cracking, calcinations, combustion, drying, coating and ore roasting had been commercialized successfully. Fluidized bed reactors are most often used in the temperature regulation of highly exothermic reactions and in continuously recycling a catalyst between a reactor and regenerator. Currently, there is much interest in the potential advantages of fluidized bed combustors and gasifiers for producing synthesis gas from coal to be used in fuel cells. For this it is necessary to latter understand the hydrodynamics of the flow and to develop processing technology.

In industrial fluidized bed reactors, turbulent fluidization and dense suspension flow regimes cover the operations of almost all the key commercial catalytic processes involving gas-solid fluidized beds which have high solids hold-up (25-35% by volume). However in past two decades, the flow regimes of bubbling, slugging and fast fluidization have received more interest than the turbulent fluidization. In addition, several researchers accepted that the bubbling, slugging and fast fluidizations are clearly defined regimes, while the turbulent fluidization is not well understood. Most of the papers in fluidization have been focused on the transition from bubble to turbulent fluidization (Grace, 2000; Du, et al., 2002; 2003). These flow regimes have received very little attention in the literature. There is a need to

understand the hydrodynamics of turbulent fluidization and dense suspension flow regimes. Since this is the regime of commercial interest.

Recently, there has been an increased interest in understanding flow of nano-size particles. Unique properties of nanoparticles arise due their very small primary particle size and very large surface area per unit mass. It is necessary to understand the hydrodynamics of nanoparticles and to develop processing technology.

The dispersions of nanoparticles are of interest in forming smoke and other obscurants. The use of smokes and obscurants has historically been used by military in various applications. Dissemination of nanoparticles from a high pressure disseminator into a cavity has been studied previously. The explosive dissemination was divided into two steps: early time hydrodynamics and dissemination into an atmosphere.

The fluidization of nanoparticles is mainly influenced by their density, size, shape, surface roughness and the interparticle forces. A combination of various interparticle forces such as van der Waals, electrostatics interactions, and liquid bridging may occur in a fluidized bed. Hence the natural tendency for nanoparticles to aggregate makes fluidization of nanoparticles difficult. The aggregation behavior of nanoparticles is dependent on the flow conditions. In the fluidized bed the clusters are continuously breaking into smaller agglomerates and reagglomerating into larger ones.

A major goal of the system designers and modelers is to be able to simulate the complex behavior in gas-solid chemically reacting flows in transport reactors and circulating fluidized bed systems through the development of Eulerian-Eulerian simulation codes such as the IIT code, MFIX and FLUENT. To support the mathematical simulation codes, research is being conducted on the hydrodynamics in

these advanced gas-solids contactors using various solids. The experimental data on the hydrodynamics of these flows provide crucial information to the modelers, by providing them with experimental data on the hydrodynamic behavior of the gas and solids with which they can tune the models. The computational fluid dynamics (CFD) has been used to predict the hydrodynamics in gas-solid flow, which can be calculated using the principles of conservation of mass, momentum and energy for each phase. In recent years, the kinetic theory for two-phase flow has been developed. One of the key points for two-fluid models is how to establish the constitutive correlations for the relationship between the solid stress and the strain. In kinetic theory model, the granular temperature can be predicted by solving partial differential equations for the balance of the fluctuating kinetic energy equation for the particles. The solids pressure and viscosity are regarded as functions of the so-called “granular temperature”, a measure of the particles’ velocity fluctuations, which is like the thermal temperature in kinetic theory of gases. Although the kinetic theory model seems to be a more reasonable approach to calculating the solids stress than empirical correlations, viscous model. This theory is basically an extension of the kinetic theory to dense particle flow, which provides explicit closure that takes energy dissipation due to non-ideal particle-particle collisions into account by means of the coefficient of restitution. (Ding & Gidaspow, 1990). The main difference between the granular particles and a molecular gas is that energy is lost in collision between grains.

In Chapter II and III we discussed the basic concept of fluidization and the theoretical hydrodynamic models. Using the hydrodynamic models the flow regime computations were shown as a function of gas velocity done at IIT. By increasing the gas velocity the bed moves from fixed bed to bubbling bed and finally to the pneumatic.

In Chapter IV, we showed that the kinetic theory based CFD model can capture the basic features of the turbulent fluidization regime, the dilute and dense regions, high dispersion coefficients and a strong anisotropy and can compute the turbulence properties, the Reynolds stresses, the kinetic energy spectra and the dispersion coefficients.

In Chapter V, we have shown that it is possible to circulate nanoparticles in a two-story pilot plant type circulating fluidized bed. The particles were 10 nm silica, Tullnox 500, measured with a transmission electron microscope, with a picture shown in Jung and Gidaspow (2002). The nanoparticle viscosity was estimated. This viscosity and the previously measured solids stress modulus were used in a multiphase CFD code to study of the behavior of explosive disseminations of mixtures of nanoparticles and micron size particles.

In Chapter VI, we have explained the observed unique fluidization properties of nanoparticles, formation of dense and dilute regimes, high bed expansion, absence of large bubbles, rapid vortex formation. The multiphase flow hydrodynamic model with the momentum balance for the particle phase and Poisson's equation for the electric field was extended to understand the fluidization of nanoparticles in two-dimensional bed.

In Chapter VII, we can identify two types of granular temperatures using the PIV technique for flow glass beads (group B particles) in bubbling bed. These two kinds of turbulence give rise to two kinds of mixing, mixing on the level of a particle and mixing on the level of cluster or bubble.

In Appendix A, a numerical technique of hydrodynamic model is presented. Organization and user menu is explained in Appendix B. A CFB1_2S.F computer code descriptions is given in Appendix C.

CHAPTER II

BASIC CONCEPTS OF FLUIDIZATION

2.1 Introduction

Fluidization has long been a field where practical applications and empirical findings have preceded fundamental experimentation and understanding. Such applications as catalytic cracking, calcinations, combustion, drying, coating and ore roasting had been commercialized successfully due to continuous powder handling ability and good heat and mass transfer.

The fluidized beds can be operated in different regimes. Four different fluidization regimes, bubbling, slugging, turbulent, and fast fluidization regimes were identified based on a transition velocity, which determined by standard deviation, amplitude and solid fraction distribution analysis (Makkawi & Wright, 2002). By increasing the gas velocity the bed moves from fixed bed to bubbling bed and finally to the pneumatic.

2.2 Minimum fluidization Velocity (U_{mf})

The minimum fluidization velocity is reached when the superficial gas velocity suspends the particles at zero particular velocity. The pressure drop versus gas velocity diagram is particularly useful as a rough indication of fluidization regime. The superficial gas velocity into a fluidized bed is gradually increased until the pressure drop across the bed no longer rises. At the point the pressure drop approximately equals to the static pressure of the bed. And this point where the pressure difference no longer increase is called the minimum fluidization velocity, U_{mf}, as shown in Figure 2.1 (Kunii and Levenspiel, 1991).

For an estimate of minimum fluidization, a momentum balance is the drag force by upward moving gas equals weight of particle, which is relating to buoyant force.

$$\frac{\beta_A}{\varepsilon_g}\left(v_g - v_s\right) = \varepsilon_s\left(\rho_s - \rho_g\right)g \qquad (2.1)$$

where the friction coefficient β_A was estimated from the Ergun equation as following

$$\beta_A = 150\frac{\varepsilon_s^2 \mu_g}{\varepsilon\left(d_p\phi_s\right)^2} + 1.75\frac{\rho_g\left|v_g - v_s\right|\varepsilon_s}{\left(d_p\phi_s\right)} \qquad (2.2)$$

For small particles or for small Reynolds numbers, the first term in Ergun equation is dominant and the minimum fluidization velocity is defined as

$$U_{mf} = \frac{d_p^2\left(\rho_s - \rho_g\right)g}{150\mu}\cdot\frac{\phi_s^2\varepsilon_{mf}^3}{1-\varepsilon_{mf}} \qquad \mathrm{Re}_{mf} < 20 \qquad (2.3)$$

For large particles, the second term is dominant and the minimum fluidization velocity can be expressed as

$$U_{mf}^2 = \frac{d_p\left(\rho_s - \rho_g\right)g}{1.75\rho_g}\varepsilon_{mf}^3\phi_s \qquad \mathrm{Re}_{mf} > 1000 \qquad (2.4)$$

2.3 Minimum Bubbling Velocity (U_{mb})

The fluidizing velocity at which bubbles are first observed is called the minimum bubbling velocity, U_{mb}. Gelderbloom et al, (2003) showed that in gas-solid system of Geldart group B, the minimum bubbling velocity approximately equals to the minimum fluidization velocity. Hence bubbles appear as soon as the gas velocity exceeds U_{mf}. For other group particles, the minimum bubbling velocity is usually larger the minimum fluidization velocity. However in the bubbling regime, the industrial applications do not operate in this regime due to the bubble formation. In

the combustion process, the bubble will carry the oxygen without the combustion. Formation of large bubbles causes gas-bypassing and hence poor reaction.

2.4 Turbulent fluidization

The turbulent regime is considered lie between bubbling fluidization and fast fluidization regime. Mori et al. (1989) estimated the transition velocity, U_c, between bubbling and turbulent fluidizations. U_c is estimated from the standard deviation of pressure fluctuations reached a maximum, at this point, the regime begins the transition to turbulent fluidization. U_c/U_t is greater than unity for group A particle and equal to or less than unity for Group B and D particles (Rhodes M., 1996). While the transition velocity, U_k, can be obtained from the standard deviation of the pressure fluctuations level off. This velocity condition was the end of the transition. In addition, the transition from turbulent to fast fluidization can be defined by the transport velocity, U_{tr}. The transport velocity is estimated from phase diagram between pressure gradient and solid circulation rate at critical point (Yerushalmi & Cankurt, 1979). U_{tr} is generally higher than U_k.

Grace et al. (2000) summarized the works on turbulent fluidization. The several researchers estimated the corrections for the transition velocity on this regime. Bi and Grace (1995) studied the correlation of 60 micron FCC particles for turbulent fluidized bed. The correlation for transition velocity U_c, that is,

$$\mathrm{Re}_c = 0.565 Ar^{0.461} \qquad (2.5)$$

Besides, the transition velocity U_k, can be defined from the differential pressure fluctuations that was calculated by Tsukada et al., (1993). The correlation is,

$$\mathrm{Re}_k = 1.31 Ar^{0.45} \qquad (2.6)$$

In addition, the transition from turbulent to fast fluidization which was estimated by Tsukada et al. (1994), determined from phase diagram between pressure gradient, solid circulation rate and gas velocity. The correlation for the transport velocity U_{tr} is,

$$\mathrm{Re}_{tr} = 1.806 Ar^{0.458} \qquad (2.7)$$

Table 2.1 Velocities at several states for FCC particles calculated from above expressions

power		FCC
d_p	μm	60
ρ_p	kg/m^3	1000
ε_{mf}		0.48
Ar		8.14
U_c	m/s	0.375
U_k	m/s	0.85
U_{tr}	m/s	1.19

A turbulent fluidized bed is characterized by two different coexisting regions: a bottom dense, bubbling region and a dilute, dispersed flow region (Berruti , et al. 1995). Matsen (1982) presented the phase diagram for vertical gas solids flow. Dilute phase theory and dense phase riser theory were applied to obtain this diagram as shown in Figure 2.2. At appropriate solid feed flux and gas superficial velocity, the system consists of two phases, which is dense phase at the bottom and dilute phase at the top, which is similar to drift flux describing in Gidaspow's book (1994).

The Equation in the dilute phase theory as following

$$\frac{W_s}{\rho_p U_t} = \frac{1-\varepsilon}{\varepsilon}\left[\frac{U}{U_t} - 10.8\varepsilon(1-\varepsilon)^{0.293}\right] \qquad (2.8)$$

where W_s is the solid feed flux, U_t is the terminal velocity, ρ_p is the solid density and ε is the bed voidage.

In the dense phase, the relation between solid flux and gas superficial velocity can be estimated in this equation.

$$\frac{W_s}{\rho_p} = \frac{1-\varepsilon}{\varepsilon}\left[U - U_{mf} - U_{mb}\left(\frac{\varepsilon - \varepsilon_{mf}}{1-\varepsilon}\right)\right] \tag{2.9}$$

where U_{mf} is the minimum fluidization velocity, ε_{mf} is the voidage at minimum fluidization and U_{mb} the minimum bubbling velocity.

However, for the high-density riser or dense suspension upflow, the system consists of two different coexisting regions, a bottom dense and dilute dispersed flow region. It is operated at high solid flux and high superficial gas velocity. The definition of turbulent fluidization does not hold by U_c , U_k, and U_{tr} in the high-density riser.

2.5 Fast Fluidization

Kunii and Levenspiel (1991) mentioned that at high gas velocity $(U_o > 20U_t)$ with very fine solids, this situation represents fast fluidization. Based on experimental finding in a 15.2 cm column, Yerushalmi and Cankurt (1979); Avidan and Yerushalmi (1982) characterized the fast fluidized bed as follow:

- Solid concentration somewhere between dense-phase beds and dilute conditions
- Cluster formation occurring
- Extensive back mixing of solids
- Slip velocity of particles one order of magnitude larger than U_t

2.6 Fluidization Regime

Figure 2.3 summarizes the flow regime computations as a function of gas velocity done at IIT. In batch fluidization, the initial condition maintains the particles in the system. No particles are added to the bed. For continuous system particles must be continually added to the bed to maintain a fluidized bed (Gidaspow et al., 2004).

In bubbling fluidization, the bubble size increases with particle diameter correspond to Geldart group A and B.

For many nanoparticles, fluidization occurs without bubbles as called agglomerate particulate fluidization (APF). When the superficial gas velocity is more than the terminate gas velocity, the nanoparticles still are inside the bed because of the internal circulation. The vertex formations are investigated in both experiments and computations. The fluidization of nanoparticles is possible due to formation of light clusters.

In the turbulent fluidization there exists normally a dense and dilute region. It has no distinct bubbles, but is characterized by clusters that move forth and back. This thesis shows that the dispersion coefficient is higher than that in other flow regimes. For Geldart A particles, the computations have to consider the modified drag, as suggested by Yang, et al. (2004).

Fast fluidization is characterized by cluster formation. For Geldart group B particles, without any assumption of cluster size or density the cluster motion has been successfully computed. The cluster formation occurs due to the Bernoulli effect of change of area and hence due to a hydrodynamic cohesive force. The change of area in Bernoulli equation makes changing of pressure, so the attractive force between particles occurs.

For the dense suspension flow the computed data are in agreement with the PSRI experimental results; the computer code can predict the snakelike density oscillations. As the fast flow rate continues to rise the particulates will be transported with gas and will be in pneumatic conveying regime.

สถาบันวิทยบริการ
จุฬาลงกรณ์มหาวิทยาลัย

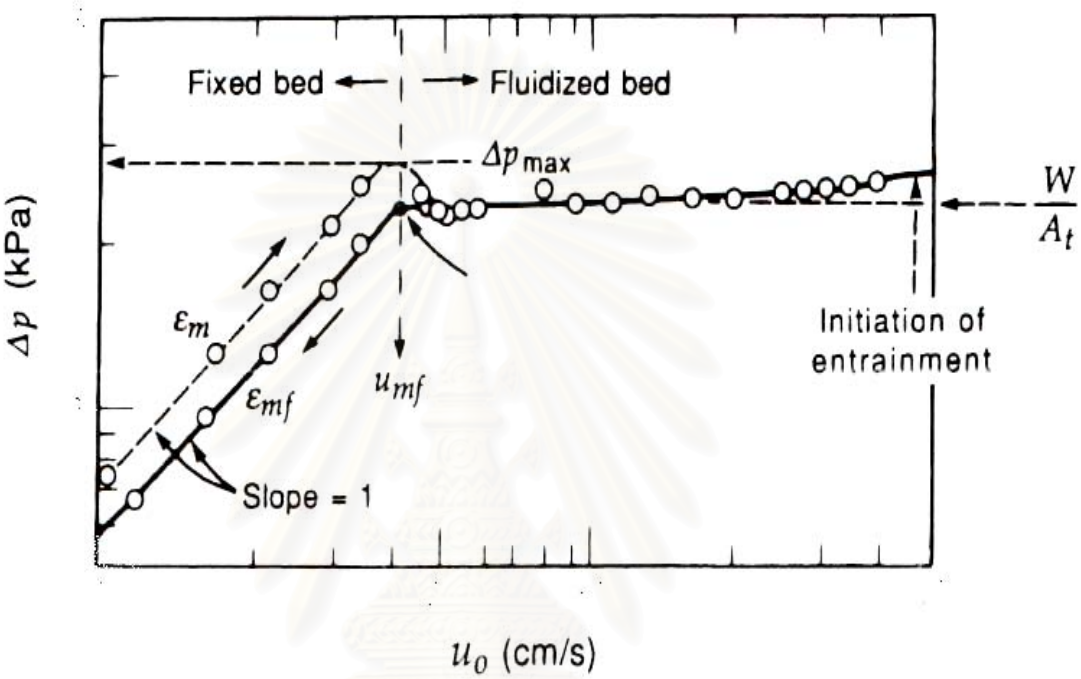

Figure 2.1 Pressure drop versus the gas velocity to determine of minimum fluidization velocity (Kunii and Levenspiel, 1991)

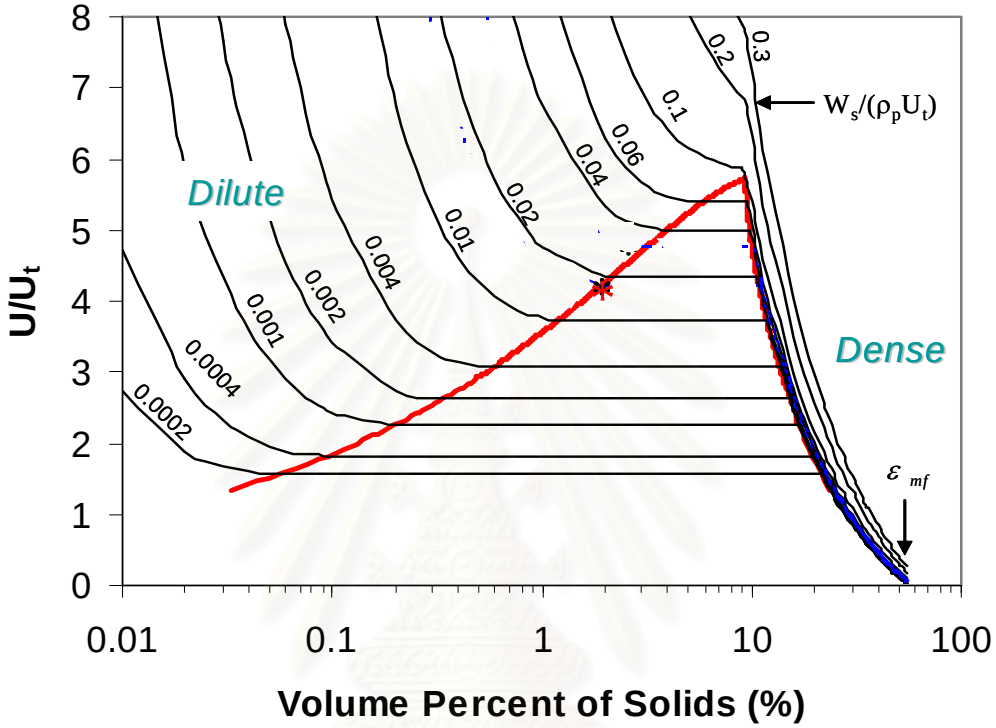

Figure 2.2 Matsen's (1982) prediction of dense and dilute volume fractions of FCC particles (Matsen,1982)

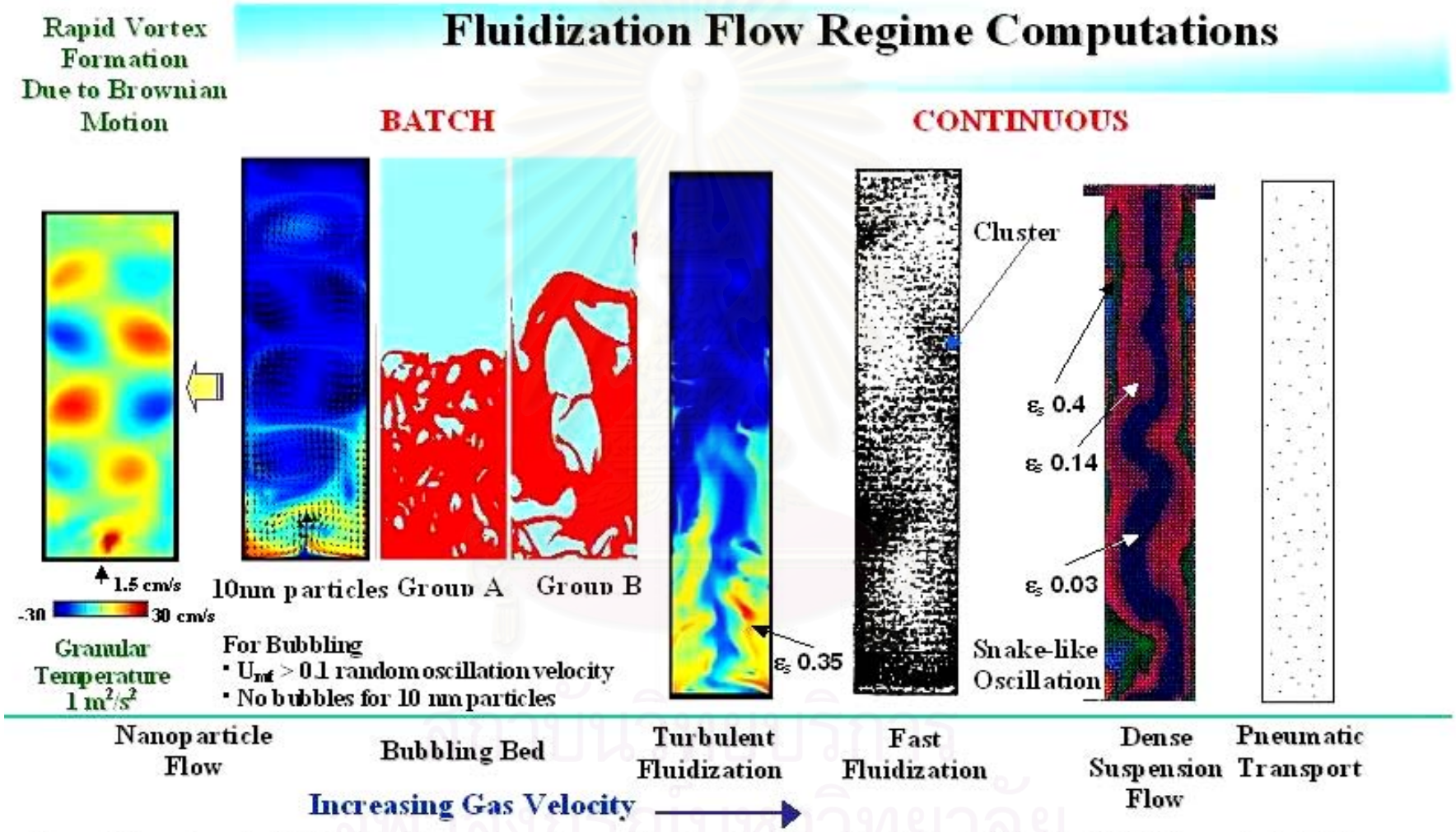

Figure 2.3 Computed fluidization flow regimes. Nanoparticle flow (Jiradilok, et al., 2005); Bubbling bed (Gelderbloom, et al., 2003); Turbulent fluidization: shows the existence of dilute & dense regions (Jiradilok, et al., 2005); Fast fluidization (Neri and Gidaspow, 2000; Tsuo and Gidaspow, 1990; Gidaspow and Mostifi, 2003); Dense suspension flow (Sun and Gidaspow, 1999).

CHAPTER III

THEORETICAL HYDRODYNAMIC MODELS

3.1 Introduction

Multiphase flow processes are key elements of several important reactor technologies such as fluid catalytic cracking reactors. It is necessary to develop tools to evaluate the operability of the multiphase flow process under specified conditions and to identify the operating regime. It is importance to develop understanding and predictive tools to simulate multiphase flow processes to develop better reactor technologies. The modeling of multiphase flow process is interesting. Two basic approaches to model multiphase flows, namely, Eulerian-Lagrangian, and Eulerian-Eulerian are discussed below with reference to dispersed flow.

A multiphase flow system is consisting of several particulate phases and a continuous phase. For the particulate phases, they can be different densities and/or sizes. The hydrodynamic model for the multiphase flow based on the generalization of Navier-Stokes equations. It was developed earlier at Illinois Institute of Technology that uses the Eulerian-Eulerian approach. The basic equations given below are the mass, momentum and energy equations for fluid phase and each of the particulate phases as a Hydrodynamic model B. The principle of mutiphase flow model is the definition of volume fraction of each phase. The numerical scheme used in this code is the Implicit Continuous Eulerian (ICE) approach as described in Appendix A. The model uses donor cell differencing. The conservation of momentum and energy equations are in mixed implicit form. It means that the momentum equations are fully explicit. The continuity equations excluding mass generation are in implicit form.

3.2 Modeling Approaches

There are two main approaches for modeling multiphase flows (Ranade, 2002):

1. Eulerian framework for the continuous phase and Largrangian framework for all the dispersed phases
2. Eulerian framework for all phases

In the Eulerian-Largrangian approach, motion of the continuous phase is modeled using a Eulerian framework. This approach is suitable for simulating dispersed multiphase flows containing a low (<10%) volume fraction of the dispersed phases or small system (not many number of particles). The motions of dispersed phase particles are explicitly simulated in a Lagrangian frameworks. Lagrangian models solve the Newtonian equations of motion for each individual particle, taking into account the effects of particle collisions and forces acting on the particle by the gas. Particle collisions are described by collision laws, that account for energy dissipation due to non-ideal particle interactions by means of the empirical coefficient of restitution and friction (hard sphere approach). or an empirical spring stiffness, a dissipation constant and a friction coefficient (soft sphere approach).

The Eulerian-Eulerian approach models the flow of all phase in a Eulerian framework based on the interpenetrating continuum assumption. This approach can be applied to multiphase flow process containing large volume fractions of dispersed phase. It may be extended to modeling and simulation of complex industrial multiphase reactors consisting of a large number of dispersed particles. The equations employed are a generalization of the Navier–Stokes equations for interacting continua. Owing to the continuum representation of the particle phases, Eulerian models require additional closure laws to describe the rheology of particles. In most recent continuum models constitutive equations according to the kinetic theory of

granular flow are incorporated. This theory is basically an extension of the classical kinetic theory to dense particle flow, which provides explicit closures that takes energy dissipation due to non-ideal particle–particle collisions into account by means of the coefficient of restitution (Huilin and Gidaspow, 2003).

3.3 Hydrodynamic Model

There are two hydrodynamic models for momentum equations:

1. Hydrodynamic Model A
2. Hydrodynamic Model B

Assumption of Hydrodynamic Model A is that the pressure drop is in all the phases. Lyczkowski et al (1987) showed that this kind of model is ill-posed.

Gas Phase:

$$\frac{\partial}{\partial t}\left(\varepsilon_g \rho_g \vec{v}_g\right) + \nabla \cdot \left(\varepsilon_g \rho_g \vec{v}_g \vec{v}_g\right) = -\varepsilon_g \nabla P_g + \varepsilon_g \rho_g g + \nabla \cdot \left[\tau_g\right] + \sum_{l=1}^{N} \beta_{Agl}\left(\vec{v}_l - \vec{v}_f\right) \tag{3.1}$$

Solids Phase:

$$\frac{\partial}{\partial t}\left(\varepsilon_k \rho_k \vec{v}_k\right) + \nabla \cdot \left(\varepsilon_k \rho_k \vec{v}_k \vec{v}_k\right) = -\varepsilon_k \nabla P_g + \nabla P_k + \varepsilon_k \rho_k g + \nabla \cdot \left[\tau_k\right] + \sum_{\substack{l=1 \\ l \neq k}}^{N} \beta_{Akl}\left(\vec{v}_l - \vec{v}_f\right) \tag{3.2}$$

Using pressure drop in fluid (or continuous) phase only, this version of the momentum balance is referred to as Hydrodynamic model B. (Bouillard et al., 1989) The momentum equation written in this form leads mathematically to well-posed problem because the characteristics are real and distinct.

Gas and Solids Phase, $k = \left(g, 1, \ldots, N\right)$:

$$\frac{\partial}{\partial t}\left(\varepsilon_k \rho_k \vec{v}_k\right) + \nabla \cdot \left(\varepsilon_k \rho_k \vec{v}_k \vec{v}_k\right) = -\nabla P_k + \omega_k g + \nabla \cdot \left[\tau_k\right] + \sum_{\substack{l=f,1 \\ l \neq k}}^{N} \beta_{Bkl}\left(\vec{v}_l - \vec{v}_f\right)$$

(3.3)

Therefore modifications in hydrodynamic model B had been made. The drag term and the apparent mass for Hydrodynamic model B must be modified to satisfy generalized Darcy's law and Archimedes's principle, respectively.

The interphase interaction coefficients (drag coefficients) are given by,

$$\beta_{Blk} = \frac{\beta_{Alk}}{\varepsilon_f} \text{ for } k = 1,\ldots,N; l = 1,\ldots,N; l \neq k \qquad (3.4)$$

The apparent mass for particular phases in Hydrodynamic model B is as following,

$$\omega_k = \frac{\varepsilon_k}{\varepsilon_f}\left(\rho_k - \sum_{l=f,1}^{N} \varepsilon_l \rho_l\right) \text{ for } k = 1,\ldots,N \qquad (3.5)$$

The Eulerian-Eulerian (two fluid model) approach is used for this work. The dispersed phase is, as well, treated as a continuum. The basic equations are given in the mass, momentum and energy equations. In the gas-solid system without heat transfer, the models consist of 2 different models, viscous model and kinetic theory model. The conservation of mass and momentum equations are the main equations of both models. However the constitutive equations are different, which are the gradient of solid pressure and the solid viscosity.

1. **The viscosity model** is one of the models to use in the numerical simulations, the particular viscosities and pressure based on empirical correlation and experimental values are used. It means that for this model, the solid viscosity and the solid pressure are the input data. The solid pressure is defined as a function of solids modulus.

2. **The kinetic theory model** is more advantage than the viscosity model because the solid viscosity and solid pressure are estimated by solving fluctuating energy equation. The solids viscosity and pressure are derived by considering the random fluctuation of particle velocity and its variations due to particle–particle collisions and the actual flow field. Such a random kinetic energy, or granular temperature, can be predicted by solving, in addition to the mass and momentum equations, a fluctuating kinetic energy equation for the particles. The solids viscosity and pressure can then be computed as a function of granular temperature at any time and position.

3.4 Model Description

To be in well posed form, Hydrodynamic model B is used to simulate the multiphase flow system. The main equations are called as governing equations consisting of continuity, momentum and energy equations. The constitutive equations are coupling with the governing equations to solve the parameters.

The code is capable of modeling the geometries of the rectangular or cylindrical coordinates. This code uses for modeling a two dimensional system. For the rectangular coordinate, R = 1 in the following equations. Calculations are done in the –x and –y directions. For symmetric cylindrical coordinates, R = r, where r is the radial coordinate. Calculations are done in the –r and –z directions. The symmetry is the offset of –z axis.

In gas-solid flows system without energy transfer (no energy equations), The continuity and momentum equations are solved. These 3(N+1) nonlinear partial differential equations are solved for 3(N+1) dependent variable; for 1 gas phase and N solid phases. The variables to be computed are the continuous phase pressure P_f, the

solid volume fraction ε_k (k=1,…,N) the fluid velocity component u_f and v_f, and solid velocity component u_k and v_k (k=1,…,N) in –x and –y directions, respectively (rectangular coordinate). In addition, the system consists of energy transfer between each phase. The energy equations must be solved; therefore these partial differential equations are 4(N+1) including the fluid, T_f and particulate temperature T_k, (k=1,…,N).

3.5 The Governing Equations

3.5.1 Continuity Equations The accumulation of mass in each phase is balanced by the convective mass flows. Mass exchanges between the phases, e.g. due to reaction or combustion, are not considered.

(a) Fluid Phase

$$\frac{\partial(\rho_f \varepsilon_f)}{\partial t} + \frac{1}{R}\nabla\cdot(R\rho_f \varepsilon_f v_f) = 0 \tag{3.6}$$

Rate of mass accumulation + Rate of convective = Mass exchanges
per unit volume mass flux

(b) Solid Phase k (=1,…,N)

$$\frac{\partial(\rho_k \varepsilon_k)}{\partial t} + \frac{1}{R}\nabla\cdot(R\rho_k \varepsilon_k v_k) = 0 \tag{3.7}$$

3.5.2 Momentum Equations

(a) Fluid Phase

$$\frac{\partial(\rho_f \varepsilon_f v_f)}{\partial t} + \frac{1}{R}\nabla\cdot(R\rho_f \varepsilon_f v_f v_f) = -\nabla P_f + \rho_f g + \sum_{l=1}^{N}\beta_{fl}\left(v_l - v_f\right)$$

$$+\frac{1}{R}\nabla\cdot R\left[\tau_f\right] - \tau_{fo}\frac{1}{R}\nabla R \tag{3.8}$$

(b) Solid Phase k (=1,…,N)

$$\frac{\partial(\rho_k \varepsilon_k v_k)}{\partial t} + \frac{1}{R}\nabla\cdot(R\rho_k \varepsilon_k v_k v_k) = -\nabla P_k + \frac{\varepsilon_k}{\varepsilon_f}\left(\rho_k - \sum_{l=f,1}^{N}\varepsilon_l \rho_l\right)g + \sum_{\substack{l=f,1\\ l\neq k}}^{N}\beta_{kl}\left(v_l - v_k\right)$$

Accumulation Net outflow Pressure Gradient Gravity force Drag force

$$+\nabla\tau_{ck} + \frac{1}{R}\nabla\cdot\underbrace{R[\tau_k] - \tau_{ko}\frac{1}{R}\nabla R}_{\text{Cohesive force}\quad\text{Shear stress}} \qquad (3.9)$$

3.5.3 Energy Equations In order to derive an equation for internal energy, it is necessary to derive a transport equation for mechanical energy, which can be subtracted from the equation for total energy to obtain the governing equation for internal energy.

(a) Fluid Phase

$$\frac{\partial\left(\varepsilon_f \rho_f H_f\right)}{\partial t} + \frac{1}{R}\nabla\cdot\left(R\varepsilon_f \rho_f H_f v_f\right) = \left(\frac{\partial P_f}{\partial t} + v_f\cdot\nabla P_f\right) + \sum_{k=1}^{N} h_{vk}\left(T_k - T_f\right)$$

Accumulation Net outflow Work due to gas pressure Heat transfer between phases

$$+\sum_{k=1}^{N}\beta_{kf}\left(v_k - v_f\right)^2 + \frac{1}{R}\nabla\cdot\left(RK_f\nabla T_f\right) + \Phi_f \qquad (3.10)$$

Phase change effect due to drag Conduction Energy Dissipation Rate

The first and second terms of the energy conservation equation represent accumulation and change of enthalpy due to convection. The third term represents reversible and irreversible change in the enthalpy due to pressure. The forth term represents heat transfer between phases due to the temperature difference. The fifth term represents the phase change effect due to drag. The sixth term represents change

in the enthalpy due to conduction. The final term represents reversible and irreversible change in the enthalpy due to viscous dissipation. The detail is in Chapter V.

(b) Solid Phase k (=1,…,N)

$$\frac{\partial(\varepsilon_k \rho_k H_k)}{\partial t} + \frac{1}{R}\nabla \cdot (R\varepsilon_k \rho_k H_k v_k) = h_{vk}(T_f - T_k) + \frac{1}{R}\nabla \cdot (RK_k \nabla T_k) + \Phi_k \tag{3.11}$$

3.6 The Constitutive Equations

3.6.1 Definitions The volume fractions are assumed to be continuous function of space and time. The volume fractions of all for the phases must sum to one.

$$\varepsilon_f + \sum_{k=1}^{N} \varepsilon_k = 1 \tag{3.12}$$

$$T_k = T_o + \frac{H_k - H_o}{c_k} \tag{3.13}$$

3.6.2 Equation of State The fluid phase can be modeled as a gas obeying the ideal gas law.

$$\rho_f = \frac{P_f}{\bar{R} T_f} \tag{3.14}$$

3.6.3 Cohesive Force Ding and Gidaspow (1994) have shown that for fine particles, like FCC particle, the cohesive force between particles is significant. This force depends on several factors such as the moisture content, the particle solid and void fraction. Therefore, the cohesive force should be added in the momentum equation for the solid phase. Cohesive force of the FCC catalyst is as following,

$$\tau_{ck} = 10^{-10.6\varepsilon_k + 5.5} \qquad \text{dyne/cm}^2 \tag{3.15}$$

3.6.4 Constitutive Equation for Stress

(a) Fluid Phase

$$[\tau_f] = \varepsilon_f \mu_f \left(\left[\nabla v_f + (\nabla v_f)^T \right] - \frac{2}{3}\frac{1}{R}\nabla \cdot (R v_f)[I] \right) \tag{3.16}$$

$$\tau_{fo} = 2\varepsilon_f \mu_f \left[\frac{1}{R} v_f \cdot \nabla R - \frac{1}{3}\frac{1}{R} \nabla \cdot \left(R v_f \right) \right] \tag{3.17}$$

(b) Solid Phase (k =1,…,N)

$$[\tau_k] = \mu_k \left(\left[\nabla v_k + (\nabla v_k)^T \right] - \left(\xi_k - \frac{2}{3}\mu_k \right) \frac{1}{R} \nabla \cdot (R v_k) [I] \right) \tag{3.18}$$

$$\tau_{ko} = \left[2\mu_k \frac{1}{R} v_k \cdot \nabla R - \left(\xi_k - \frac{2}{3}\mu_k \right) \frac{1}{R} \nabla \cdot \left(R v_f \right) \right] \tag{3.19}$$

3.6.5 Interphase Momentum Exchange In order to couple the two momentum balances, a model for the interface force is required.

3.6.5a Gas-Solid Drag Coefficients (Classical Drag) (Gidaspow, 1994)

For $\varepsilon_f < 0.8$, the pressure drop due to friction between gas and particles can be described by the Ergun equation.

$$\beta_{gk} = 150 \frac{\varepsilon_k^2 \mu_g \rho_k}{\left(\varepsilon_g d_k \phi_k\right)^2 \left(\rho_k - \rho_g\right)} + 1.75 \frac{\rho_g \rho_k \left| v_g - v_k \right| \varepsilon_k}{\left(\varepsilon_g d_k \phi_k\right)\left(\rho_k - \rho_g\right)} \tag{3.20}$$

For $\varepsilon_f > 0.8$, such a relation for pressure drop leads to the following expression for the interface momentum transfer coefficient which can be described by the Wen and Yu correlation.

$$\beta = \frac{3}{4} C_d \frac{\rho_g \rho_k \varepsilon_k \left| v_g - v_k \right|}{d_k \phi_k \left(\rho_k - \rho_g\right)} \varepsilon_f^{-2.65} \tag{3.21}$$

3.6.5b Gas-Solid Drag Coefficients (Modified Drag) In the heterogeneous system, the particles move as clusters and individual particles. It means that the system consists of 3-scales: micro-, meso- and macro-scales. Therefore the gas-solid interactions considered are: gas-particle interaction in dense phase, gas-particle interaction in dilute phase and gas-cluster interaction in the inter-phase. The energy-

minimization multi scale (EMMS) approach should be considered as a closure law for drag coefficient (Yang et al., 2004).

when $\varepsilon < 0.74$

$$\beta_{gk} = 150\frac{\varepsilon_k^2 \mu_g \rho_k}{(\varepsilon_g d_k \phi_k)^2 (\rho_k - \rho_g)} + 1.75\frac{\rho_g \rho_k |v_g - v_k| \varepsilon_k}{(\varepsilon_g d_k \phi_k)(\rho_k - \rho_g)} \tag{3.22}$$

when $\varepsilon \geq 0.74$

$$\beta = \frac{3}{4} C_d \frac{\rho_g \rho_k \varepsilon_k |v_g - v_k|}{d_k \phi_k (\rho_k - \rho_g)} \omega(\varepsilon) \tag{3.23}$$

The difference between the classical drag and modified drag is the term ($\varepsilon_f^{-2.65}, \omega(\varepsilon)$) in the Wen and Yu correlation.

$$\omega(\varepsilon) = \begin{cases} -0.5760 + \dfrac{0.0214}{4(\varepsilon - 0.7463)^2 + 0.0044} & (0.74 < \varepsilon \leq 0.82) \\ -0.0101 + \dfrac{0.0038}{4(\varepsilon - 0.7789)^2 + 0.0040} & (0.82 < \varepsilon \leq 0.97) \\ -31.8295 + 32.8295\varepsilon & (\varepsilon > 0.97) \end{cases} \tag{3.24}$$

where,

$$C_d = \frac{24}{\mathrm{Re}_k}\left(1 + 0.15\,\mathrm{Re}_k^{0.687}\right) \qquad \text{for } \mathrm{Re}_k < 1000 \tag{3.25}$$

$$= 0.44 \qquad \text{for } \mathrm{Re}_k > 1000 \tag{3.26}$$

$$\mathrm{Re}_k = \frac{\varepsilon_g \rho_g |v_g - v_k| d_k \phi_k}{\mu_g} \tag{3.27}$$

3.6.5c Particle – Particle Drag Coefficients (k =1,…,N) The particle - particle interaction has been derived by Nakamura and Capes (1976).

$$\beta_{\substack{kl \\ k,l \neq f}} = \frac{3}{2}\alpha(1+e)\frac{\rho_k \rho_l \varepsilon_k \varepsilon_l (d_k + d_l)^2}{\rho_k d_k^3 + \rho_l d_l^3} |\vec{v}_k - \vec{v}_l| \tag{3.28}$$

The Kinetic theory model

The granular temperature can be predicted by solving a fluctuating kinetic energy equation for the particles (Ding and Gidaspow, 1990). Besides the solid viscosity and pressure can be computed as a function of granular temperature. In order to solve the fluctuating energy equation, we need to specify the collisional energy dissipation, γ_s due to inelastic collisions of particles and the granular conductivity, κ_s.

3.6.6 Fluctuating Energy Equation $\frac{3}{2}\theta = \frac{1}{2}\langle C^2 \rangle$ (k = s)

$$\frac{3}{2}\left[\frac{\partial}{\partial t}(\varepsilon_s \rho_s \theta) + \nabla \cdot (\varepsilon_s \rho_s v_s \theta)\right] = \tau_s : \nabla v_s + \nabla \cdot (\kappa_s \nabla \theta) - \gamma_s \qquad (3.29)$$

The first term of right hand side is the production of fluctuating energy by the effective shear stresses, the second term is the conduction due to the gradient of granular temperature, and the third term is the dissipation due to the inelastic collision of particles.

a) Solid Stress Tensor

$$\tau_s = (-P_s + \xi_s \nabla \cdot v_s)I + 2\mu_s \tau_s \qquad (3.30)$$

b) Solid Pressure

$$P_s = \rho_s \varepsilon_s \theta [1 + 2(1+e) g_o \varepsilon_s] \qquad (3.31)$$

c) Shear Solid Viscosity

$$\mu_s = \frac{2\mu_{s_{dil}}}{(1+e)g_0}\left[1 + \frac{4}{5}(1+e) g_o \varepsilon_s\right] + \frac{4}{5}\varepsilon_s^2 \rho_s d_s g_o (1+e)\sqrt{\frac{\theta}{\pi}} \qquad (3.32)$$

d) Particle Phase Dilute Viscosity

$$\mu_{s_{dil}} = \frac{5\sqrt{\pi}}{96}\rho_p d_p \theta^{1/2} \qquad (3.33)$$

e) Bulk Solid Viscosity

$$\xi_s = \frac{4}{3}\varepsilon_s^2 \rho_s d_s g_o (1+e)\sqrt{\frac{\theta}{\pi}} \tag{3.34}$$

f) Collisional Energy Dissipation

$$\gamma_s = 3\left(1-e^2\right)\varepsilon_s^2 \rho_s g_o \theta \left(\frac{4}{d_s}\sqrt{\frac{\theta}{\pi}} - \nabla \cdot v_s\right) \tag{3.35}$$

g) Granular Conductivity of Fluctuating Energy

$$\kappa_s = \frac{2}{(1+e)g_0}\left[1+\frac{6}{5}(1+e)g_o\varepsilon_s\right]^2 \kappa_{dil} + 2\varepsilon_s^2 \rho_s d_s g_o (1+e)\sqrt{\frac{\theta}{\pi}} \tag{3.36}$$

h) Dilute Phase Granular Conductivity

$$\kappa_{dil} = \frac{75}{384}\sqrt{\pi\rho_s}\, d_s \theta^{1/2} \tag{3.37}$$

i) Radial Distribution Function

$$g_o = \left[1-\left(\frac{\varepsilon_s}{\varepsilon_{s,\max}}\right)^{1/3}\right]^{-1} \tag{3.38}$$

3.6.7 The Constitutive Equations for The Viscous Model

3.6.7a Solid Stress Modulus

$$\nabla P_k = G(\varepsilon_k)\nabla \varepsilon_k \tag{3.39}$$

Three correlations of solid modulus were obtained based on empirical correlation and experimental data.

Sun s' solid modulus $G(\varepsilon_g) = 10^{-8.686\varepsilon_g + 6.385}$ (3.40)

Jung s' solid modulus $G(\varepsilon_g) = 10^{-14.926\varepsilon_g + 18.667}$ (3.41)

Huilin s' solid modulus $G(\varepsilon_g) = 10^{-2.475\varepsilon_g + 6.837}$ (3.42)

The first correlation of solid modulus was used in Sun and Gidaspow (1999) to predict a new phenomenon for FCC catalyst flow. The computed data were in agreement with the PSRI experimental results; the computer code can predict the snakelike density oscillations. The solid stress modulus was estimated from the critical velocity equal to 1 m/s at maximum solid volume fraction.

$$V_s = \sqrt{\frac{G}{\rho_s}} \tag{3.43}$$

For the second solid modulus, Jung and Gidaspow (2002) estimated the solid stress modulus of nano-size particle, 10 nm Tullanox. They measured the solid volume fraction as a function of bed height using a γ -ray densitometer in a settling experiment giving the solid pressure as a function of the solids volume fraction, so the derivative of solid pressure equals to solid stress modulus.

The new modulus was calculated by using Huilin's experimental data. He measured the solid pressure of FCC particles in fast-fluidization regime. The solid pressure consisted of 3 parts: kinetic part, collisional part and cohesive part, which was proposed by Gidaspow and Huilin(1998).

$$\frac{P_s}{\rho_s \varepsilon_s \theta} = 1 + 2(1+e)\varepsilon_s g_0 - \left(0.73\varepsilon_s + 8.957\varepsilon_s^2\right) \tag{3.44}$$

The solid modulus is described by solid pressure and solid volume fraction derivative; therefore the new solid modulus included the effect of 3 forces, kinetic, collisional and cohesive forces.

3.6.7b Solids Viscosity

Equation 3.45 for the solids viscosity is based on the experimental data of flow of silica 10 nm in the IIT two-story riser (Gidaspow et al., 2005).

$$\mu_k = 0.017\varepsilon_k^{1/3} g_0 \qquad \text{poise} \tag{3.45}$$

$$g_0 = \left[1 - \left(\frac{\varepsilon_s}{\varepsilon_{s,\max}}\right)^{1/3}\right]^{-1} \tag{3.46}$$

For FCC particle, at the dilute condition ($\varepsilon_s < 0.04$) Miller and Gidaspow estimated the empirical correlation of solids viscosity corresponding to solids volume fraction. This correlation is similar to the correlation which defined by Tuso and Gidaspow (1990).

$$\mu_k = 5\varepsilon_k \qquad \text{poise} \tag{3.47}$$

3.6.8 The Constitutive Equations for Energy Equation (Syamlal and Gidaspow, 1985)

3.6.8a Energy Dissipation Rate (k= f ,1,…,N)

$$\Phi_k = [\tau_k] : \nabla v_k + \tau_{ko} \frac{1}{R} v_k \cdot \nabla R \tag{3.48}$$

3.6.8b Gas-Phase Heat Transfer

$$K_f = 8.65\left(\frac{T_f}{1400}\right)^{1.786} \quad \text{W/m.K} \tag{3.49}$$

3.6.8c Gas-Particle Heat Transfer k (=1,…,N)

for $\varepsilon_f \leq 0.8$ $\quad Nu_k = \left(2 + 1.1\,\mathrm{Re}^{0.6}\,\mathrm{Pr}^{1/3}\right)S_k \quad \mathrm{Re} \leq 200$ (3.50)

$$= 0.123\left(\frac{4\,\mathrm{Re}}{d_k}\right)^{0.183} S_k^{0.17} \quad 200 < \mathrm{Re} \leq 2000 \tag{3.51}$$

$$= 0.61\,\mathrm{Re}^{0.67}\, S_k \quad \mathrm{Re} > 2000 \tag{3.52}$$

for $\varepsilon_f > 0.8$ $\quad Nu_k = \left(2 + 0.16\,\mathrm{Re}^{0.67}\right)S_k \quad \mathrm{Re} \leq 200$ (3.53)

$$= 8.2\,\mathrm{Re}^{0.6}\, S_k \quad 200 < \mathrm{Re} \leq 2000 \tag{3.54}$$

$$= 1.06\,\mathrm{Re}^{0.457}\, S_k \quad \mathrm{Re} > 2000 \tag{3.55}$$

where, $$\mathrm{Re} = \frac{\rho_f \left|\vec{v}_f - \vec{v}_k\right| d_k}{\mu_f} \tag{3.56}$$

$$S_k = \varepsilon_k \frac{6}{d_k} \tag{3.57}$$

$$Nu = \frac{h_{vk} d_k}{k_f} \tag{3.58}$$

3.6.8d Particulate-Phase Heat Transfer k (=1,…,N)

$$\frac{K_k}{K_f} = \left(1 - \sqrt{1-\varepsilon_f}\right)\left[1 + \varepsilon_f \frac{\lambda_R}{\lambda}\right] + \sqrt{1-\varepsilon_f}\left[\varphi \frac{\lambda_s^*}{\lambda} + (1+\varphi)\frac{\lambda_{SO}^*}{\lambda}\right] \tag{3.59}$$

with, $$\frac{\lambda_{SO}^*}{\lambda} = \frac{2}{(N-M)}\left(\frac{B\left(\frac{\lambda_S^*}{\lambda} + \frac{\lambda_R}{\lambda} - 1\right)}{(N-M)^2\left(\frac{\lambda_S^*}{\lambda}\right)} \cdot \ln\left(\frac{\left(\frac{\lambda_S^*}{\lambda} + \frac{\lambda_{SO}^*}{\lambda}\right)}{B}\right)\right.$$

$$\left. - \frac{B-1}{N-M} + \frac{B+1}{2B}\left(\frac{\lambda_R}{\lambda} - B\right)\right) \tag{3.60}$$

$$N - M = 1 + \frac{(\lambda_R/\lambda) - B}{(\lambda_S^*/\lambda)} \tag{3.61}$$

$$B = 1.25\left(\frac{1-\varepsilon_f}{\varepsilon_f}\right)^{10/9} \quad \text{(for spheres)} \tag{3.62}$$

$$\frac{\lambda_R}{\lambda} = \frac{0.0004 C_k}{(2/\varepsilon_r - 1)}\left(\frac{T}{100}\right)^3 \cdot d_k \tag{3.63}$$

$$\frac{\lambda_S^*}{\lambda} = 12.227 \tag{3.64}$$

$\varphi = 7.26 \times 10^{-3}$ The contact area fraction (3.65)

$C_k = 5.67 \times 10^{-8}$ W/m^2.K^4 Stefan-Boltzmann Constant (3.66)

$\varepsilon_r = 0.93$ Emission Ratio (3.67)

CHAPTER IV

KINETIC THEORY BASED CFD SIMULATION OF TURBULENT FLUIDIZATION OF FCC PARTICLES IN A RISER

4.1 Introduction

Fluidization is widely used industrially because of its continuous powder handling ability and its good heat and mass transfer characteristics. The turbulent fluidization regime occurs between the bubbling and the fast fluidization regimes (Berruti, et al. 1995; Bi, et al. 2000; Du, et al. 2003; Gidaspow, et al. 2004; Andreux, et al. 2005). We agree with the recent review by John Grace (2000) that turbulent fluidization and dense suspension flow regimes cover the operations of almost all the key commercial catalytic processes involving gas-solid fluidized beds and that these flow regimes have received very little attention in the literature. Du, et al, 2003 also stated that much remains to be known about this regime.

A turbulent fluidized bed is characterized by two different coexisting regions: a bottom dense, bubbling region and a dilute, dispersed flow region (Berruti, et al. 1995). The solids volume fractions in these two regions can, in principle, be estimated using the drift flux method (Gidaspow, 1994). Unfortunately in this one dimensional approach the slip has to be increased by an order of magnitude above that given by standard correlations to obtain the dense and the dilute volume fractions of solid. In this study we show that the coexistence of these two regions can be computed using the transient, two-dimensional kinetic theory model.

The second characteristic of turbulent fluidization is the high value of the dispersion coefficients for the solids. Du, et al. (2002) show that the dispersion coefficients in the turbulent regime are much higher than in the neighboring flow

regimes. The turbulence can be characterized by the fluctuating properties, the Reynolds stresses. Here we show that our model computes such high dispersion coefficients due to high Reynolds stresses.

In recent years, computational fluid dynamics (CFD) has become a viable tool for process simulation of multiphase flow systems. Further understanding of the hydrodynamic phenomena, including turbulence characteristics is necessary so that a better closure relationship for turbulence can be developed for CFD modeling. The granular flow kinetic theory model was first used by Sinclair and Jackson (1989) to compute the core-annular flow regime in the developed section of the riser. Since the publication of their 1989 classical paper, it has been used by many groups in several countries, -such as by Arastoopour's group (Benyahia, et al. 2000), Sundaresan's group (Agrawal, et al. 2001), Hjertager's group (Mathiesen, et al. 2000), Hrenya and Sinclair (1997), Kuipers' group (Goldschmidt, et al. 2001) and by Simonin (2003) for modeling a complete loop.

In the present study, the standard kinetic theory CFD model (Gidaspow, 1994) with the modified drag, as suggested by Yang, et al. (2004) using the energy minimization multiscale approach has been applied to the study of a gas-particle flow of FCC particles in the riser. This is the first paper to show that the kinetic theory model based CFD can compute the turbulence properties, the Reynolds stresses, the kinetic energy spectra and the dispersion coefficients of gas-solid flow in the turbulent fluidization regime.

4.2 Hydrodynamics Model

For simulation, the IIT code (Ding and Gidaspow, 1990) developed earlier at Illinois Institute of Technology by using the Eulerian-Eulerian approach (or two-fluid

models) is used. The dispersed phase is treated as a continuum. The basic equations given below are the mass, momentum and fluctuating energy equations. The hydrodynamic model B with no gas pressure gradient in the particulate phase momentum is used for gas-solids systems, as discussed by Gidaspow (1994). This multiphase model is based on the fundamental concept of interpenetrating continua for multiphase mixtures. According to this theory, different phases can be presented in the same computational volume at the same time. Such an idea is made possible by the introduction of a new dependent variable, the concentration, ε_i, of each phase *i*.

One of the key points for two-fluid models is how to establish the constitutive correlations for the relationship between the solid stress and the strain. In kinetic theory model, the granular temperature can be predicted by solving partial differential equation for the balance of the fluctuating kinetic energy equation for the particles. The solids pressure and viscosity are regarded as functions of the so-called "granular temperature", a measure of the particles' velocity fluctuations. Although the kinetic theory model seems to be a more reasonable approach to calculate the solid stress than empirical correlations, viscous model.

A kinetic theory based hydrodynamics model with Johnson and Jackson (1987) boundary condition has been developed by Neri and Gidaspow (2000) for flow of FCC particles in the fast fluidization regime. For interphase momentum exchange, this model is used in this study with the Wen and Yu drag law modified as suggested by Li's group (Yang, et al. 2004). This modification proved necessary to achieve the co-existence of dilute and dense regimes. The details are given in appendix 1.

4.2.1 Continuity Equations

$$\frac{\partial(\rho_g \varepsilon_g)}{\partial t} + \nabla \cdot (\rho_g \varepsilon_g \vec{v}_g) = 0 \qquad (4.1)$$

$$\frac{\partial(\rho_s \varepsilon_s)}{\partial t} + \nabla \cdot (\rho_s \varepsilon_s \vec{v}_s) = 0 \tag{4.2}$$

where ρ is the density of each phases, ε is the volume fraction, and $\vec{v}$ is the velcoity vector

4.2.2 Momentum Equations

$$\frac{\partial(\rho_g \varepsilon_g \vec{v}_g)}{\partial t} + \nabla \cdot (\rho_g \varepsilon_g \vec{v}_g \vec{v}_g) = -\nabla P_g + \nabla \vec{T}_g + \beta_B \left(\vec{v}_s - \vec{v}_g\right) + \rho_g \vec{g} \tag{4.3}$$

$$\frac{\partial(\rho_s \varepsilon_s \vec{v}_s)}{\partial t} + \nabla \cdot (\rho_s \varepsilon_s \vec{v}_s \vec{v}_s) = \nabla \vec{T}_s - \beta_B (\vec{v}_s - \vec{v}_g) + \varepsilon_s (\rho_s - \rho_g) \vec{g} \tag{4.4}$$

where P is the pressure, $\vec{T}_g, \vec{T}_s$ is the stress tensor, β is the interface momentum transfer coefficient, and g is the gravity acceleration.

4.2.3 Constitutive Equations

Definitions

$$\varepsilon_g + \varepsilon_s = 1 \tag{4.5}$$

The ideal gas law is used to calculate the gas pressure where T is temperature.

$$P_g = \rho_g \tilde{R} T \tag{4.6}$$

The stress tensor of gas phase using the compressible Newtonian fluid property can be represented as:

$$\vec{T}_g = 2\varepsilon_g \mu_g \vec{\tau}_g \tag{4.7}$$

The solid stress tensor is calculated from the solid pressure, P_s bulk solid viscosity, ξ_s, and shear solid viscosity, μ_s, as

$$\vec{T}_s = \left(-P_s + \xi_s \nabla \cdot \vec{v}_s\right)\vec{I} + 2\mu_s \vec{\tau}_s \tag{4.8}$$

with $(i = g, s)$

$$\vec{\tau}_i = \frac{1}{2}\left[\nabla\vec{v}_i + (\nabla\vec{v}_i)^T\right] - \frac{1}{3}(\nabla\cdot\vec{v}_i)\vec{I} \tag{4.9}$$

4.2.4 Kinetic theory of granular flow

The granular temperature is computed by solving a fluctuating kinetic energy equation for the particles. The solid viscosity and pressure are computed as a function of granular temperature. In order to solve the fluctuating energy equation, we need to specify the collisional energy dissipation, γ_s due to inelastic collisions of particles and the granular conductivity, κ_s.

$$\frac{3}{2}\left[\frac{\partial}{\partial t}(\varepsilon_s\rho_s\theta) + \nabla\cdot(\varepsilon_s\rho_s v_s\theta)\right] = \vec{T}_s : \nabla\vec{v}_s + \nabla\cdot(\kappa_s\nabla\theta) - \gamma_s \tag{4.10}$$

The first term of right hand side is the production of fluctuating energy by the effective shear stresses as described in equation (4.8), the second term is the conduction due to the gradient of granular temperature, and the third term is the dissipation due to the inelastic collision of particles.

The solid properties, the solid pressure, P_s bulk solid viscosity, ξ_s, and shear solid viscosity, μ_s, can be expressed as a function of granular temperature in terms of the following equations:

$$P_s = \rho_s\varepsilon_s\theta\left[1 + 2(1+e)g_o\varepsilon_s\right] \tag{4.11}$$

$$\mu_s = \frac{2\mu_{s_{dil}}}{(1+e)g_0}\left[1 + \frac{4}{5}(1+e)g_o\varepsilon_s\right] + \frac{4}{5}\varepsilon_s^2\rho_s d_s g_o(1+e)\sqrt{\frac{\theta}{\pi}} \tag{4.12}$$

$$\xi_s = \frac{4}{3}\varepsilon_s^2\rho_s d_s g_o(1+e)\sqrt{\frac{\theta}{\pi}} \tag{4.13}$$

where μ_{sdil} is the particle phase dilute viscosity, g_0 is the radial distribution function and e is the restitution coefficient of particles.

$$\mu_{s_{dil}} = \frac{5\sqrt{\pi}}{96}\rho_p d_p \theta^{1/2} \tag{4.14}$$

$$g_o = \left[1 - \left(\frac{\varepsilon_s}{\varepsilon_{s,\max}}\right)^{1/3}\right]^{-1} \tag{4.15}$$

where $\varepsilon_{s,\max}$, the maximum particle packing was 0.64.

The collisional energy dissipation, γ_s, and the granular conductivity of fluctuating energy, κ_s, are calculated as follows:

$$\gamma_s = 3\left(1-e^2\right)\varepsilon_s^2 \rho_s g_o \theta \left(\frac{4}{d_s}\sqrt{\frac{\theta}{\pi}} - \nabla \cdot \vec{v}_s\right) \tag{4.16}$$

$$\kappa_s = \frac{2}{(1+e)g_0}\left[1 + \frac{6}{5}(1+e)g_o \varepsilon_s\right]^2 \kappa_{dil} + 2\varepsilon_s^2 \rho_s d_s g_o (1+e)\sqrt{\frac{\theta}{\pi}} \tag{4.17}$$

where $\kappa_{dil} = \frac{75}{384}\sqrt{\pi \rho_s} d_s \theta^{1/2}$ (4.18)

4.2.5 Interphase momentum exchange

Yang, et al (2004) has shown that for heterogeneous structure, it has the dense-solid rich phase and the dilute-gas rich phase; therefore the drag force can be calculated from three interaction, gas-particle interaction in dense phase, gas-particle interaction in dilute phase and gas-cluster interaction in inter-phase. The energy-minimization multiscale approach was applied for this system. The drag model is very importance for two-phase model and the energy-minimization multiscale approach should be considered as a closure law for drag coefficient. They mentioned that the correction factor computed with the EMMS model is much smaller than that computed with the Wen and Yu/Ergun correlations, which is in reasonable agreement with the conclusions from experimental observations that the drag coefficient decreases as a result of cluster formation.

The Energy Minimization Multi-Scale Approach is used to calculate the drag coefficient using the concept of a cluster (Yang, et al. 2004). In the heterogeneous system, the particles move as clusters and individual particles. It means that the system consists of 3-scales: micro-, meso- and macro-scales. Therefore the gas-solid interactions considered are: gas-particle interaction in dense phase, gas-particle interaction in dilute phase and gas-cluster interaction in the inter-phase as shown in Figure 4.1.

The drag forces are calculated from the three interactions as follows:

$$F_D = M_c F_{dense} + M_i F_{cluster} + M_f F_{dilute} \tag{4.19}$$

where F_D - Drag force

$F_{dense}, F_{cluster}, and\ F_{dilute}$ - Drag force acting on a single or cluster in dense phase, interphase, and dilute phase, respectively

$M_c, M_i, and\ M_f$ - Number of particles or clusters per unit volume in dense phase, interphase, and dilute phase, respectively

The drag coefficient can be estimated from the drag force. The equations are as follows;

$$\beta = 150\frac{\varepsilon_s^2 \mu_g}{\varepsilon_g^2 d_p^2} + 1.75\frac{\rho_g \varepsilon_s}{\varepsilon_g d_p}\left|\vec{v}_g - \vec{v}_s\right| \qquad \text{when} \quad \varepsilon < 0.74 \tag{4.20}$$

$$\beta = \frac{3}{4}C_d \frac{\rho_g \varepsilon_s \left|\vec{v}_g - \vec{v}_s\right|}{d_p}\omega(\varepsilon) \qquad \text{when} \quad \varepsilon \geq 0.74 \tag{4.21}$$

$$\omega(\varepsilon)=\begin{cases}-0.5760+\dfrac{0.0214}{4(\varepsilon-0.7463)^2+0.0044} & (0.74<\varepsilon\le 0.82)\\ -0.0101+\dfrac{0.0038}{4(\varepsilon-0.7789)^2+0.0040} & (0.82<\varepsilon\le 0.97)\\ -31.8295+32.8295\varepsilon & (\varepsilon>0.97)\end{cases} \qquad \textbf{(4.22)}$$

with $C_d=\dfrac{24}{\mathrm{Re}}\left(1+0.15\,\mathrm{Re}^{0.687}\right)$ $\qquad \mathrm{Re}<1000$ (4.23)

$C_d=0.44$ $\qquad \mathrm{Re}\geq 1000$ (4.24)

where Re is the Reynolds number, $\mathrm{Re}=\dfrac{\varepsilon_g\rho_g d_p\left|\vec{v}_g-\vec{v}_s\right|}{\mu_g}$

The modified drag relation for the dense flow used here needs experimental verification. To carry out such a study one needs to measure gas and solids velocities simultaneously. This had been done for dilute vertical gas-solids flow, as reviewed by Gidaspow (1994). Unfortunately for dense flow the measurement of gas velocity requires the development of better experimental techniques. The experimental technique for measurement of oscillations of clusters and of individual particles has been developed by Tartan and Gidaspow (2004) for flow of Geldart group B particles in a riser and for bubbling fluidization by Jung et al. (2005a). The calculations in this study show that the oscillations are mainly due to clusters, as in the experimental study of Jung et al. (2005a) for bubbling beds. In the dilute riser flow studied by Tartan and Gidaspow (2004) the particle oscillations were dominated by individual particle motion in the center of the riser and by cluster motion near the wall.

4.2.6 Initial and boundary Conditions

For initial and boundary conditions, the system conditions studied are those for Wei's cases (1998). Three cases were simulated. Table 4.1 shows the inlet, outlet and boundary conditions. At the inlet, all velocities and volume fractions of both

phases were specified. Initially the riser column was empty and the velocities of both phases were assumed to be zero. At the outlet, an atmosphere pressure was prescribed.

At the wall, the gas a no-slip boundary condition was used, which means the gas tangential and normal velocities were set to zero as described in Figure A.5 in Chapter of Appendix A. The normal velocity of the particles was also set at zero. The following boundary equations were applied for the tangential velocity and granular temperature of particles at the wall. For the granular temperature wall boundary condition, it is obtained by equating the granular flux to collisional dissipation (Johnson & Jackson, 1987)

Table 4.1 Inlet, Outlet and Boundary Conditions Used in the simulation.

Inlet Conditions	Case I	Case II	Case III
Solid mass flux, kg/m^2-s	98.8	132	167
Gas superficial velocity, m/s	3.25	4.57	6.1
Solid volume fraction	0.1	0.1	0.1
Granular temperature, m^2/s^2	0.01	0.01	0.01
Gas Pressure, kPa	118.6	118.6	118.6
Outlet Conditions			
Continuous outflow			
Boundary Conditions			
Solid Phase (Johnson and Jackson, 1987) :			

$$u_{s,w} = -\frac{6\mu_s \varepsilon_{s,\max}}{\sqrt{3}\pi\phi\rho_s\varepsilon_s g_0\sqrt{\theta}}\frac{\partial v_{s,w}}{\partial n}$$

$$\theta_w = -\frac{\kappa\theta}{\gamma_w}\frac{\partial\theta_w}{\partial n} + \frac{\sqrt{3}\pi\phi\rho_s\varepsilon_s v_{s,slip}^2 g_0\theta^{3/2}}{6\varepsilon_{s,\max}\gamma_w}$$

where $$\gamma_w = \frac{\sqrt{3}\pi\left(1-e_w^2\right)\varepsilon_s\rho_s g_0\theta^{3/2}}{4\varepsilon_{s,\max}}$$

Gas Phase :

$$v_{x,w} = v_{y,w} = 0$$

4.2.7 Computational Domain and Scope

The simulations were carried out for the riser section of a circulating fluidized bed based Wei's apparatus shown in Figure 4.2. A Two-dimensional Cartesian coordinates system was used. The system geometry and system properties are defined in Table 4.2. Uniform grids were used. A grid dependency study is described in Appendix 2. In this study, the restitution coefficient (*e*) was approximately determined to be 0.90 (Appendix 3). The specularity coefficient ϕ was 0.6, estimated roughly by Johnson and Jackson (1987) and the restitution coefficient at the wall was assumed to be 0.6 for the particle phase.

Table 4.2 System Geometry and System Properties

Riser diameter	0.186	m.
Riser inlet diameter	0.093	m.
Riser height	8	m.
Particle size	54	μm
Particle density	1398	kg/m^3
Restitution coefficient, e	0.9	
Wall restitution coefficient, e_w	0.6	
Specularity coefficient, ϕ	0.6	
Grid size, $(\Delta x \times \Delta y)$	0.465 cm	× 2.68 cm
Grid number	42 (radial)	× 300 (axial)
Time step	5×10^{-5}	

4.3 Simulation Results

Several simulations have been performed in order to investigate the effect of different operating conditions, model assumptions, and to get an adequate description of the observed two-phase flow pattern in the riser. Most of the results reported below pertain to the same operating condition, but similar considerations can be done for the

other cases performed. Emphasis here is placed particularly on the solid phase volume fraction distribution, power spectrum, velocity distribution of both phases, Reynolds stresses, kinetic energy spectra, granular temperature, turbulent intensity, Particle Pressure, FCC viscosity and dispersion coefficient.

4.3.1 Solid Phase Volume Fraction Distribution

In order to compare the simulation results with the experimental observation of Wei, et al. (1998), time averaged distributions of flow variables have been computed. Several simulations have been performed in order to investigate the effect of different drag coefficients, operating conditions and the flow structure.

Figure 4.3(a) displays the flow structure at the solid flux of 98.8 kg/m^2-s and the gas velocity of 3.25 m/s. The top part of the riser is dilute and the bottom part is dense. The structure at the bottom part is core-annular. There is a low concentration of solids at the center and a high solid volume fraction near the wall, which approximately agrees with the experimental data. The particles move upwards at the center and downwards at the wall. Figure 4.3(b) shows a comparison of experimental and computed void profiles. The computed results were obtained by averaging from 6 sec to 13 sec. The profiles clearly show the transition level of the interface, as presented in Figure 4.3(b). The system consists of 3 parts, the bottom, the interface and the top parts. Over the riser height of 4 to 6 m, there is a fair agreement with the experimental results. But in the bottom and the top parts of the riser, the solid holdup in the simulation is more dilute than in the experiment. The errors of voids are shown in Table 4.3. It may be possible to obtain a denser phase at the bottom, by adding a coulomb type solids stress to the model as describing in Gidaspow's book (1994), but such a study must wait for measurements of the solids stress for FCC particles at dense conditions, 25 to 50 % solids.

Table 4.3 Errors of voids for case I: A comparison of the experiment to computations at three different heights

Heights	2.31 m	3.92 m	6.26 m
Experiments	0.754	0.843	0.958
Simulations	0.806	0.860	0.960
% Error	6.401	1.995	0.164

Figure 4.4 shows a comparison of the dimensionless solids volume fraction profiles for the simulations and the experiments at three different heights at the solid flux of 132 kg/m^2-s and the gas velocity of 4.57 m/s. The computed results were obtained from 6 sec to 13 sec. The computed core-annular structure is similar to the experimental data. In term of average the cross section of bed voidge, the errors of voids at three different heights are given in Table 4.4.

Table 4.4 Errors of voids for case II: A comparison of the experiment to computations at three different heights

Heights	2.31 m	3.92 m	6.26 m
Experiments	0.760	0.934	0.957
Simulations	0.786	0.825	0.922
% Error	3.307	13.269	3.777

Figure 4.5 shows the radial distribution of solids fractions at different axial positions, which are 1.50 m, 2.2 m, 2.9, 5.1 m and 6.20 m. The flux was 167 kg/m^{2}s and the superficial gas velocity was equal to 6.1 m/s. The computed results were obtained from 4 sec to 8 sec. At 1.5 m, 2.2 m and 2.9 m, the flow structures are also core-annular, which is computed at the bottom part of the riser. Moreover at 5.1 cm and 6.2 cm, the profiles are almost flat at the center and high near the right hand sidewall due to the outlet. At the intersection, 2.2 m and 2.9 m, the simulation

computed a denser flow than the experiment. The errors of voids for five different heights are presented in Table 4.5.

Table 4.5 Errors of voids for case III:A comparison of the experiment to computations at four different heights

Height	**1.5 m**	**2.2 m**	**2.9 m**	**5.1 m**	**6.2 m**
Experiments	**0.770**	**0.923**	**0.937**	**0.958**	**0.963**
Simulations	**0.795**	**0.810**	**0.820**	**0.909**	**0.95**
% Error	**3.105**	**13.927**	**14.237**	**5.372**	**1.417**

4.3.2 Power Spectrum

A power spectrum of density fluctuations can distinguish between a well-defined structure, such as a large bubble or a core-annular regime and turbulent flow. When a well-defined structure exits, a sharp peak is obtained for the spectrum. For turbulent flow the spectrum is flat. Du, et al. (2003) studied the power spectrum densities covering the bubbling, the transition and the turbulent regimes. They stated that in the turbulent regimes the dominant frequency is less than 1 Hz due to the large cluster in the emulsion phase. In the dilute section for the core-annular structure the dominant frequency was about 0.2 Hz for the IIT riser. (Huilin, et al. 2001)

The time series solids holdup characteristics in the dense and the dilute phases above the riser inlet, on the right hand side wall, were obtained at the solid flux of 98.8 kg/m^2-s and the gas velocity of 3.25 m/s. Figure 4.6 shows the power spectrum densities corresponding the fluctuations of the solids holdup computed at two points located at 2 and 6 m, respectively. The magnitude of the fluctuations in the dilute section is higher than in the dense section due to larger oscillations. The profiles of power spectrum densities are almost flat in the dense section, as shown in Figure 4. 6(a) due to the movement of bubble and expansion of the emulsion phase with, a

quantitative agreement with Huilin, et al. (2001) and Du, et al. (2003). From Figure 4. 6(b), the diagram highlights a dominant frequency at about 0.28 Hz identifying the core-annular structure in this section. Such estimates are in reasonable agreement with the power spectrum diagrams shown in the box for FCC particles reported by Huilin, et al. 2001. Figure 4.7 shows a comparison of dominant frequency for the measurement for the riser of Miller and Gidaspow (1992), the computation of Neri and Gidaspow (2000) and for this study to an analytical solution obtained from the basic equations of motion, with many approximations. The dominant frequency is obtained from the gravity divided by the riser height. It is corrected by the square root of the solids volume fraction.

4.3.3 Velocity Distribution of Both Phases

Figure 4.8 shows the computed solids velocity vectors in the axial direction at 7, 10 and 13 secs at a solid flux of 98.8 kg/m^2-s and the gas velocity of 3.25 m/s. Figure 4.9 shows a comparison of radial distribution of dimensionless solids axial velocity for the experiment and the simulation at different axial positions. Both the experiment and the computation show the same profiles, parabolic. The particles move upward at the center and downward near the wall. However the value from the experiment is higher than from the simulation, as previously described by Yang, et al. (2004)

A balance between buoyancy and drag obtained from the basic momentum balances for one-dimensional, developed flow is as follows:

$$g(\rho_s - \rho_g) = \frac{\beta_A (v_g - v_s)}{\varepsilon \varepsilon_s} \qquad (4.25)$$

In developed flow, the slip velocity is approximately the terminal velocity. For the Geldart group A particles, the solid velocity is close to the gas velocity in the

direction of the flow. Figure 4.10 shows radial distributions of the time-averaged axial velocity profiles of gas and solids phases at various heights. In the developing section, the slip velocity occurs over the whole cross section of the riser as shown in Figure 4.10(a). At 2 m, the slip was computed only at the center of the riser, due to the effect of inlet as shown in Figure 4.10(c). When the modified drag is used to compute the phenomenon, the drag coefficient decreases as a result of cluster formation. Therefore, the slip velocity is higher than the terminal velocity in this case. The slip velocity is, however, quite small, as expected for FCC particles. Hence the drag correction did not radically affect the flow.

4.3.4 Reynolds Stresses

The principal characteristic of turbulent flow is the production of additional stresses due to random velocity fluctuations, called Reynolds stresses. About two decade ago, NASA funded research has shown that turbulent developed flow in a channel can be computed by the direct numerical simulation of the Navier-Stokes equations. Reynolds stresses and the logarithmic velocity profiles were found to agree with the experiments originally obtained in the 1920 and 1930s. (Kim, et al 1987; Mansour, et al. 1988) The numerical method used was the spectral method originated by Orzag and others in the geophysics community.

Here we have used a similar approach to compute three-phase turbulence, but using the ICE method for solving two coupled Navier-Stokes equations, one for fluid and other for the solid particles.

In the CFD simulation, the hydrodynamic velocities $v(r,t)$ are obtained. The method to define the averaged quantities, the mean velocity particle $\bar{v}(r)$, solid phase normal Reynolds stresses $\overline{v_i^{'}v_i^{'}}$ and shear Reynolds stresses $\overline{v_i^{'}v_j^{'}}$ are given in Table 4.6.

A similar method was used by Dudukovis group (Pan, et al. 2000) to analyze the particle image velocimeter data of Fan's group (Mudde, et al. 1997). Matonis, et al. (2002) used the same method for computation of the stresses for gas-liquid-solid flow.

Table 4.6 Equations for obtaining the averaged velocity and stresses

The mean velocity particle	$\bar{v}_i(r) = \frac{1}{m}\sum_{k=1}^{m} v_{ik}(r,t)$
The normal Reynolds stress	$\overline{v_i^{'}v_i^{'}} = \frac{1}{m}\sum_{k=1}^{m}\left(v_{ik}(r,t)-\bar{v}_i(r)\right)\left(v_{ik}(r,t)-\bar{v}_i(r)\right)$
The shear Reynolds stress	$\overline{v_i^{'}v_j^{'}} = \frac{1}{m}\sum_{k=1}^{m}\left(v_{ik}(r,t)-\bar{v}_i(r)\right)\left(v_{jk}(r,t)-\bar{v}_j(r)\right)$

where, i and j represent x and y directions, m is the total number of data over a given time period.

At the fixed point, the simulation predicted axis and radial hydrodynamics velocity as a function of time. They are fluctuating in a chaotic fashion. The turbulence component or the fluctuated velocities are irregular deviations from a mean valve. The mean value is obtained from the hydrodynamics velocity by making a time average over a number of fluctuations. The hydrodynamics velocity can be regarded as the sum of the mean value and the fluctuating velocities.

Figure 4.11 and 4.12 shows the axial and radial velocity component as well as their time-mean value and their fluctuation for steadily driven turbulent flow in which mean value does not depend on time in difference positions r/R 0.85 and r/R 0.1 at 200 cm.

The computations of turbulence intensities $\overline{v_y^{'}v_y^{'}}$, $\overline{v_x^{'}v_x^{'}}$ and shear Reynolds stress $\overline{v_x^{'}v_y^{'}}$ at the solid mass flux of 98.8 kg/m^2-s and the superficial gas velocity of 3.25 m/s were made. Figure 4.13(a) shows radial distributions of the normal Reynolds stress per unit bulk density in axial direction at three difference heights. At 2 and 4m,

the profiles are almost flat in the dense phase. The oscillations show the same phenomena as occurs in the bubble fluidization (Jung, et al. 2005). At 6 m, the oscillations are high due to the outlet. The time-average values of the normal Reynolds stress per unit bulk density in the radial direction as a function position are plotted in Figure 4.13(b). The normal Reynolds stresses contribute to non-zero Reynolds stresses in the near-wall region. A comparison of the normal Reynolds stresses between axial and radial directions is shown in Figure 4.13(a) and (b). The anisotropic characteristics of the particle fluctuations are clearly shown. The velocity fluctuation is large in the direction of the flow. Figure 4.13(c) shows the time average shear Reynolds stress. It is similar to the computations of the shear Reynolds stress for single-phase flow.

4.3.5 Energy Spectrum

Spectral analysis of turbulent oscillations is common in the study of turbulent single phase flow (Hinze, 1959; Tennekes and Lumley, 1972; Pope, 2000). Frequently the energy spectrum rises sharply with the wave number, reaches a maximum at a low frequency and finally follows the Kolmogorov -5/3 power law at high wave numbers or frequencies. A similar behavior is beginning to be observed in bubble columns (Cui Z. and Fan L. S., 2005, 2004; Pan et al., 2000; Mudde et al., 1997b). In this study we show that our gas-solid model has computed such a behavior in the turbulent fluidization regime.

We can estimate the vertical energy spectrum or the distribution function, $E_y(n)$ from the Fourier transforms of $v'_y v'_y$ using the fast Fourier transform (FFT) technique. Also $E_x(n)$ can be determined from the Fourier transforms of $v'_x v'_x$ which corresponds to a constant average value of $\overline{v'_x v'_x}$ in the lateral direction.

The sum of the distribution function, $E_y(n)$ of all the frequencies, n equals a constant average value of $\overline{v_y^{'} v_y^{'}}$ as follows, $\int_0^\infty dnE_y(n) = \overline{v_y' v_y'}$ (4.26)

Hinze (1959) stated that if the turbulence contains only large eddies, the distribution function $E(n)$ will exist mainly in the region of low frequencies; if there are only small eddies, $E(n)$ will exist mainly in the region of high frequencies

Figure 4.14 shows a comparison of computed spectral distribution, $E_y(n)$ of the vertical turbulence component at 2 m. to Hinze (1959) representation for single phase flow in a channel. For the operating condition in this study the solids flux is 98.8 kg/m^{2}s and the superficial gas velocity is 3.25 m/s.

To estimate the spectral distribution of the turbulence component in the dimensionless form as $\frac{\overline{v_y} E_y(n)}{\overline{v_y' v_y'} \Lambda_f}$ and $\frac{n\Lambda_f}{\overline{v_y}}$ the space integral scale, Λ_f is obtained for the simple relation between the Eulerian integral time scale, T_E (see Dispersion Coefficient section) and time-mean velocity, $\overline{v_y}$.

The procedure to estimate the spectral distribution of the turbulence component in the dimensionless form as $\frac{\overline{v_y} E_y(n)}{\overline{v_y' v_y'} \Lambda_f}$ and

- Plot the time series of $v_y' v_y'$
- Take the Fourier transforms of $v_y' v_y'$ to get the distribution function or the one-dimensional energy spectrum, $E_1(n)$ as a function of frequencies, n
- Estimate a constant average value of $\overline{v_y^{'} v_y^{'}}$ by calculating the area under the graph of $E_y(n)$ versus n

- Calculate the space integral scale, Λ_f by the simple relation between the Eulerian integral time scale, T_E (see dispersion coefficient section) and time-mean velocity, $\overline{v_y}$ which are defined as

$$\Lambda_f = \bar{v}_y T_E \tag{4.27}$$

The dimensionless forms of the spectral distribution in lateral direction can be treated in the same way. The Fourier transforms $E_x(n)$ can be determined.

Dimensions are given in terms of length (L), time (t). Next check the dimensions of the distribution function, $E(n)$, the energy-spectrum function, $E_1(k_1)$, the frequency n and the wave number, k

$$[E(n)] = [L^2 t^{-1}]$$

$$[E(k)] = [L^3 t^{-2}]$$

$$[n] = [t^{-1}]$$

$$[k] = [L^{-1}]$$

The parameters used to calculate the dimensionless forms of the spectral distribution are represented in Table 4.7 the near wall and in the central regions.

Table 4.7 Time-mean velocity, $\overline{v_y}$, the Eulerian integral time scale, T_E and a constant average value of $\overline{v_y' v_y'}$

	$\overline{v_y}$	T_E	$\overline{v'_y v'_y}$
Wall Region	2.462	0.247	3.046
Central Region	4.805	0.102	6.105

The Reynolds number based on the solids flux of 98.8 kg/m^{2}s at 2 m. is 1,200. The simulation results of energy spectral distribution agreed with the single phase flow in a channel at Re 21,500 (Hinze, 1959).

Similar to that for single-phase flow, the energy-containing range and inertial range (Kolmogorov range) can be identified in the energy spectrum. Figure 4.15 shows the computed vertical energy spectra at various heights at solids flux of 98.8 kg/m^2s and superficial gas velocity of 3.25 m/s. For all positions the famous –5/3 Kolmogorov power law is obeyed in the inertial range at high frequencies. At low frequencies the gravity wave and the internal solids circulation play an important role for all positions. The oscillations of particles and clusters increased with the height of the riser which corresponds to the laminar granular temperature and normal Reynolds stress (see Table 4.8). Therefore at high frequencies the turbulent energy varies with the height of the riser. Experiments conducted in the IIT riser with flow of FCC particles showed a similar behavior. The oscillations of volume fractions in the upper dilute section of the riser are much higher than these in the dense bottom section.

To determine the frequency of energy-containing range and inertial range, a comparison of vertical and horizontal wall region energy spectra to the central vertical spectrum in solids phase were obtained and analyzed in the riser at a position of 2 m. ,as shown in Figure 4.16 The power spectra for the central and the near-wall regions show significant differences. The Kolmogorov –5/3 power law is obeyed in the inertial range for both power spectra.

At low frequencies, the energy spectrum, which characterizes the gravity wave and the internal solids circulation, is the same for both the central and the near-wall region due to the existence of a large eddy. In the transition from the energy-containing range to the inertial range, the largest eddy breaks and transfers the energy to smaller eddies with high frequencies. In the near-wall and center regions the transition occurs at 6 Hz. The turbulent energy in the central region is much stronger than that in the near-wall region.

Figure 4.16 also shows that the turbulent energy in the vertical direction is much stronger than that in the horizontal direction due to high Reynolds stress in direction of flow. The Kolmogorov –5/3 power law is obeyed for both directions

4.3.6 Granular Temperature

The granular temperature concept was introduced into the literature by Savage (1983) and accepted as a useful idea in several discussions at multiphase flow meetings sponsored by the National Science Foundation and the U.S. Department of Energy in the 1980 and 1990s. Gidaspow (1994) has reviewed this theory. The first systematic measurements of granular temperature were made by Cody, et al.(1996) at EXXON. They used a shot noise technique to make the measurements. Jung, et al. (2005a) have recently shown that their measurements in the bubbling bed give the granular temperature due to the motion of bubbles and not the true granular temperature due to the random oscillations of particles. Tartan and Gidaspow (2004) used their kinetic theory based particle image method to determine the oscillations, both due to particles and due to clusters.

Neri and Gidaspow (2000) modeled to predict hydrodynamics in riser using kinetic theory. The fluidized particle is FCC catalyst, group A particle. The most significant features of hydrodynamics, the oscillatory-type motion of dense cluster, the time-average core-annular flow regime and the radial and axial nonhomogeneities of the flow were able to predict. Besides the computed granular temperature and the solids viscosity are in a good agreement with experiment. The simulation predicted of granular temperature of 1.5-2 m^2/s^2 and solid viscosity of 0.005-0.008 Pa.s

Tartan and Gidaspow (2004) improved CCD camera technique to estimate instantaneous velocity, hydrodynamic velocity, solid phase normal and shear stresses

Reynolds stresses and granular temperature of 530 micron glass beads in a riser. They have shown that the normal stresses in three directions were obtained of difference values; therefore standard kinetic theory, assuming isotropic flow does not hold. In addition, Reynolds stresses are much smaller in the center region, and larger in near the wall than shear stresses because of the particle oscillation. It means that for fast fluidization, granular temperature due to laminar flow is high at the core region and due to turbulence flow is high at the annular region. Besides they proved that the flow of group B particles oscillates as individual particles.

Jung and Gidaspow (2003) applied the same technique as Tartan and Gidaspow to obtain the hydrodynamics in bubbling fluidization of 530 micron glass beads. The particle granular temperature is lower than the bubble-like granular temperature because in bubbling fluidization, the oscillation is caused by motion of bubble. Both granular temperatures are almost constant at lateral direction. Beside they computed and compared the bubble between simulation and experiment. In simulation, it needs the high order numerical schemes to predict the bubble. There was a good agreement in both results.

Jung, et al. (2005a) and Tartan and Gidaspow (2004) had used a kinetic theory based particle image velocity meter. There are two kinds of turbulence in fluidization (Gidaspow, et al., 2004) :

1. A “laminar” type, due to random oscillations of individual particles, measured by the classical granular temperature and

2. A “turbulent” type, caused by the motion of clusters of particles or bubbles, measured by the average particle normal Reynolds stress.

These two kinds of turbulence give rise to two kinds of mixing, mixing on the level of particles and mixing on the level of clusters or bubbles. To compute the

granular temperature, it must be programmed into the CFD codes. The code itself computes the Reynolds stresses, similar to the calculation of single-phase turbulence by direct numerical computation.

The turbulent granular temperature is defined as the average of the normal Reynolds stresses (Jung, et al. 2005a), which is the average of the three squares of the velocity components in the three directions, by using the following definition;

$$\theta(t,x) \cong \frac{1}{3}\overline{v'_y v'_y} + \frac{1}{3}\overline{v'_x v'_x} + \frac{1}{3}\overline{v'_z v'_z} \tag{4.28}$$

The turbulent kinetic energy in the solid phase can be calculated by

$$E = \frac{1}{2}\overline{v'_y v'_y} + \frac{1}{2}\overline{v'_x v'_x} + \frac{1}{2}\overline{v'_z v'_z} \tag{4.29}$$

where E is the turbulent energy in the solid phase. The simple relation between turbulent granular temperature and the turbulent kinetic energy can be defined as,

$$\theta = \frac{2}{3}E \tag{4.30}$$

Assuming the velocity fluctuations in x and z directions to be equal, the turbulent granular temperature can be calculated as follows:

$$\theta(x,t) = \frac{1}{3}\overline{v'_y v'_y} + \frac{2}{3}\overline{v'_x v'_x} \tag{4.31}$$

Table 4.8 shows a comparison of the computed granular temperature due to the particle oscillations and cluster oscillations as a function of the solid volume fraction. The values were averaged from 6 sec to 13 sec at the solid mass flux of 98.8 kg/m^2-s and the superficial gas velocity of 3.25 m/s for three sections, bottom, interphase and top sections. The laminar granular temperatures were computed from the equation in the CFD code. Similar to the measurement of Cody, et al. (1996) and Jung, et al. (2005b), the granular temperatures are low in the dense, bubbling bed and high in the dilute portion of the riser, as measured by Gidaspow and Huilin (1996;

1998b). Most of the particles move as clusters for Geldart group A particles. Hence the turbulent granular temperature dominates the oscillations.

Table 4.8 A comparison of computed laminar and turbulent granular temperature

Section	Height	ε_s	Granular Temperature $(m/s)^2$	
			Laminar	Turbulent
Bottom	2 m.	0.202	0.001	0.558
Interface	4 m.	0.138	0.016	1.014
Top	6 m.	0.048	0.142	1.675

A comparison of experimental data (Gidaspow and Huilin, 1998b) and the computed values of the property of the turbulent energy of solid phase is given in Table 4.9. The measurements of granular temperature of Gidaspow and Huilin (1996;1998b) were made non-intrusively in the dense annular portion of the riser. They were not velocity averaged, as in the later study of Tartan and Gidaspow (2004) for B particles. Hence they are similar to the measurements of Cody, et al. (1996). They represent the sum of oscillations due to particles and due to clusters. In the riser study at IIT (Gidaspow and Huilin, 1996; 1998b) for flow of FCC particles, visible wall clusters were formed. Hence the reported granular temperature is clearly a combination of "laminar" and "turbulent" components. It is seen that in both experiments and simulations the turbulence in the direction of flow in much stronger than that the horizontal direction.

Table 4.9 Turbulence energy for the solid phase

for W_s = 98.8 kg/m^2-s and U_g = 3.25 m/s

ε_s	Turbulent energy, (m/s)^2		Simulations	Experiments
	$\overline{v'_y v'_y}$	$\overline{v'_x v'_x}$	$\overline{v'_y v'_y} / \overline{v'_x v'_x}$	$\overline{v'_y v'_y} / \overline{v'_x v'_x}$
0.0284	5.083	0.072	70.8	103.9
0.0383	3.696	0.062	59.2	181.7
0.0521	3.512	0.037	93.9	123.0
0.0924	4.239	0.013	320.3	371.1

The sum of the granular temperature due to the particle oscillations and due to the cluster oscillations is the total granular temperature. The cluster oscillations play an importance role in the turbulent fluidization. Figure 4.17 shows the 2/3 of the turbulent kinetic energy or total granular temperature as a function of solid concentrations. The trend agrees with the experiments of Gidaspow and Huilin (1996; 1998b). The percent difference between experiments and simulations is in 40 - 5 % range at the solid volume fraction 0.03 – 0.19. The 2/3 of the turbulent kinetic energy consists of two regimes, kinetic and collisional regimes. In the kinetic regime, the granular temperature is proportional to the solids concentration raised to the power of 2/3. In the collisional regime, the granular temperature decreases due to the decrease of the mean free path.

Figure 4.18 presents a summary of the 2/3 of the turbulent kinetic energy or total granular temperature as a function of gas velocity from the literature and this study for Geldart A and B particles (Campbell and Wang 199; Gidaspow and Huilin 1996; 1998b; Cody, et al 1996; Polasenski and Chen 1999; 1997; Jung, et al. 2005a; Tartan and Gidaspow 2004). It is interesting to see that at the higher superficial gas

velocity the 2/3 of the turbulent kinetic energy is higher than in the lower superficial gas velocity case.

4.3.7 Turbulent Intensity of Geldart A & B

Figure 4.19 shows a comparison of the radial distribution of the turbulent intensity, $\sqrt{\theta}/v_s$ for Geldart A and B particles. For Geldart B particles, Tartan and Gidaspow (2004) measured the granular temperature and the various Reynolds stresses for flow of 530 μm glass beads in a symmetric riser using a kinetic theory based particle image velocity technique. They had found that the Geldarl B particles had a much higher granular temperature in the center of the riser than the corresponding average normal Reynolds stress, that is the turbulent granular temperature due to clusters. Thus mixing for B particles was due to individual particles. However, at the wall the cluster motion dominated the process. The computations in this study show that in the turbulent flow regime the mixing is due to motion of clusters in the center of the riser. This conclusion is consistent with the need for drag law modification. The final proof of this phenomenon awaits direct experimented verification.

In Figure 4.19 the computed granular temperature for the “A” FCC particles is considerably lower than the analytical solution for developed flow and elastic particles. This difference is due to the restitution coefficient of 0.9, found to be the best value in this study. An approximate analytical solution found by Tartan (2003) supports the shape of the computed curve.

4.3.8 Particle Pressure

Gidaspow and Huilin (1998) studied the equation of state and radial distribution functions of 75 micron FCC catalyst in a circulation fluidized bed. The solid pressure was measured using particle pressure transducer and the radial distribution function was obtained using CCD camera technique. In addition, the equation of state is relation between the solid pressure, granular temperature and bulk density. It consisted of three parts, kinetic, collisional and cohesive parts.

In the dilute regime and the ideal gas/solid system, the mechanism employed is the same as the ideal gas law. The equation of state is

$$P = \varepsilon_s \rho_s \theta \qquad \text{Kinetic Mechanism} \qquad (4.32)$$

When the system become high density, the addition term of a collisional part is necessary, as following

$$P = [2(1+e)\varepsilon_s g_o]\rho_s \varepsilon_s \theta \qquad \text{Collisional Part} \qquad (4.33)$$

When the system is the flow of group A or C particles, there is a decrease in the overall solids pressure due to the cohesive force between the particles and defined as

$$P = -(0.73\varepsilon_s + 8.957\varepsilon_s^2)\rho_s \varepsilon_s \theta \quad \text{Cohesive Part} \qquad (4.34)$$

As stated by Gidaspow and Huilin (1998) the combination of all these forces gives an overall solids pressure as

$$\frac{P_s}{\rho_s \varepsilon_s \theta} = 1 + 2(1+e)\varepsilon_s g_0 - (0.73\varepsilon_s + 8.957\varepsilon_s^2) \qquad (4.35)$$

For relation between solid pressure and radial distribution function, the granular temperature of FCC catalyst was obtained of 1-2 m/s^2. The granular temperature increased with solid mass flux at the same gas velocity.

The profile of the particulate pressure based on the calculated total granular temperature as a function of solid volume fraction is shown as Figure 4.20 at the gas

velocity and solid mass flux of 3.25 m/s and 98.8 kg/m^2-s, respectively. In the range of solid concentration about 0.03-0.3, the particulate pressure increases with increasing solid concentration. The computation agrees with the experimental data measured with a special particle pressure transducer by Huilin and Gidaspow (1998).

The solid stress modulus is the gradient of solids pressure, as described in Gidaspow (1994). If we look at the balance of momentum for the solid in the y direction, the gradient can be written as,

$$\nabla P_s = \frac{\partial P_s}{\partial y} \tag{4.36}$$

The solid pressure is a function of gas volume fraction in the system

$$P_s = P_s(\varepsilon) \tag{4.37}$$

Applying the chain rule, we get the relation.

$$\nabla P_s = G(\varepsilon_g)\nabla \varepsilon_g \tag{4.38}$$

The particle-to-particle interaction coefficient is defined as:

$$G = \frac{\partial P_s}{\partial \varepsilon_s} \tag{4.39}$$

The solid modulus is expressed as a function of the gas volume fraction. An exponential form is used. From the computed particular pressure, the solid stress modulus is obtained as follow:

$$G(\varepsilon_g) = 10^{-2.475\varepsilon_g + 6.837} \tag{4.40}$$

4.3.9 FCC viscosity

One of the transport coefficients is the solid viscosity. In the kinetic theory model, the solids viscosity is a function of granular temperature as following;

$$\mu_s = \frac{2\mu_{s_{dil}}}{(1+e)g_0}\left[1+\frac{4}{5}(1+e)g_o\varepsilon_s\right] + \frac{4}{5}\varepsilon_s^2\rho_s d_s g_o(1+e)\sqrt{\frac{\theta}{\pi}} \tag{4.41}$$

where μ_{sdil} is the particle phase dilute viscosity and e is the restitution coefficient of particles.

$$\mu_{s_{dil}} = \frac{5\sqrt{\pi}}{96}\rho_p d_p \theta^{1/2} \tag{4.42}$$

Figure 4.21 shows the computed solids viscosity as a function of solid concentration based on the calculated total granular temperature. The solid viscosity increases with increasing the solid concentration. The empirical correlation is given by Huilin and Gidaspow (1998), corrected for slightly different solids density and diameter, as

$$\mu_s = 0.014\varepsilon_s^{1/3} g_0 \tag{4.43}$$

The radial distribution function at contact, g_0, is calculated as follows:

$$g_o = \left[1 - \left(\frac{\varepsilon_s}{\varepsilon_{s,\max}}\right)^{1/3}\right]^{-1} \tag{4.44}$$

where the maximum solids packing, $\varepsilon_{s,\max}$ was 0.64.

There is an excellent agreement between the computed FCC viscosity and the correlation near 5 %solids. At high solids concentration, there is a systematic deviation probably because the concentration was obtained for much lower solids fluxes and hence probably lower shear rates. Also Huilin and Gidaspow (2003) presented the same type of graph for FCC particles. They showed the values of solid viscosity were the same order of magnitude. They mentioned that it is mainly due to the under-prediction of the total granular temperature in the simulations. The prediction of a more accurate granular temperature would lead to a more realistic prediction of solids viscosity and flow pattern of gas–solids flow in the riser. This granular temperature under-prediction may possibly be linked to the formulation of the solids velocity and granular temperature boundary conditions.

4.3.10 Dispersion Coefficient

A measurement of the quality of mass transfer is the particle diffusivity or dispersion coefficient. A review of the literature (Potter, 1971; Bi, et al. 2000; Du, et al. 2002; Gidaspow, et al. 2004) shows that they vary by five orders of magnitude.

Similar to the granular temperature we can identify two types of dispersion coefficients:

1. due to particle oscillations, “laminar”
2. due to cluster or bubble, “turbulent”

These two kinds of turbulence give rise to two kinds of mixing, mixing on the level of particles and mixing on the level of clusters or bubbles. Furthermore, it is well known in fluidization that the dispersion coefficients are very anisotropic.

Dispersion coefficient due to individual particles oscillations An order of magnitude estimate of the dispersion coefficient due to individual particles oscillations can be obtained from the laminar granular temperature divided by the dominant frequency

$$D_{particles\quad oscillations} \approx \frac{\theta_{la\min ar}}{f} \tag{4.45}$$

In the dilute section (6 m), the main frequency is 0.28 Hz (see Figure 4.6b) and the laminar granular temperature is 0.142 m^2/s^2 (see Table 4.8). Therefore an order of magnitude estimate of dispersion coefficient due to individual particle motion is approximately 0.5 m^2/s. However in the dense section, the laminar granular temperature is very low, so the overall dispersion coefficient comes from the fluctuations of the clusters.

Dispersion coefficient due to cluster oscillations can be defined as a function of normal Reynolds stress corresponding the Lagrangian integral time scale. The

long-time diffusion coefficients in the radial and axial directions are expressed as in Taylor (1921),

$$D_L(a) = \overline{v'(a)^2} T_L \tag{4.46}$$

where $\overline{v'(a)^2}$ is the mean square particle fluctuating velocity corresponding to normal Reynolds stress and T_L is the Lagrangian integral time scale of the particle motion, defined by

$$T_L = \int_0^\infty R_L(\vec{a}, t')dt' = \int_0^\infty \frac{\overline{v'(t)v'(t+t')}}{\overline{v'^2}} dt' \tag{4.47}$$

where v' here is Largrangian velocity fluctuations and the particle autocorrelation, given by

$$R_L(\vec{a}, t') = \frac{\overline{v'(t)v'(t+t')}}{\overline{v'^2}} \tag{4.48}$$

Eulerian turbulence characteristics can be obtained from Lagrangian turbulence characteristic. (Hinze, 1965) The relationship between the Eulerian and the Lagrangian turbulence characteristics has been given by Hay and Pasquil as,

$$T_L = \beta T_E \tag{4.49}$$

where, β is the coefficient, T_E is the Eulerian integral time scale of the particle motion, given by

$$T_E = \int_0^\infty \frac{\overline{v'(t)v'(t+t')}}{\overline{v'^2}} dt' \tag{4.50}$$

and v' refers to Eulerian velocity fluctuations at a point.

Tennekes and Lumley (1972) stated that we should not take the values of the coefficients too seriously. In order to estimate the order of magnitude of the diffusion coefficient, the Eulerian integral time scale approximately equals Lagrangian integral time scale.

$$T_L \approx T_E \tag{4.51}$$

Figure 4.22 shows some typical plots of the autocorrelation coefficients in the radial and axial directions at the solid flux of 98.8 kg/m^2-s and the gas velocity of 3.25 m/s. The autocorrelation coefficients decay with the time from the maximum value of one, and go to zero. For the radial autocorrelation, the profile dips below zero, then oscillates to a stationary value of zero due to the wall limitation of x direction. For the direction of flow, the autocorrelation coefficient simply decayed exponentially, corresponding to Roy, et al. (2005) in a liquid-solid riser.

Figure 4.23 shows the radial distribution of the dispersion in radial and axial directions, respectively. The axial dispersion coefficient is larger in the direction of flow. Therefore dispersion coefficients are frequently anisotropic. The effect of gas superficial velocity on the radial and axial dispersion coefficient is shown as Figure 4. 24. The computed dispersion coefficients showed the same order of magnitude as the literature. (Du, et al. 2002; Thiel and Potter 1978; Avidan and Yerushalmi 1985; Wei, et al. 1995; Wei, et al. 1998; Koenigsdorff and Werther, 1995) Also reviews of the literature (Potter, 1971, Bi, et al. 2000 and Du, et al. 2002) show that they vary by five orders of magnitude and that there exits no reliable predictive theory for estimating these diffusivities.

Figure 4.25 shows the snapshot of solid volume fractions to show the computed clusters at 6.5, 7.5 and 8.5 seconds. The length and width of clusters can be approximated from characteristic lengths estimated from the relation between the diffusivity and the oscillating velocity as (Gidaspow 1994);

Diffusivity (D) = characteristics length x oscillating velocity (4.52)

The oscillating velocities are obtained from the square root of normal Reynolds stress. Figure 4.26 shows radial the distribution of characteristics lengths in

the axial and the radial directions. The length and width of clusters depended on the position corresponding to Figure 4.25. The lengths and widths of cluster are approximately 10-100 cm and 0.5-4 cm, respectively.

We have shown that the anisotropic behavior of turbulent flow can be computed using the present kinetic theory CFD code, with only a small correction for the drag. To compute the isotropy for the “laminar” part, one must add the moment equation for the radial component of the stress to the present theory. Strumendo (2003) and Strumendo, et al. (2005) have solved such an equation set for the developed flow in the riser. This was a generalization of the classical paper of Sinclair and Jackson (1987). However, the dissipation was taken to be primarily due to gas-particle interaction. Hence the normal stresses turned out to be much smaller than those measured by Tartan and Gidaspow (2004).

4.3.11 The Production Terms of Turbulent Kinetic Energy

A complete numerical study of gas-particle flow should involve the computation of Reynolds stress budgets for the particle and gas phases. For single-phase flow, this has been done (Mansour, et al. 1988; Kitoh 1991) for direct numerical simulation of fully developed flow in a channel. For gas-particle flow, there is still a debate going on as to whether the production of turbulence is due to the gradient of particle velocity, as in the kinetic theory based CFD used here a whether it is due to production of turbulence due to slip (Bryan, et al. 1998). Table 4.10 shows the production terms of turbulent kinetic energy that can be calculated from the Reynolds stresses multiplied by the gradient of solids velocity. The production due to slip velocity can be expressed as follows:

$$P_{slip\quad velocity} = \beta_B v_{slip}^2 \tag{4.53}$$

Table 4.10 The production terms of turbulent kinetic energy

yy component	$2\overline{v'_y v'_y}\dfrac{\partial v_y}{\partial x}$
xx and zz components	0
xy component	$\overline{v'_x v'_y}\dfrac{\partial v_y}{\partial x}$

We show here the production due to velocity gradient and due to slip. The results are presented in dimensionless form following the theory of Strumendo, et al. (2005). The scale factors are the radius of the riser, R_r, the intrinsic density of FCC particle, ρ_s and average solid velocity, c_{vel}. The constant c_{vel} was expressed as $\sqrt{|g|R_r}$. Therefore, the production terms of turbulent kinetic energy are multiplied by R_r and divided by the cube of c_{vel} to get dimensionless form. Figure 4.27 shows the production term of turbulent kinetic energy in the yy direction for three different operating conditions. The profiles have two peaks due to the motion of downward of gas and solid phase along the wall. The production is high near the wall and then decreases toward the center of the riser. The profiles are similar for the three operating conditions. A dimensionless of production terms of turbulent kinetic energy in xy direction is shown in Figure 4.28. The trends of profiles show the same behavior as the gradient of particles velocity and shear Reynolds stress. For production of turbulence due to slip, to get a dimensionless form, this term $\beta_B v_{slip}^2$ is multiplied by R_r, divided by ρ_s and the cube of c_{vel}. Figure 4.29 shows the production term due to slip at a solid flux of 98.8 kg/m^2-s and the gas velocity of 3.25 m/s. The slip productions decrease with increasing the height.

4.4 Conclusions

1. We have shown that the standard kinetic theory based CFD model with a modified drag as suggested by Jinghai Li group, is capable of correctly describing the coexistence of the dense and dilute regimes for flow of FCC particles in a riser in the turbulent regime.

2. The CFD simulations compare well with the high density riser experiment of Wei, et al. (1998) for three high solid fluxes of commercial interest. The computed void fractions agree within 10% with the experiment at three different heights. For the three fluxes, we computed the observed core-annular regime at the bottom of the riser. However the computed ratio of particles to gas velocity at the center of the riser was considerably below that reported for the measurement of Wei, et al. (1998) similar to that computed by Jinghai Li group. The computed solids and gas velocity were close to each other, as expected for Geldart group A particles. The developed slip velocity was, however, almost two times higher than the terminal velocity of FCC particles, reflecting the Li group drag correction.

3. In the dense portion of the riser, the power spectrum of solid volume fraction is almost flat, in agreement with measurements reported in the literature (e.g. Gidaspow, et al. 2001). However, in the dilute phase of the riser, there was a distinct peak at a frequency of about 0.28 Hz. This is an indication of a distinct core-annular structure.

4. Frequency analysis reveals the famous –5/3 Kolmogorov power law at the higher frequencies, similar to many single-phase flows.

5. The turbulent kinetic energy, essentially the total granular temperature, of the FCC particles agreed with the measurements of the granular temperature of Gidaspow and Huilin (1996) determined in the dense-annular region of the riser, where clusters

were observed. The computed solids pressure also agreed with the measurements done with a special transducer. The computed solid viscosity, again, agreed with the measurements in the riser done with the three different instruments: PIV meter, Brookfiled viscometer and pressure drop minus weight of the bed measurements. Near 5% the computed solids viscosity compares well with the correlation for FCC particles of Gidaspow and Huilin (1998), but is about 30% lower at 25% solids holdup.

6. The CFD code also computed the turbulent characteristics of flow, of importance for the dispersion of particles. In the literature (e.g. Du, et al. 2002) it is well known that the radial dispersion coefficient is much smaller than the dispersion coefficient in the direction of the flow. Dispersion coefficients were computed as a function of radial and axial position. The computed dispersion coefficients are similar to the measurements reported in the literature.

7. The computed dispersion coefficients and the normal stresses allow the computation of characteristic lengths of clusters. The length and width agree with snapshot of volume fraction of solids.

สถาบันวิทยบริการ
จุฬาลงกรณ์มหาวิทยาลัย

4.5 Appendix 1. Comparison of modified drag to classical drag

The corresponding snapshots of the solids concentration distribution at 7.8 s from the beginning of the simulation at a gas velocity and a solids mass flux of 4.57 m/s and 132 kg/m^2-s respectively, are shown in Figure 4.30. It can be seen that the simulated flow structures for the two drag models are different. The turbulent regime, the dilute phase at the top section and the dense phase at the bottom section was computed correctly using the modified drag, because the drag coefficient decreases as a result of cluster formation, which is described in Yang, et al. (2004).

4.6 Appendix 2. The convergence due to increment size

No numerical simulation is complete without a study of grid size dependence. (Gelderbloom, et al. 2003) In the two-dimensional computational domain, the increment sizes in x and y directions were varied. When the coefficient of restitution equals 0.99, the computed solid volume fraction due to changing grid size in y direction is shown in Figure 4.31(a). The riser domains were 298×2.68, 596×1.34 and 894×0.893 in y direction and 20×0.93 in x direction of the numbers of cell multiply by increment size. Figure 4.31(b) shows the computed solid volume fraction due to changing grid size in x direction, 20×0.93, 40×0.465, and 60×0.31 and 298×2.68 in y direction. In order to get the reasonable results and minimize the round-off errors, the computational domain was 298×2.68 in y direction and 40×0.465 in x direction.

4.7 Appendix 3. The coefficient of restitution

The coefficient of restitution is an empirical input in the kinetic theory based CFD model. It is obtained by matching the experiment with the theory. It can, in

principle, be obtained from an independent measurement using a CCD camera. However, such a measurement must be done in the dense region near the experimental particle velocity. Therdthianwong, et al. (2003) showed that in the kinetic theory model there is a degree of sensitivity to the coefficient of restitution, e. A comparison of the coefficient of restitution as a function of the bed void in the axial direction is shown in Figure 4.32. The condition is 98.8 kg/m^2-s for the solid flux and 3.25 m/s for the superficial velocity. The simulation with the coefficient of restitution 0.99 cannot give a good resolution for the bubble formation at the bottom part. Hence the solid concentration is almost the same value along the riser, as described by Jung, et al. (2005b). Therefore reducing the coefficient of restitution helps to get reasonable results for the turbulent regime due to the increased effect of particle-particle collisions in the dense phase. In order to obtain this regime, the coefficient of restitution was maintained as 0.9. The simulation results then came close to the experimental data.

4.8 Appendix 4. The electrostatic effect

In previous study, we have shown that the standard kinetic theory based CFD model with a modified drag as suggested by Yang, et al. (2004), is capable of correctly describing the coexistence of the dense and dilute regimes for flow of FCC particles in a riser in the turbulent regime. The CFD simulations compared well with the high density riser experiment of Wei, et al. (1998) for three high solid fluxes of commercial interest.

In the multiphase flow consortium meetings the effect of surface charge was discussed. Al-Adel, et al. (2002) have given an alternate explanation for the development of the core-annular regime in a riser. Here we have applied their model

to predict segregation. The detail of the momentum equation with the electric field was described in Chapter VI.

Guo Y. (1997) used a ball probe to measure the charge of 75 micron FCC particles in the IIT riser. The probe was placed into the solid flow stream and picked up the current. Table 4.11 shows the charge of FCC particles at different conditions. The particle charge increases with superficial velocity and average solid flux.

Table 4.11 Charge of FCC particles

Superficial gas velocity	U_g	m/s	2.61	2.89	2.89	3.48
Solid flux	G_s	kg/m^2.s	19.5	11.5	18.6	21.5
Particle charge	$q_e \times 10^{-13}$	coulomb	1.98	2.22	2.26	3.13
Charge per mass	$Q_e \times 10^{-4}$	coulomb/kg	5.42	6.08	6.13	8.5

Riser simulation based on the experiment of Wei, et al. (1998) was obtained. The particles carry a prescribed charge. We examine the influence of this charge on the hydrodynamics. The measurements of particle charge suggest that the amount of charge carried by the particles should change with flow conditions. To compute the flow of FCC particles in a riser the charge is decreased from the measured values (Guo Y., 1997) to obtain the simulation results. The 75 micron FCC particles are negatively charged with approximately, 3.25×10^{-7} C/kg.

Figure 4.33 shows the corresponding snapshots of the solids concentration distribution at a gas velocity and a solids mass flux of 4.57 m/s and 132 kg/m^2-s, respectively. The FCC charge used in this simulation is approximately 3.25×10^{-7} C/kg. The CFD codes with electric field effect can capture important qualitative features of turbulent regime, the dilute phase at the top section and the dense phase at the bottom section. Hence the bed gets denser all over the riser because

the electric force exists in the whole riser. If the mechanism of changing the charge of particles is due to the collision, at the bottom part the charge of particle should be higher than at the top part due to high collision of particles. Hence the simulations with the electric force might predict the right phenomena.

We have compared the forces between gravity force, $F_g = \rho_s \varepsilon_s g$ and electric force, $F_e = q_e \rho_s \varepsilon_s \vec{E}$. At 2 m, at the center of the riser, the solid volume fraction and the electric filed strength are 0.17 and 495,203 V/m, respectively. Hence the gravity force and the electric force are approximately 2332 and 38.3 $\frac{kg}{m^2 s^2}$, respectively. The electric force is another body force similarly to the gravity force that helps keeping the bed inside the system.

Figure 4.34 shows a comparison of the solids volume fraction profiles with the simulation with the electric field effect and the experiment at bottom section, 2.31 m at the solid flux of 132 kg/m^2-s and the gas velocity of 4.57 m/s. The computed core-annular structure is similar to the experimental data. At the annular section the computed solid volume fraction is close to that of the experimental data. Hence the computed solid volume fraction is denser than that of the experimental data. In terms of average cross section of bed voidge, the errors of voids at three different heights are given in Table 4.12.

Table 4.12 Errors of voids: A comparison of the experiment to computations with the electric field at three different heights

	2.31 m	3.92 m	6.26 m
Experiments	0.77	0.81	0.85
Simulations	0.76	0.93	0.96
% Error	0.88	13.34	11.12

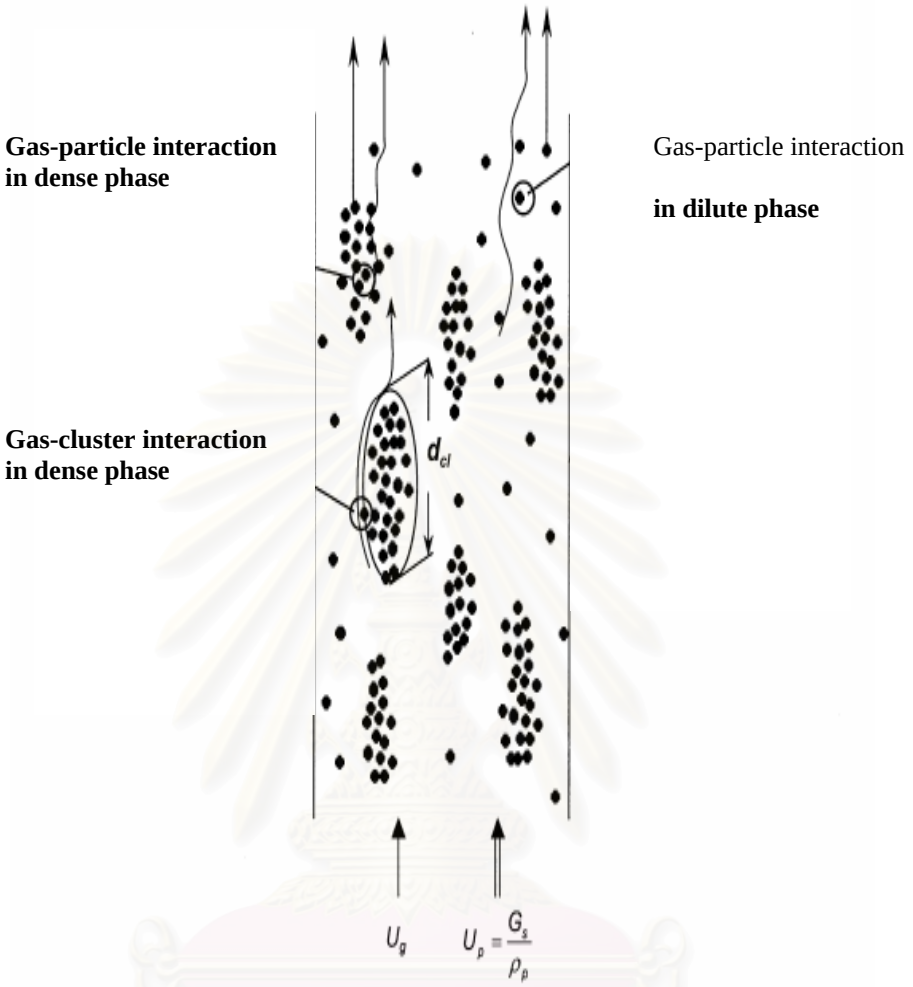

Figure 4.1 Three interactions in heterogeneous flow structure

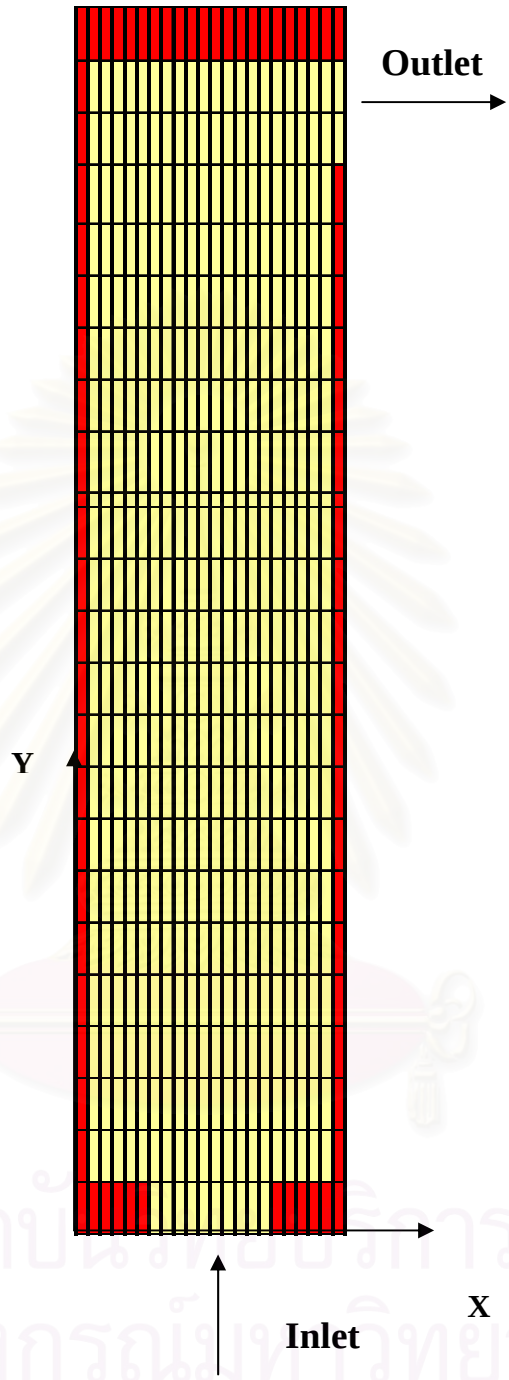

Figure 4.2 System geometry for simulations of Wei et al., (1998a) experiments.

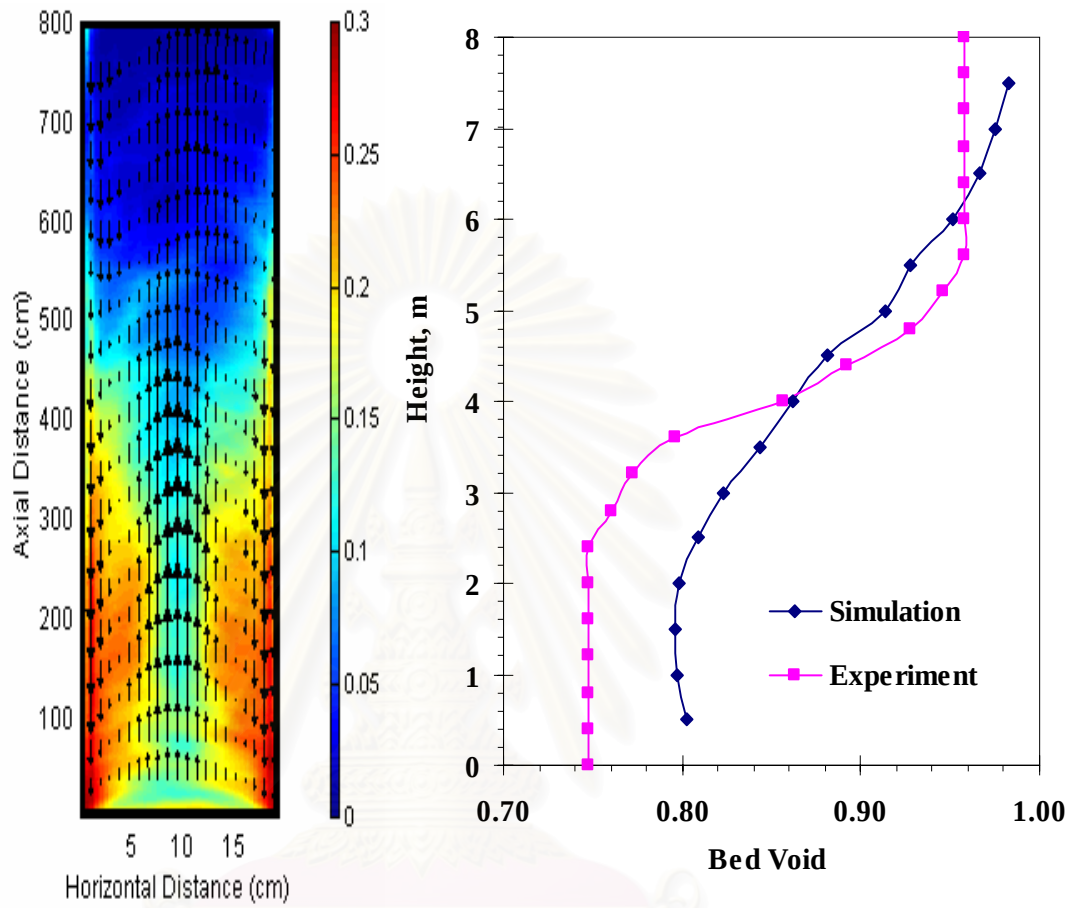

(a) (b)

Figure 4.3 (a) The computed solid volume fraction structure.
(b) A comparison of experimental and computed void profiles for W_s = 98.8 kg/m^2-s and U_g = 3.25 m/s averaged from 6 sec to 13 sec.

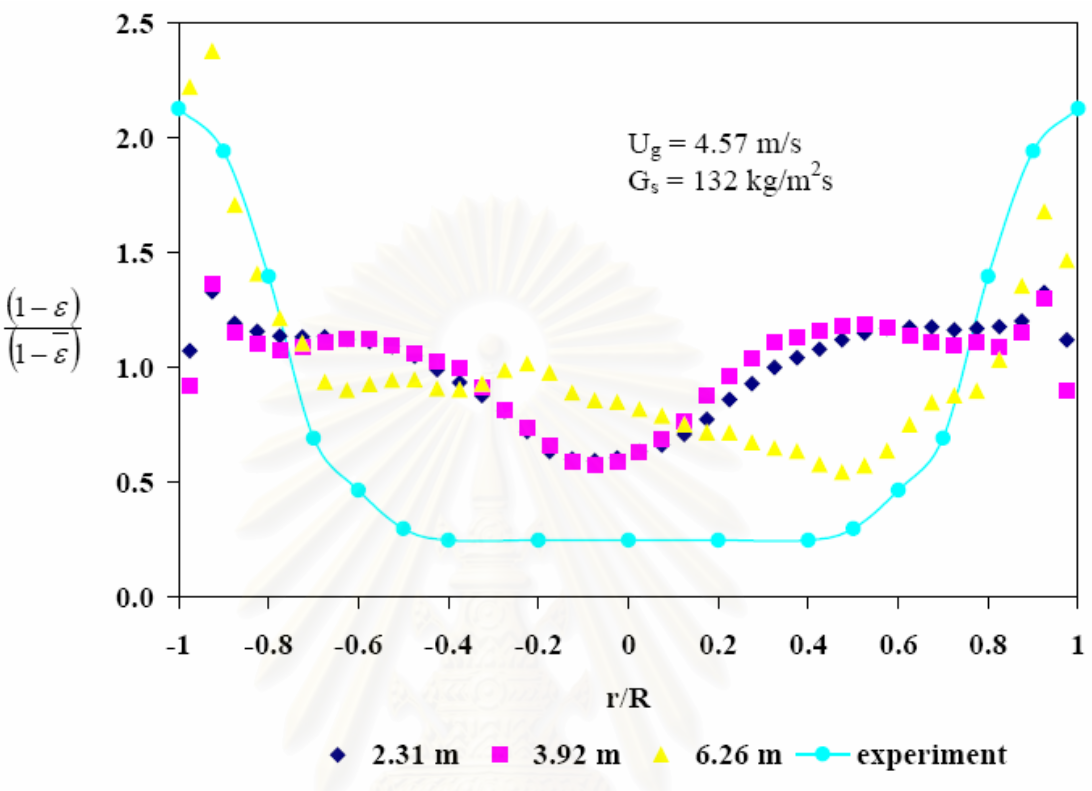

Figure 4.4 Comparison between experimental and computational results of dimensionless computed solids volume fraction profiles. Solids flux = 132 kg/m^{2}s and superficial gas velocity = 4.57 m/s. Computed values were averaged from 6 sec to 13 sec. Experiments values were averaged from three difference heights.

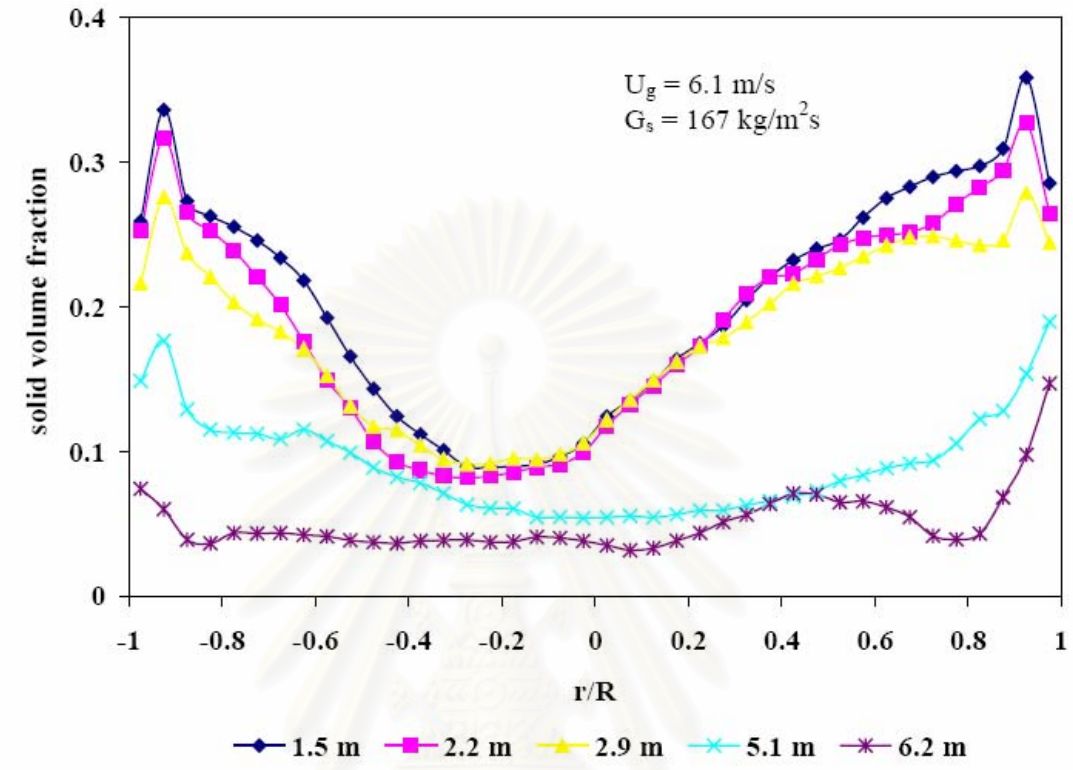

Figure 4.5 Radial distributions of computed solids fraction at various axial positions

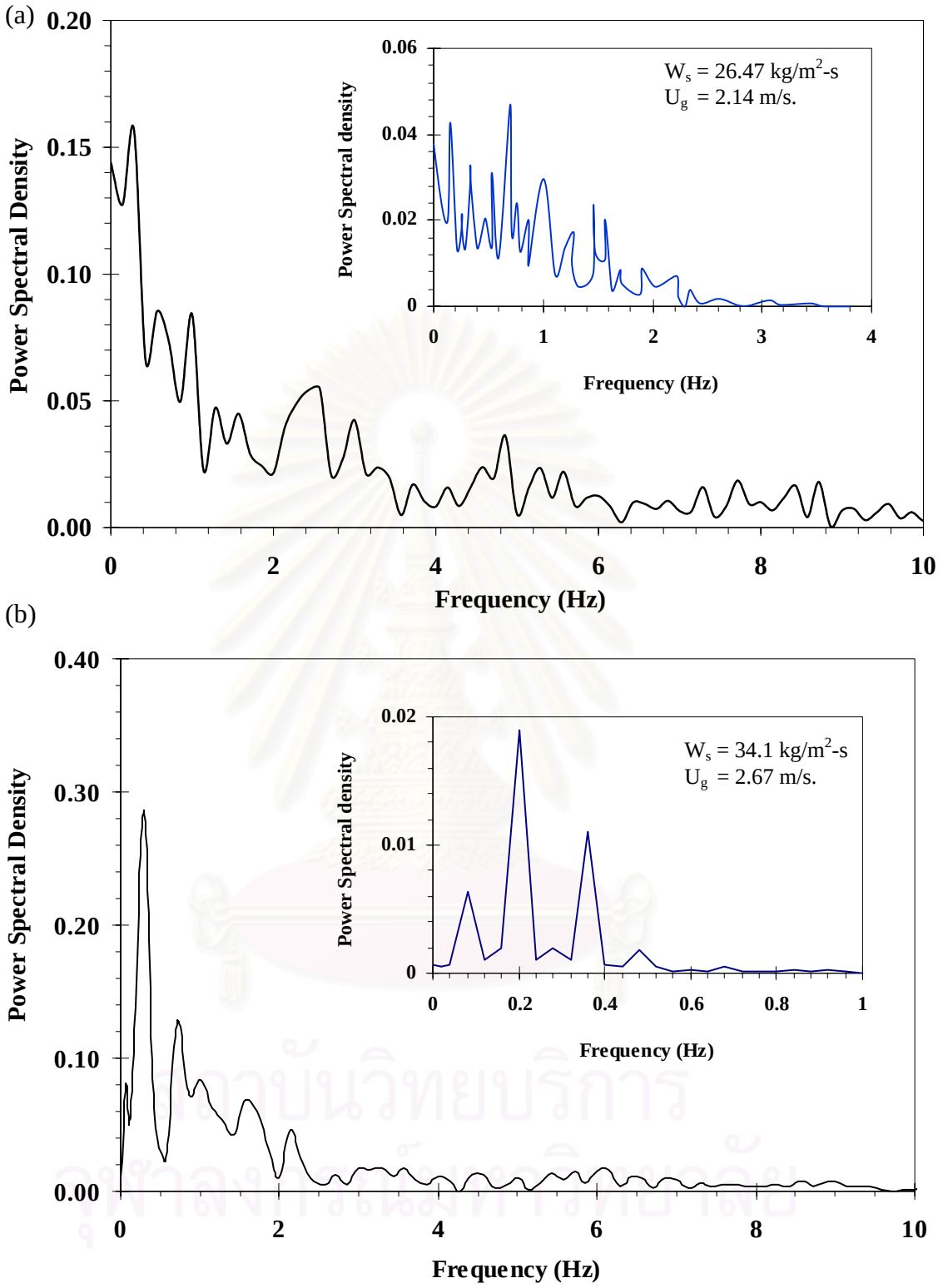

Figure 4.6 Power spectrum density of solids volume fraction fluctuations at (a) dense region, 2m. (b) dilute region, 6m. on right hand side wall for W_s = 98.8 kg/m^2-s and U_g = 3.25 m/s.

The box represents power spectrum density of porosity fluctuations (Gidaspow et al. 2001)

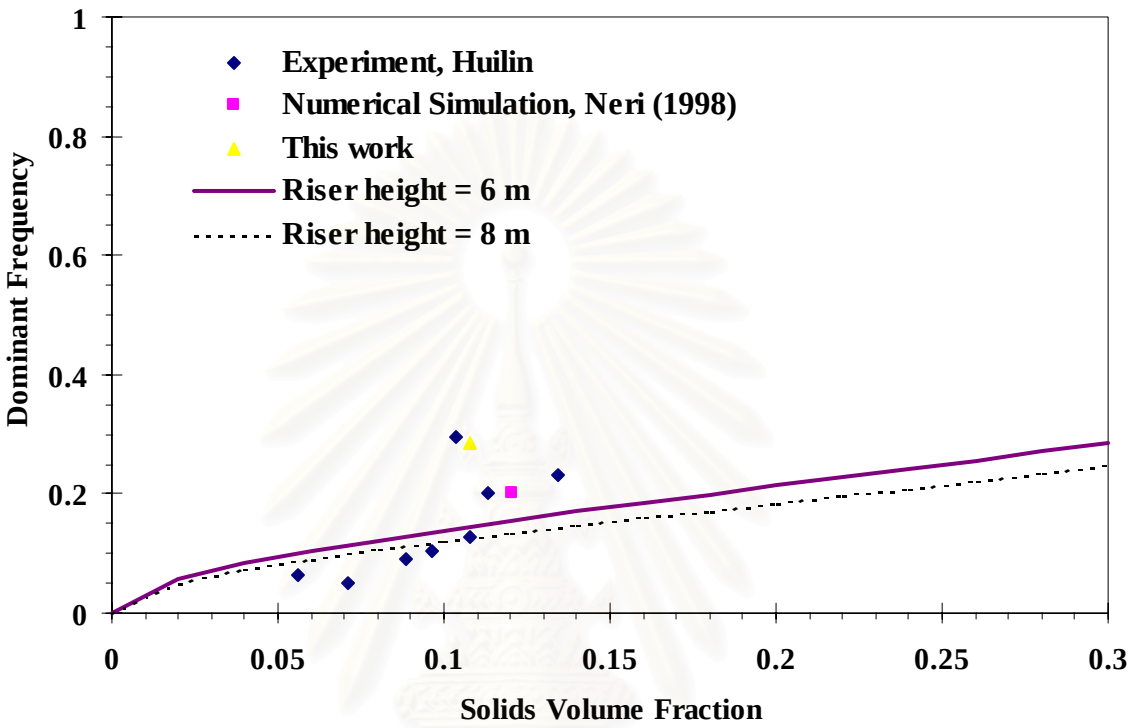

$$f = \frac{1}{2\pi}\left(\frac{g}{X_0}\right)^{\frac{1}{2}}\left[\frac{(3\varepsilon_s/\varepsilon+2)\varepsilon_s}{\varepsilon_{so}}\right]^{\frac{1}{2}} \quad ; \quad \varepsilon_{s0} = 0.5 \quad ; \quad X_0 \text{ is riser height}$$

Figure 4.7 A Comparison of riser dominant frequency, f to the analytical solution

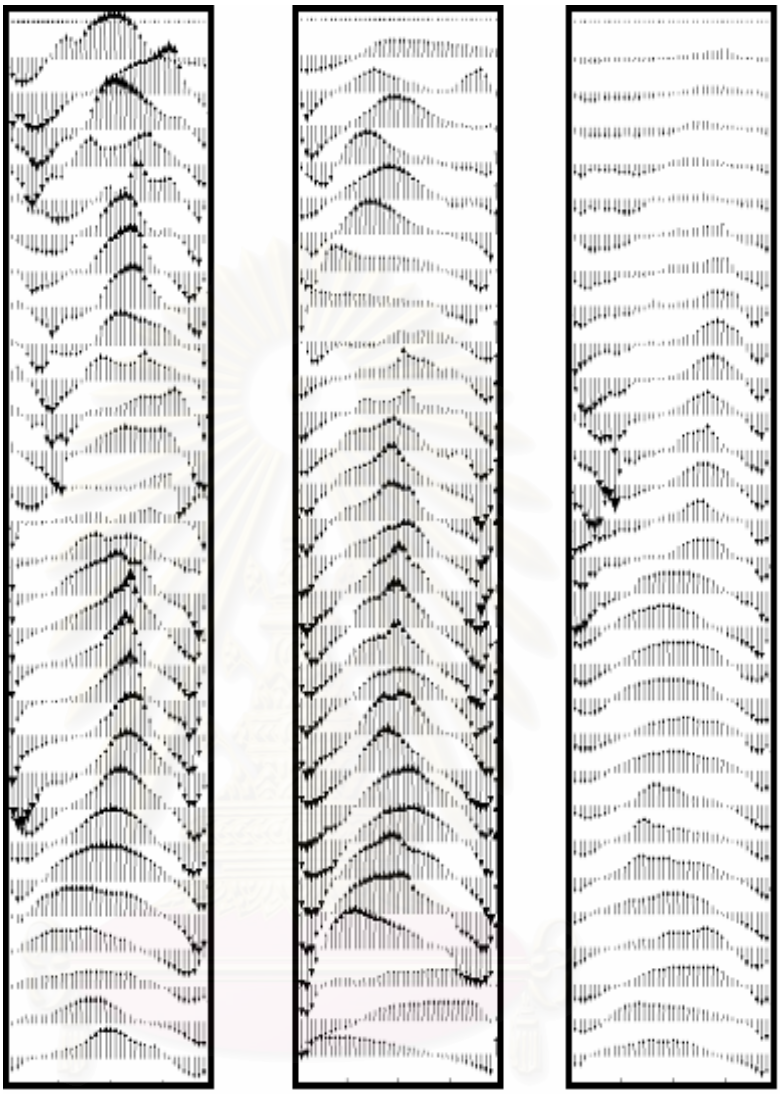

7 sec 10sec 13sec

Figure 4.8 The computed solids velocity vectors in axial direction at 7, 10 and 13secs for W_s = 98.8 kg/m^2-s and U_g = 3.25 m/s.

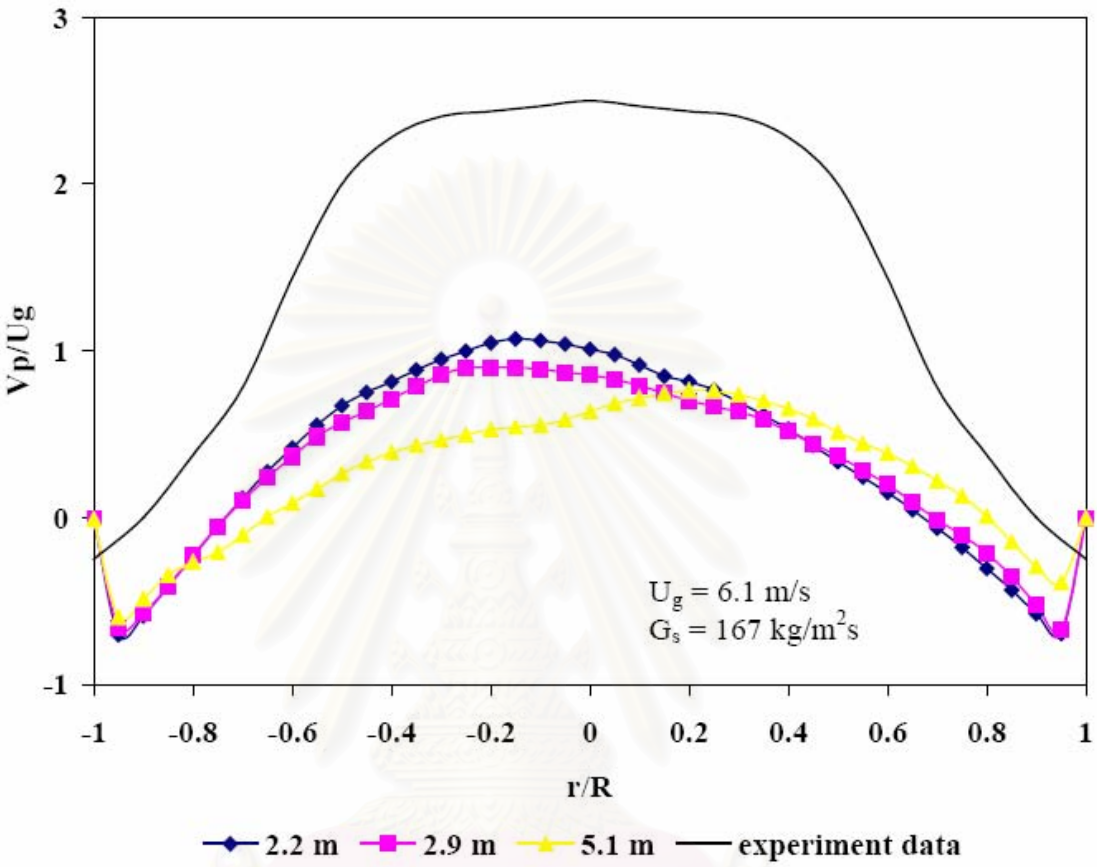

Figure 4.9 A comparison of radial distributions of dimensionless solids axial velocity to the experiment of Wei, et al. (1998).

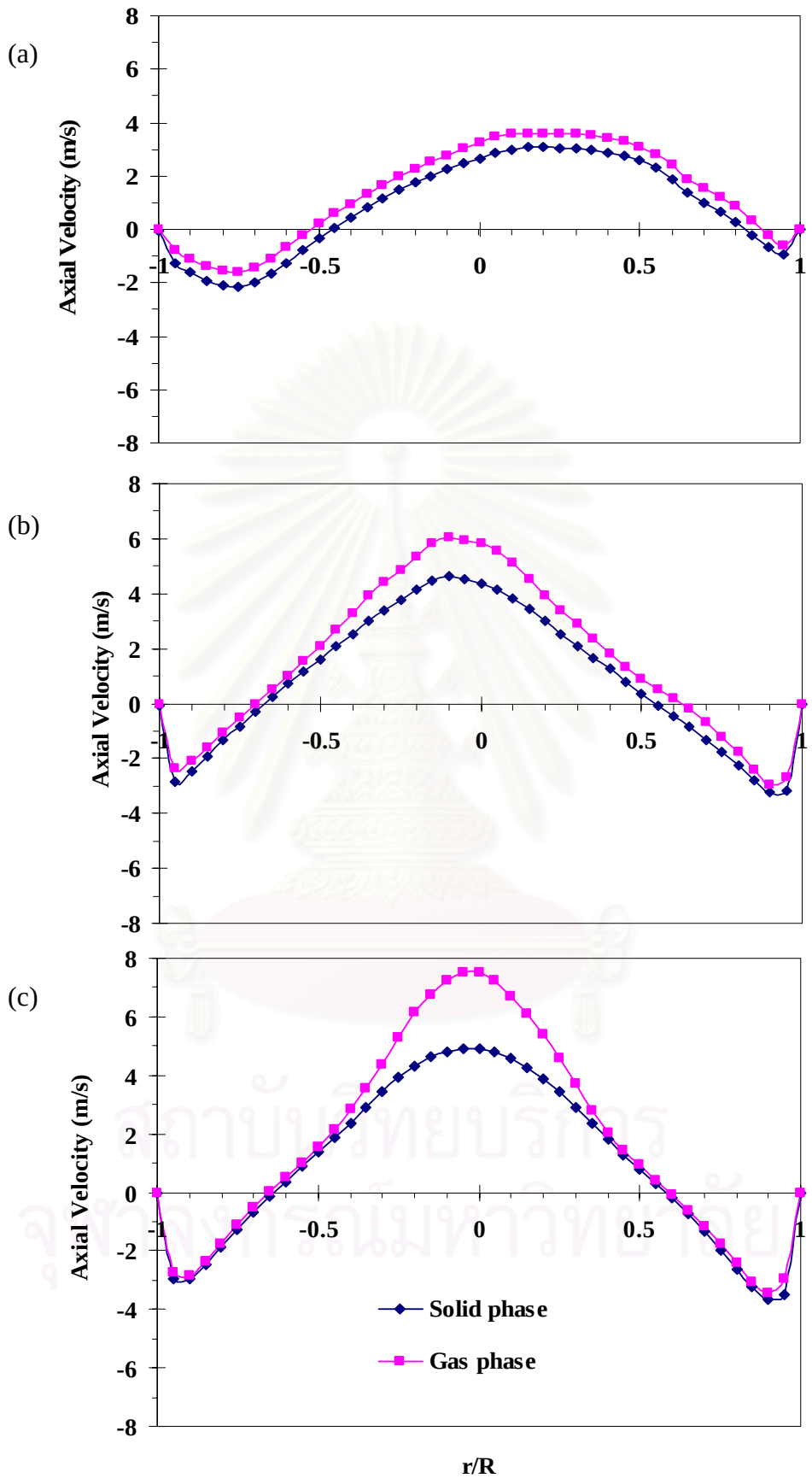

Figure 4.10 Radial distributions of axial velocity of solid and gas phases at (a) 600 cm, (b) 400 cm and (c) 200 cm

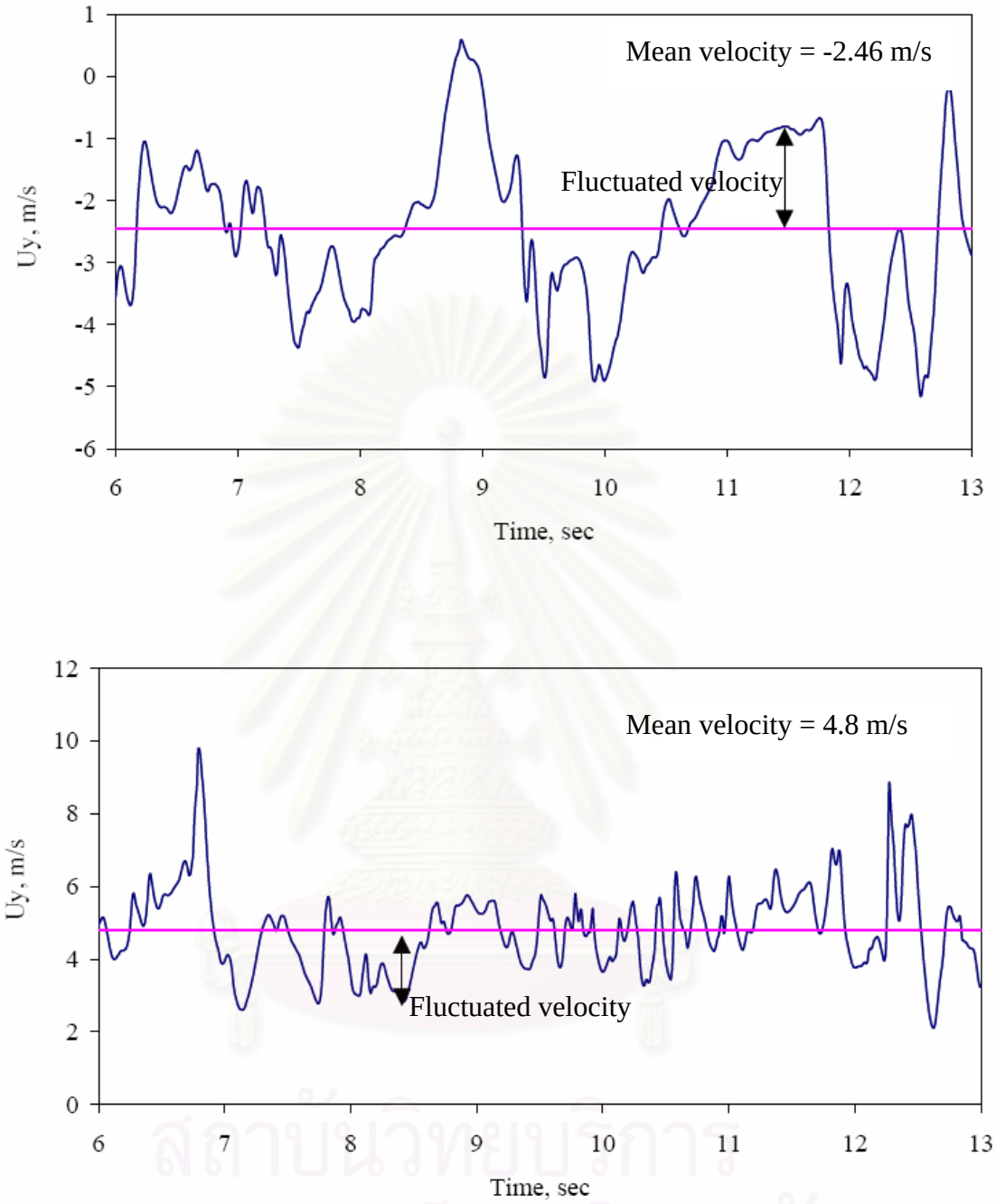

Figure 4.11 The vertical component velocity (hydrodynamics velocity) as well as their time-mean value and their fluctuation at 200 cm (a) r/R = 0.85 (b) r/R = 0.1

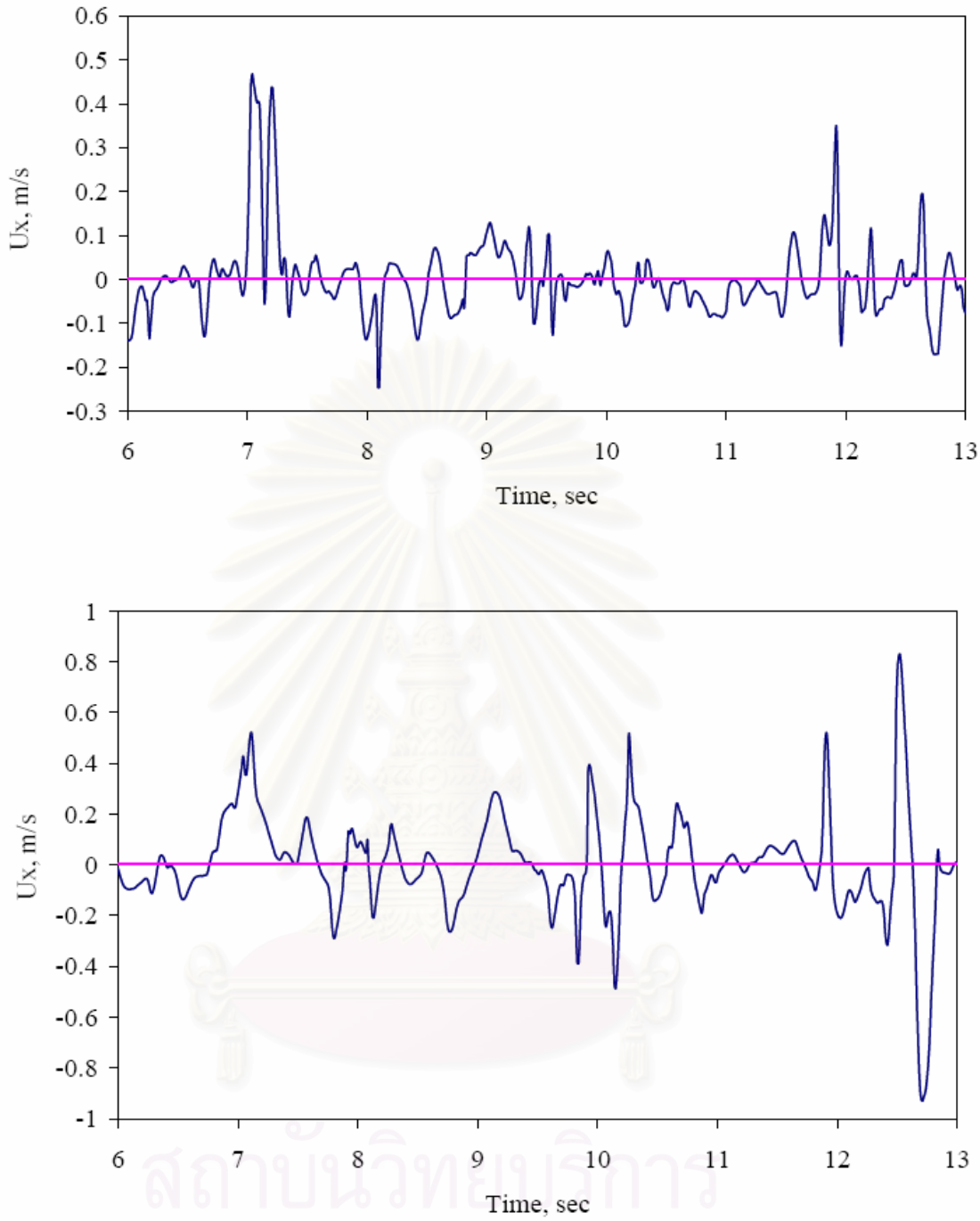

Figure 4.12 The lateral component velocity (hydrodynamics velocity) as well as their time-mean value and their fluctuation at 200 cm (a) r/R = 0.85 (b) r/R = 0.1

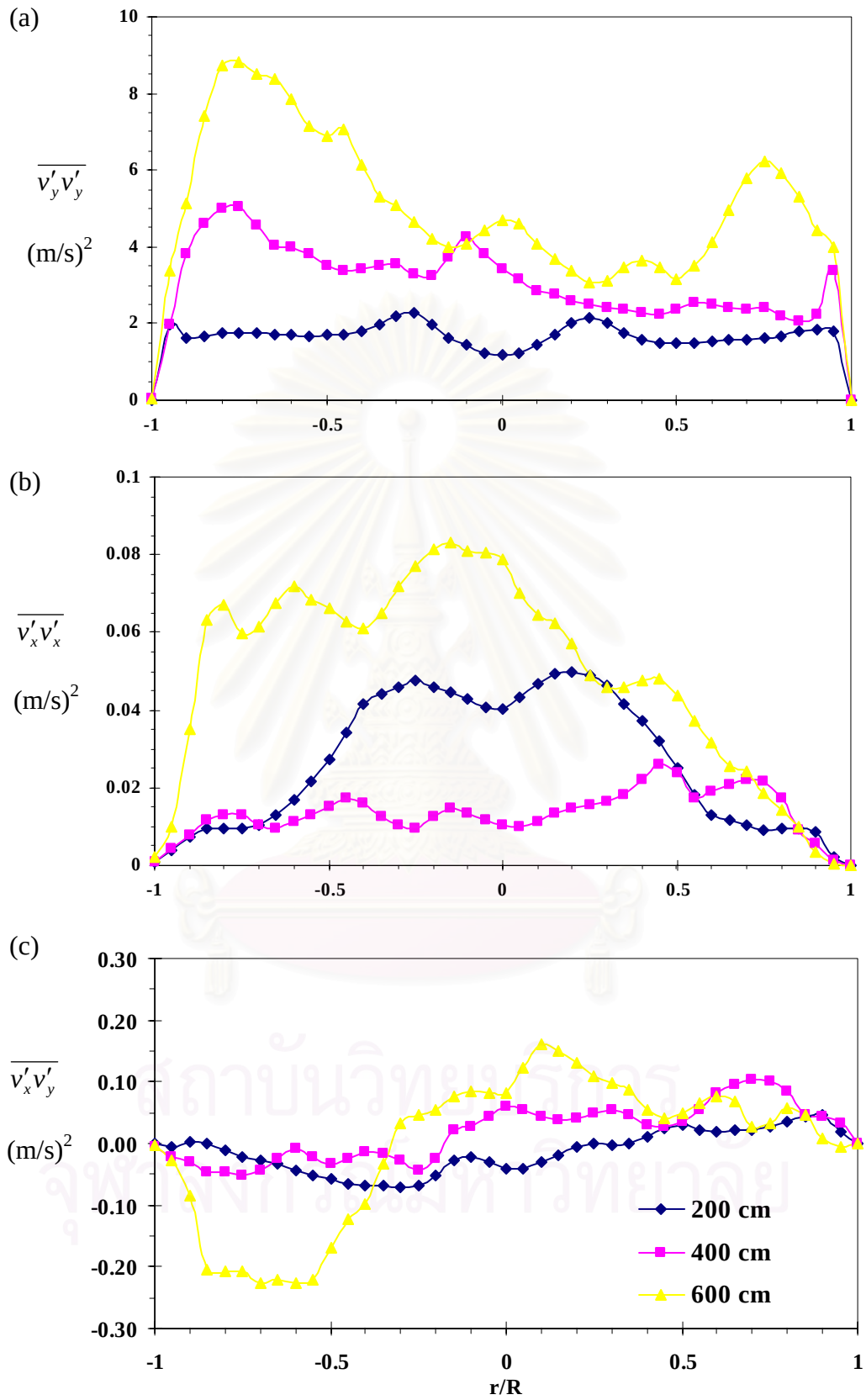

Figure 4.13 Radial distributions of the computed Reynolds stresses for W_s = 98.8 kg/m^2-s and U_g = 3.25 m/s.

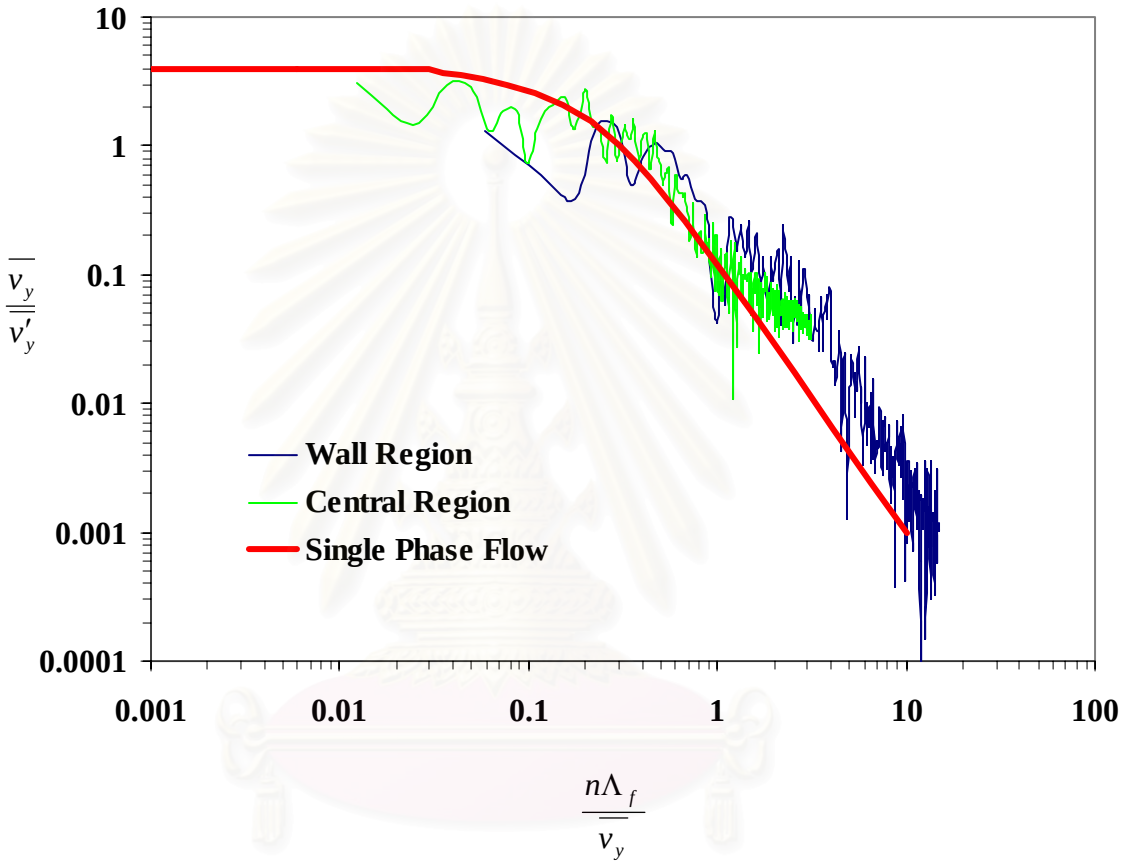

Figure 4.14 A comparison of computed spectral distribution $E_y(n)$ of the vertical turbulence component (W_s = 98.8 kg/m^2-s and U_g = 3.25 m/s. at 2 m.) to Hinze (1959) representation for single-phase flow in a channel (Re 21,500)

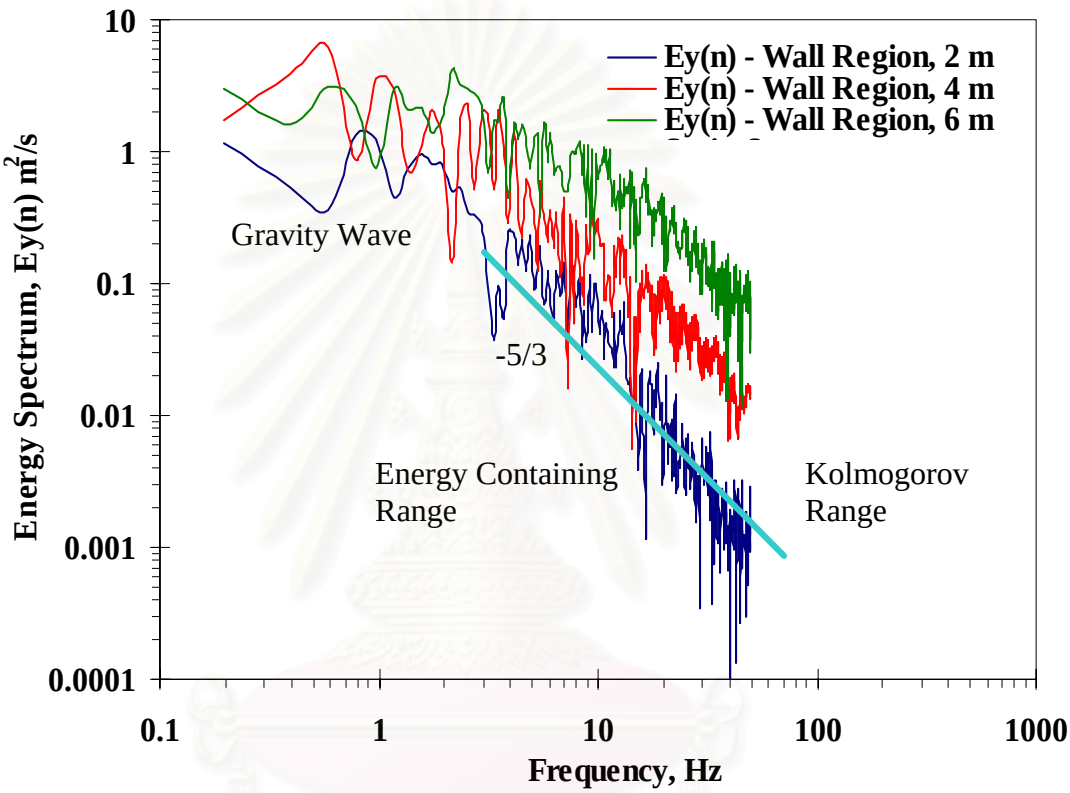

Figure 4.15 Computed vertical energy spectra in a riser at various heights for W_s = 98.8 kg/m^2-s and U_g = 3.25 m/s.

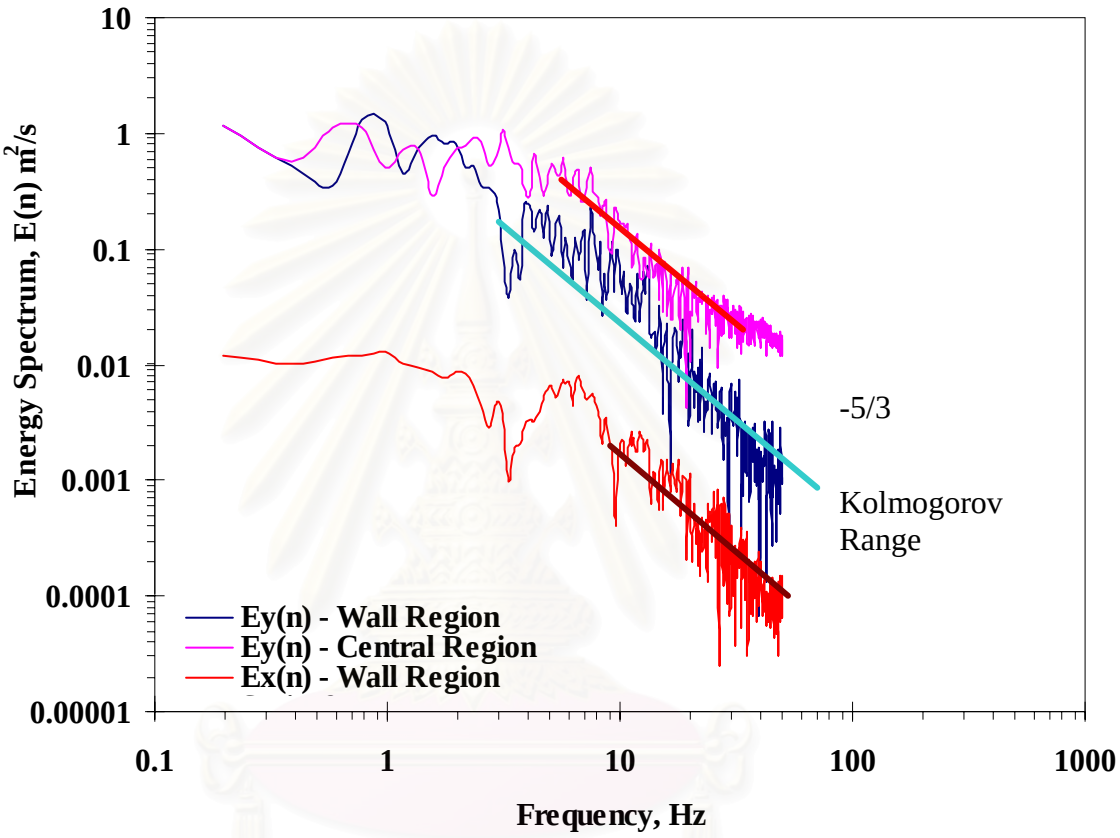

Figure 4.16 A comparison of vertical and horizontal wall region energy spectra to the central vertical spectrum for W_s = 98.8 kg/m^2-s and U_g = 3.25 m/s.

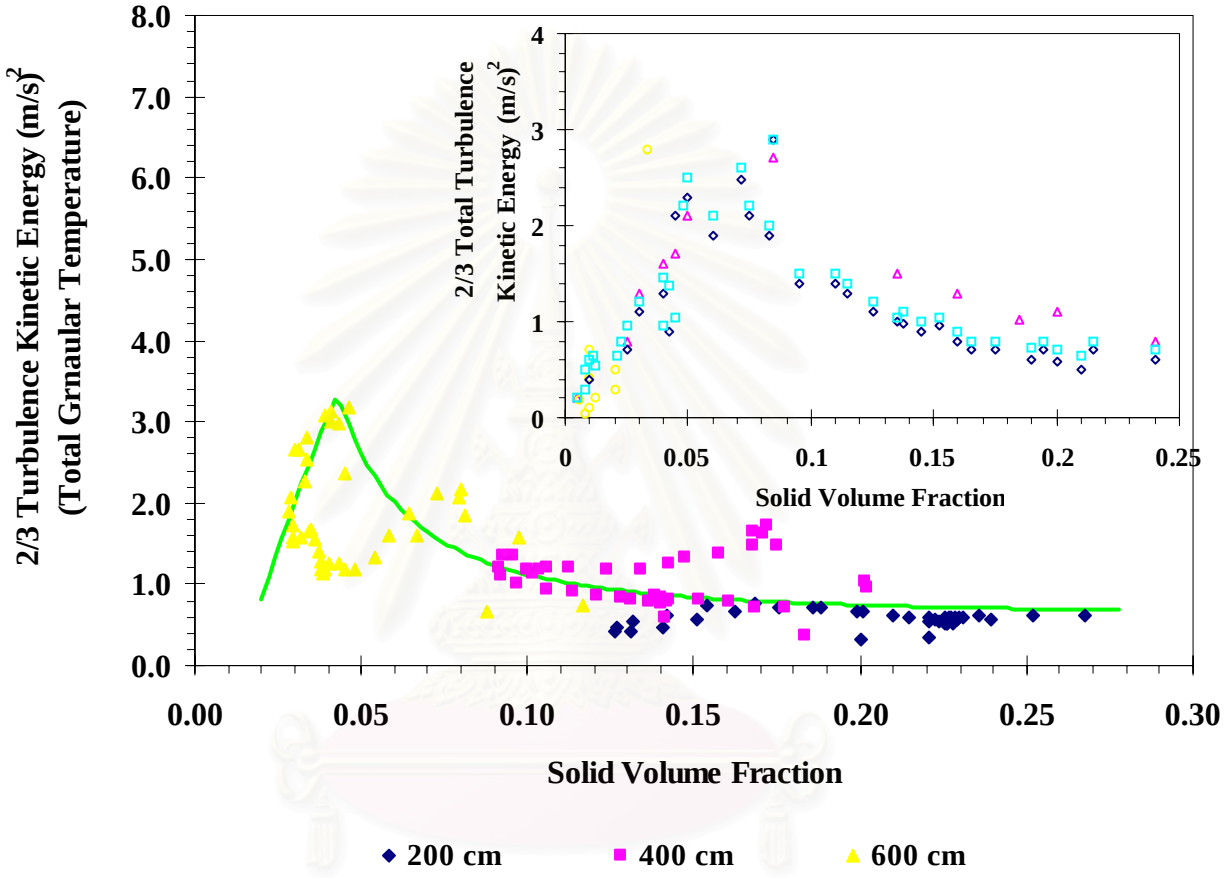

Figure 4.17 Computed the 2/3 turbulent kinetic energy as a function of solid volume fraction for W_s = 98.8 kg/m^2-s and U_g = 3.25 m/s.

The box shows experimental 2/3 turbulent kinetic energy values (Gidaspow and Huilin, 1998b)

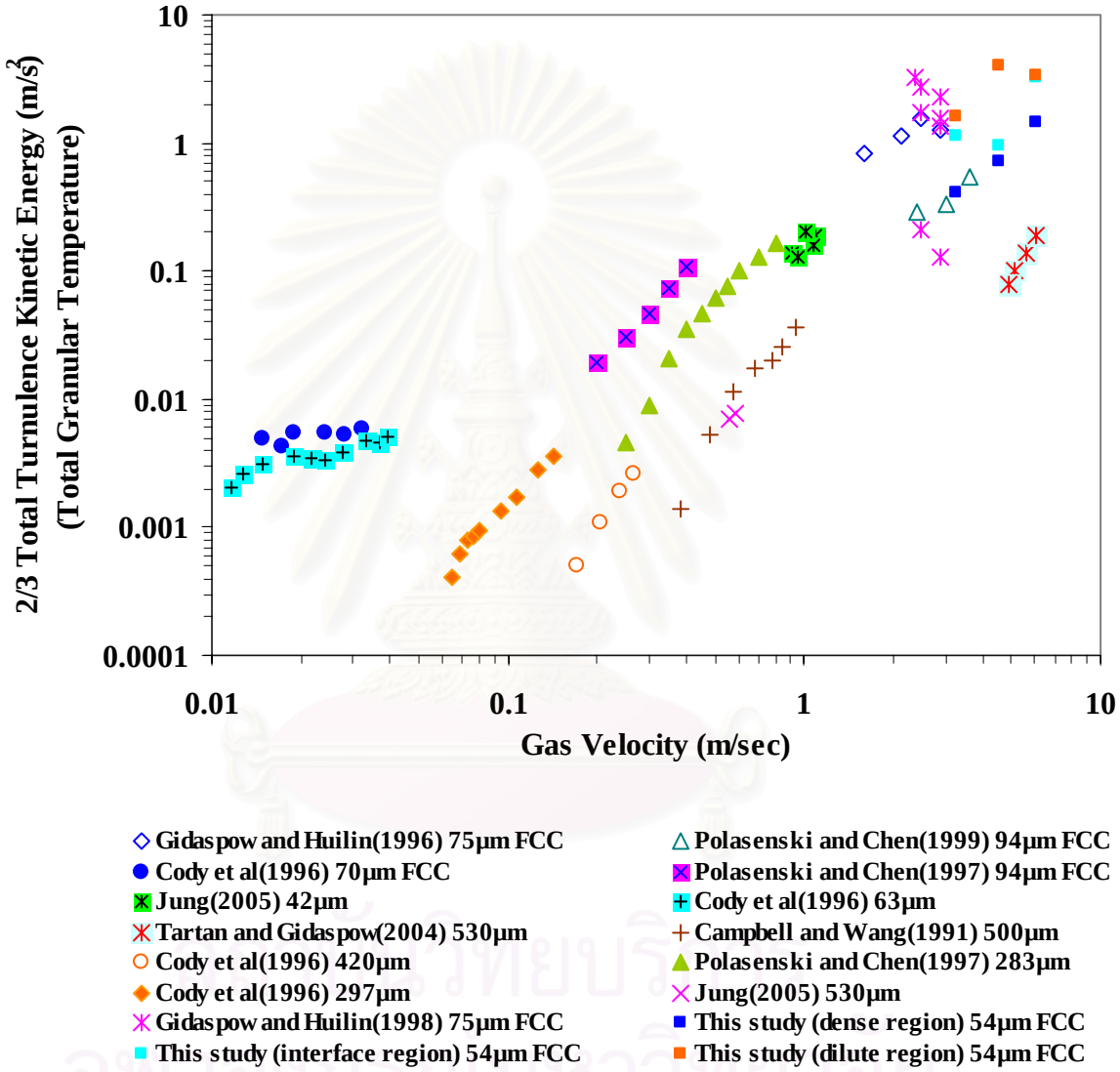

Figure 4.18 Effect of gas velocity on the 2/3 total turbulent kinetic energy of Geldart type A and B particles

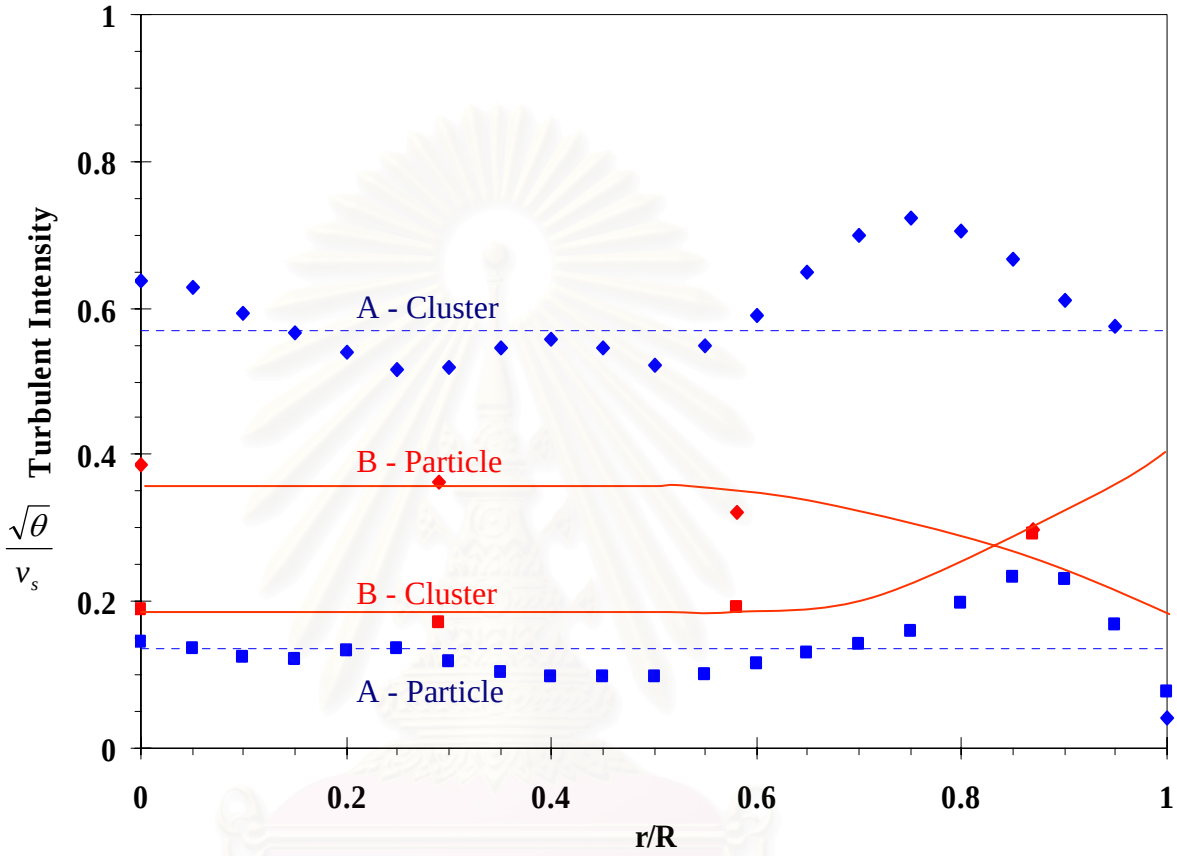

Figure 4.19 A Comparison of radial distributions of two kinds of turbulent intensity for Geldart group A (computed) and B (measured, Tartan and Gidaspow, 2004) W_s = 98.8 kg/m^2-s and U_g = 3.25 m/s for simulation at 6 m. W_s = 21.4 kg/m^2-s and U_g = 5.1 m/s for experiment.

A – Cluster oscillations – Computed from turbulence
A – Particle oscillations – Computed from granular temperature equation
B – Cluster oscillations – Measured by computing Reynolds stresses
B – Particle oscillations – Measured by averaging over velocity space close to analytical solution

$$\theta = 4/15\ V_M^2[1-(r/R)^4]$$

The dilute kinetic theory gives the approximation of turbulent intensity

$$\frac{\sqrt{\theta}}{v_s} = 0.5$$

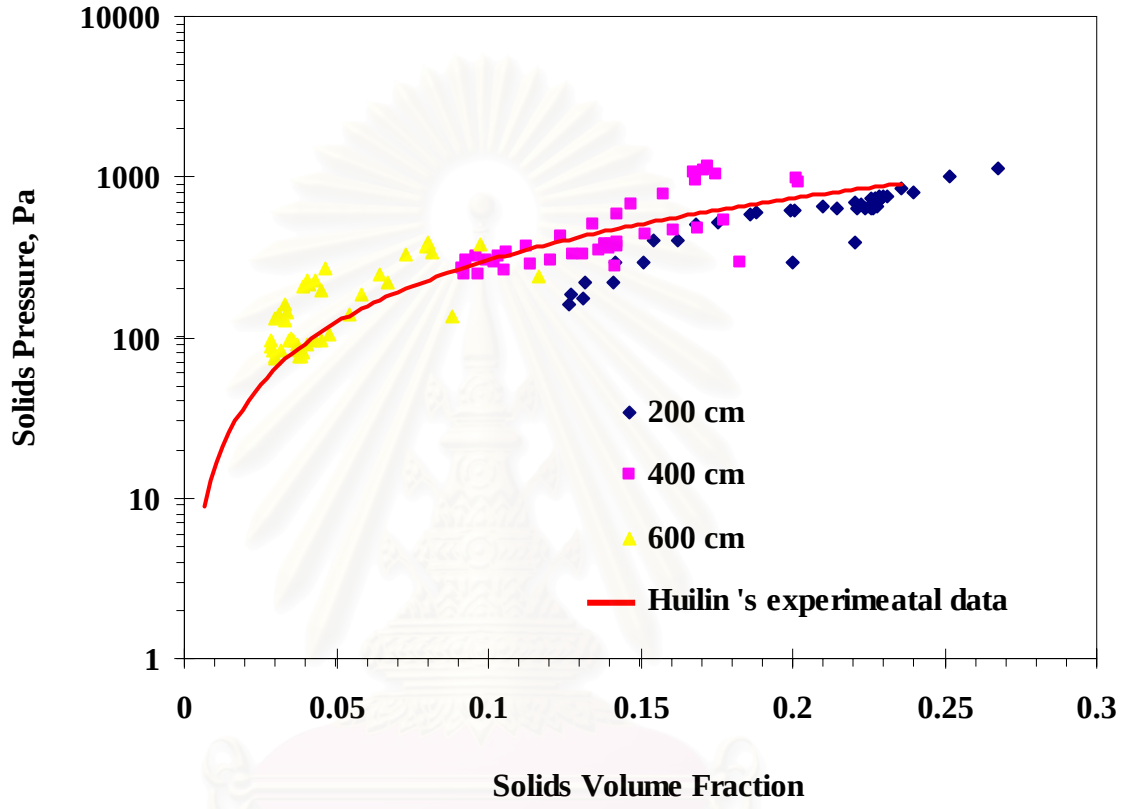

Figure 4.20 Computed solid pressure based 2/3 total turbulent kinetic energy as a function of solid volume fraction for W_s = 98.8 kg/m^2-s and U_g = 3.25 m/s.

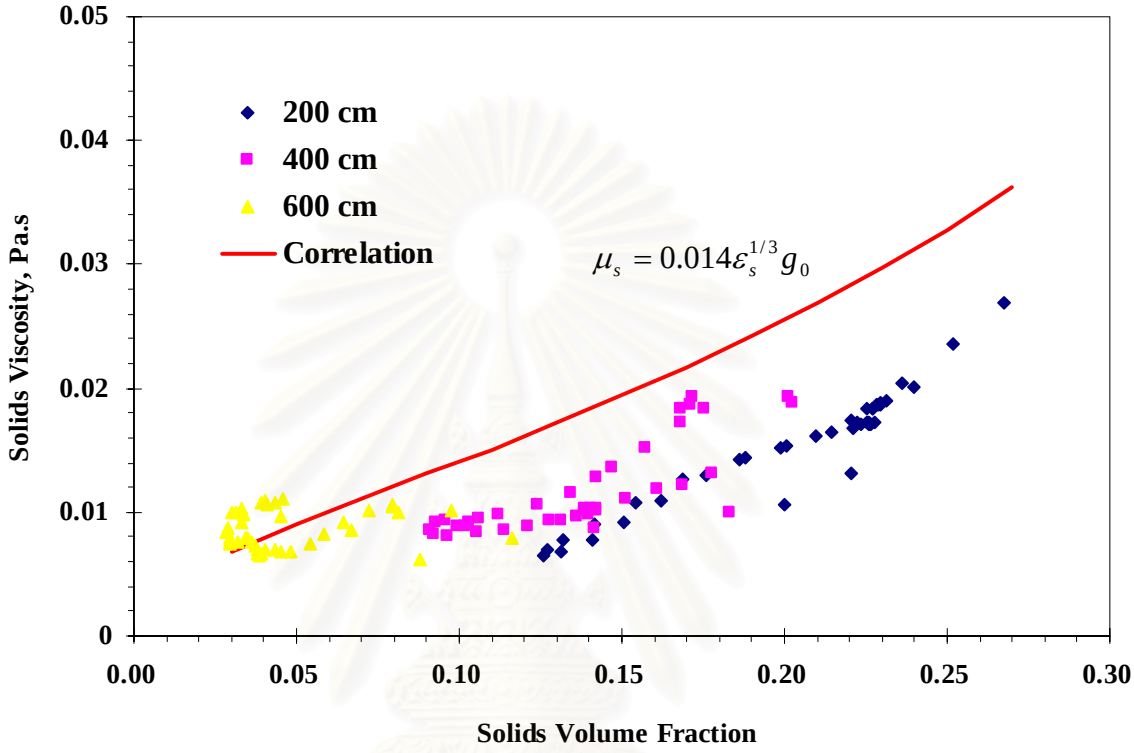

Figure 4.21 Computed solid viscosity 2/3 total turbulent kinetic energy as a function of solid volume fraction for W_s = 98.8 kg/m^2-s and U_g = 3.25 m/s.

(a)

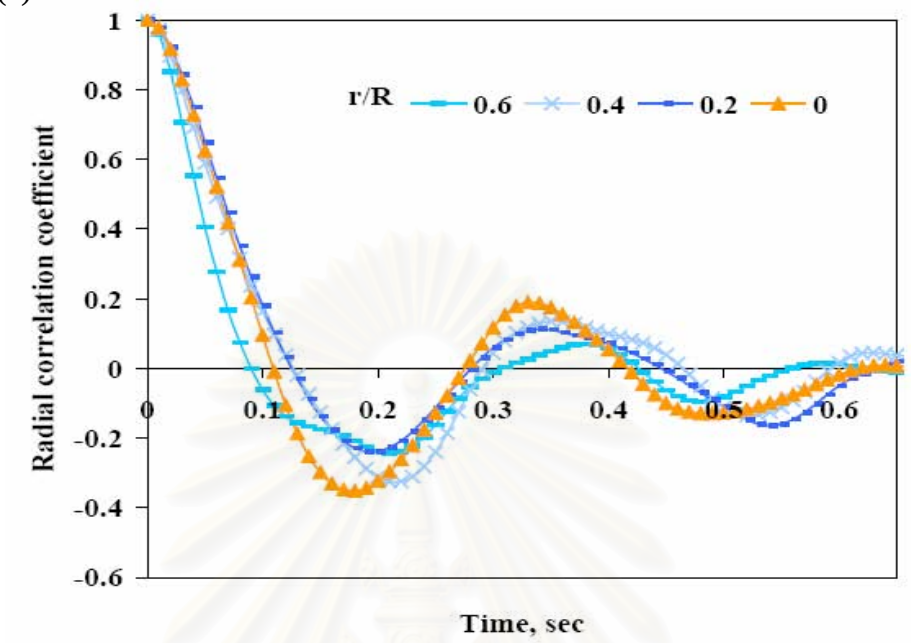

(b)

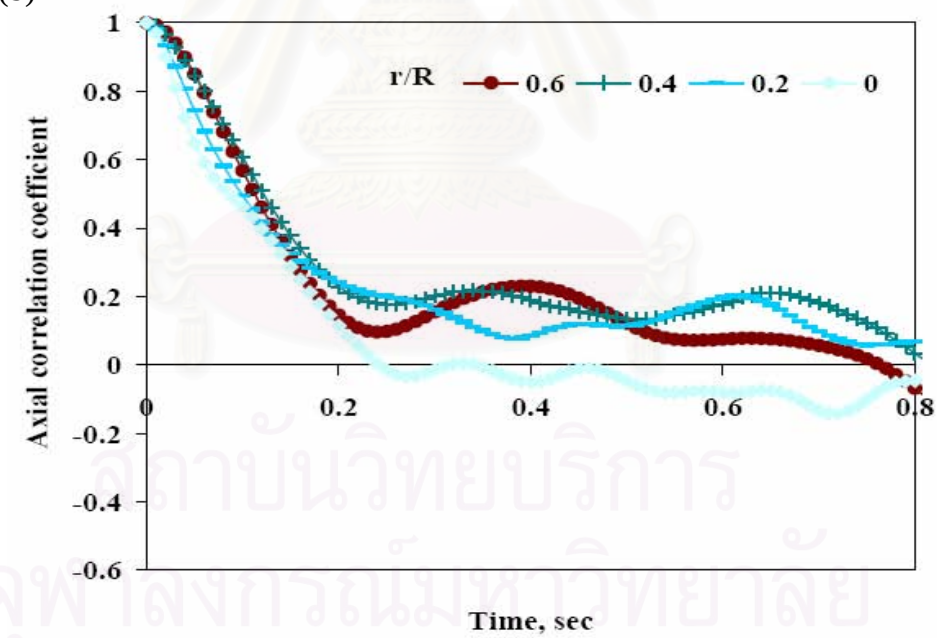

Figure 4.22 Autocorrelation functions (a) Radial; (b) Axial for W_s = 98.8 kg/m^2-s and U_g = 3.25 m/s.

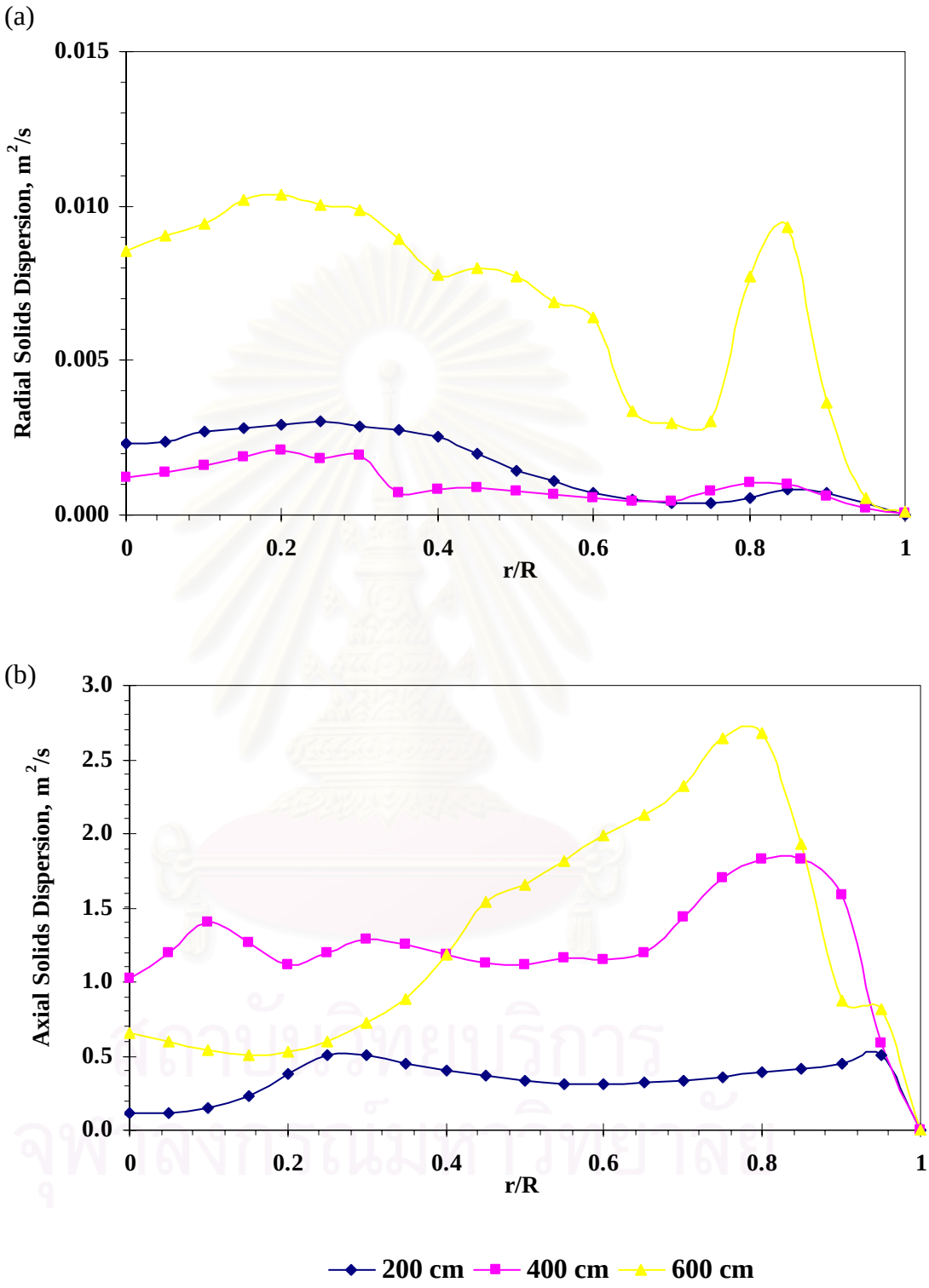

Figure 4.23 Computed solid radial and axial dispersions (a) Radial; (b) Axial for W_s = 98.8 kg/m^2-s and U_g = 3.25 m/s.

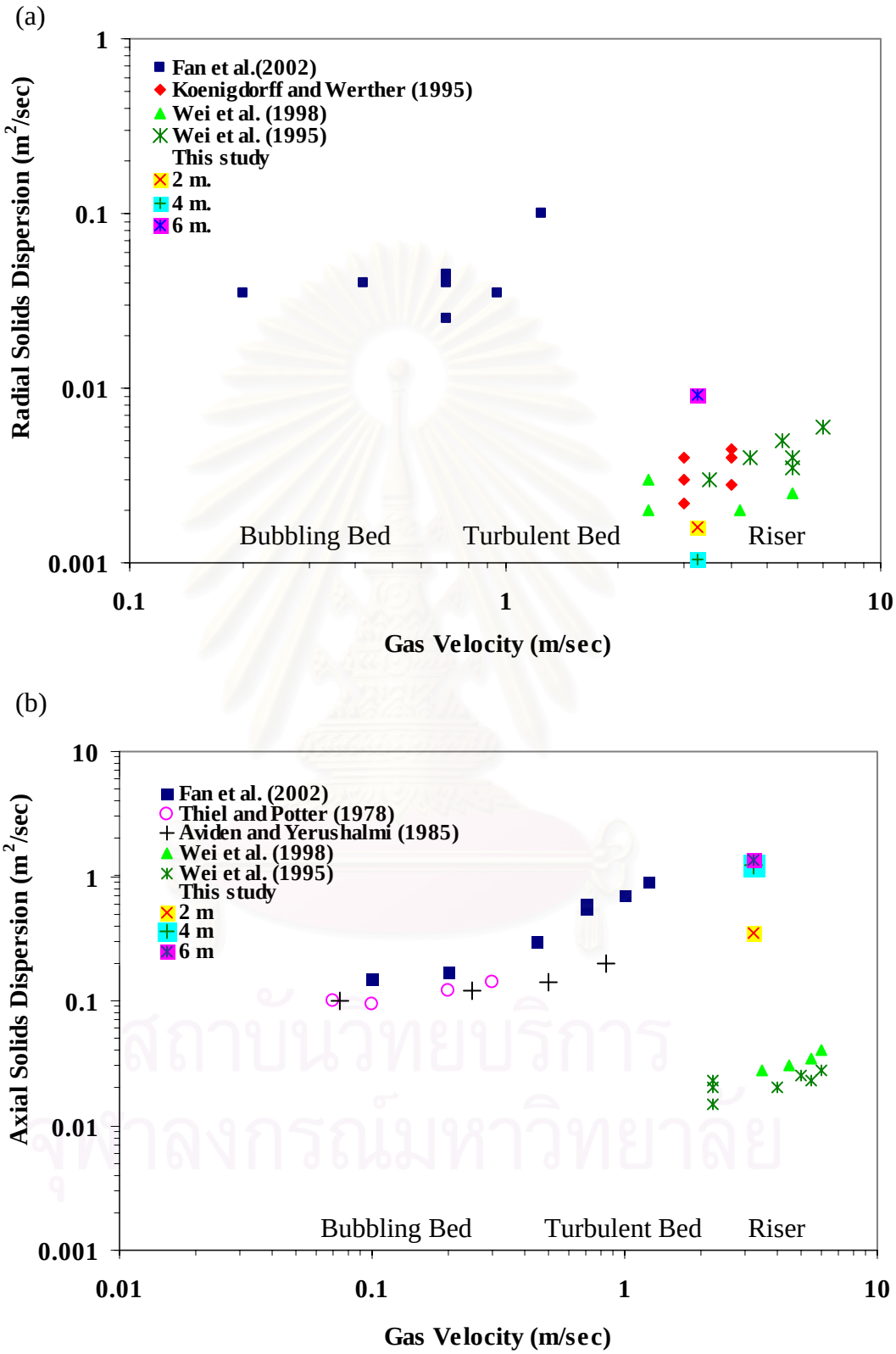

Figure 4.24 Effect of gas velocity on solids dispersion (a) Radial; (b) Axial

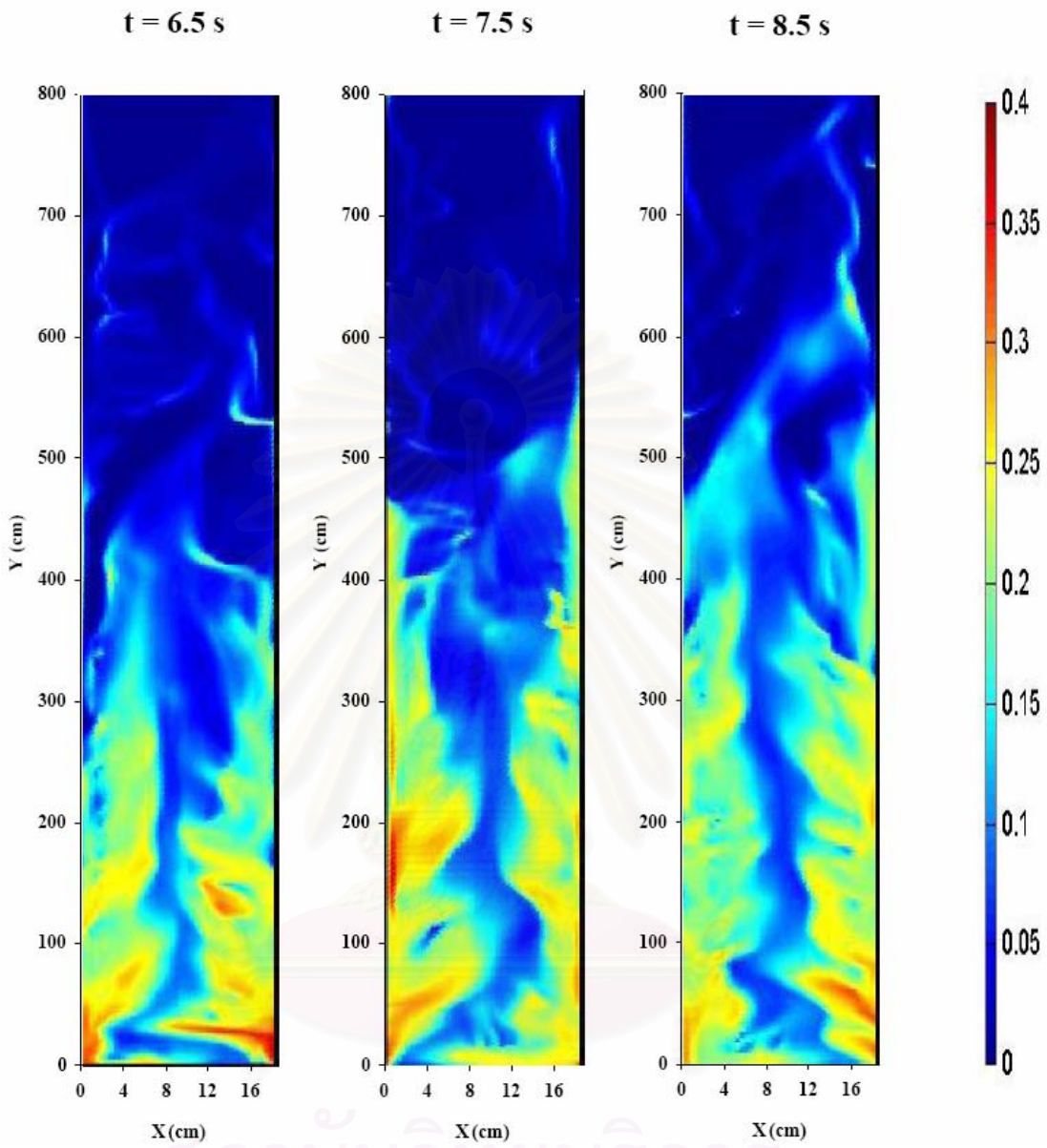

Figure 4.25 Snapshots of solid volume fraction at 6.5 , 7.5 and 8, seconds for W_s = 98.8 kg/m^2-s and U_g = 3.25 m/s.

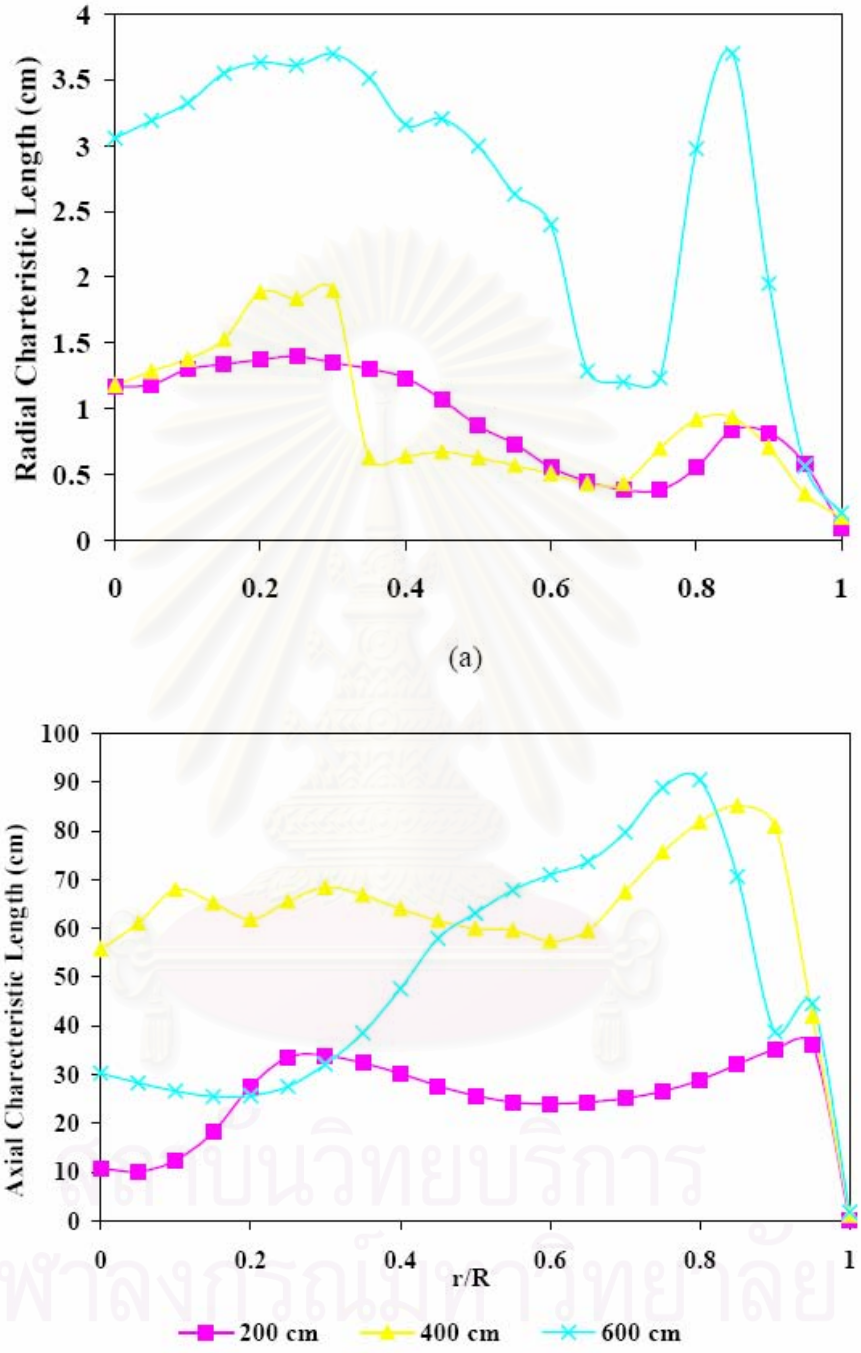

Figure 4.26 Radial distributions of characteristics lengths (a) Radial; (b) Axial for W_s = 98.8 kg/m^2-s and U_g = 3.25 m/s.

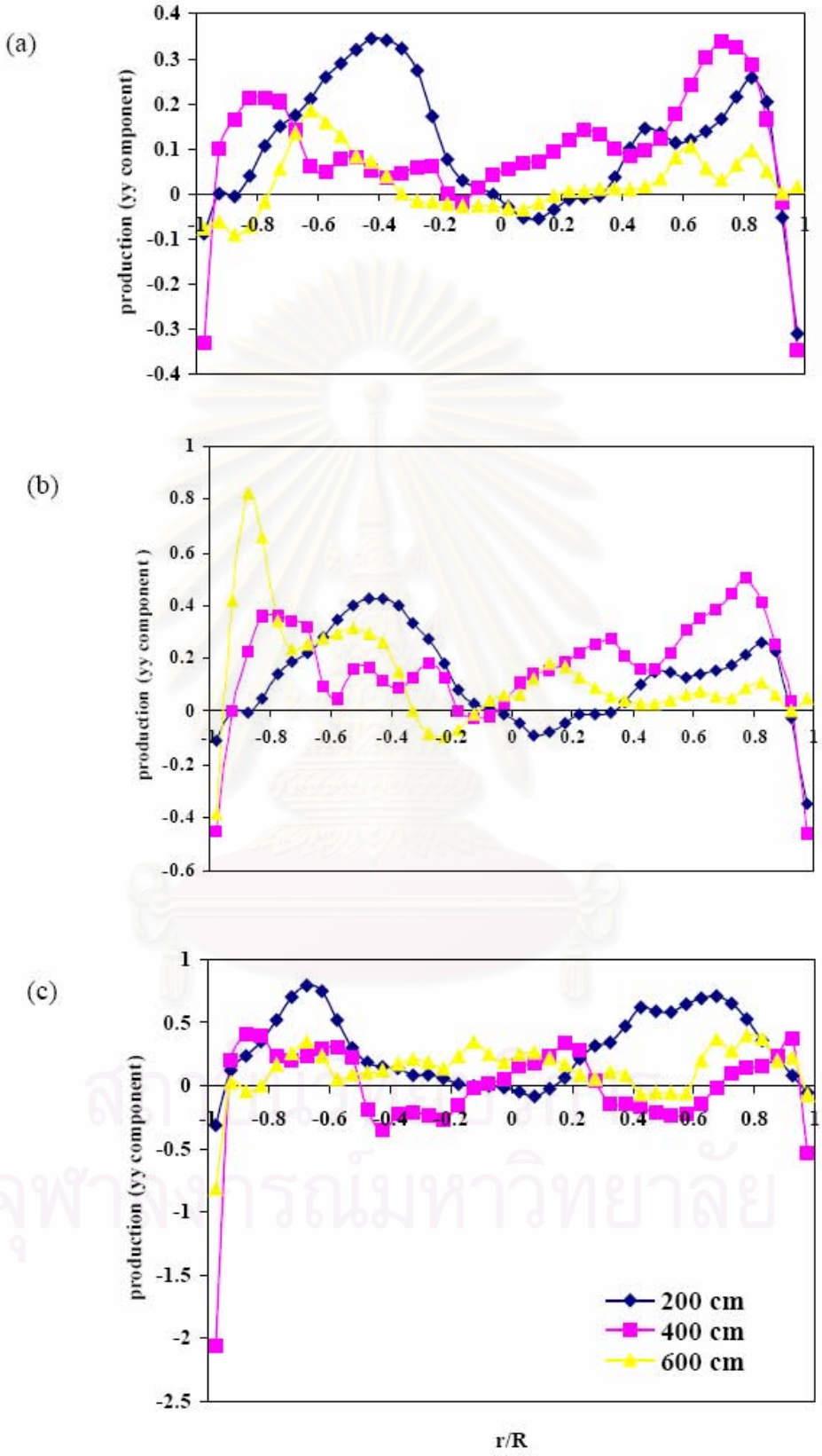

Figure 4.27 Radial distribution of the dimensionless of production of Reynolds stresses in yy direction for three different operating conditions.
(a) case I (b) case II (c) case III

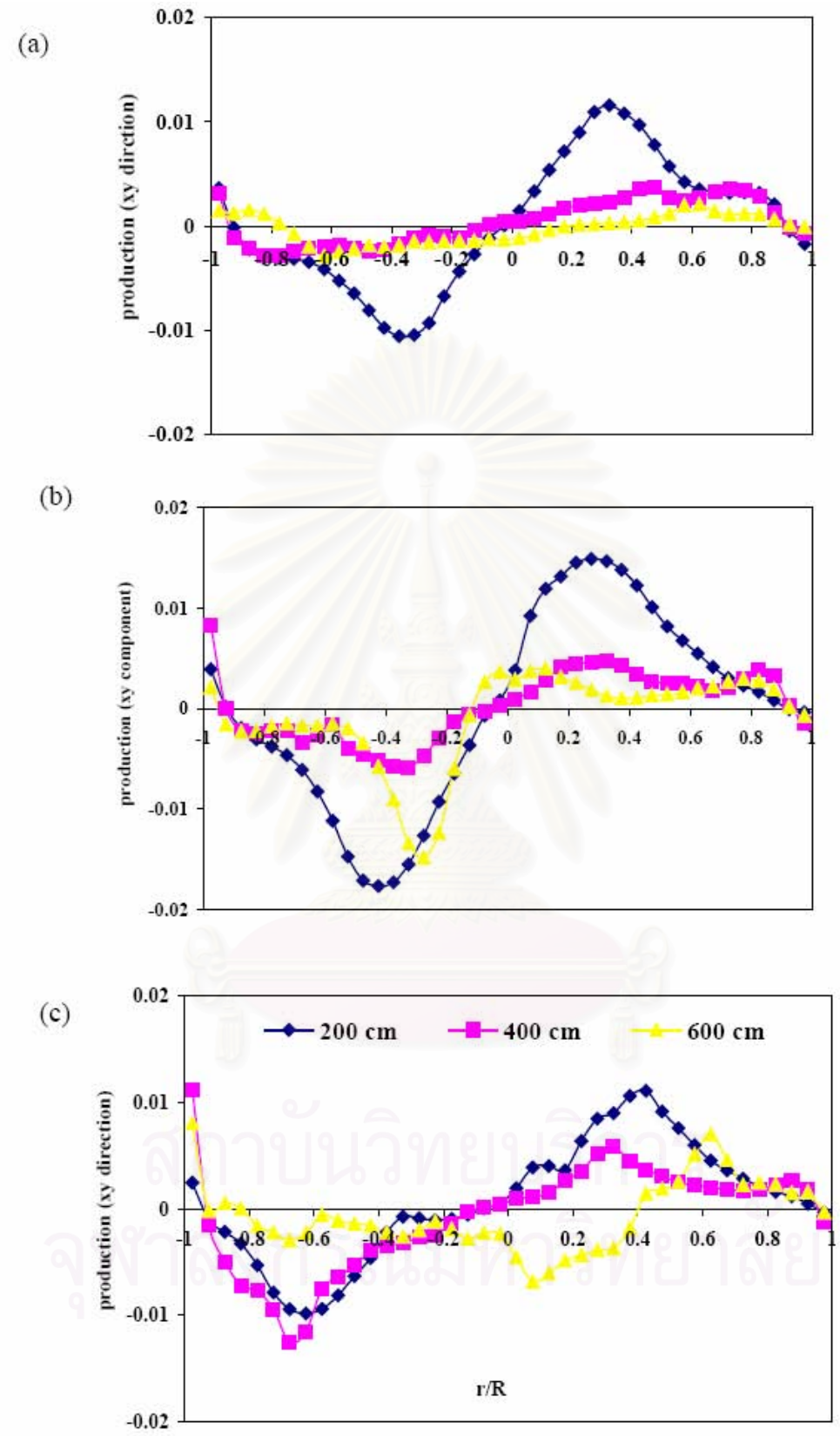

Figure 4.28 Radial distribution of the dimensionless of production of Reynolds stresses in xy direction for three different operating conditions.
(a) case I (b) case II (c) case III

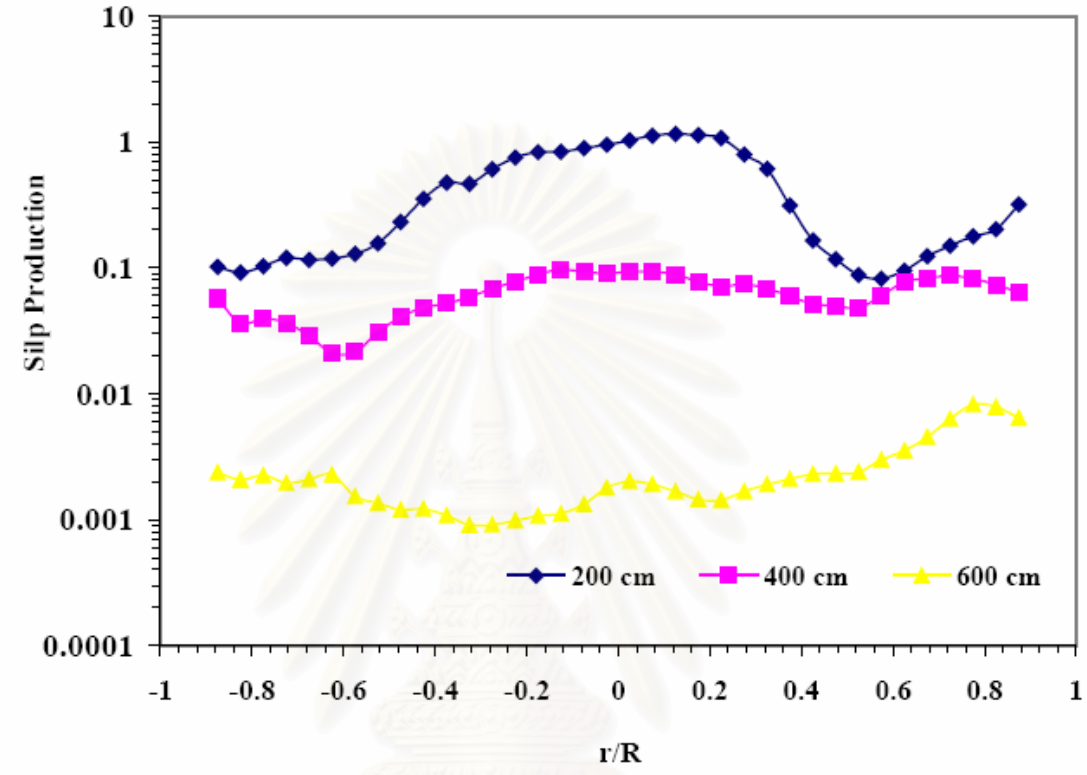

Figure 4.29 Radial distribution of the dimensionless of slip production for W_s = 98.8 kg/m^2-s and U_g = 3.25 m/s.

Appendix 1

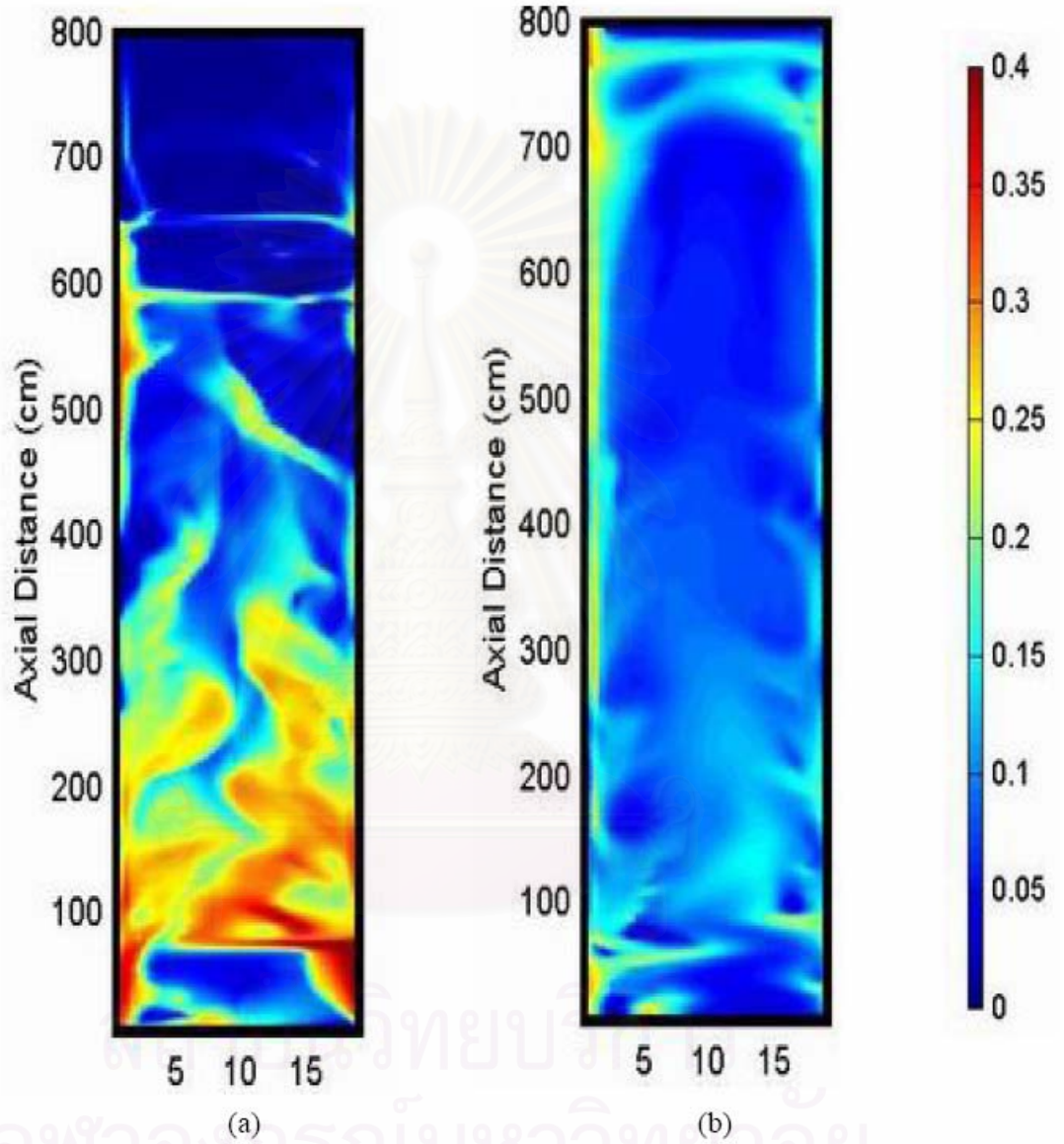

Figure 4.30 The computed solid volume fraction structure for (a) modified and (b) classical drags

Appendix 2

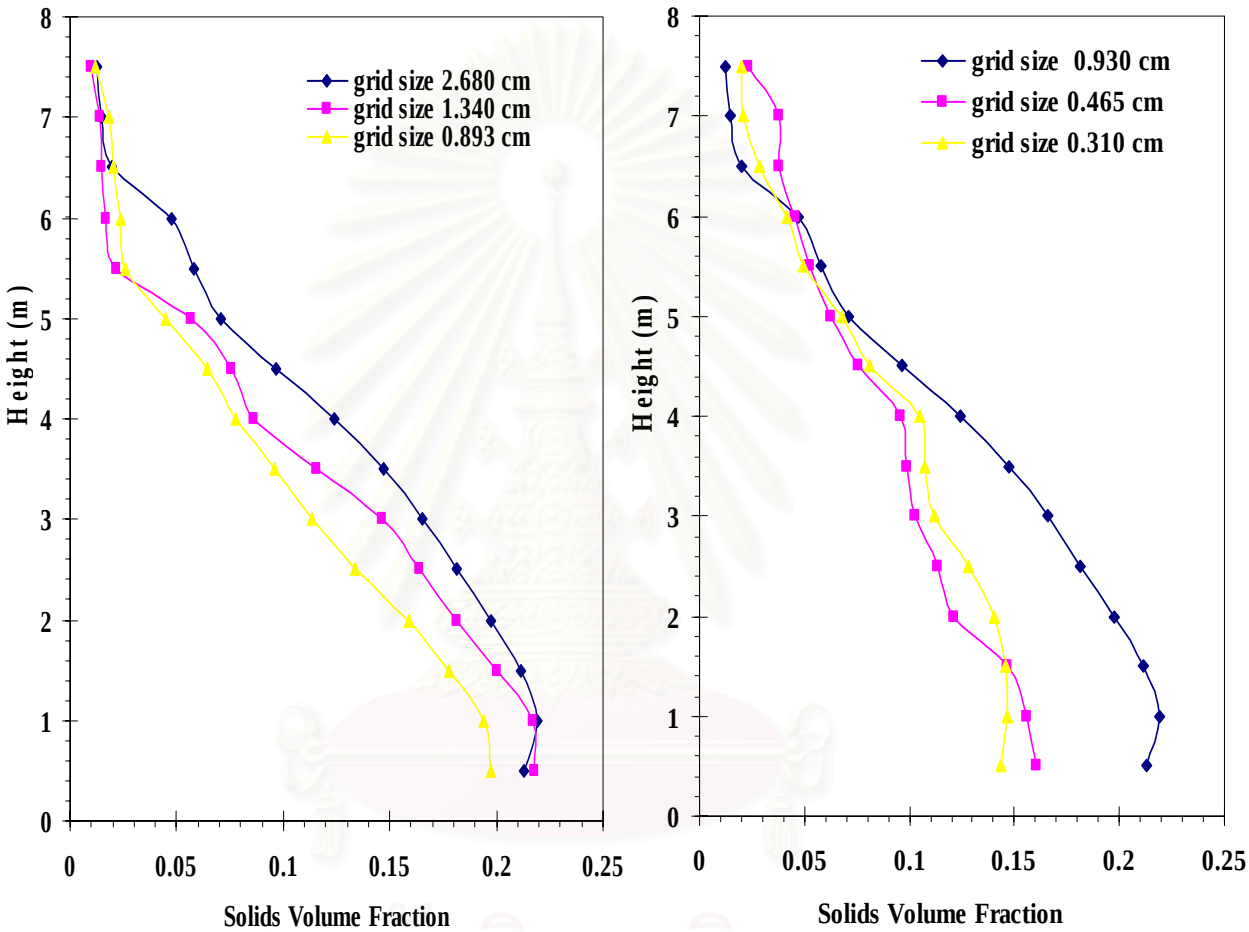

(a) (b)

Figure 4.31 Time averaged axial profiles of solid volume fraction due to the effect of grid size in (a) x and (b) y direction for W_s = 98.8 kg/m^2-s and U_g = 3.25 m/s.

Appendix 3

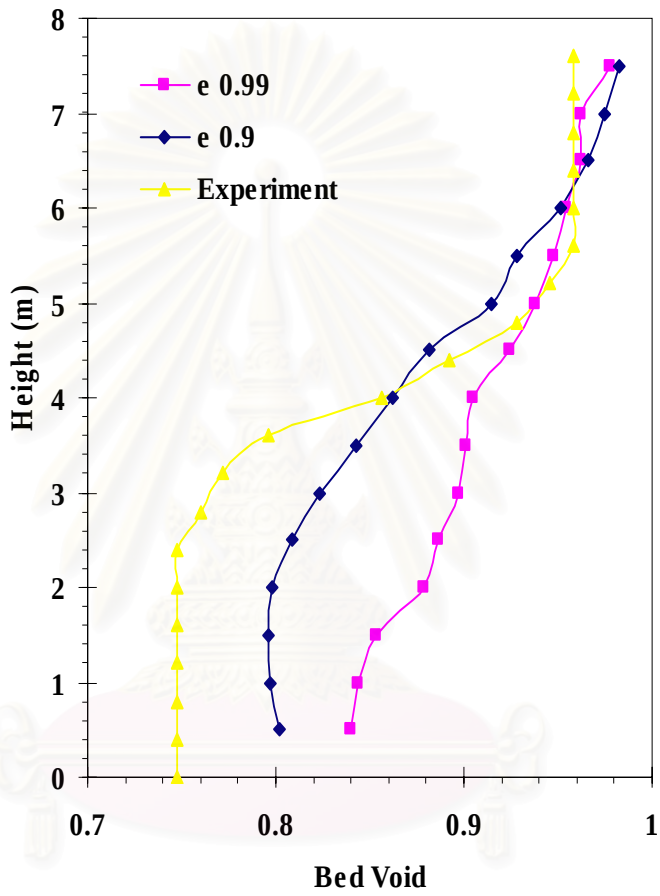

Figure 4.32 Time averaged axial profiles of solid volume fraction due to the effect of restitution coefficient for W_s = 98.8 kg/m^2-s and U_g = 3.25 m/s.

Appendix 4

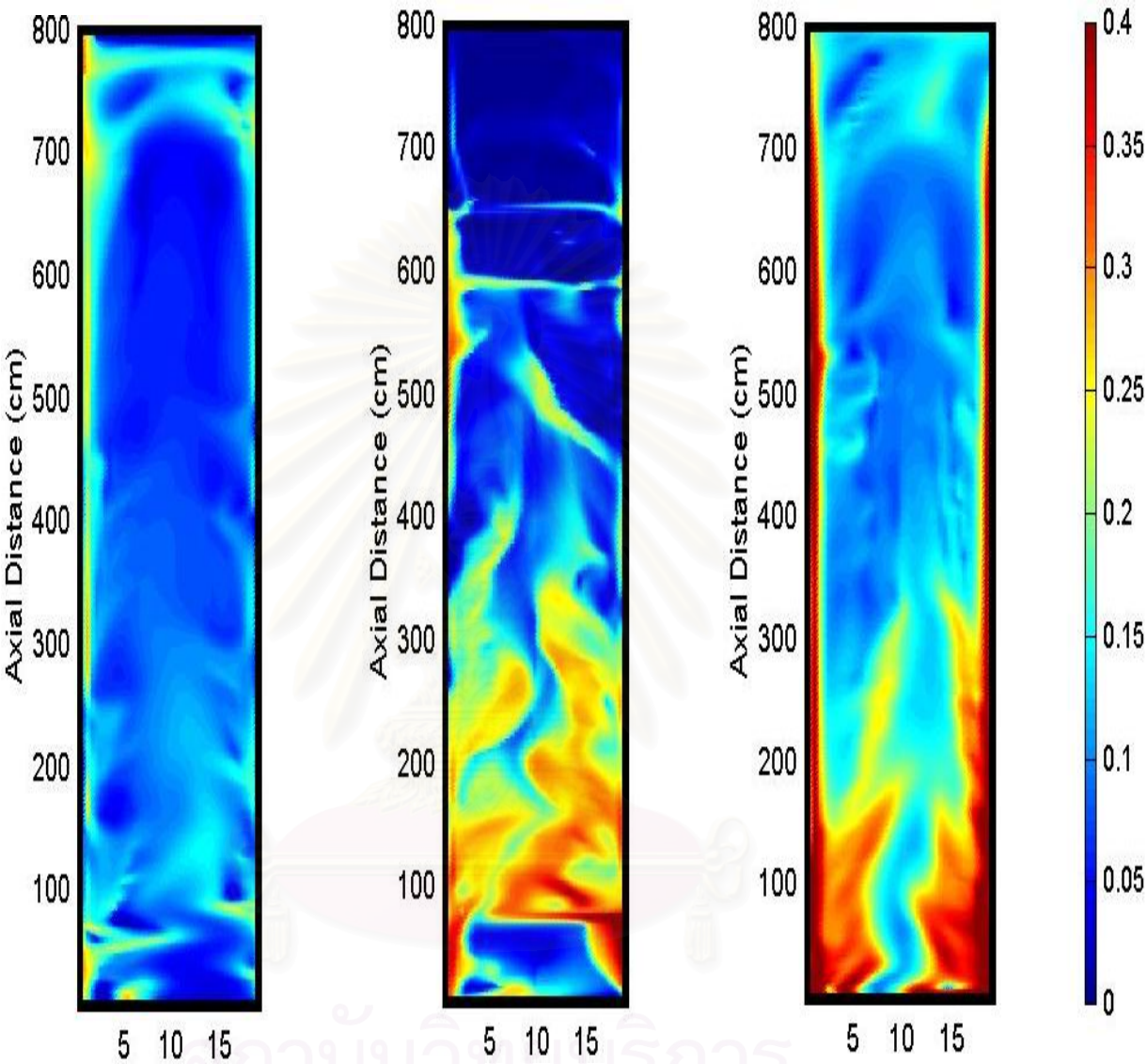

(a) (b) (c)

Figure 4.33 The computed solid volume fraction structure for W_s = 132 kg/m^2-s and U_g = 4.57 m/s.
(a) classical drags (b) modified (c) electric field with -3.25×10^{-7} C/kg

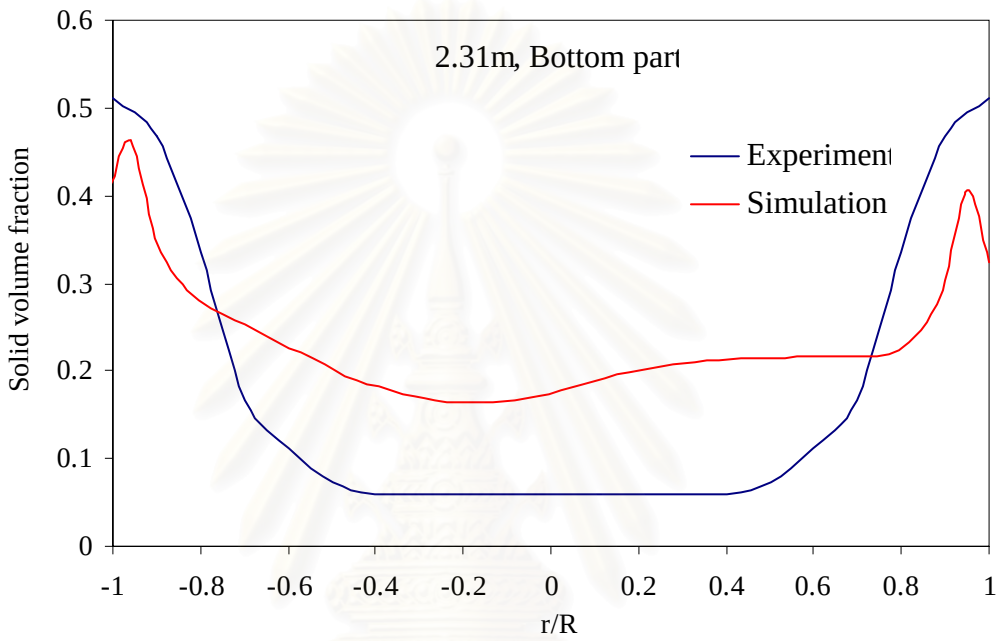

Figure 4.34 Comparison of volume fraction profiles between experiment and simulation with electric field at 2.31m. for W_s = 132 kg/m^2-s and U_g = 4.57 m/s.

CHAPTER V

EXPLOSIVE DISSEMINATION AND FLOW OF NANOPARTICLES

5.1 Introduction

Nanoparticles have some unique flow and dispersion properties that make them useful for a number of applications (Gidaspow, et al. 2004b). Fumed nanoparticle silica has long been used as a flow agent to disperse sticky particles such as TNT. Recently, we (Jung and Gidaspow, 2002; Gidaspow, et al. 2004a,b; Yu, et al. 2005; Zhu, et al. 2005) have shown that many nanoparticles fluidize without the formation of bubbles. Instead of forming bubbles upon the increase of gas velocity, like the FCC particles used to convert oil into gasoline, they keep expanding upon an increase of gas velocity. If the silica particles used here are coated with catalysts using chemical vapor deposition techniques, they may be an alternative to the conventional FCC particles used in the oil industry, Here we demonstrate that the silica nanoparticles can be circulated in a pilot plant type circulating fluidized bed. We have also used this apparatus to estimate the nanoparticle viscosity that is needed as an input into CFD models. Then we demonstrate that our CFD models (Gidaspow, 1994) can be used to predict the dispersion of nanoparticles, that are of interest in forming smoke and other obscurants. (Gidaspow and Jiradilok, 2005).

Computational Fluid Dynamics (CFD) explosive dissemination started at IIT about 20 years ago (Gidaspow, et al. 1984). The process was divided into 2 steps: early time hydrodynamic and dissemination into an atmosphere or a bag. In early time

hydrodynamics, pressure wave propagation was computed in a dissemination device containing powder. When the dissemination device broke, the flow of powder into atmosphere began using the initial conditions of velocity, pressure, and powder concentration. The equations used were the conservation of mass, momentum and energy for each phase (Gidaspow, 1994). The multiphase computer code for N phases or particle sizes was developed at IIT by M. Syamlal (Syamlal, 1985). At Morgantown, Syamlal and others have developed a similar CFD code, which includes high order numerics and has been released as the open-source code MFIX (Syamlal, et al., 1993; Syamlal, 1998).

The best-known explosive dissemination in nature is the eruption of Vesuvius in the AD 79 and the burial of Pompei by a pyroclastic cloud. CFD simulation of volcanoes began at Los Alamos in 1984 (Wohletz, et al. 1984). Valentine and Wohletz (1989) used an ill-posed set of equations discussed in Gidaspow's book (1994), stabilized by viscosity for single-size particles. Multisize particle simulations of Volcanoes were reported by Neri, et al. (2003). Explosive dissemination of multisize particles simulating experiments at IIT Research Institute were reported in Gidaspow, et al. (1984); Gidaspow, et al. (1986); Gidaspow and Aldis, (1988a); Gidaspow, et al. (1988b); Jayaswal, et al. (1990); Jayaswal (1991); Sun, et al. (1994).

The objectives of this study are to circulate the silica nanoparticles in a pilot plant type circulating fluidized bed and to estimate the nanoparticle viscosity that is needed as an input into CFD models in order to predict the flow structure of nanoparticles, that are of interest in forming smoke and other obscurants.

5.2 Flow of 10nm Silica Particles in a Riser

We have shown that it is possible to circulate nanoparticles in a two-story pilot plant type circulating fluidized bed. The particles were 10 nm silica, Tullnox 500, measured with a transmission electron microscope, with a picture shown in Jung and Gidaspow (2002). The circulating fluidized bed with a splash plate was the apparatus, fully described for flow of 530 micron glass beads by Tartan and Gidaspow (2004). Figure 5.1 shows a sketch of the apparatus. The cyclone proved somewhat effective in separating the particles from the air, probably due to formation of large agglomerates. The air from the cyclone was directed into a large bag located in a hood. After about 40 minutes, the bag was full and the experiment had to be stopped. The CCD camera used by Tartan and Gidaspow (2004) was not useful in this study. Hence the earlier technique, extraction probe used by Miller and Gidaspow (1992) was used to characterize the flow of nanoparticles. The particle concentration was measured with the gamma densitometer described by Gidaspow, et al. (2001) and Tartan and Gidaspow (2004). We uses the extraction probe to estimate the solid velocity by using following relation:

$$W_s = \varepsilon_s \rho_s V_s \tag{5.1}$$

where W_s is solids flux, kg/m^{2}s., ε_s is particle concentration, ρ_s is solids density, kg/m^3, and V_s is solids velocity. Using the extraction probe, the solids flux is obtained, so the solids velocity can be estimated by knowing the particle concentration at the same point.

Figure 5.2 shows the bed expansion of nanoparticles at the gas velocity of 30 cm/s. The interface moves approximately with the superficial gas velocity. Figure 5.3 shows the solid volume fraction measured with the gamma densitometer described by Tartan and Gidaspow (2004) and by J. Kalra (2005). The densitometer consisted of a 500 mCi Cs 137 source with the NaI crystal scintillation detector. It was calibrated by

measuring the radiation with a full and empty tube, as shown in Figure 5.3. The oscillations in Figure 5.3 are due to turbulence and random emission of radiation. The initial solid fraction with no flow is very low compared to flow of micron size particles due to the low initial bulk density. After the air was turned on, a compressed wave traveled up the tube. Figure 5.3 also shows that the particles were compressed to a solid volume fraction of about 6%. Then its density decreased. The hydrodynamic model used by Jung and Gidaspow (2002) computed such a behavior.

5.2.1 Concentrations and Velocities

Figure 5.4 shows a typical concentration profile at the velocity of 32.4 cm/s. Similar to flow of micron size particles a core-annular flow regime was observed.

The solids flux was measured with an extraction probe, Figure 5.5, Miller and Gidaspow (1992). Figure 5.5 shows the upward and downward fluxes at a velocity 27.6 cm/s. Figure 5.6 shows that the net flux is parabolic. Figure 5.7 shows the computed particle velocity at three different air flow rates. They were calculated from the knowledge of net fluxes and particle concentrations. We see that similarly to the flow 530 micron glass beads and other particles (Gidaspow, et al. 2004a) the flow is parabolic.

5.2.2 Pressure Drop

A differential handheld pressure digital manometer (475-FM Dwyer Instrument Inc.) and a wall mounted water column manometer were used for pressure drop measurement. The handheld pressure manometer and the water column manometer were hooked up along the length of the riser, with a distance of 1.96 m between the two ports. (Kalra, 2005) Figure 5.8 shows the pressure drop per unit

length. The pressure drop behavior is typical of the flow of micron size particles in a CFB (Gidaspow, 1994). It decreases with an increase of air velocity due to a decrease of the density of the mixture and then increases due to friction. Here the pressure drop is, however, much lower than that for flow of micron size particles. Hence it requires far less work to transport nanoparticles. The conventional FCC particles have a large mass that is not useful for catalysis. Hence these is exists a waste of energy in the transport of this useless mass.

5.2.3 Viscosity

For circulating fluidized bed the mixture momentum balance may be written by Tsuo and Gidaspow (1990) as,

$$\frac{\partial\left(\varepsilon_s \rho_s V_s^2 + \varepsilon_g \rho_g V_g^2\right)}{\partial z} = -\frac{\partial P}{\partial z} + \frac{1}{r}\frac{\partial}{\partial r}\left(r\left(\mu_s \frac{\partial V_s}{\partial r} + \mu_g \frac{\partial V_g}{\partial r}\right)\right) - \left(\varepsilon_s \rho_s + \varepsilon_g \rho_g\right)g \tag{5.2}$$

Miller and Gidaspow represented the mixture momentum balance base on the experiment of the flow of 75 micron FCC particles. The assumptions have been made that:

- The solids density is much greater than the gas density.
- The solids viscosity is much greater than the gas viscosity.
- The radial solids velocity and velocity gradient are of the same order of magnitude as the radial gas velocity and velocity gradient

$$\frac{\partial\left(\varepsilon_s \rho_s V_s^2\right)}{\partial z} = -\frac{\partial P}{\partial z} + \frac{1}{r}\frac{\partial}{\partial r}\left(r\mu_s \frac{\partial V_s}{\partial r}\right) - \varepsilon_s \rho_s g \tag{5.3}$$

After integration and algebraic manipulation, the flowing equation is obtained as

$$\frac{2}{R^2}\int_0^R \frac{\partial\left(\varepsilon_s \rho_s V_s^2\right)}{\partial z} r dr - \frac{2}{R}\mu_s \frac{\partial V_s}{\partial r}\bigg|_{r=R} = -\frac{\partial P}{\partial z} - \frac{2}{R^2}\int_0^R \varepsilon_s \rho_s r dr \tag{5.4}$$

Axial acceleration + Shear rate = Pressure drop – Weight of the bed

This equation means that for any position R, the axial acceleration plus shear rate is equal to the pressure drop minus the weight of the bed. For the flow of nanoparticles, the acceleration effect is not included.

The particle viscosity was calculated from the equation given below, as in Miller and Gidaspow (1992):

$$\frac{\Delta P}{\Delta z} - \frac{2}{R^2}\int_0^R \varepsilon_s \rho_s g r dr = \frac{2}{R}\mu_s \left.\frac{\partial v_s}{\partial r}\right|_{r=R} \tag{5.5}$$

Pressure Drop – Weight of Particles = Shear stress/length

Table 5.1 summarizes the results at r/R = 0.577, near the interface of the core-annular region. The viscosity of nanoparticles decreases from 0.68 to 0.45 mPa.s with increasing gas velocity. Similar viscosities were obtained with a dropping bob apparatus described by Kalra (2005).

Nanoparticle viscosity from kinetic theory

In a mixture of nanoparticle and air molecules the diffusivity (Chapman and Cowling, 1961) and hence the viscosity involve the reciprocals of the masses of air molecules and nanoparticles. Since the mass of the nanoparticles is larger than the mass of air molecules, using the relations

$$\theta_{molecular} = \frac{1}{3}\cdot m_{molecular}\cdot \langle C_{molecular}\rangle^2 \tag{5.6}$$

$$n_{nano} = \frac{6\varepsilon_{s_{nano}}}{\pi d^3_{p_{nano}}} \tag{5.7}$$

$$\mu_s = \varepsilon_s \rho_s D \tag{5.8}$$

the expression for viscosity becomes as follows:

$$\mu_s = \frac{\pi \rho_{s_{nano}} d_{p_{nano}}}{16} \left\{ \frac{\langle C_{molecular} \rangle^2}{6\pi} \right\}^{1/2} \tag{5.9}$$

The density and the diameter of nanoparticles are 2220 kg/m^3 and 10 nm, respectively. The mean speed of molecules of air, $\langle C_{molecular} \rangle$, is 467 m/sec. The corresponding value of solids viscosity, μ_s, is approximately 0.5 mPa.s. This value is close to that given in Table 5.1.

Granular temperature due to Brownian motion

The Brownian motion of the nanoparticles can be computed by equating the kinetic energy of the air molecules to the kinetic energy of the nanoparticles, as shown below:

$$\frac{3}{2} kT = \frac{1}{2} m_{nano} \langle C^2 \rangle_{nano} \tag{5.10}$$

where Boltzmann constant, k = 1.38 × 10^{-23} m^2 kg s^{-2} K^{-1}

At room temperature, 298 K, the kinetic energy of molecules of air is

$$\frac{3}{2} kT = 6.17 \times 10^{-21} \text{ J} \tag{5.11}$$

The mass of primary nanoparticles is

$$m_{nano} = \frac{4}{3} \rho_s \pi \cdot r^3 = 1.16 \times 10^{-21} \text{ kg} \tag{5.12}$$

This gives

$$\theta_{\max imun} = \frac{\langle C^2 \rangle_{nano}}{3} \approx 3.3 \qquad \text{m}^2/\text{s}^2 \tag{5.13}$$

These values are close to the maximum granular temperature measured by V. N. Vasishta (2004; Gidaspow, et al. 2004b) for 10 nm Tullanox. Other nanoparticles give order of magnitude lower values.

The solids stress modulus determined by Jung and Gidaspow (2002) for 10 nm particles is not far off from this maximum value of the granular temperature. A typical value is

$$G' = G / \rho_s = 0.25 \qquad \mathrm{m^2/s^2} \tag{5.14}$$

We see that the production of granular temperature of nanoparticles is not primarily due to shear but due to interaction of the nanoparticles with air. A complete kinetic theory model must include both effects. In the absence of such a complete model, a model with input viscosity and stress must be used for simulations.

5.3 Hydrodynamics Model

The hydrodynamics model utilized to compute the dissemination of the nanoparticles uses the principles of the conservation of mass, momentum and energy of each phase. It is a predictive hydrodynamics multi-phase model developed originally to model fluidization. (Gidaspow and Ettehadieh, 1983 and Syamlal and Gidaspow, 1985)

In this study, we used the viscous model to predict the hydrodynamics of nanoparticles. The equations are the conservation of mass momentum and energy equations for each phase given in Gidaspow's book as model B. All equations are written in rectangular coordinates, as summarized in Table 5.2. These are 4(N+1) nonlinear coupled partial differential equations for 4(N+1) dependent variables, for 1 gas phase and N solids phases. The variables to be computed are the pressure P, the solids volume fractions ε_k (k=1,…,N), the gas velocity components U_g and V_g and the solids velocity components U_k and V_k (k = 1,…,N) in the –x and –y direction,

respectively, and the temperature T_g and T_k (k = 1,…,N) of gas and solids phases, respectively. The numerical scheme used in the IIT code is the Implicit Continuous Eulerian (ICE) approach. The model uses donor cell differencing. The conservation of momentum and energy equations are in mixed implicit form. The continuity equations excluding mass generation are in implicit form.

For the viscous model, the solid viscosity and solids modulus are input data into the model. The solid viscosity increases with increasing solid concentration, which was estimated as a function of radial distribution function.

$$\mu_s = 0.0017\varepsilon_s^{1/3} g_0 \qquad \text{Pa.s} \qquad (5.15)$$

The above expression for the solids viscosity is based on the experimental data presented here. The radial distribution function at contact, g_0, is calculated as follows:

$$g_o = \left[1 - \left(\frac{\varepsilon_s}{\varepsilon_{s,\max}}\right)^{1/3}\right]^{-1} \qquad (5.16)$$

where the maximum solids packing, $\varepsilon_{s,\max}$ was estimated from the solid compression in the IIT fluidized bed and simulation data which was 0.08.

The correlation for particulate viscosity given by equation (5.11) is a semi-empirical equation based on kinetic theory. The viscosity increases to the one third power due to isentropic compression (Gidaspow and Huilin, 1998). The radial distribution function is based on Bagnold's equation. It is similar to the viscosity of a concentrated suspension of Frankel and Acrivos (1967).

The solid stress modulus is the gradient of solids pressure, as described in Gidaspow (1994). If we look at the balance of momentum for the solid in the y direction, the gradient can be written as,

$$\nabla P_s = \frac{\partial P_s}{\partial y} \qquad (5.17)$$

The solid pressure is a function of gas volume fraction in the system

$$P_s = P_s(\varepsilon) \tag{5.18}$$

Applying the chain rule, we get the relation.

$$\nabla P_s = G(\varepsilon_g)\nabla \varepsilon_g \tag{5.19}$$

The particle-to-particle interaction coefficient is defined as:

$$G = \frac{\partial P_s}{\partial \varepsilon_s} \tag{5.20}$$

The solid modulus is expressed as a function of the gas volume fraction. An exponential form is used.

$$G(\varepsilon_g) = 10^{-14.926\varepsilon_g + 18.667} \quad \text{dyne cm}^{-2} \tag{5.21}$$

Jung and Gidaspow (2002) estimated the solid stress modulus for the nano-size particles, 10 nm Tullanox, used here. They measured the solid volume fraction as a function of bed height using a γ -ray densitometer in a settling experiment.

The energy equations in Table 5.2 are discussed in Syamlal and Gidaspow (1985). For nearly equal gas and particle temperatures and rapid pressures, they reduce to the balance between the change of enthalpy of the gas and the mechanical flow work, given below.

$$\rho c_p \frac{dT}{dt} = \frac{dP}{dt} \tag{5.22}$$

Integration of the equation, written for a mass of gas moving with its velocity, gives the usual adiabatic expansion formula. It shows the cooling upon the reduction of pressure.

Conservation of energy

For the conservation of energy, the internal energy balance for the gas phase is written in terms of enthalpy which corresponding to gas temperature:

$$\frac{\partial}{\partial t}\left(\varepsilon_g \rho_g H_g\right) + \nabla \cdot \left(\varepsilon_g \rho_g H_g \vec{v}_g\right) = \left(\frac{\partial P}{\partial t} + \vec{v}_g \cdot \nabla P\right) - H_{g1} - H_{g2} - \nabla \cdot q_g \quad (5.23)$$

where $\left(\frac{\partial P}{\partial t} + \vec{v}_g \cdot \nabla P\right)$ is the work term due to compression or expansion, H_{g1} and H_{g2} describes gas-solids interphase heat transfer (solid phase1 and solid phase2), and q_g is the gas phase conductive heat flux. The thermal energy balance for the fist phase of solids phase (k=1) is given by

$$\frac{\partial}{\partial t}\left(\varepsilon_k \rho_k H_k\right) + \nabla \cdot \left(\varepsilon_k \rho_k H_k \vec{v}_k\right) = H_{g1} - \nabla \cdot q_{s1} \quad (5.24)$$

where H_{g1} describes gas-solids phase 1 interphase heat transfer, and q_{s1} is the solids phase 1 conductive heat flux.

1. A number of simplified assumptions have been made in the formation of thermal energy equation of gas-solids phase.
2. The irreversible rate of increase of integral energy due to viscous dissipation has been neglected.
3. No reaction occurs in this process, so the heat of reaction term is negligible.
4. Heat transfer between different solid phase is negligible.
5. Radiative heat transfer is not considered.

For gas solids heat transfer, the heat transfer between the gas and solids is a function of temperature difference between both phases:

$$H_{gk} = -h_{vk}\left(T_k - T_g\right) \quad (5.25)$$

where h_{vk} is the heat transfer coefficient between the gas phase and the solid phase k which is related to the particle Nusselt number Nu_m:

$$Nu = \frac{h_{vk} d_k}{K_g} \tag{5.26}$$

For conductive heat flux in gas phase, it is decribes by Fourier's law:

$$q_g = -\varepsilon_g K_g \nabla T_g \tag{5.27}$$

where K_g is the gas thermal conductivity.

For conductive heat flux in solids phase, it is assumed to have a form similar to that in the fluid phase

$$q_k = -\varepsilon_k K_k \nabla T_k \tag{5.28}$$

where K_k is the particle thermal conductivity.

Therefore, the energy balance can be expressed as a function of temperature as following:

The internal energy balance for the fluid phase is

$$\varepsilon_g \rho_g c_{pg} \left(\frac{\partial T_g}{\partial t} + \vec{v}_g \cdot \nabla T_g \right) = \left(\frac{\partial P}{\partial t} + \vec{v}_g \cdot \nabla P \right) + h_{g1}\left(T_{s1} - T_g\right) + h_{g2}\left(T_{s2} - T_g\right) + \nabla \cdot \left(K_g \varepsilon_g \nabla T_g\right) \tag{5.29}$$

The thermal energy balance for the solids phase 1 is

$$\varepsilon_{s1} \rho_{s1} c_{ps1} \left(\frac{\partial T_{s1}}{\partial t} + \vec{v}_{s1} \cdot \nabla T_{s1} \right) = h_{g1}\left(T_g - T_{s1}\right) + \nabla \cdot \left(K_{s1} \varepsilon_{s1} \nabla T_{s1}\right) \tag{5.30}$$

Initial and boundary Conditions

The computational program was carried out in two steps, (1) the early-time hydrodynamics describing the pressure wave propagation and solids compaction in the device following the detonation, (2) the dissemination hydrodynamics describing

the dispersal of powder from the device into the surrounding atmosphere. Therefore two sets of initial and boundary conditions were required.

The system configuration used for the early-time hydrodynamics and dissemination steps is shown in Figures 5.9 and 5.10, respectively. The system consisted of 10 nm silica and various sizes of aluminum particles, 0.5 micron, 5 micron, 50 micron and 100 microns. In the experiments at IITRI (Sun, et al., 1994), alumina particles were used to prevent pre-ignition of particles. As shown here, it served as a thermal barrier.

For the early-time hydrodynamics, the cell allocation and the initial and boundary conditions are summarized in Table 5.3. Uniform grids were used for this step. The initial conditions of pressure and temperature for the dispersal charge which was located in the first cell are estimated from a covolume equation of state, as follows:

$$P = \rho_e \left(n\tilde{R}T + \alpha P \right) \tag{5.31}$$

where, α = 0 m^3/kg. The quantity of gas formed in the reaction, n, was 0.037155 kmol/kg of explosive. The density, ρ_e, of the explosion reaction products was taken to be 83 kg/m^3 which occupies the first cell having a thickness of 1 mm.

For the dissemination step, the initial conditions were averaged from the early-time hydrodynamics computation at the time when the device broke up.

The computed constant-pressure heat capacity of the reaction products was 1.9 kJ/(kg.K). The heat capacity was assumed to be 1.5 kJ/(kg.K) for the solids phases.

The time increment (e.g. Table 5.3 and 5.4) was of the order of 10^{-6} seconds. This satisfies the Courant stability condition $\Delta t \leq \Delta x$ /sonic velocity. The dissemination computation was of the order of 3 hours on a laptop computer (Acer, Model TravelMate 290 Series).

For the boundary conditions, partial derivatives of velocities are set to zero. These are the continuous outflow. They are used to simulate the explosion and dissemination processes. In the case of the temperatures, the boundary conditions represent non-conducting walls. These conditions were adequate since the variation in temperature of the phases was small far away from the explosion center.

5.4 Early-Time Hydrodynamics Simulation

The energy for dissemination comes from a plastic explosive, marked as “dispersal charge” in Figure 5.9. The explosive is instantaneously converted to a high pressure, high temperature gas. For the experiments done at IITRI, the equilibrium pressure and temperature, computed with an equilibrium code (Pape and Gidaspow, 1998) were 100 MPa and 3900 K, respectively. This high pressure, high temperature gas accelerates the particles in the container, shown in Figure 5.9. In region I, aluminum particles of various sizes are put into the device to serve as a thermal barrier. The simulations presented here show that the thermal barrier was effective in reducing the high temperature of the nanoparticles. The cooling is primarily due to nearly adiabatic expansion. The pressure, radial gas velocity, radial solids velocities, solids volume fractions and solids temperature gradients are computed in the device at five different times in order to determine the time when the device breaks up and dissemination begins. Four particles sizes of aluminum were studied, namely, 0.5 micron, 5 micron, 50 micron and 100 micron.

5.4.1 Horizontal Velocities

Figure 5.11 shows the solids velocities of 10nm silica particles for four aluminum particles of sizes 0.5, 5, 50, 100 microns as a function of time. The energy

of the high pressure gas was quickly converted to the kinetic energy of particles. The larger particles in the container produced higher velocities of nanoparticles. For 100 micron and 50 micron aluminum particles the nanoparticles reached the end of the container, 77 mm, at approximately 0.75 ms. For the smaller aluminum particles the end of the container was reached at 1 ms. These breakage times approximately corresponded to the dissemination times in the experiments at IITRI. The dissemination processes began at these times. Figure 5.12 shows the gas velocities for the four aluminum particles. The computed gas velocities are equal to the nanoparticles velocities at the same positions and times. This is due to the large drag. Figure 5.13 shows the solid velocities of the four aluminum particles. The smaller particles moved with the gas velocities, but not the larger particles.

5.4.2 Pressure Propagation

Figure 5.14 exhibits the early-time hydrodynamic pressures for the four aluminum particles in the device at four different times, 0.25 ms, 0.5 ms, 0.75 ms and 1 ms. For 0.5 and 5 micron particles, the pressure wave reached the outer edge of the container at 1 ms. For 50 and 100 micron particles, it was 0.75 ms. Hence, this was the time at which the particles began to be disseminated from the device, as already discussed in terms of velocities.

5.4.3 Solids Volume Fractions

The computed solids volume fractions of nanoparticles and aluminum particles are depicted in Figures 5.15 and 5.16. The 0.5 micron and the 5 micron aluminum particles get more compressed than the 50 micron and 100 micron aluminum particles. Therefore the pressure wave moved through the nanoparticles for

the smaller aluminum system slower than for the larger particle system. The nanoparticles were compressed up to volume fractions of 0.06 - 0.07. These compressions agreed with the solid compression in the IIT two story riser, which was 0.065.

5.4.4 Temperatures

The computed particle temperatures of the nanoparticles and the aluminum particles in the device are shown in Figures 5.17 and 5.18, respectively. The temperatures of the nanoparticles were approximately 350 - 400 K. This shows that the aluminum particles were effective in reducing the temperatures of the nanoparticles. Some aluminum particles are still hot at dissemination. No thermal wave motion was observed, similar to pressure propagation.

5.5 Particles Dissemination into the Open Channel

The early-time hydrodynamic computational velocities, volume fractions, pressure and temperatures were used to start the dissemination processes into an open channel. The cell allocation, the initial conditions and the boundary conditions for the dissemination are summarized in Table 5.4. The system configuration used for the dissemination step was shown in Figure 5.10. Variable computational grids were used in the simulation. The dissemination device was approximated by two cells in the horizontal direction. The device is located in the middle of the channel. The initial conditions used in the dissemination hydrodynamics simulation were averaged from the early-time hydrodynamics computations at the time at which the solids just began to move from the device. For the system of 5 micron aluminum particles and 10 nm

silica, the device broke up at 1 ms. For 100 micron aluminum particles, the device broke up at 0.75 ms.

Figure 5.19 shows the pressure propagation for dissemination of a mixture of 10 nm and 5 micron particles. For short times the pressure isotherms are nearly circular, as expected from a small source. The figure clearly shows compression and reflection phenomena.

Figure 5.20 exhibits snapshots of flow structure of nanoparticles at 0.05, 0.1, 0.15 and 0.2 secs for the case of 5 micron aluminum particles and 10 nm silica. These snapshots show jet-like behavior dominated by a vortex ring structure. At 0.15 sec, this computation is similar to the experiments of Longmire and Eaton (1992). The particles are pulled out of the streaming regions inside the vortex rings and pushed into the regions downstream of the cores, where the clusters appear. Due to the presence of compressed gas without particles in the first cell, the maximum concentration of particles has moved away from the dissemination device. The aluminum particles move with the same speed as the nanoparticles. Hence the flow structures of both particles are identical to that shown in Figure 5.20. In the cloud, the concentration of nanoparticles is smaller than the concentration of aluminum particles. This is shown in the color bar for the solid volume fractions in Figure 5.21.

Figure 5.22 shows the flow structures of 100 micron aluminum particles and 10 nm silica particles at a dissemination time of 0.15 ms. The large aluminum particles settled on the ground, as expected and observed in the experiments done at IITRI. With the dissemination of 100 micron aluminum particles and the nanoparticles the computations did not show the vortex ring structure observed for the case of 5 micron aluminum particles and 10 nm silica. Hence we see that the flow structure can be controlled by varying the size distribution of particles. For example,

it may be possible to precipitate an aerosol cloud by dispersing a mixture of large particles and nanoparticles into the cloud.

สถาบันวิทยบริการ
จุฬาลงกรณ์มหาวิทยาลัย

5.6 Conclusions

1. The particulate viscosity of 10 nm silica nanoparticles flowing in a pilot plant circulating fluidized bed was estimated to be almost half of that of liquid water. This estimate was obtained from measurements of pressure drops, particle fluxes and particle concentrations using the technique developed by Miller and Gidaspow (1992). This value of viscosity agrees with an estimate obtained from elementary kinetic theory, assuming that the Brownian type nanoparticle oscillations are caused by the rapid random motion of the air molecules.

2. The measured nanoparticle viscosity was used in a CFD code developed earlier for explosive dissemination of micron size particles into an atmosphere, such as the pyroplastic flow of dust and the covering of ground by hot particles during eruption of volcanoes. This study shows that nanoparticle flow together with 5 micron particles, modeled earlier, without appreciable segregation. The computed ground concentrations allow a comparison to be made to observations. Eulerian-Lagrangian models found in FLUENT cannot compute such ground concentrations due to the diluteness assumption.

3. The new nanoparticle flow model allows further exploration of some unusual flow behavior of nanoparticles, such as bubbleless fluidization and multiple vortex formation (V. Jiradilok, 2006) during bed expansion, Fig 5.2. In such computations, the nanoparticle viscosity reported here plays a major role.

4. In this study we also show how to use CFD to design an explosive dissemination device that will prevent the overheating of the particles to be disseminated.

Appendix A: Grid dependency

Early time hydrodynamics

For the design of the disseminator there is no grid dependence, as shown in Table 5.5.

Dissemination

For the dissemination of particles into the cavity, there exits some small grid dependency, as shown in Figure 5.23. The cloud and vortex structures are very similar for coarse and fine grid simulations. Unlike in the study of fluidization, the dissemination process is over very quickly, in one second or less.

สถาบันวิทยบริการ
จุฬาลงกรณ์มหาวิทยาลัย

Table 5.1 Viscosity Calculations Using the Pressure Drop Balance Equation.

Ug (cm/sec)	**Av. Conc ε_s**	**Gradient Pressure Drop (N/m^3)**	**Weight of the bed (N/m^3)**	**Viscosity (mPa.s)**
50.1	0.0058	43	41.9	0.45
34.2	0.0051	40	36.4	0.51
27.6	0.0060	40	38.5	0.68

สถาบันวิทยบริการ
จุฬาลงกรณ์มหาวิทยาลัย

Table 5.2 Hydrodynamic Model

Continuity Equations

Gas phase

$$\frac{\partial(\rho_g \varepsilon_g)}{\partial t} + \nabla \cdot (\rho_g \varepsilon_g \vec{v}_g) = 0$$

Solid phase

$$\frac{\partial(\rho_k \varepsilon_k)}{\partial t} + \nabla \cdot (\rho_k \varepsilon_k \vec{v}_k) = 0$$

Momentum Equations

Gas momentum

$$\frac{\partial(\rho_g \varepsilon_g \vec{v}_g)}{\partial t} + \nabla \cdot (\rho_g \varepsilon_g \vec{v}_g \vec{v}_g) = -\nabla P + \sum_{k=1}^{N} \beta_{gk}(\vec{v}_k - \vec{v}_g) + \nabla \cdot 2\varepsilon_g \mu_g \nabla^s \vec{v}_g + \varepsilon_g \rho_g \vec{g}$$

Solids momentum

$$\frac{\partial(\rho_k \varepsilon_k \vec{v}_k)}{\partial t} + \nabla \cdot (\rho_k \varepsilon_k \vec{v}_k \vec{v}_k) = \beta_{gk}(\vec{v}_g - \vec{v}_k) + \sum_{l=1}^{N} \beta_{kl}(\vec{v}_l - \vec{v}_k) - G_s \nabla \varepsilon_k$$
$$+ \nabla \cdot 2\varepsilon_k \mu_k \nabla^s \vec{v}_k + \varepsilon_k \rho_k \vec{g}$$

Energy Equations

Gas Phase

$$\frac{\partial}{\partial t}(\varepsilon_g \rho_g H_g) + \nabla \cdot (\varepsilon_g \rho_g H_g \vec{v}_g) = \left(\frac{\partial P}{\partial t} + \vec{v}_g \cdot \nabla P\right) + \sum_{k=1}^{N} h_{vk}(T_k - T_g) + \nabla \cdot (K_g \varepsilon_g \nabla T_g)$$

Solid Phase

$$\frac{\partial}{\partial t}(\varepsilon_k \rho_k H_k) + \nabla \cdot (\varepsilon_k \rho_k H_k \vec{v}_k) = h_{vk}(T_g - T_k) + \nabla \cdot (K_k \varepsilon_k \nabla T_k)$$

Constitutive equations

$$\varepsilon_g + \sum_{k=1}^{N} \varepsilon_k = 1$$

$$T_k = T_0 + \frac{H_k - H_0}{c_k}$$

Equation of State – Ideal Gas Law

$$\rho_g = \frac{P}{\tilde{R} T_g}$$

Empirical Solids Viscosity and Stress Model

$$\nabla P_k = G(\varepsilon_k) \nabla \varepsilon_k$$

$$G(\varepsilon_g) = 10^{-14.926\varepsilon_g + 18.667} \text{ dyne/cm}^2$$

for nanoparticles

$$\mu_k = 0.017\varepsilon_k^{1/3} g_0 \qquad \text{poise}$$

for aluminum particles

$$\mu_k = 5\varepsilon_k \qquad \text{poise}$$

The radial distribution function

$$g_0 = \left[1 - \left(\frac{\varepsilon_s}{\varepsilon_{s,\max}}\right)^{1/3}\right]^{-1}$$

Gas-Solid Drag Coefficients

for $\varepsilon_f < 0.8$ (based on Ergun equation)

$$\beta_{gk} = 150\frac{\varepsilon_k^2 \mu_g \rho_k}{(\varepsilon_g d_k \phi_k)^2 (\rho_k - \rho_g)} + 1.75\frac{\rho_g \rho_k |\vec{v}_g - \vec{v}_k| \varepsilon_k}{(\varepsilon_g d_k \phi_k)(\rho_k - \rho_g)}$$

for $\varepsilon_f > 0.8$ (based on empirical equation)

$$\beta_{gk} = \frac{3}{4} C_d \frac{\rho_g \rho_k \varepsilon_k |\vec{v}_g - \vec{v}_k|}{d_k \phi_k (\rho_k - \rho_g)} \varepsilon_f^{-2.65}$$

where,

$$C_d = \frac{24}{\mathrm{Re}_k}\left(1 + 0.15\,\mathrm{Re}_k^{0.687}\right) \qquad \text{for } \mathrm{Re}_k < 1000$$

$$= 0.44 \qquad \text{for } \mathrm{Re}_k > 1000$$

$$\mathrm{Re}_k = \frac{\varepsilon_g \rho_g |\vec{v}_g - \vec{v}_k| d_k \phi_k}{\mu_g}$$

Particle – Particle Drag Coefficients

$$\beta_{\substack{kl \\ k,l \neq g}} = \frac{3}{2}\alpha(1+e)\frac{\rho_k \rho_l \varepsilon_k \varepsilon_l (d_k + d_l)^2}{\rho_k d_k^3 + \rho_l d_l^3}|\vec{v}_k - \vec{v}_l|$$

Gas-Phase Heat Transfer

$$K_g = 8.65\left(\frac{T_g}{1400}\right)^{1.786} \qquad \text{W/m.K}$$

Gas-Particle Heat Transfer ,k (=s)

for $\varepsilon_g \leq 0.8$

$$Nu_k = \left(2 + 1.1\,\mathrm{Re}^{0.6}\,\mathrm{Pr}^{1/3}\right)S_k \qquad \mathrm{Re} \leq 200$$

$$= 0.123\left(\frac{4\,\mathrm{Re}}{d_k}\right)^{0.183} S_k^{0.17} \qquad 200 < \mathrm{Re} \leq 2000$$

$$= 0.61\,\mathrm{Re}^{0.67}\, S_k \qquad \mathrm{Re} > 2000$$

for $\varepsilon_g > 0.8$

$$Nu_k = \left(2 + 0.16\,\mathrm{Re}^{0.67}\right)S_k \qquad \mathrm{Re} \leq 200$$

$$= 8.2\,\mathrm{Re}^{0.6}\,S_k \qquad 200 < \mathrm{Re} \le 2000$$

$$= 1.06\,\mathrm{Re}^{0.457}\,S_k \qquad \mathrm{Re} > 2000$$

where,

$$\mathrm{Re} = \frac{\rho_g \left|\vec{v}_g - \vec{v}_k\right| d_k}{\mu_g}$$

$$P_r = \frac{c_g \mu_g}{K_g}$$

$$S_k = \varepsilon_k \frac{6}{d_k}$$

$$Nu = \frac{h_{vk} d_k}{K_g}$$

Particulate-Phase Heat Transfer

$$\frac{K_k}{K_g} = \left(1 - \sqrt{1-\varepsilon_g}\right)\left[1 + \varepsilon_g \frac{\lambda_R}{\lambda}\right] + \sqrt{1-\varepsilon_g}\left[\varphi \frac{\lambda_s^*}{\lambda} + (1+\varphi)\frac{\lambda_{SO}^*}{\lambda}\right]$$

with,

$$\frac{\lambda_{SO}^*}{\lambda} = \frac{2}{(N-M)}\left(\frac{B\left(\frac{\lambda_S^*}{\lambda} + \frac{\lambda_R}{\lambda} - 1\right)}{(N-M)^2\left(\frac{\lambda_S^*}{\lambda}\right)} \cdot \ln\left(\frac{\left(\frac{\lambda_S^*}{\lambda} + \frac{\lambda_{SO}^*}{\lambda}\right)}{B}\right) - \frac{B-1}{N-M} + \frac{B+1}{2B}\left(\frac{\lambda_R}{\lambda} - B\right)\right)$$

$$N - M = 1 + \frac{(\lambda_R/\lambda) - B}{(\lambda_S^*/\lambda)}$$

$$B = 1.25\left(\frac{1-\varepsilon_g}{\varepsilon_g}\right)^{10/9} \quad \text{(for spheres)}$$

$$\frac{\lambda_R}{\lambda} = \frac{0.0004 C_k}{(2/\varepsilon_r - 1)}\left(\frac{T_k}{100}\right)^3 \cdot d_k$$

$$\frac{\lambda_S^*}{\lambda} = 12.227$$

$$\varphi = 7.26 \times 10^{-3}$$

$C_k = 5.67 \times 10^{-8}$ W/m^2.K^4 Stefan-Boltzmann Constant

$\varepsilon_r = 0.93$ Emission Ratio

Table 5.3 Cell allocation and initial and boundary conditions for the early-time hydrodynamics of coarse grid

Cell Allocation

Number of Horizontal Cells	77	
Number of Vertical Cells	1	
Cell Size in Horizontal direction	0.1	cm
Cell Size in Vertical direction	29.1	cm
Time Interval	10^{-6}	sec

Initial Conditions

Dispersal Explosive Pressure	100	MPa
Dispersal Explosive Temperature	3900	K
Solids	Nanoparticles	Al particles
Particle Size, micron	10	0.5, 5, 50 and 100
Solids Density, kg/m^3	2200	2700
Volume Fraction		
Region I	0.00	0.217
Region II	0.025	0.00
Gas Velocity	$U_g = V_g = 0$	
Solids Velocity	$U_k = V_k = 0$	k = 1,2
Solids Temperature	$T_k = 300$ K	k = 1,2

Boundary Conditions

At x = 0.0 cm

$$\varepsilon = 1.0$$
$$U_g = V_g = 0$$
$$\frac{\partial T_g}{\partial x} = \frac{\partial T_k}{\partial x} = 0 \qquad k=1, 2$$

At x = 7.7 cm (Outer boundary)

$$\frac{\partial U_g}{\partial x} = \frac{\partial U_k}{\partial x} = 0 \qquad k=1, 2$$

$$\frac{\partial T_g}{\partial x} = \frac{\partial T_k}{\partial x} = 0 \qquad k=1, 2$$

At y = 0 and 29.1 cm (Bottom and Top boundary)

$$U_g = V_g = 0$$
$$U_k = V_k = 0$$
$$\frac{\partial T_g}{\partial y} = \frac{\partial T_k}{\partial y} = 0 \qquad k=1, 2$$

Table 5.4 Cell allocation and initial and boundary conditions for the dissemination hydrodynamics of coarse grid

Cell Allocation

	Number of Horizontal Cells	52
	Number of Vertical Cells	96
Horizontal direction		
	Number cell x Cell Size, cm	1*2.2 1*5.5 50*19.85
Vertical direction		
	Number cell x Cell Size, cm	43*1.99 10*2.91 43*1.99
	Time Interval, sec	10^{-6}

Initial Conditions

Size of aluminum particles, micron		100		5	
Position of radial cell of the device		1	2	1	2
Pressure, MPa		2.36E-01	2.43E-01	2.65E-01	2.59E-01
Gas volume fraction		0.937	0.915	0.989	0.894
Solids volume fraction	Nanoparticles	0.000	0.025	0.000	0.025
	Al particles	0.063	0.060	0.011	0.081
Horizontal gas velocity, m/s		8.70	31.48	12.06	36.84
Horizontal solids velocity, m/s	Nanoparticles	0.00	29.46	0.00	36.84
	Al particles	11.50	32.22	12.83	36.61
Temperature of gas, K		643	303	761	319
Temperature of solids, K	Nanoparticles	300	302	300	318
	Al particles	381	300	695	319

Remark: The device consisted of first two cells in horizontal direction (1*2.2, 1*5.5) and located in the middle of domain in vertical direction (10*2.91)

Boundary Conditions

At x = 10.0 m (Outer boundary)

$$\frac{\partial U_g}{\partial x} = \frac{\partial U_k}{\partial x} = 0 \qquad k=1, 2$$

At x = 0 m, at y = 0 m (Ground boundary)

$$U_g = V_g = 0 \qquad k=1, 2$$
$$U_k = V_k = 0 \qquad k=1, 2$$

At y = 2 m (Top boundary)

$$\frac{\partial V_g}{\partial y} = \frac{\partial V_k}{\partial y} = 0 \qquad k=1, 2$$

Subscripts: k = 1 - nanoparticles, 2 - aluminum particles

Table 5.5 Cell allocation and initial and boundary conditions for the dissemination hydrodynamics of fine grid

Cell Allocation

	Number of Horizontal Cells		102	
	Number of Vertical Cells		182	
Horizontal direction				
	Number cell x Cell Size, cm	1*2.2	1*5.5	100*9.925
Vertical direction				
	Number cell x Cell Size, cm	86*0.995	10*2.91	86*0.995

Initial Conditions

Size of aluminum particles, micron		100		5	
Case		10*2.91		10*2.91	
Position of radial cell of the device		1	2	1	2
Pressure, MPa		2.36E-01	2.43E-01	2.65E-01	2.59E-01
Gas volume fraction		0.937	0.915	0.989	0.895
Solids volume fraction	Nanoparticles	0	0.025	0	0.025
	Al particles	0.063	0.060	0.011	0.081
Horizontal gas velocity, m/s		8.7	31.48	**12.07**	**36.83**
Horizontal solids velocity, m/s	Nanoparticles	0.0	29.46	0.00	**34.40**
	Al particles	11.50	**32.21**	12.83	**36.60**
Temperature of gas, K		643	303	761	319
Temperature of solids, K	Nanoparticles	300	302	300	318
	Al particles	381	300	695	319

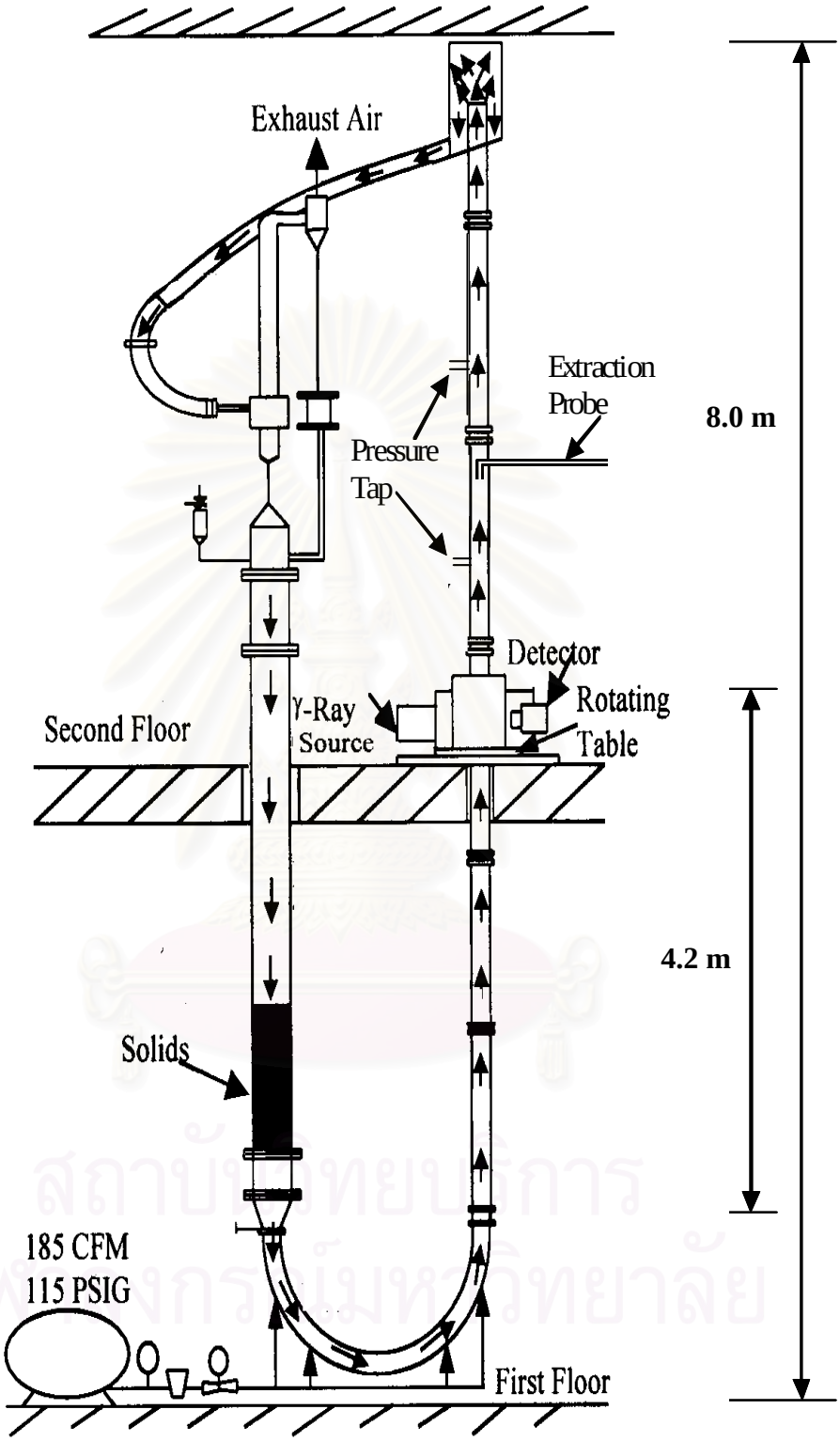

Figure 5.1 IIT Circulating Fluidized Bed with Splash Plate
Riser tube Diameter: 7.62 cm, Downcomer tube Diameter: 10.2 cm

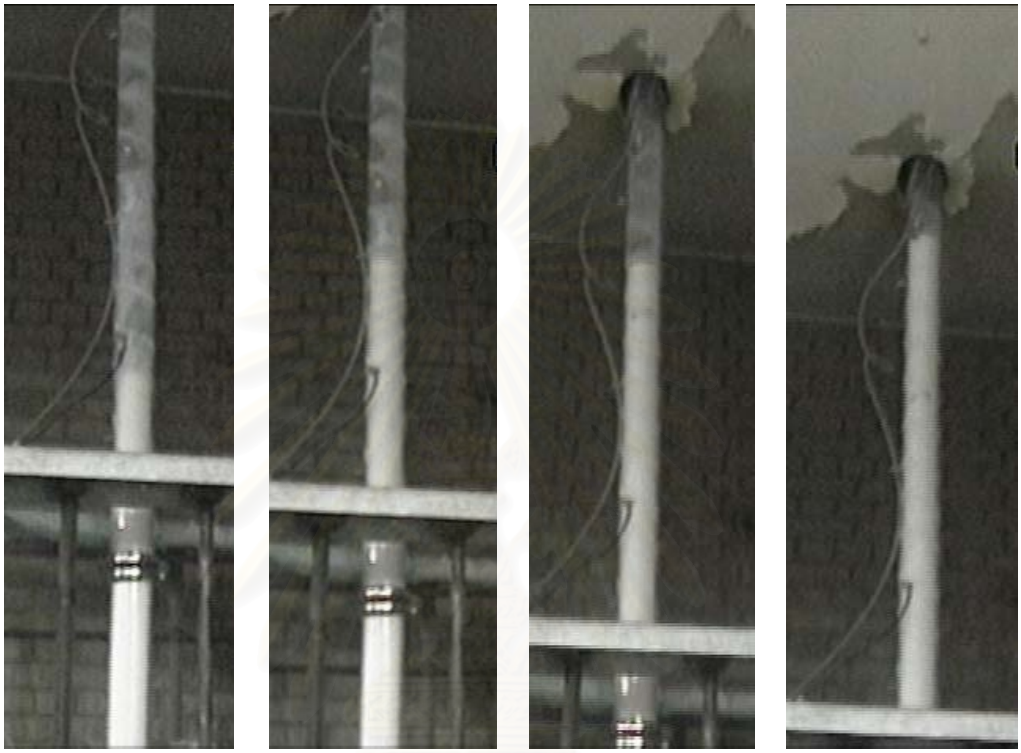

(a) 4 sec (b) 5 sec (c) 6 sec (d) 7 sec

Figure 5.2 Motion of 10 nm silica particles during start-up of circulating fluidized bed at Ug = 30 cm/sec

สถาบันวิทยบริการ
จุฬาลงกรณ์มหาวิทยาลัย

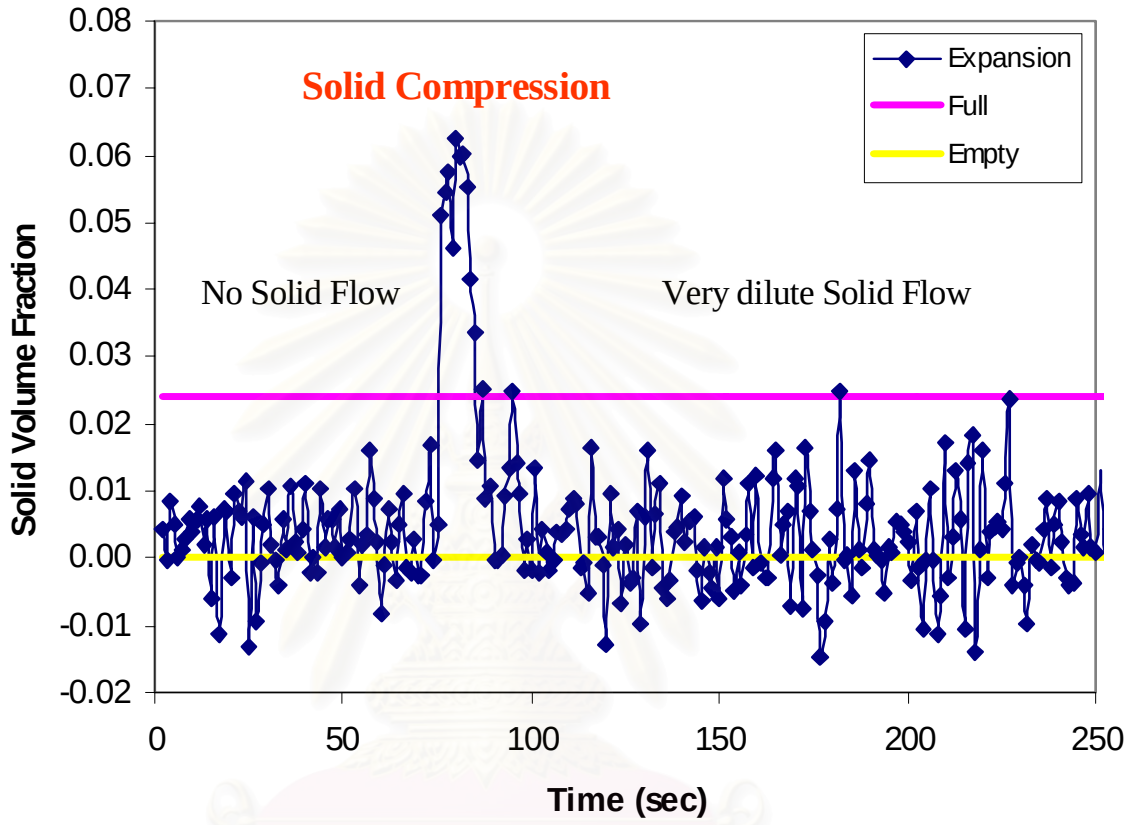

Figure 5.3 Gamma ray densitometer reading on the second flow of the riser, Fig 5.1, converted to solid volume fraction for flow of nanoparticles during start-up, Fig 5.2.

Horizontal lines represent volume fraction for an empty and a riser filled with nanoparticles with no airflow.

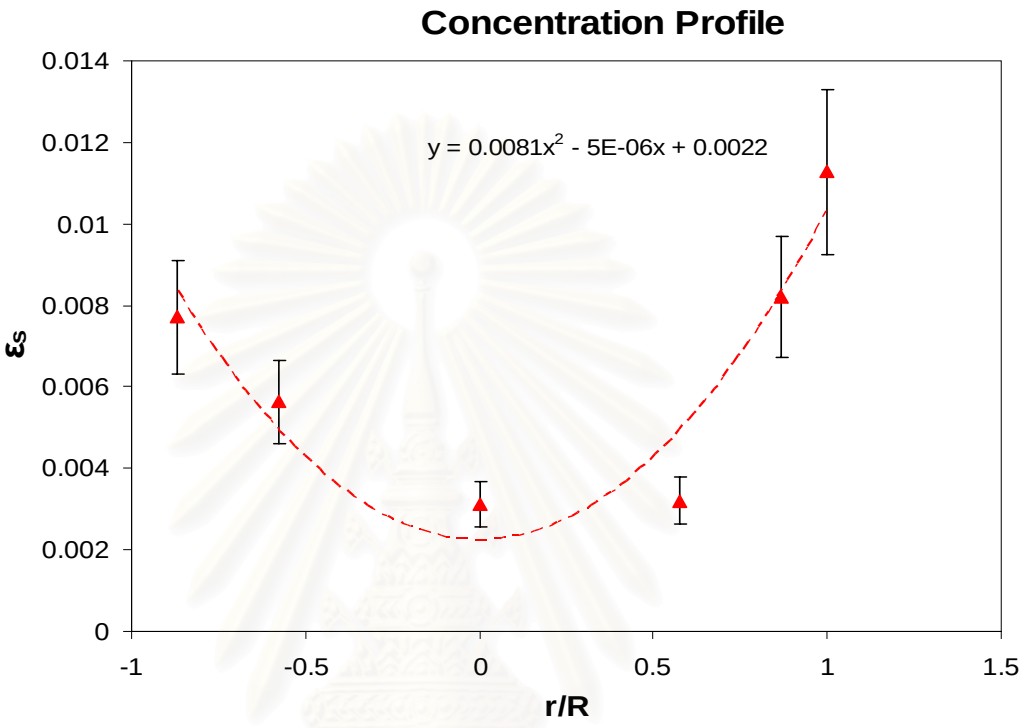

Figure 5.4 Radial solid concentration for Tuallnox particles at Ug = 34.2 cm/sec

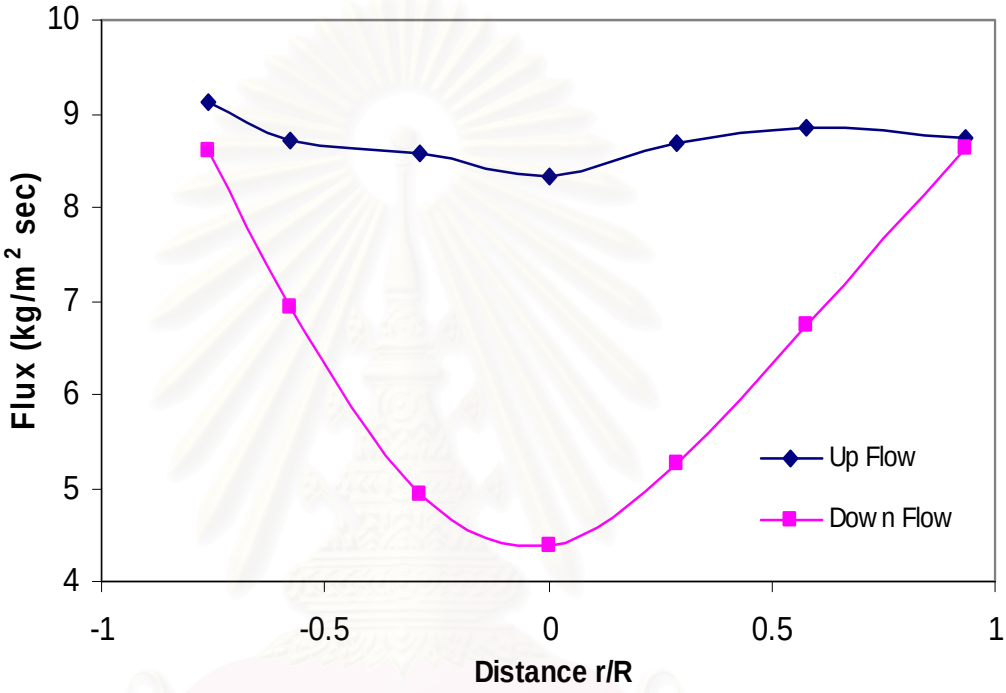

Figure 5.5 Radial Upward and Downward Solid Flux for Tullanox at Ug 27.6 cm/s

สถาบันวิทยบริการ
จุฬาลงกรณ์มหาวิทยาลัย

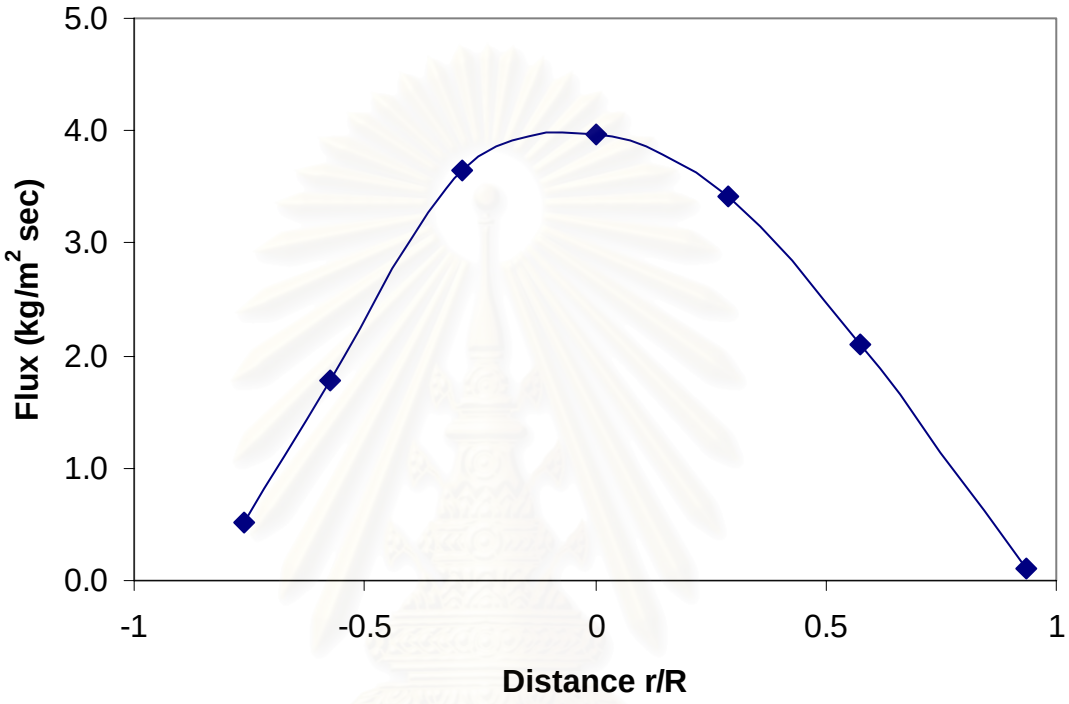

Figure 5.6 Radial net solid flux for Tuallnox particles in the IIT riser at Ug = 27.6 cm/sec

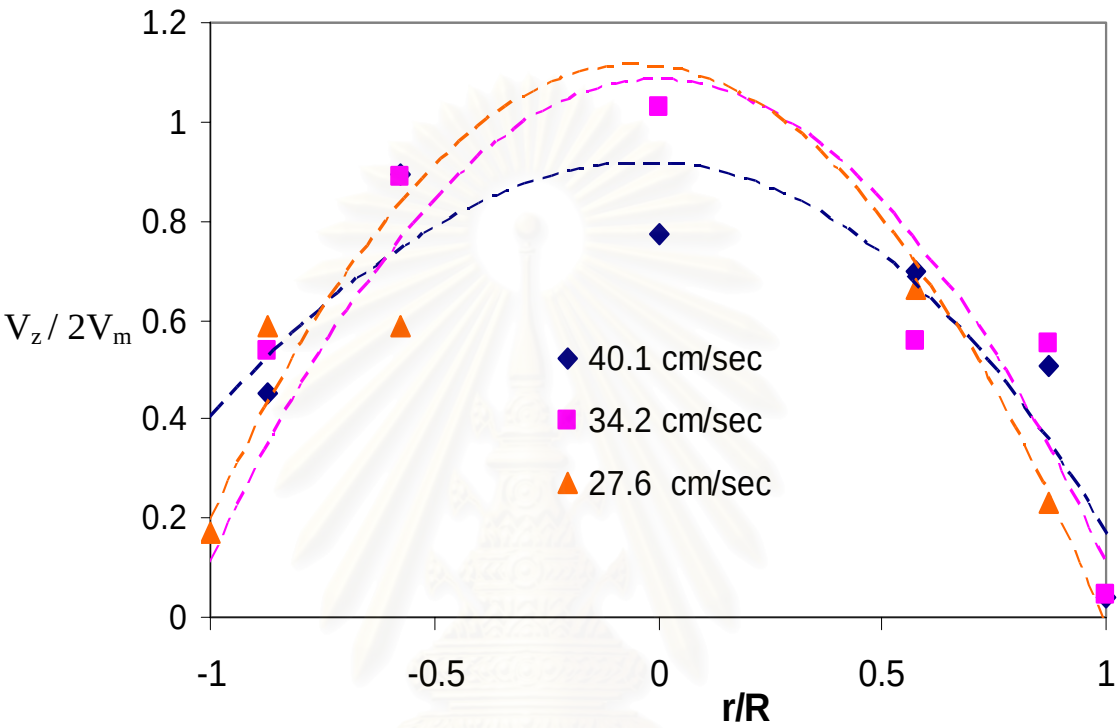

Figure 5.7 Radial Dimensionless velocity of Tuallnox particles vs. gas velocity in the IIT riser

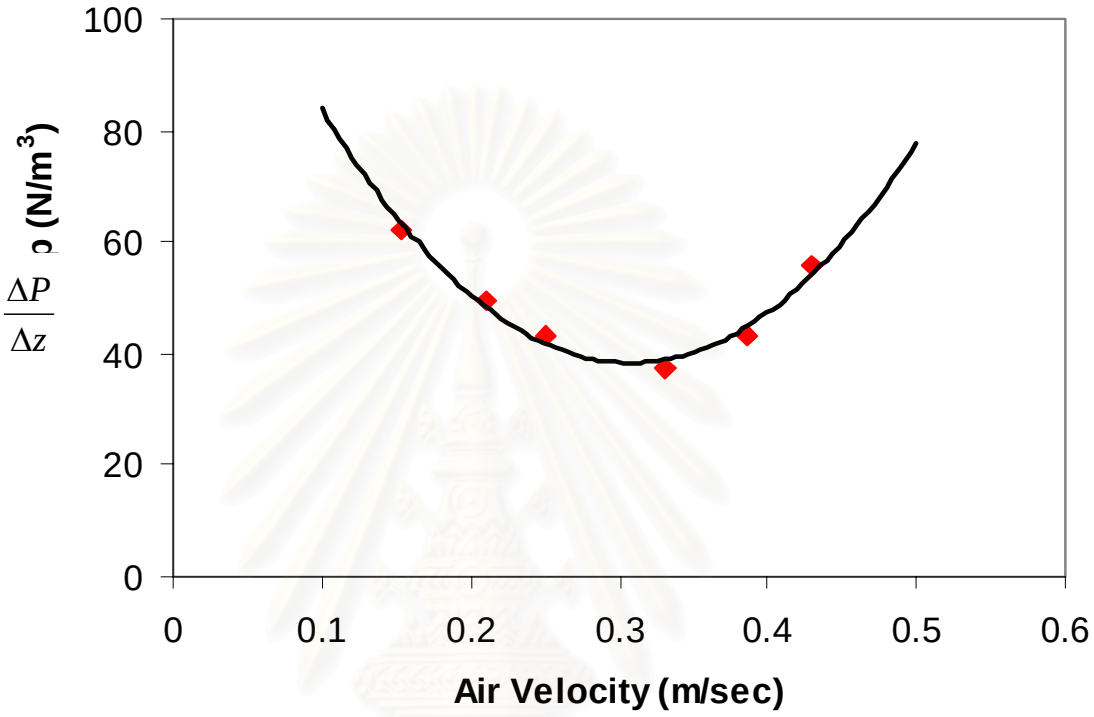

Figure 5.8 Pressure drop/ length as a function of gas velocity for Tullanox in the IIT CFB.

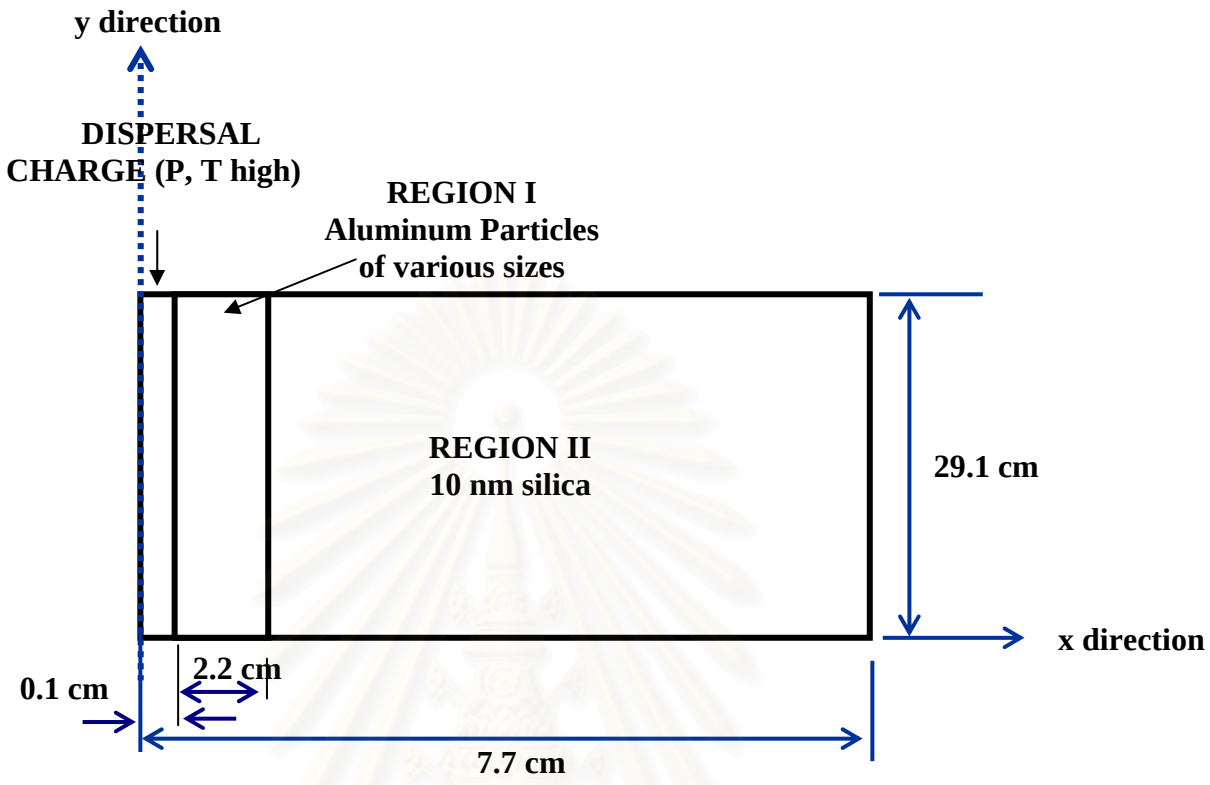

Figure 5.9 System configuration for the early-time hydrodynamics

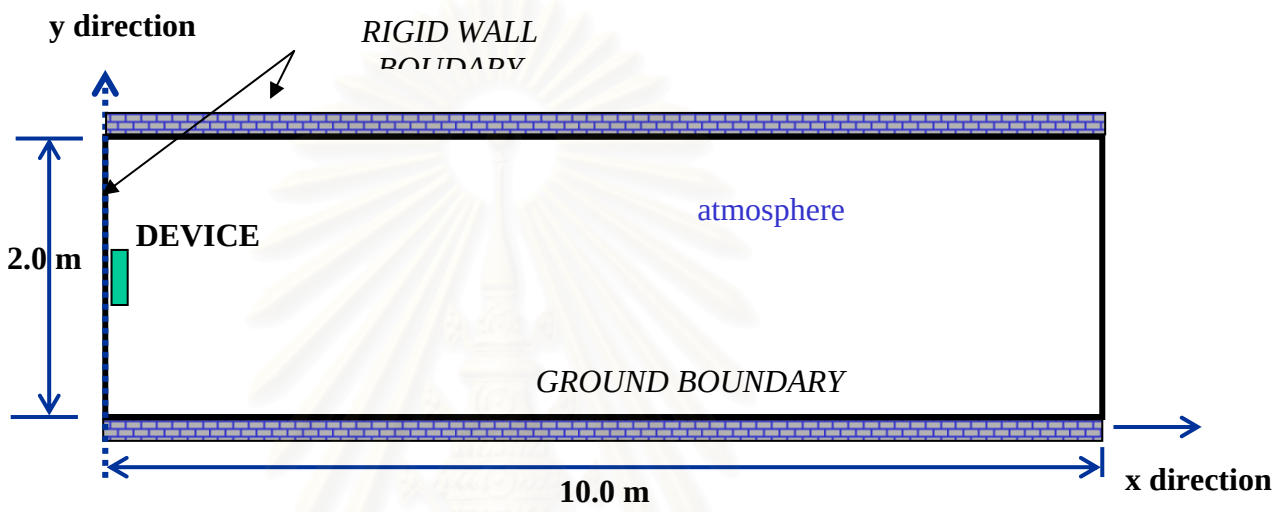

Figure 5.10 System configuration for the dissemination process

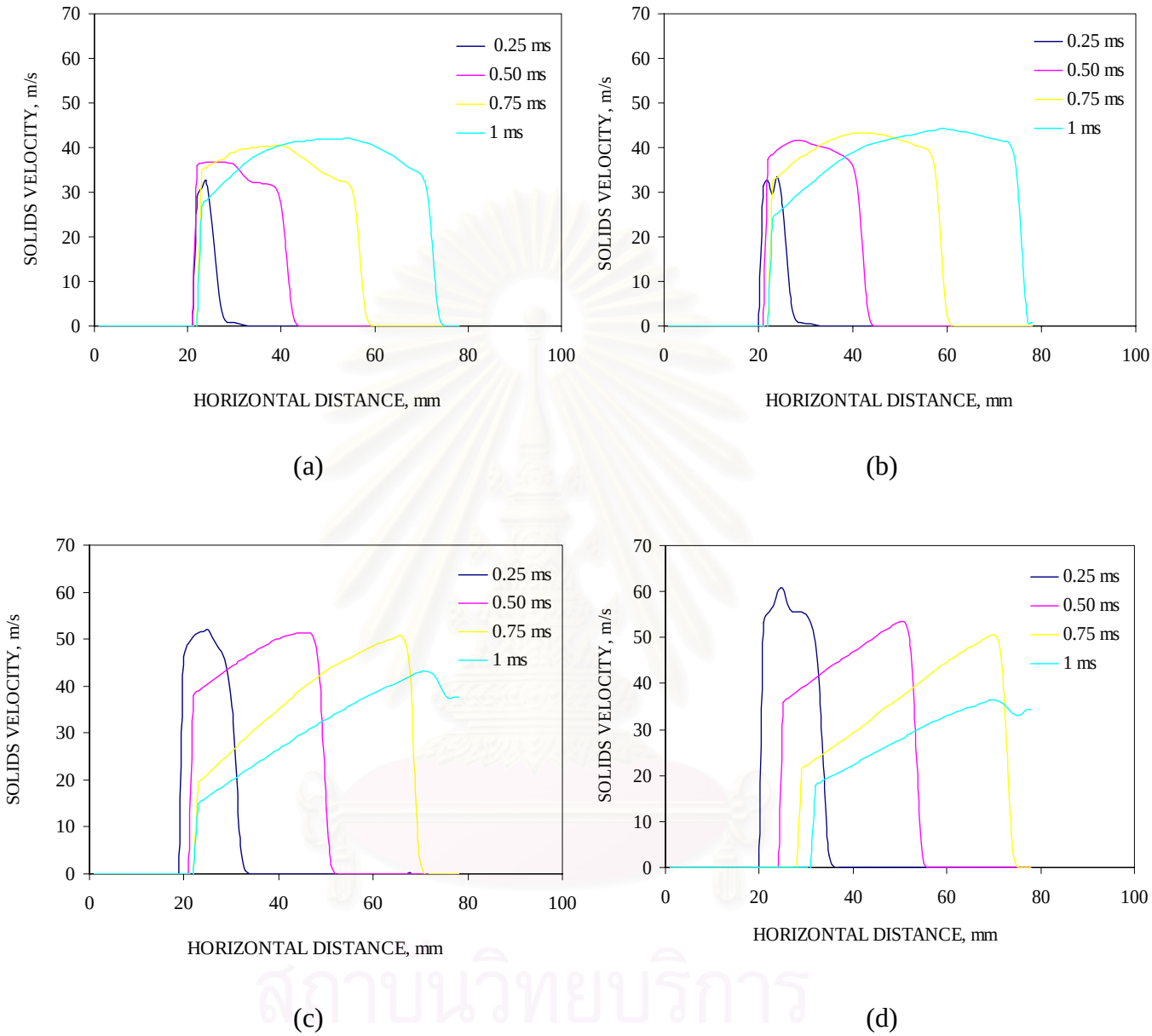

Figure 5.11 Early-time hydrodynamics solids velocity gradients of 10nm silica for four aluminum particles
(a) 0.5 micron (b) 5micron (c) 50 micron (d) 100 micron

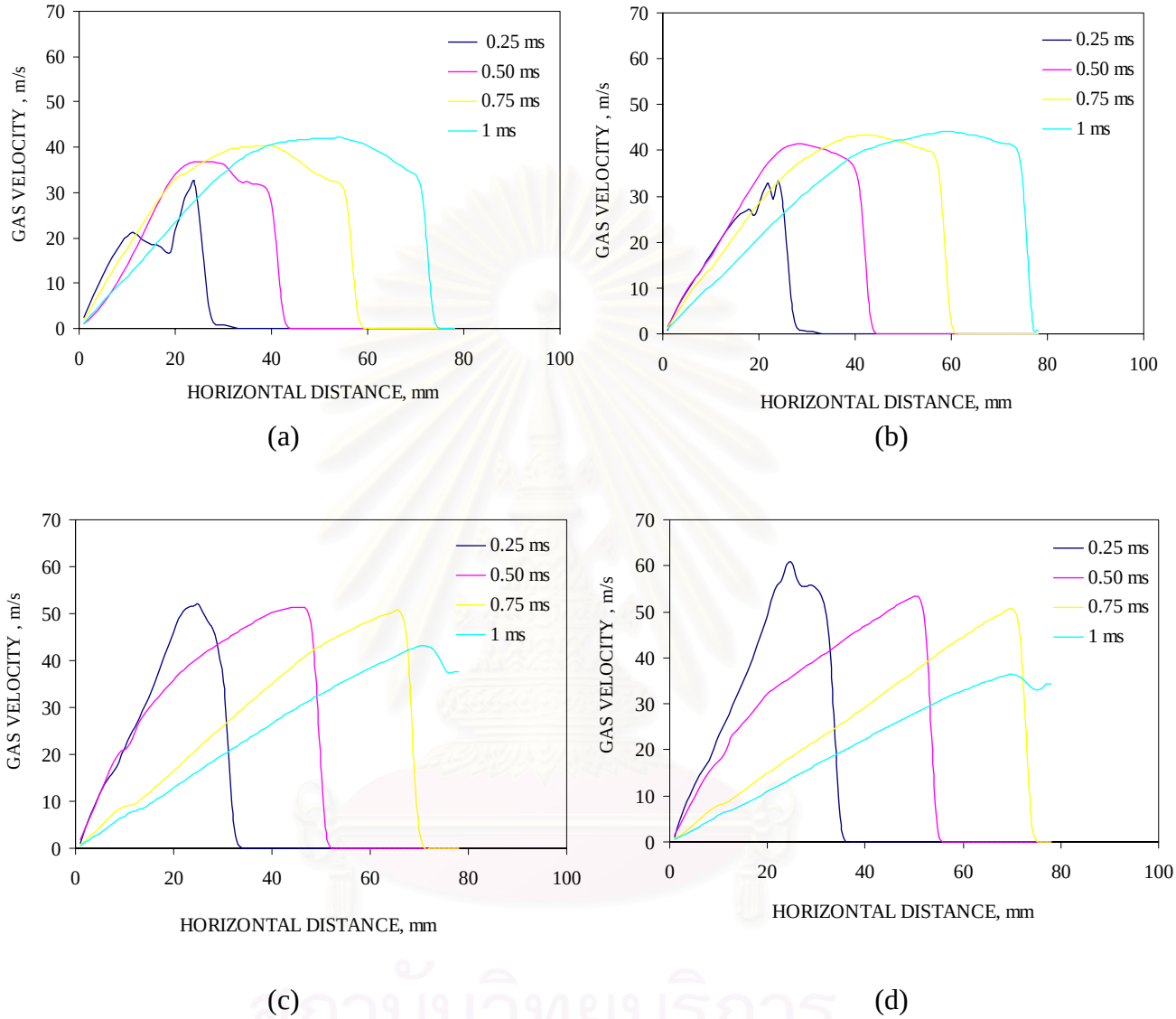

Figure 5.12 Early-time hydrodynamics gas velocity gradients for four aluminum particles
(a) 0.5 micron (b) 5micron (c) 50 micron (d) 100 micron

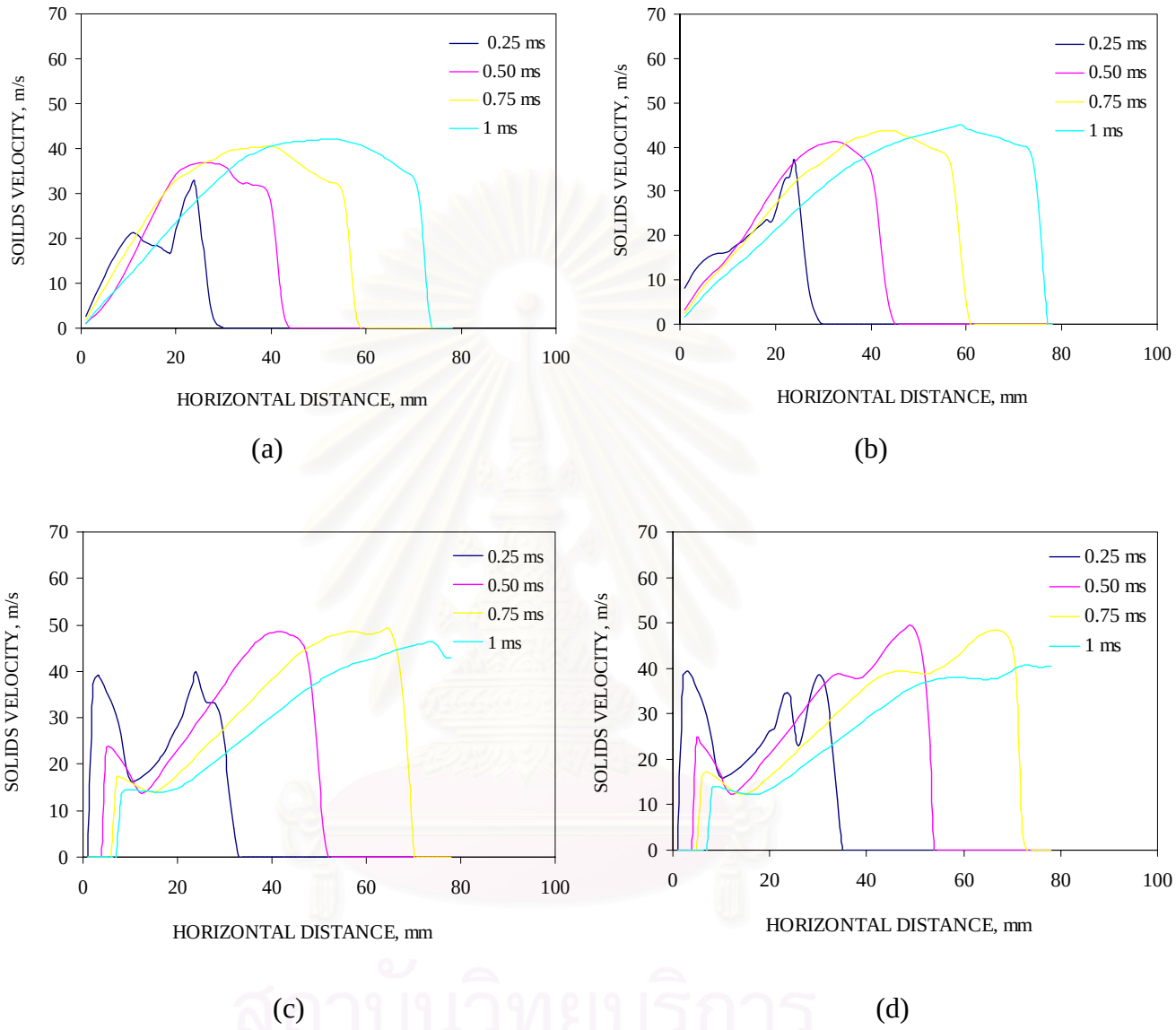

Figure 5.13 Early-time hydrodynamics solids velocity gradients for four aluminum particles
(a) 0.5 micron (b) 5micron (c) 50 micron (d) 100 micron

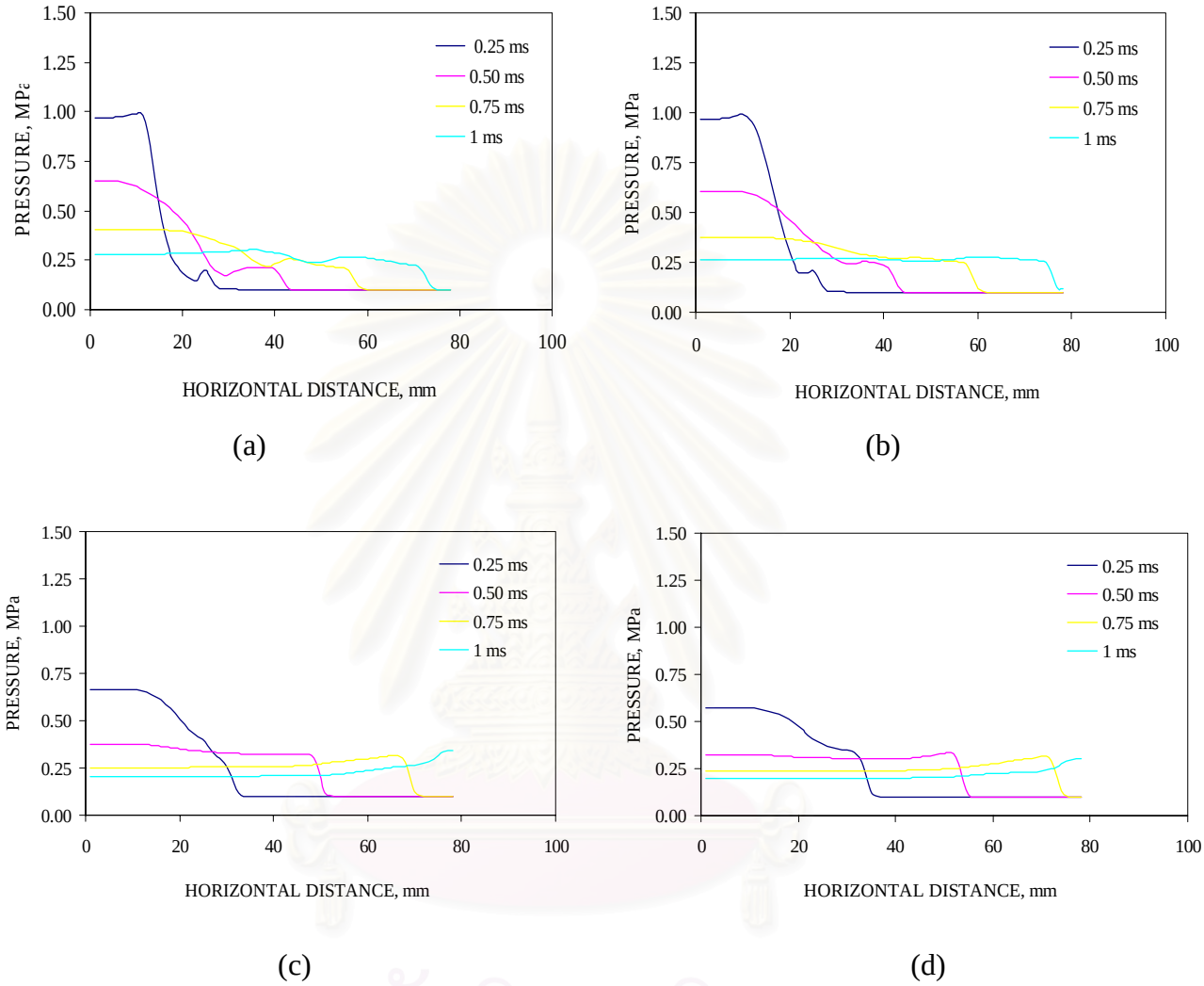

Figure 5.14 Early-time hydrodynamics. Pressure gradients for four aluminum particles
(a) 0.5 micron (b) 5micron (c) 50 micron (d) 100 micron

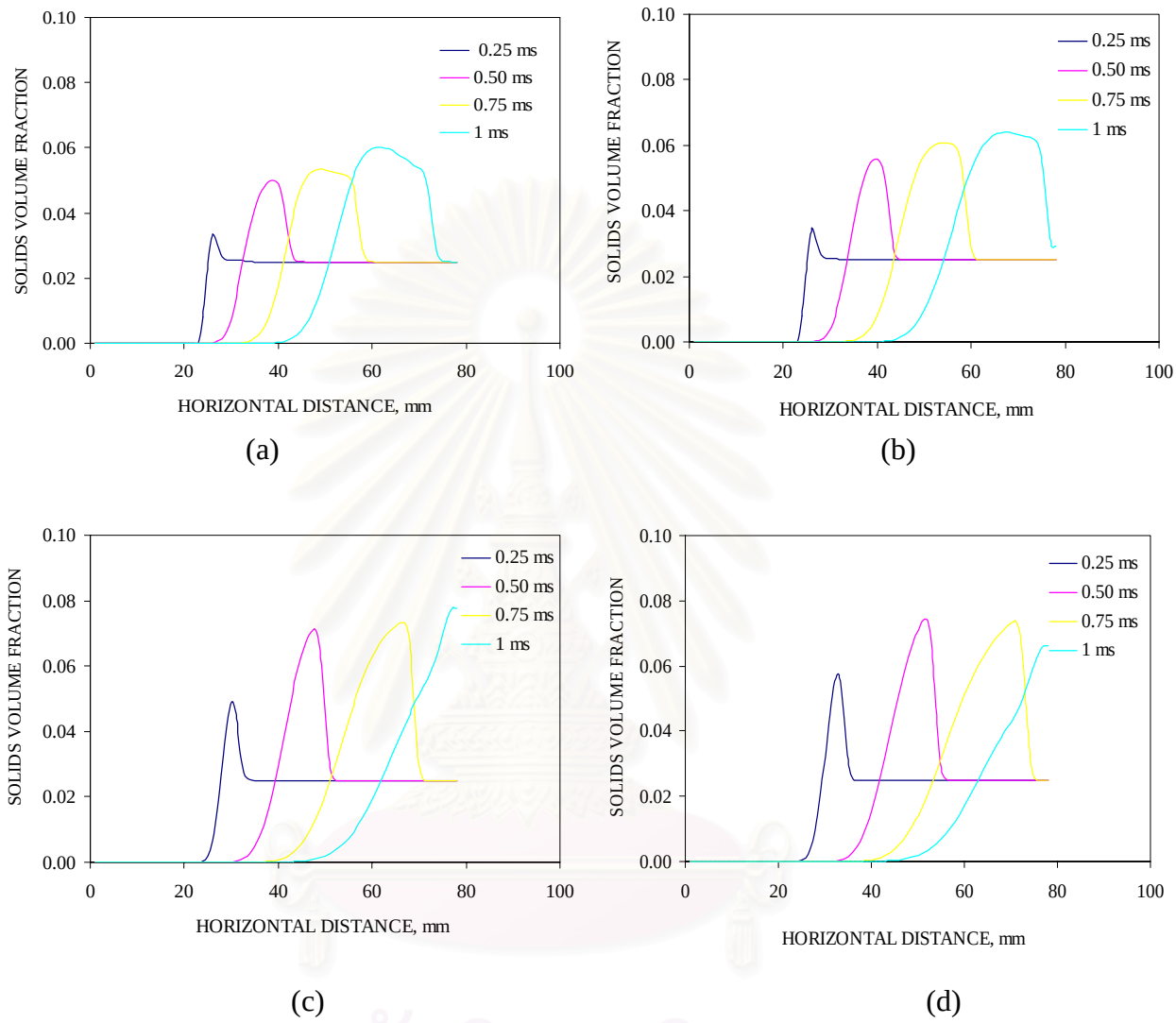

Figure 5.15 Early-time hydrodynamics solids volume fractions of 10nm silica for four aluminum particles
(a) 0.5 micron (b) 5micron (c) 50 micron (d) 100 micron

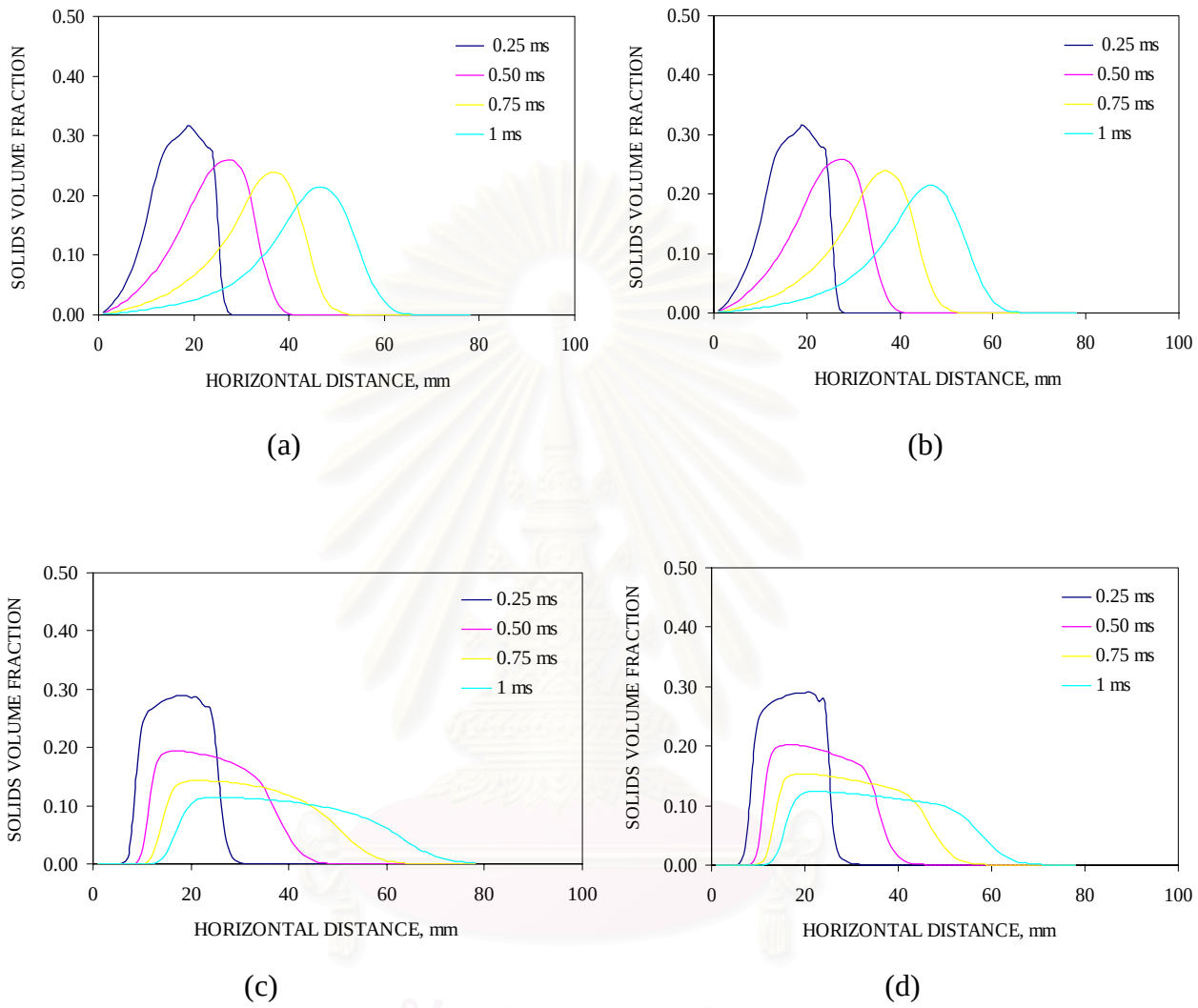

Figure 5.16 Early-time hydrodynamics solids volume fraction
For four aluminum particles
(a) 0.5 micron (b) 5micron (c) 50 micron (d) 100 micron

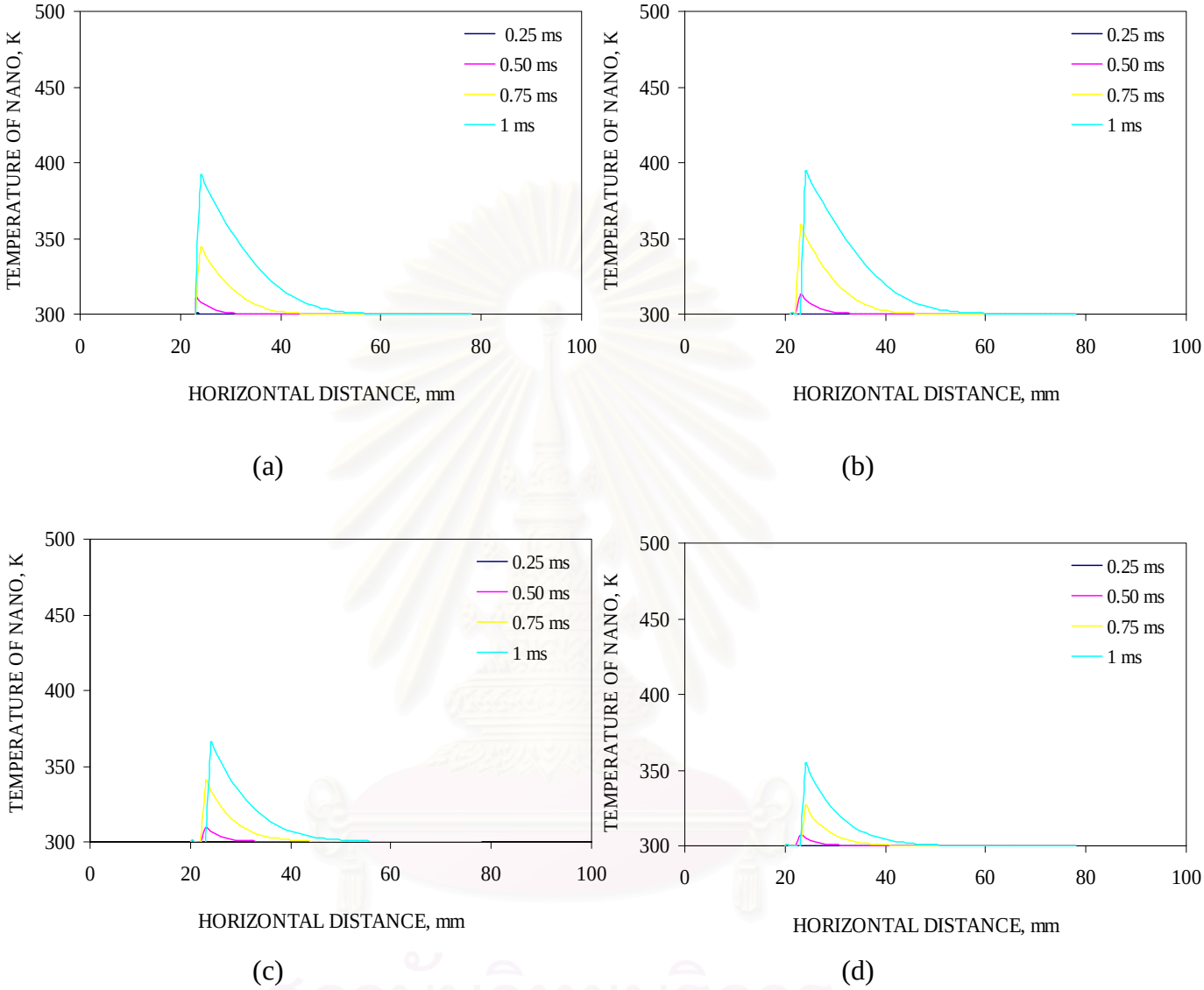

Figure 5.17 Early-time hydrodynamics temperature gradients of 10nm silica for four aluminum particles
(a) 0.5 micron (b) 5micron (c) 50 micron (d) 100 micron

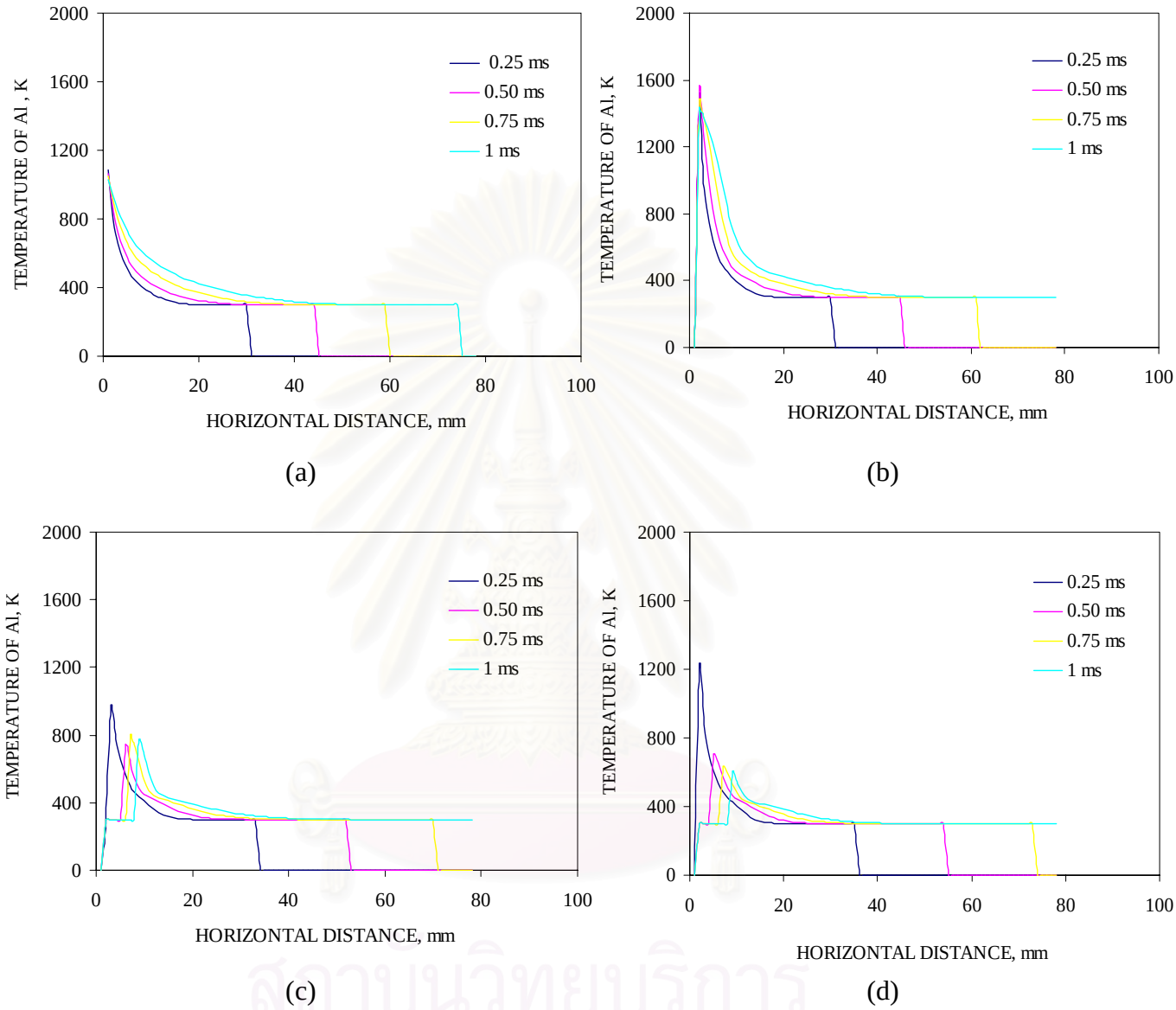

Figure 5.18 Early-time hydrodynamics temperature gradients for four aluminum particles
(a) 0.5 micron (b) 5micron (c) 50 micron (d) 100 micron

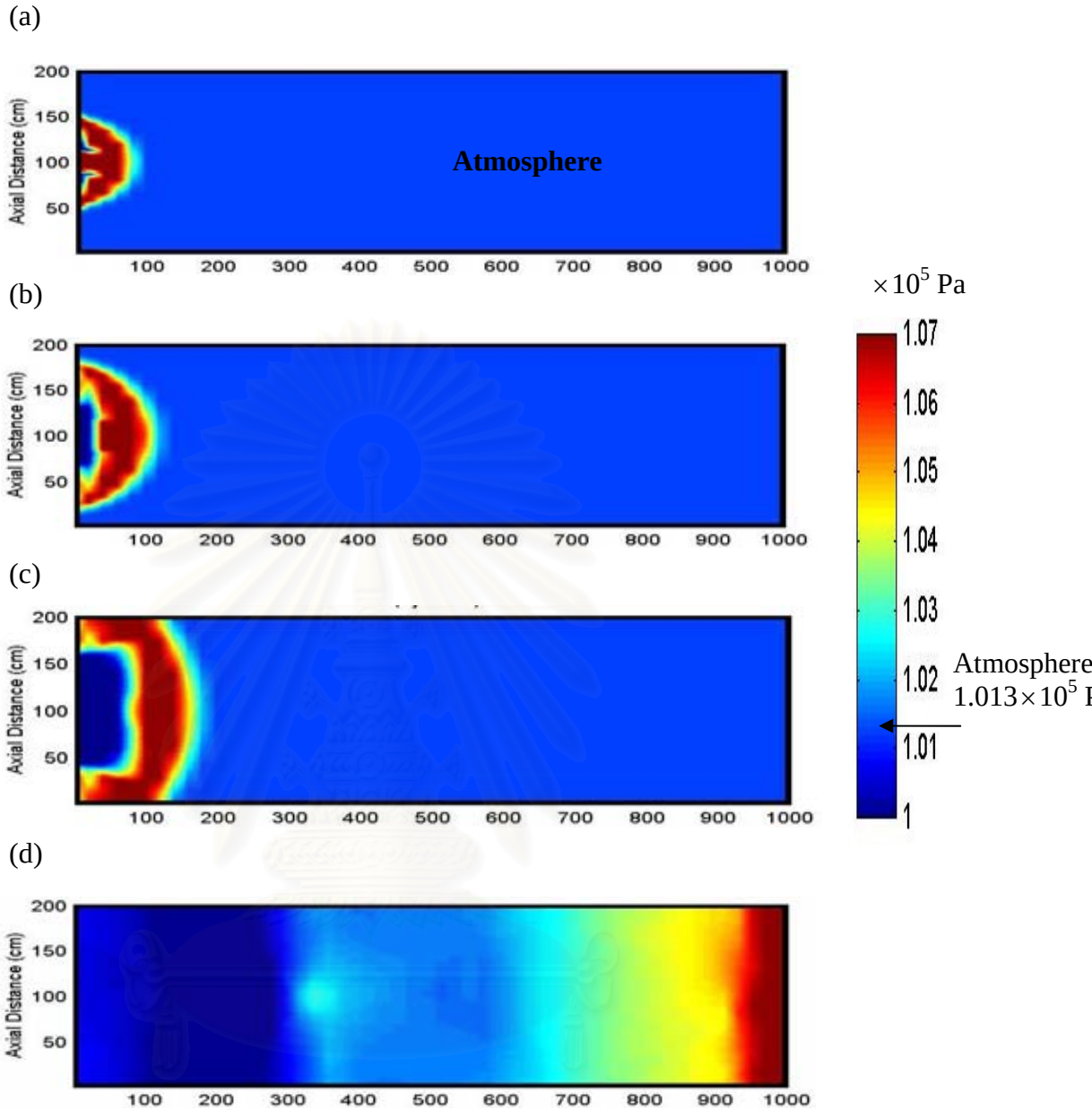

Figure 5.19 Pressure propagation during dissemination.
The pressure color scale is on the right-hand side.
The results are for 5 micron aluminum particles at times of
(a) 0.001 sec (b) 0.002 sec (c) 0.004 sec (d) 0.033 sec

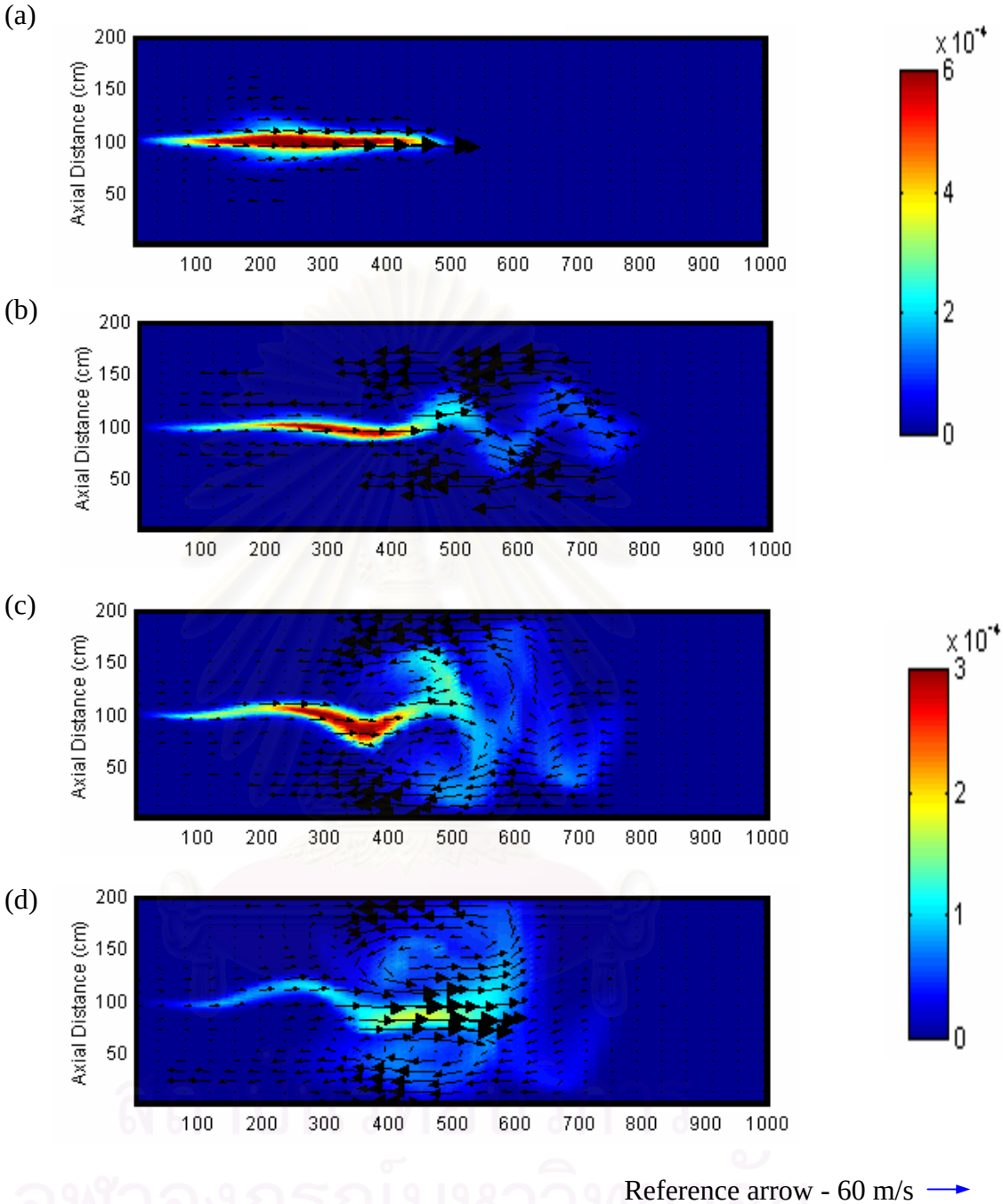

Figure 5.20 Filled contour plots of volume fraction of 10 nm silica particles superimposed with solid velocity vectors.
The volume fraction color scale is on the right-hand side and a reference arrow is shown below.
The results are for 5 micron aluminum particles at times of (a) 0.05 sec (b) 0.10 sec (c) 0.15 sec (d) 0.20 sec

(a)

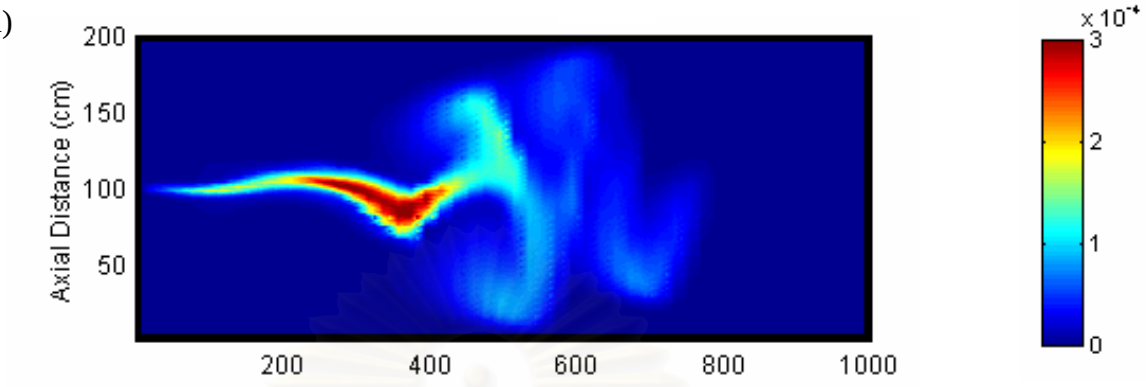

(b)

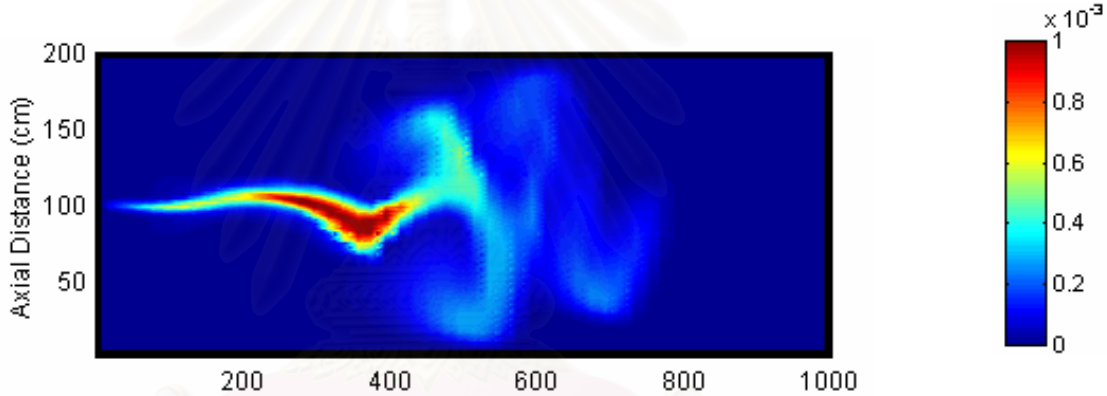

Figure 5.21 Filled contour plots of solids volume fraction for the dissemination hydrodynamics of a mixture of particles.
The volume fraction color scale is on the right-hand side.
(a) 10nm silica and (b) 5 micron of aluminum particles at 0.15 sec

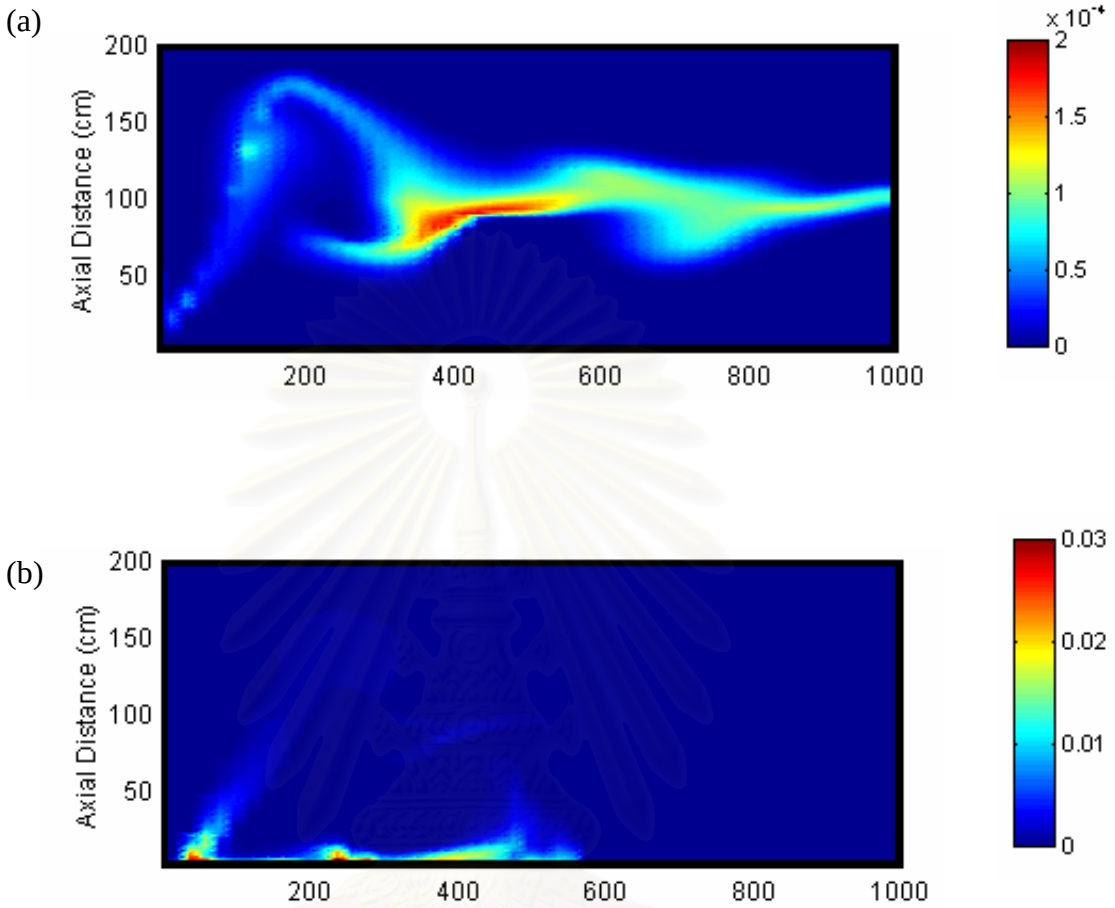

Figure 5.22 Cloud and ground concentration for dissemination of a mixture of particles. The volume fraction color scale is on the right-hand side.
(a) 10 nm silica and (b) 100 micron of aluminum particles at 0.15 sec

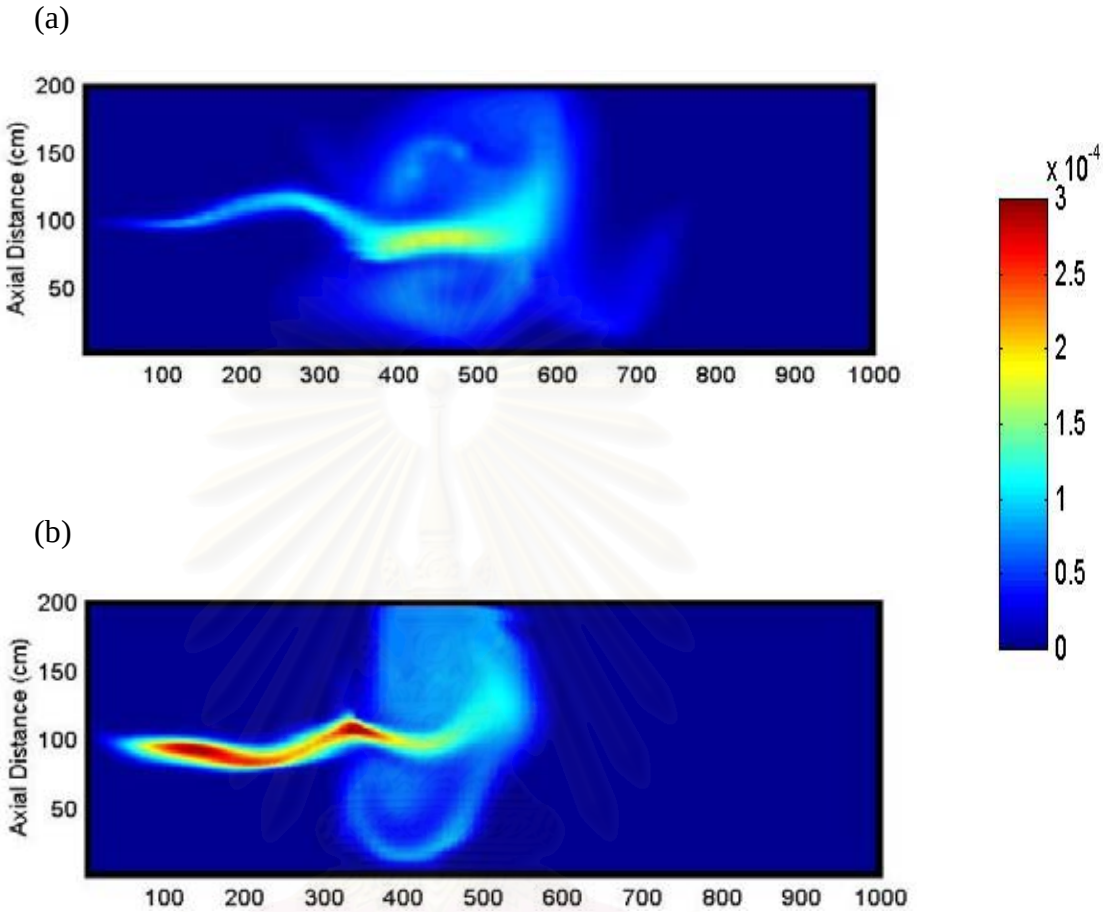

Figure 5.23 Filled contour plots of volume fraction of 10 nm silica particles for dissemination of a mixture for 5 micron aluminum particles at 0.2 sec. The volume fraction color scale is on the right-hand side
(a) Coarse grid (b) Fine grid

CHAPTER VI

FLUIDIZATION OF NANOPARTICLES IN A TWO DIMENSIONAL BED

6.1 Introduction

Unique properties of nanoparticles arise due to their very small primary particle size and very large surface area per unit mass. It is necessary to understand the flow of nanoparticles and to develop processing technology. Much interest is being given to the fluidization of nanoparticles. Several types of nanoparticles already studied by Pfeffer's groups (Zhu et al., 2005; Yu et al., 2005) and by Jung and Gidaspow (2002) were fluidized in a two-dimensional fluidized bed with a uniform grid to allow flow visualization and measurement of particle concentrations.

The fluidization of nanoparticles is mainly influenced by their density, size, shape, surface roughness and the interparticle forces. A combination of various interparticle forces such as van der Waals, electrostatics interactions, and liquid bridging may occur in a fluidized bed. Two-dimensional beds have been used in the practice of fluidization for over a quarter of a century (Rowe, 1971). Yang et al. (1985) at Westing-house, has made particular good use of similar beds, semi-circular, as well as two-dimensional beds to observe meter-size bubbles. Such large bubbles cause gas by passing and are not desirable. As already reported by Pfeffer's group, many, but not all nanoparticles do not form large bubbles. Gidaspow, et al (2004) have suggested a criterion for the absence of bubbles. For no bubble formation, the random oscillating velocity of particles must exceed their minimum fluidization velocity. The measurement of particle concentration distributions described here

allows us to obtain an estimate of such random oscillations by the use of a particle momentum balance and an equation of state for the particles.

Zhu et al, (2005) showed that the nanoparticles exist in the form of multistage subagglomerates. The primary nanoparticles form chainlike clusters, into subagglomerates of a typical size around 20 to 40 microns, and then these subagglomerates group together to 100-400 micron clusters. The aggregation behavior of nanoparticles is also dependent on the flow conditions. In the fluidized bed the clusters are continuously breaking into smaller agglomerates and reagglomerating into larger ones. To understand the behavior of the nanoparticles flow and the process of agglomeration, simulations of primary nanoparticles are run. In the CFD code with the correct interparticle forces, the characteristics of the flow should be predicted.

6.2 Experimental Part

6.2.1 Fluidization Apparatus

A schematic diagram of the experimental fluidization system is shown in Figure 6.1. The system consists of a fluidized bed of nanoparticles with flow and pressure measurement devices and a flow visualization system. The fluidized bed is a vertical transparent column with a gas distributor at the bottom. The bed is constructed from normal glass sheets to prevent particles from sticking to the walls of the bed and to facilitate good visual observation and video recording of the bed operations, such as bed expansion, collapsing and mixing. The gas distributor is covered with 165 * 1400 mesh 304L stainless steel wire (Newark Wire Cloth Company). The bed dimensions are 127.00 * 15.24 * 2.54 cm and the distributor dimensions are 17.78 * 15.24 * 2.54 cm. The fluidizing gas is air dried in a silica filter drier before entering the fluidized bed. Gas flows are measured with a rotameter. The

pressure measurements are made by a digital manometer and a light- diode assembly is used for measuring the solid volume fractions

The fluidized powders are synthetic silicon dioxide from Degussa and Tulco and their properties are listed in Table 6.1. The average primary particle sizes range from 7 to 16 nm and these particles have a similar primary density of 2,220 – 2,560 kg/m3. Due to the surface treatment by the manufacturer, all the nanoparticles are hydrophobic. To minimize any effect of humidity on the nanoparticle fluidization, compressed air is dried in a silica filter dryer before entering the fluidized bed. The gas flow rate is measured and adjusted by a rotameter.

6.2.2 Light - Diode Assembly

The light diode assembly was used to measure the time averaged volume fractions by means of the light absorption technique. It consists of 2 parts, a source and a detector

The source is a high intensity light source [Fiber liter- A3200] with a 200-watt bulb. The source incorporates a precise aperture intensity control, which provides uniform light while maintaining a constant color temperature. The intensity of light emitted is measured by using a high speed response borosilicate detector [NT55-338 - 15.0mm^2 high speed response with a diameter of 0.84 cm and lead length of 1.27 cm]. Through the photovoltaic effect detectors provide a means of transforming light energy to an electrical current. The signal from the detector is measured by a voltmeter.

6.2.3 Calibration of the Light-Diode Assembly.

The absorption of light was calibrated in order to calculate the time averaged volume fractions of the particles from the readings of the light-diode assembly. A rectangular column was constructed from the same material and dimensions as the fluidized bed column [15.24 * 2.54] cm as shown in Figure 6.2. Then it was divided into five sections by a glass plate. First we filled section 1 with the nanoparticles and took readings with the light-diode assembly and then filled sections 1 and 2 with particles and took readings again. The same procedure was followed until we obtained five different readings with the Light-diode assembly. These correspond to five different volume fractions of the particles. The procedure was repeated for all the remaining particles to be analyzed. The absorption of light ray was calibrated in order to calculate the volume fractions of the particles and the gas from the readings of the Light-Diode assembly. Figure 6.3 shows the result of calibration for Tullanox particles with the Light assembly**.** Unlike the Gamma ray technique, which gives a linear relationship for the absorbed radiation, it is seen that the Light readings for these particles do not have a linear relationship even with the logarithm of the detected counts. Hence, the calibration readings were fitted with two curves. The slopes of the two curves were used in the calculation of volume fractions. Several tests were performed with different volume fractions. These calibrations were found to give a reasonable resolution (Vasishta, 2004).

6.2.4 Pressure Drop and Minimum Fluidization

The measured pressure drop or bed height depends on whether the velocity is increased (from a packed bed to a fluidized bed) or decreased (from a fluidized bed to a packed bed). The pressure drop curves for increasing and decreasing superficial gas

velocity are shown in the Figure 6.4. From the figure we can observe that the pressure drop increases with increasing superficial gas velocity and then reaches a plateau and becomes independent of the gas velocity. The value of the pressure drop plateau is usually close to the weight of the bed per unit area, indicating that the total weight of the particles is balanced by the pressure drop and the bed is fully fluidized. The critical point beyond which a pressure drop plateau is reached is commonly called the "Minimum Fluidization Velocity". For Tullanox nanoparticles, the minimum fludization velocity was already measured by Jung and Gidaspow (2003). It was determined to be 1.15 cm/s at the unusually low volume fraction of 0.0077. Zhu et al. (2005) measured the minimum fluidization velocity of R 974 and R 106 nanoparticles in a circular bed. They reported the fluidization velocity to be 0.23 cm/s for both particles.

Figure 6.4(a) shows that for R974 particles the pressure drop increased from 0.05 inches of water at a velocity of 0.25 cm/sec to a constant value 0.2 inches of water, which was the weight of the bed. The minimum fluidization velocity was determined empirically by the intersection of the pressure drop versus the superficial velocity curves. The minimum fluidization velocity was determined to be 0.65 cm/sec. The fluidized bed height at the minimum fluidization velocity was about 3 times the static bed height.

In Figure 6.4(b) for R106 particles, the pressure drop increased from 0.04 inches of water at a velocity of 0.2 cm/sec to a constant value of 0.21 inches of water. The minimum fluidization velocity was determined to be 0.73 cm/sec.

In Figure 6.4(c) for Tullanox, the pressure drop increased from 0.02 inches of water at a velocity of 0.2 cm/sec to a constant value of 0.16 inches of water. The minimum fluidization velocity was determined to be 1.05 m/sec.

The channeling phenomenon was not observed in this superficial gas velocity range. But, with the broad agglomerated particle size distribution, this phenomenon was observed up to gas velocity of 0.4 cm/sec and then the agglomerated particles were fluidized. There is a hysteresis between the measurements of pressure drop for increasing and decreasing gas flows. This strongly suggests the existence of yield stresses in the particle assemblies that form expanded, but non-bubbling beds (Tsinontides and Jackson, 1993).

6.2.5 Analysis of Bed Expansion

Zhu et al. (2005) have already showed that for the agglomerate particulate fluidization (APF), the bed fluidizes and expands uniformly without bubbles with a large expansion ratio of up to 500% or more. The bed expansion increases with the increasing gas velocity. Figure 6.5 shows that the bed starts to expand at a gas velocity much smaller than the minimum fluidization velocity, hence the bed appears to exhibit a “fluid-like” behavior at velocities much lower than the minimum fluidization velocity. The expanded beds have a texture that is closer to the particulate fluidization in a liquid-solids system than to the bubbling fluidization in gas-solids system. Thus, it is reasonable to call the behavior of agglomerate particulate fluidization (APF). The three kinds of SiO_2 powders are quite similar in primary particle sizes and bulk densities. They can all be homogeneously fluidized as agglomerates, but their bed expansions are quantitatively different at certain gas velocities.

6.2.6 Solid Volume Fraction Analysis

The time averaged volume fractions as a function of gas velocities of R106, R 974 and Tullanox are shown in Figure 6.6, 6.7, and 6.8. From the figures we can observe that the fluidization is uniform through the entire length of the bed. We also observe that there exists a dense region at the bottom of the bed. This dense region could be accounted by the formation of agglomerates at the bottom of the bed. The volume fraction at the bottom of the bed is almost 0.2%. In other words there are few fine particles in this region. As we move towards the top of the bed, we observe very little agglomeration.

6.2.7 One-dimensional particle momentum balance

In fluidization practice the one dimensional particle momentum balance involves a balance between buoyancy and drag. Such a balance lacks the solids pressure exerted by the solid. The more general steady state momentum balance (Gidaspow, 1994) with negligible wall friction and zero average solids velocity is as follows:

$$\frac{d\sigma}{dx} + g\varepsilon_s\left(\rho_s - \rho_g\right) = \beta_B V_g \qquad (6.1)$$

Solid pressure + Buoyancy = Drag

The average solids velocity is zero, since there is a negligible particle loss during fluidization. In the two-dimensional bed, the upward flux equals the downward flux. Such a behavior is clearly visible. The kinetic theory shows that the solids pressure, σ , is given by the ideal equation of state, analogous to the ideal equation of state for gases, as follows:

$$\sigma = \rho_s \varepsilon_s \theta \qquad (6.2)$$

Solid pressure = Particle density × Solids volume fraction × Granular temperature

The collisional term in the equation of state involves the square of the volume fraction which has been neglected in equation (6.2). With these simplifications the particle momentum balance becomes, as follows

$$\rho_s \theta \frac{d\varepsilon_s}{dx} + g\varepsilon_s\left(\rho_s - \rho_g\right) = \beta_B V_g \qquad (6.3)$$

In using equation (6.2) in equation (6.1), granular temperature, θ was assumed to be a constant. This is 100% valid when θ determined by the temperature of the fluid and the simplified equation of state.

Integration of equation (6.3) gives an exponential homogeneous solution and a particular solution. The particular solution involves a balance of buoyancy equal to drag. Since, we do not know the precise form of the drag for nanoparticles, the particular solution, which we (Vasishta, 2004) call ε_{S_L} must be regarded as an experimental parameter to be determined by fitting the volume fraction data to the theoretical equation given, below.

$$\mathrm{Ln}\left[\frac{\varepsilon_{S_0} - \varepsilon_{S_L}}{\varepsilon_S - \varepsilon_{S_L}}\right] = \frac{g}{\theta} X \qquad (6.4)$$

Here the values of ε_{S_L} were those at the top of the bed and ε_{S_0} is the solids volume fraction at the bottom. Vasishta used slightly different values of ε_{S_0} than reported here, resulting in somewhat different values of ε_{S_L}. J. Kalra (2005) had repeated her experiments and obtained values of granular temperatures that are not too different from those presented here. Equation (6.4) resembles the well-known barometric formula for pressure distribution in the atmosphere presented in some books on Unit Operations of Chemical Engineering. Density variations in the atmosphere (Tolstoy, 1973) involve the ratio of gravity to the square of the sonic velocity, as in Equation (6.4).

6.3 Simulation Part

6.3.1 Hydrodynamic model

The hydrodynamic approach to multiphase flow systems is based on the principles of mass conservation and momentum balance for each phase. A transient, two-dimensional hydrodynamics model for fluid and particular phases based on the generalization of Navier-Stokes equations was developed at IIT. This approach is similar to that Soo (1967) for multiphase flow and of Jackson (1985; 2000). Table 6.2 summarizes the conversation of mass and momentum equations for each phase given in Gidaspow (1994) as model B, which to be well posed by Lyczkowski et al (1978). Model A and B differ in that Model B considers no pressure drop applied to the particular phases. Lyczkowski et al (1978) showed that the Model A form is ill-posed, and numerical anomalies could results. The implicit continuous Eulerian (ICE) approach is the numerical scheme using in the IIT code. The model uses donor cell differencing. The continuity equations excluding mass generation are in implicit form. The momentum equations are fully explicit. It means the conservation of momentum equations are in mixed implicit form. The viscosity model is used for this study; the solids viscosity and solids modulus are input data to the CFD code.

6.3.2 Estimate of solids viscosity and solids modulus using kinetic theory

6.3.2a Solids viscosity

It is well known in kinetic theory of gases that a simple, non-rigorous treatment of transport phenomena produced surprisingly accurate values of transport coefficients, solids diffusivity and solids viscosity. For the gas-solid flow system, the gas and solids phases can be assumed to be rigid elastic spheres to estimate transport coefficients of binary mixtures.

Chapman and Cowling(1970) showed that the general equation of diffusion for a binary mixture can be put in the form

$$D_{ij} = \frac{3}{8nd_{P_{ij}}^2}\left\{\frac{\theta_{ij}}{2\pi}\left(\frac{1}{m_i}+\frac{1}{m_j}\right)\right\}^{1/2} \tag{6.5}$$

where i is the molecules of air and j is nanoparticles. Therefore the mass of nanopartilces is much more than the mass of molecules of air. The diffusivity can be reduced to be

$$D_{ij} = \frac{3}{8nd_{P_{ij}}^2}\left\{\frac{\theta_{ij}}{2\pi}\left(\frac{1}{m_{molecular}}\right)\right\}^{1/2} \tag{6.6}$$

Using the relations

$$\theta_{molecular} = \frac{1}{3}\cdot m_{molecular}\cdot\left\langle C_{molecular}\right\rangle^2 \tag{6.7}$$

$$n_{nano} = \frac{6\varepsilon_{s_{nano}}}{\pi d_{p_{nano}}^3} \tag{6.8}$$

$$\mu_s = \varepsilon_s \rho_s D \tag{6.9}$$

The mean speed of air molecules is obtained from this correlation

$$P = \frac{1}{3}\rho\overline{C^2} \tag{6.10}$$

At standard temperature and pressure (25 ^{o}C, 1.013×10^5 Pa) the density of air is 1.184 kg/m^3. The corresponding value for $\sqrt{\overline{C^2}}$ is 507 m/sec. Thus the corresponding values of mean speed, $\overline{C}$ is 467 m/sec.

$$\overline{C} = \sqrt{\overline{C^2}}\,/1.087 \tag{6.11}$$

Then the solids viscosity of nanoparticles becomes

$$\mu_s = \frac{\pi\rho_{s_{nano}} d_{p_{nano}}}{16}\left\{\frac{\left\langle C_{molecular}\right\rangle^2}{6\pi}\right\}^{1/2} \tag{6.12}$$

where the density and the diameter of nanoparticles are 2220 kg/m^3 and 10 nm, respectively. The mean speed of molecules of air, $\langle C_{molecular} \rangle$, is approximately 467 m/sec. The corresponding value of solids viscosity, μ_s, is 0.5 centipoises, which is the same order of magnitude as the experiment obtained in the IIT two-story riser (Kalra, 2005).

6.3.2b Solids modulus

In the 1980s, dense phase kinetic theory of gases (Chapman and Cowling, 1970) was applied to granular flow of solids by Savage and his colleagues (Jenkins and Savage, 1983; Lun et al., 1984; Savage, 1988). This theory gives explicit expressions for the solids pressures or the normal stresses in terms of the fluctuation velocity of the particles. Lun et al. (1984) have shown that the solids pressure consists of the kinetic pressure due to the motion of the particles and a collisional pressure due to inelastic collision of particles with a restitution coefficient. Gidaspow and Huilin (1998) showed that an additional term in the solid pressure is cohesion. The solid pressure then becomes:

$$P_s = P_{kinetic} + P_{collsion} + P_{cohesion} \tag{6.13}$$

The equation of state is obtained as follows:

$$P_s = \rho_s \varepsilon_s \theta + 2\varepsilon_s^2 \rho_s \left(1+e\right) g_0 \theta - \rho_s \varepsilon_s \theta \left(0.73\varepsilon_s + 8.97\varepsilon_s^2\right) \tag{6.14}$$

For fluidization of nanoparticles, we considered that the collisional pressure is dominant, so

$$P_s = 2\varepsilon_s^2 \rho_s (1+e) g_0 \theta \tag{6.15}$$

The elastic bulk modulus for particular phase G_s, similar to Young's modulus for solids is defined to be

$$G_s = \frac{\partial P_s}{\partial \varepsilon_s} \tag{6.16}$$

The solid modulus then becomes:

$$G_s = \rho_s \theta \frac{\varepsilon_s}{\varepsilon_{s0}} \tag{6.17}$$

Then

$$\nabla P_s = \rho_s \theta \frac{\varepsilon_s}{\varepsilon_{s0}} \nabla \varepsilon_s \tag{6.18}$$

The solid stress modulus then vanishes, when the bed is empty, $\varepsilon_s = 0$; $G_s = 0$

6.3.3 Limiting value of granular temperature of nanoparticles due to Brownian motion

Any minute particle suspended in gas moves chaotically under the action of collisions with surrounding molecules. The intensity of this chaotic motion is increased with an increase in temperature. The main physical principle of Brownian motion is that the mean kinetic energy of any molecule of gas is equal to the mean kinetic energy of a particle suspended in this ambience. The mean kinetic energy of onward motion $< E >$ can be written as:

$$< E > = m<v^2>/ 2 = 3kT/2 \tag{6.19}$$

where m is the mass of a particle, v is the velocity of a particle, k is the Boltzman constant, and T is the temperature. We can see from this formula that mean kinetic energy of Brownian motion is proportional to the temperature.

The mechanism of fluctuating velocity for larger size particles (larger than micron-size particles) is due to the shear production. The mechanism to estimate the kinetic energy using fluctuating velocity of nanoparticles can be explained by concept

of Brownian motion. To estimate the limiting value of granular temperature we make an assumption that nanoparticles move according to Brownian motion

$$\frac{3}{2}kT = \frac{1}{2}m_{nano}\left\langle C^2 \right\rangle_{nano} \tag{6.20}$$

Boltzmann constant, k = 1.3806503 × 10^{-23} m^2 kg s^{-2} K^{-1}

At Room Temperature, 298 K the kinetic energy of molecules of air,

$$\frac{3}{2}kT = 6.17\times 10^{-21}\ \mathrm{m^2\ kg\ s^{-2}\ (J)} \tag{6.21}$$

$$m_{nano} = \frac{4}{3}\rho_s \pi \cdot r^3 = 1.16\times 10^{-21}\ \mathrm{kg} \tag{6.22}$$

We know the mean kinetic energy of any molecule of gas and the mass of each nanoparticles. The square of mean velocity of nanoparticles can be obtained as

$$\left\langle C^2 \right\rangle_{nano} = 10 \tag{6.23}$$

$$\theta_{nano} = \frac{\left\langle C^2 \right\rangle_{nano}}{3} \approx 3.3\ \mathrm{m^2\ s^{-2}} \tag{6.24}$$

If a number of particles subject to Brownian motion are present in a given medium and there is no preferred direction for the random oscillations, then over a period of time the particles will tend to be spread evenly throughout the medium. We know that in the reality the nanoparticles are suspended and expand inside the bed, so there are other mechanisms that pull the effect of Brownian motion down due to interparticle forces. A combination of various interparticle forces such as, Van der Waals, electrostatic interactions and liquid may occur in a fluidized bed (Hakim et al, 2005).

6.3.4. Electrical force

Many industrial and biomedical processes involve powders; the electrostatic charges in these powders often play an important role in the process involved. Also we know from the experiment of application of electric field that when we apply the high voltage to the bed that expands the bed collapses. This shows that the charge should have a large effect on the bed expansion.

Al-Adel et al (2002) have shown that by solving the Poisson equation for the electric field and by using the radial momentum balance for the particle phase, the model can capture important qualitative features of riser flows: core-annular particle distribution, annular particle downflow at low riser gas velocities, and annular upflow at high gas velocities.

Using Gauss's law, the balance can be obtained as

$$\oint_{Surface} \vec{D} \cdot d\vec{S} = \int_{V} \hat{\sigma} dV \tag{6.25}$$

$$\nabla \cdot \vec{D} = \hat{\sigma} = q_e \rho_s \varepsilon_s \tag{6.26}$$

where $\hat{\sigma}$ represents the volume charge density (coulomb per volume). , q_e represents the mass charge density (coulomb per mass)

$$\vec{D} = \in \cdot \vec{E} = \in_r \in_0 \cdot \vec{E} \tag{6.27}$$

where $\in_r$ is the dielectric constant of the gas-solid mixture, and $\in_0$ is the permittivity of free space [8.8542 $\times 10^{-12}$ C ^{2}/(N m^2)]. For air $\in_r$ equals 1.0006. Gupta (1990) presented a summary of dielectric constants.

$$\nabla \cdot \in \nabla \Psi = -q_e \rho_s \varepsilon_s \tag{6.28}$$

The starting point for the electrostatic potential calculation is the Poisson equation.

$$\nabla^2 \Psi = \frac{-q_e \rho_s \varepsilon_s}{\in} \tag{6.29}$$

The electric strength is

$$\vec{E} = \nabla\Psi \tag{6.30}$$

where $\vec{E}$ represents electric potential, V/m

In the momentum equation, the force on a charged particle in an electric field is given by the charge times the field

$$F = q_e \rho_s \varepsilon_s \vec{E} \tag{6.31}$$

$$F = \left(\frac{C}{kg}\right)\cdot\left(\frac{kg}{m^3}\right)\cdot\left(\frac{V}{m}\right) = \frac{kg}{m^2 s^2} \tag{6.32}$$

Units

$$V = J/C$$

$$J = N \cdot m$$

$$N = kg \cdot m/s^2$$

For the nanoparticles, one of the most important parameters is the electric force due to the presence of the large surface charge. Jung and Gidaspow (2002) showed that the surface charge of Tullanox measured using a Faraday cup is –2.4 $\times 10^{-4}$ C/kg.

Mukherjee A. (1987) measured the charge of particles (coal and pyrite) using a ball probe. He studied the following parameters which changed the charge of particles

1. Solid velocity — The electric charge increases as a function of solid velocity. The charge acquired by a particle depends not only on the momentum transfer during collision but also on the rate of separation after collision.
2. Gas velocity — With various gas velocities, no change in particle charge was be observed.

3. Humidity — The humidity of the carrier gases affects the charge of the particles. The electric charge decreases as a function of humidity. The humidity content of the surrounding atmosphere is high; the charge accumulated by the particles tends to leak back into the atmosphere due to the increase in conductivity. Also H_3O^+ ions may have adsorbed on the surface.

4. Particle concentration — The concentration increases the charge of the charge drops. Hence the particles getting charged on contact with the wall is greater than with the particle-particle interactions.

5. Particle size — With an increase of particle size there is an increase in charge.

6.3.5 Interphase momentum exchange

The Ergun equation is used to estimate the drag coefficient. From our simulations the slip velocity is negligible. The gas velocity is almost equal to the solids velocity. The pressure drop obtained from the Ergun equation is small due to very low slip velocity

$$\frac{\Delta P}{\Delta x} = 150\frac{\varepsilon_s^2 \mu_g \left(v_g - v_s\right)}{\varepsilon^2 \left(d_p \phi_s\right)^2} + 1.75\frac{\rho_g \left(v_g - v_s\right)^2 \varepsilon_s}{\varepsilon \phi_s d_p} \tag{6.33}$$

6.3.6 Initial and boundary conditions

To obtain the structure of flow of nanoparticles the unit of bed should be small enough to capture this structure. All simulations are carried out in a two-dimensional

Cartesian coordinates with a total of 100 × 500 computational uniform meshes. The initial conditions and the configuration for simulations are shown in Figure 6.9. The material used as the solid is Tullanox 500 with an average particle diameter of 10±1 nm and density of 2220 kg/m^3. The primary nanoparticle properties were used. For both phases, no slip velocity boundary conditions are used at the left and right wall. At the outlet, Neumann boundary conditions are applied to the solid-gas flow with the constant pressure of 1.01325 N/m^2. Dirichlet boundary conditions are used with a defined the gas velocity and the gas velocity is set to zero at the walls

6.3.7 Boundary condition for electrical potential

Two kinds of boundary conditions for electrical potential at the wall are used to obtain the flow structure of nanoparticles.

1. Al-Adel et al. (2002) used potential of zero, $\Psi_w = 0$. This boundary condition is valid when the pipe is metal. It means the particles get discharged by contacting the wall.

2. Since the electrical field penetrates out of the bed, to get a more realistic boundary condition, Poisson ‘s equation for the electric fields with charge is solved analytically outside the bed, as follows:

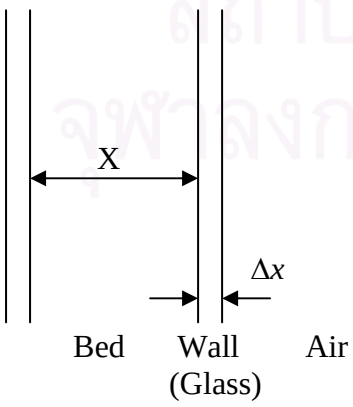

The balance of the electric field between the bed and the wall becomes as6

$$\in_{bed} \frac{\partial \Psi_b}{\partial x} = \in_{wall} \frac{\partial \Psi_w}{\partial x} \qquad (6.34)$$

Poisson ‘s equation at walls is

$$\frac{d^2 \Psi_w}{dx^2} = 0 \qquad (6.35)$$

The Eq. (35) gives

$$\frac{d\Psi_w}{dx} = C_1 \tag{6.36}$$

And

$$\Psi_w = C_1 x + C_2 \tag{6.37}$$

The boundary conditions can be obtained as,

$$\Psi(X) = \Psi_w(X) \tag{6.38}$$

And

$$\Psi_w(X + \Delta x) = 0 \tag{6.39}$$

Substituting Eq. (36) into (34)

$$\in_{bed} \frac{\partial \Psi_b}{\partial x} = \in_{wall} C_1 \tag{6.40}$$

Combining Eqs. (37) and (39)

$$C_1(X + \Delta x) + C_2 = 0 \tag{6.41}$$

Using Eqs. (37) and (38)

$$\Psi(X) = C_1 X + C_2 = \Psi_w(X) \tag{6.42}$$

Substituting Eq. (41) into (42)

$$C_1 = -\frac{\Psi_w(X)}{\Delta x} \tag{6.43}$$

Substituting Eq. (43) into (40)

$$\frac{\partial \Psi_b}{\partial x} = -\frac{\in_{wall}}{\in_{bed} \cdot \Delta x} \Psi_w(X) \tag{6.44}$$

The boundary condition becomes as

$$\Psi = -A \frac{\partial \Psi_{s,w}}{\partial n} \tag{6.45}$$

where

$$A = \frac{\in_{bed} \cdot \Delta x}{\in_{wall}} \tag{6.46}$$

The dielectric constants of the bed and glass wall are 2 and 10, respectively. The thickness of the wall is assumed to be 0.5 cm. Then the constant, A is 0.1 cm.

6.3.8 10 nm silica simulation

The simulation of 10 nm silica particles using the granular temperature of 1 m^2/s^2 for 1.46 m/s flow was obtained without adding other external forces into the momentum equation, as shown in Figure 6.10(a). The bed still keeps expanding with time. Thus the simulations miss some other forces that keep the particles inside the bed.

6.3.9 The electrostatics effect

We know from our experiment of applying electric field that when we apply a high voltage to the expanding bed, the bed is collapsed. This proves that the surface charge has a large effect on the bed expansion. We have to understand the mechanisms better what make the beds stop expanding. Some researchers have discussed about the agglomeration of naoparticles, Van der waal forces and the charge effects. The electric force is one of the body forces that acts on nanoparticles. An assumption of simulations is that the particles carry a prescribed charge. We examine the influence of this charge on the hydrodynamics. Figure 6.10 (b) shows the filled contour plots of the volume fraction of 10 nm silica particles with the electric field effect, with the granular temperature of 1 m^2/s^2 at 1.46 m/s with $\psi = 0$ boundary condition at 0.25 sec. This boundary condition is applicable when the pipe is made by metal. This means that the particles get discharged by contacting the walls. This figure clearly shows that the electrostatic effect improves the flow structure. It is closer to the experiment. The bed has a solid volume fraction gradient in the y direction. The simulation with the electric field gives a denser bed than that without.

6.3.10 Effect of boundary conditions

To obtain a realistic situation, where the electric field the charge can penetrate out of the system, the boundary condition, $\Psi = -A\frac{\partial \Psi_{s,w}}{\partial n}$ is used. This type of boundary condition depends upon the thickness of the wall and the material of the wall. This realistic boundary condition can help the process of the charging as shown in Figure 6.10(c). At 1.46 m/s the solids get denser than with using the boundary condition that of Al-Adel et al, (2002).

Figure 6.11 summarizes the flow regime computations as a function of gas velocity done at IIT. Fluidization of nanoparticle occurs without bubbles as called agglomerate particulate fluidization (APF). When the superficial gas velocity is more than the terminate gas velocity, the nanoparticles still are inside the bed because of the internal circulation. This Figure of nanoparticles flow shows the rapid vertex formations as observed in experiments.

6.3.11 Effect of granular temperature

Equating the kinetic energy of the air molecules to the kinetic energy of the 10 nm nanoparticles gives a theoretical granular temperature of nanoparticles of 3 m^2/s^2. We know that in reality the nanoparticles are suspended and expand inside the bed, so there is another mechanism that pulls the effect of Brownian motion down interparticle forces. A combination of various interparticle forces, such as the Van der Waals, electrostatic interactions and liquid may occur in a fluidized bed (Hakim et al, 2005). Figure 6.12 shows the filled contour plots of the volume fraction of 10 nm silica particles of 1.46 m/s at 0.35 sec. with ψ = 0 boundary condition. The bed expansion increases with an increase of granular temperature from 0.25 to 0.75 m^2/s^2.

Figure 6.13(a) shows the filled contour plots of 10 nm silica particles, superimposed with solid velocity vectors, for granular temperature of 0.25 m^2/s^2 at 0.6 sec, with the boundary condition, $\Psi = -A\frac{\partial \Psi_{s,w}}{\partial n}$. Figure 6.13 (a) and (b) show the solids volume fraction and solids axial velocity of nanoparticles, respectively. As expected a rapid vortex formation is predicted. The superficial velocity is 1.46 cm/s. But the vortices move with a velocity of 15 cm/s. This clearly shows that this effect comes from the Brownian motion. The observed unique fluidization properties of nanoparticles, formation of dense and dilute regimes, high bed expansion, absence of large bubbles, rapid vortex formation are all captured as shown in Figure 6.13. The bed approximately expands with the gas velocity following the characteristic method analysis as discussed in Gidaspow (1994). The velocity of bed expansion is obtained from the slope, 2.07 cm/s as shown in Figure 6.14.

6.3.12 Effect of superficial gas velocity

Figure 6.15 shows time averaged of filled contour plots of 10 nm silica particles for a granular temperature of 0.25 m^2/s^2 with $\Psi = -A\frac{\partial \Psi_{s,w}}{\partial n}$ boundary condition. Figure 6.15 (a), (b) and (c) show the flow structures with the superficial gas velocity of 1.46, 1.65, 1.84 cm/s, respectively. The bed expansion increases with an increasing superficial gas velocity. Figure 6.16 shows the comparison of expansion ratios as a function of superficial gas velocity for the experiments and simulations of 10 nm silica particles. From the simulations we see that the bed expands more than in the experiments. This might be due to too high input granular temperature or due to missing inter-particle forces such as the cohesive force.

The values of granular temperature of nanoparticles, R 106, R 974 and Tullanox are extremely high compared with other particles in the same range of gas velocities. The extremely large fluctuation velocity of the nanoparticles is due to the collision of gas molecules with the nanoparticles. It is similar to Brownian motion of particles in a liquid. The data in Figure 6.17 scatter around this theoretical value. Figure 6.17 also presents a summary of the total granular temperature as a function of gas velocities from the literature.

In the simulation, we postulate that the particles carry a prescribed charge and then examine the influence of this charge on the hydrodynamics. The bed expands more then observed in the experiments. We have to better understand the charge mechanism of particles. The charge should be change due to the particle-particle collisions and particle-wall collisions. For FCC particles such a production of charge can be derived from the physics of collisions. For nanoparticles it will be more difficult to get at the right physics.

สถาบันวิทยบริการ
จุฬาลงกรณ์มหาวิทยาลัย

6.4 Conclusions

1. The observed unique fluidization properties of nanoparticles, formation of dense and dilute regimes, high bed expansion, absence of large bubbles, rapid vortex formation have been explained using a two-phase CFD model with the random kinetic energy of nanoparticles estimated from the random motion of air molecules.

2. To obtain stable fluidization, electrical forces computed from a solution of a Poisson equation for electric potential were added to the momentum equations for particles. The CFD model has also computed the observed bed collapse due to an application of an electric field.

3. We have shown that the model with electric charge increases segregation of nanoparticles markedly.

4. However we believe that the model must be improved to give production of charge due to collisions of particles to give quantitative results.

สถาบันวิทยบริการ
จุฬาลงกรณ์มหาวิทยาลัย

6.5 Appendix A.

Numerical Technique for the Poisson equation

$$\nabla^2 \Psi = \frac{-q_e \rho_s \varepsilon_s}{\in} \tag{6.47}$$

The bulk density is $\rho_s \varepsilon_s = \rho_b$ (6.48)

So
$$\nabla^2 \Psi = \frac{-q_e \rho_s \varepsilon_s}{\in} = \frac{-q_e \rho_b}{\in} \tag{6.49}$$

$$\left(\frac{\partial^2 \Psi}{\partial x^2}\right)_{i,j} = \frac{\Psi_{i+1,j} + \Psi_{i-1,j} - 2\Psi_{i,j}}{(\Delta x)^2} = \frac{-q\rho_{i+1/2,j}}{\in} \tag{6.50}$$

With
$$\rho_{i+1/2,j} = \frac{1}{2\Delta x_{i+1/2}}\left(\Delta x_{i+1}\rho_{i,j} + \Delta x_i \rho_{i+1,j}\right) \tag{6.51}$$

The Poisson equation becomes

$$\frac{\Psi_{i+1,j} + \Psi_{i-1,j} - 2\Psi_{i,j}}{(\Delta x)^2} = -\frac{q}{\in} \cdot \frac{1}{2\Delta x_{i+1/2}}\left(\Delta x_{i+1}\rho_{i,j} + \Delta x_i \rho_{i+1,j}\right) \tag{6.52}$$

The electric potential in x direction is

$$\Psi_{i,j} = \frac{1}{2} \cdot \left(\frac{q}{\in} \cdot \frac{1}{2\Delta x_{i+1/2}}\left(\Delta x_{i+1}\rho_{i,j} + \Delta x_i \rho_{i+1,j}\right) \cdot (\Delta x)^2 - \Psi_{i+1,j} - \Psi_{i-1,j}\right) \tag{6.53}$$

The electric potential in y direction is

$$\Psi_{i,j} = \frac{1}{2} \cdot \left(\frac{q}{\in} \cdot \frac{1}{2\Delta y_{i+1/2}}\left(\Delta y_{i+1}\rho_{i,j} + \Delta y_i \rho_{i+1,j}\right) \cdot (\Delta y)^2 - \Psi_{i,j+1} - \Psi_{i,j-1}\right) \tag{6.54}$$

The sum of potential in x and y direction is

$$\Psi_{i,j} = \frac{1}{4} \cdot \left(\frac{q}{\in} \cdot \frac{1}{2\Delta x_{i+1/2}}\left(\Delta x_{i+1}\rho_{i,j} + \Delta x_i \rho_{i+1,j}\right) \cdot (\Delta x)^2 - \Psi_{i+1,j} - \Psi_{i-1,j}\right) +$$

$$\frac{1}{4} \cdot \left(\frac{q}{\in} \cdot \frac{1}{2\Delta y_{i+1/2}}\left(\Delta y_{i+1}\rho_{i,j} + \Delta y_i \rho_{i+1,j}\right) \cdot (\Delta y)^2 - \Psi_{i,j+1} - \Psi_{i,j-1}\right) \tag{6.55}$$

Momentum Equations.

The momentum equation with the electric force of solid phase is obtained as

$$\frac{\partial(\rho_s \varepsilon_s \vec{v}_s)}{\partial t} + \nabla \cdot (\rho_s \varepsilon_s \vec{v}_s \vec{v}_s) = -\nabla P_s + \nabla[\vec{\tau}_s] + q_e \rho_s \varepsilon_s \vec{E} - \beta_B(\vec{v}_s - \vec{v}_g) + \varepsilon_s(\rho_s - \rho_g)g \tag{6.56}$$

The momentum equations are differenced over a staggered mesh using a scheme in which the convection terms are treated explicitly and all other terms are treated implicitly. The difference equations in x and y direction are,

$$\begin{aligned}
\left(\varepsilon_k \rho_k u_k\right)^{n+1}_{i+\frac{1}{2},j} &= \left(\overline{\varepsilon_k \rho_k u_k}\right)_{i+\frac{1}{2},j} - \frac{\delta t}{\delta r_{i+\frac{1}{2}}}\left(\left(p_k\right)^{n+1}_{i+1,j} - \left(p_k\right)^{n+1}_{i,j}\right) \\
&+ \frac{\delta t}{\delta x_{i+\frac{1}{2}}}\left(\left(\Psi\right)^{n+1}_{i+1,j} - \left(\Psi\right)^{n+1}_{i,j}\right) \cdot q_e \cdot \left(\rho_s \varepsilon_s\right)_{i+\frac{1}{2},j} \\
&- \left(w_k\right)^{n+1}_{i+\frac{1}{2},j} g_x \delta t + \delta t \sum_{\substack{l=f,1 \\ l \neq k}}^{N} \left(\beta_{lk}\right)^{n}_{i+\frac{1}{2},j} \left(\left(u_l\right)^{n+1}_{i+\frac{1}{2},j} - \left(u_k\right)^{n+1}_{i+\frac{1}{2},j}\right)
\end{aligned} \tag{6.57}$$

$$\begin{aligned}
\left(\varepsilon_k \rho_k v_k\right)^{n+1}_{i,j+\frac{1}{2}} &= \left(\overline{\varepsilon_k \rho_k v_k}\right)_{i,j+\frac{1}{2}} - \frac{\delta t}{\delta y_{j+\frac{1}{2}}}\left(\left(p_k\right)^{n+1}_{i+1,j} - \left(p_k\right)^{n+1}_{i,j}\right) \\
&+ \frac{\delta t}{\delta y_{i+\frac{1}{2}}}\left(\left(\Psi\right)^{n+1}_{i.j+1} - \left(\Psi\right)^{n+1}_{i,j}\right) \cdot q_e \cdot \left(\rho_s \varepsilon_s\right)_{i,j+\frac{1}{2}} \\
&- \left(w_k\right)^{n+1}_{i,j+\frac{1}{2}} g_y \delta t + \delta t \sum_{\substack{l=f,1 \\ l \neq k}}^{N} \left(\beta_{lk}\right)^{n}_{i,j+\frac{1}{2}} \left(\left(v_l\right)^{n+1}_{i,j+\frac{1}{2}} - \left(v_k\right)^{n+1}_{i,j+\frac{1}{2}}\right)
\end{aligned} \tag{6.58}$$

Table 6.1 Properties of nanoparticles used in this study

Powder	Wettability	Effective Diameter (nm)	Material Density (kg/m^3)	Bulk Density (kg/m^3)
Tullanox	Hydrophobic	10	2,220	48.00
R 106	Hydrophobic	7	2,560	41.49
R 974	Hydrophobic	12	2,560	33.24

สถาบันวิทยบริการ
จุฬาลงกรณ์มหาวิทยาลัย

Table 6.2 Hydrodynamic Model

1. Governing Equations

(1) Continuity Equations $k = g, s$

$$\frac{\partial}{\partial t}\left(\varepsilon_k \rho_k\right) + \nabla \cdot \left(\varepsilon_k \rho_k \vec{v}_k\right) = 0$$

(2) Momentum Equations

Gas momentum

$$\frac{\partial(\rho_g \varepsilon_g \vec{v}_g)}{\partial t} + \nabla \cdot (\rho_g \varepsilon_g \vec{v}_g \vec{v}_g) = -\nabla P_g + \nabla \vec{T}_g + \beta_B\left(\vec{v}_s - \vec{v}_g\right) + \rho_g g$$

Solids momentum

$$\frac{\partial(\rho_s \varepsilon_s \vec{v}_s)}{\partial t} + \nabla \cdot (\rho_s \varepsilon_s \vec{v}_s \vec{v}_s) = -\nabla P_s + \nabla\left[\vec{\tau}_s\right] + q_e \rho_s \varepsilon_s \vec{E} - \beta_B(\vec{v}_s - \vec{v}_g) + \varepsilon_s(\rho_s - \rho_g)g$$

2. Constitutive equations

(1) Definition

$$\varepsilon_g + \varepsilon_s = 1$$

(2) Equation of State – Ideal Gas Law

$$\rho_g = \frac{P}{RT_g}$$

(3) Constitutive equations for stress $k = g, s$

$$\vec{T}_g = 2\varepsilon_g \mu_g \vec{\tau}_g$$

$$\tau_k = \frac{1}{2}\left[\nabla \vec{v}_k + \left(\nabla \vec{v}_k\right)^T\right] - \frac{1}{3}\left(\nabla \cdot \vec{v}_k\right)I$$

(4) Empirical Solids Viscosity and Stress Model

$$\nabla P_s = G\left(\varepsilon_s\right)\nabla \varepsilon_s$$

$$G\left(\varepsilon_s\right) = \rho_s \theta \frac{\varepsilon_s}{\varepsilon_{so}}$$

$$\mu_s = 0.5 \times 10^{-2} \quad \text{poise}$$

(5) Gas-Solid Drag Coefficients

$$\beta_B = 150\frac{\varepsilon_s^2 \mu_g}{\varepsilon_g^2 d_p^2} + 1.75\frac{\rho_g \varepsilon_s}{\varepsilon_g d_p}\left|v_g - v_s\right|$$

(6) Electric potential

$$\nabla^2 \Psi = \frac{-q_e \rho_s \varepsilon_s}{\in}$$

$$\vec{E} = \nabla \Psi$$

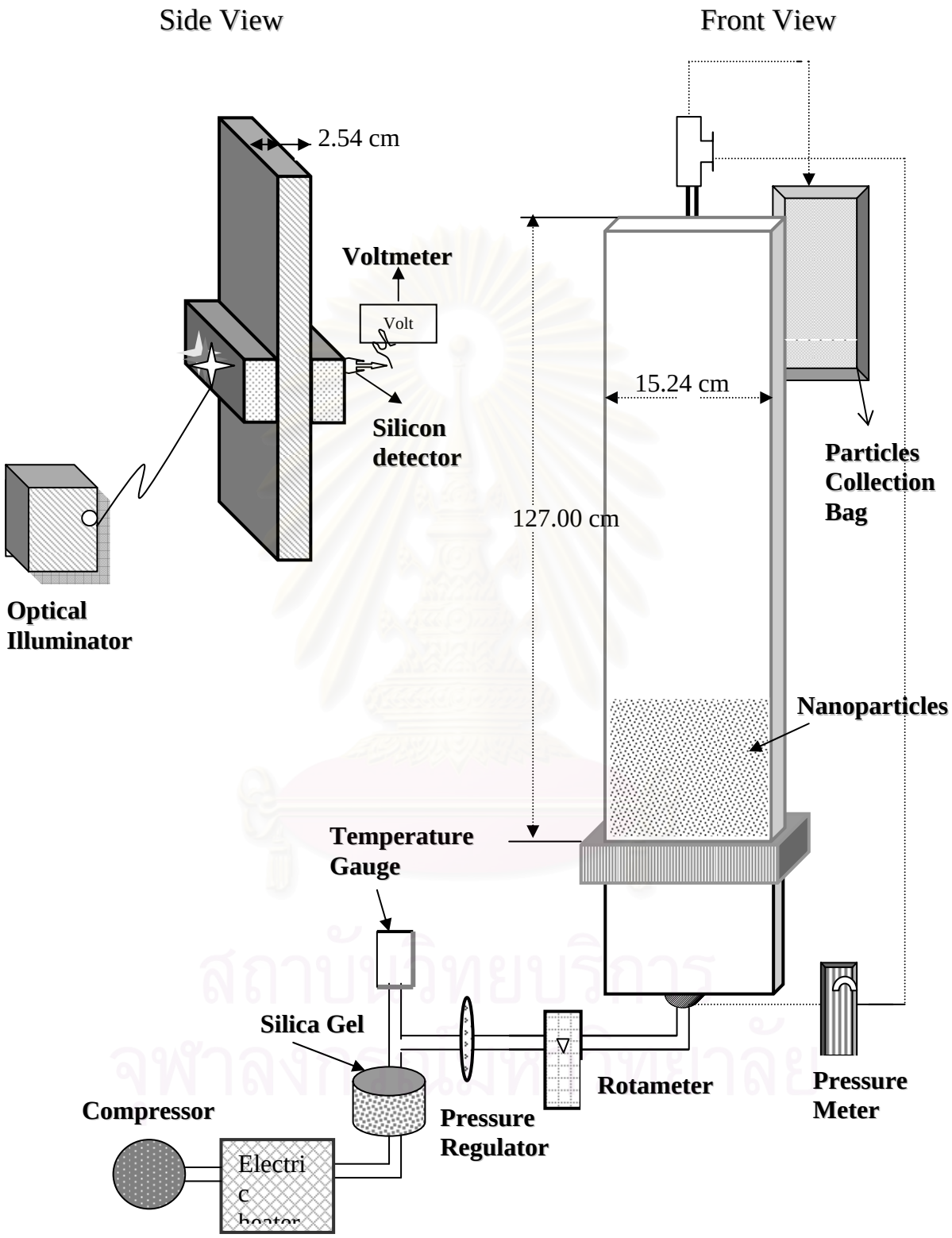

Figure 6.1 Schematic Diagram of 2-Dimensional Bed System

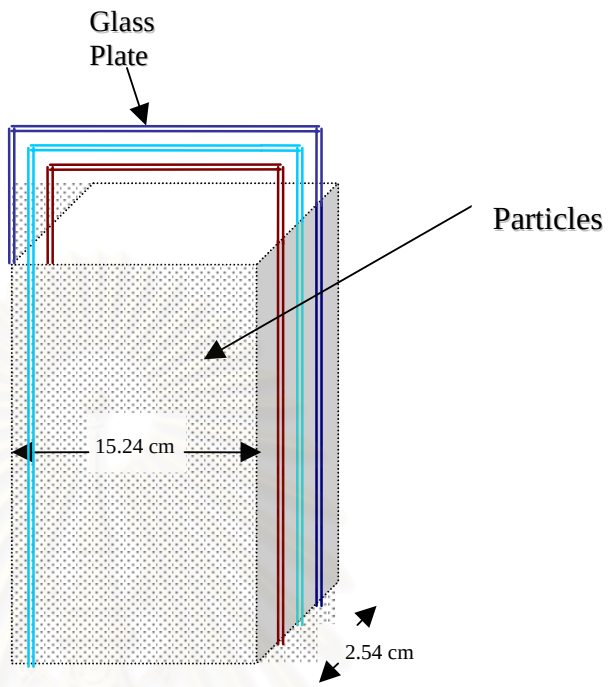

Divided into 5 sections, each section is 0.508 cm thick)

Figure 6.2 Model for Calibration of solid volume fraction

สถาบันวิทยบริการ
จุฬาลงกรณ์มหาวิทยาลัย

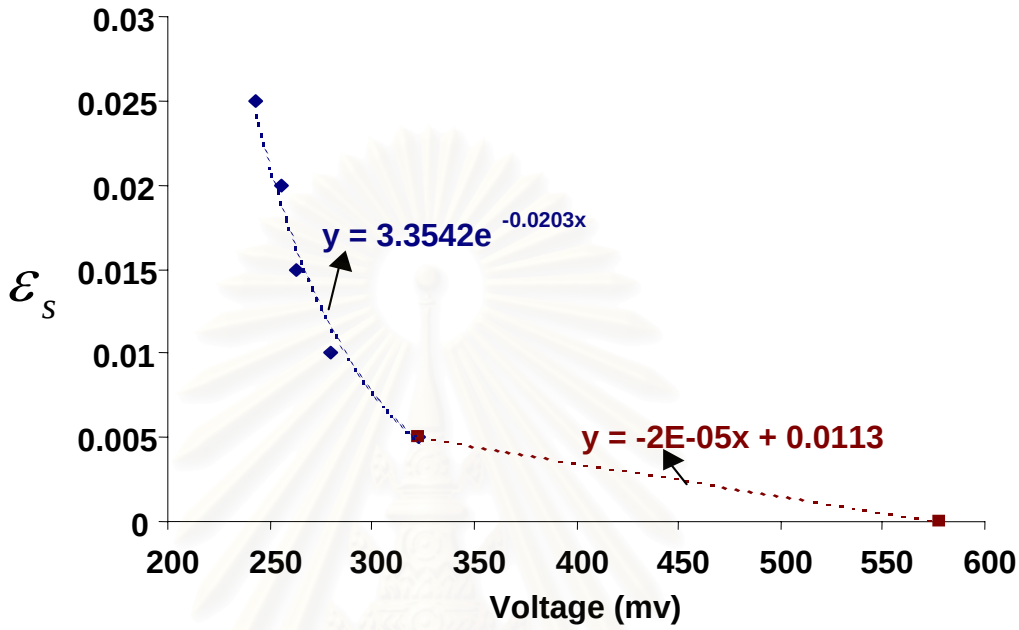

Figure 6.3 Calibration of Light Ray Versus Tullanox Particles

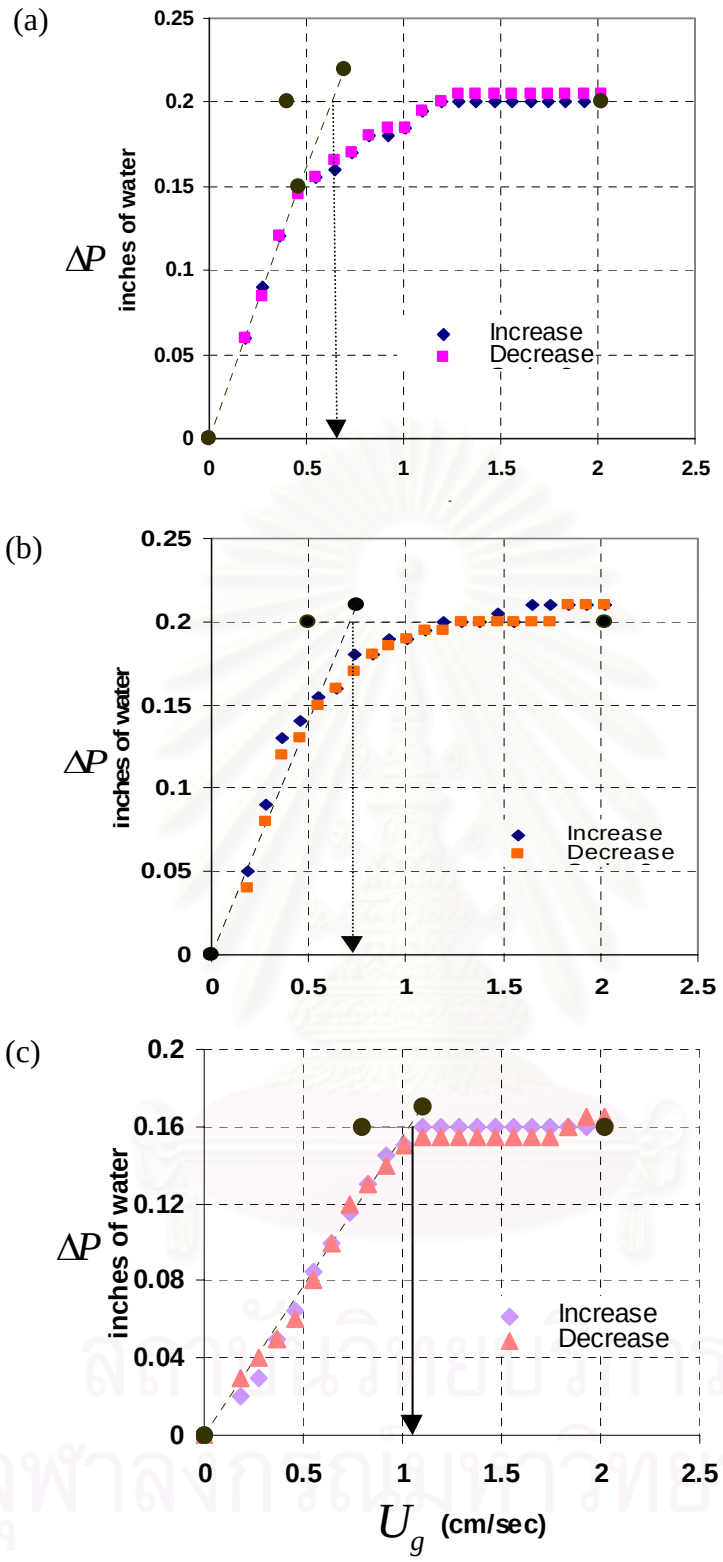

Figure 6.4 Determination of Minimum Fluidization Velocity(Tullanox)

(a) R974 (b) R106 (c) Tullanox

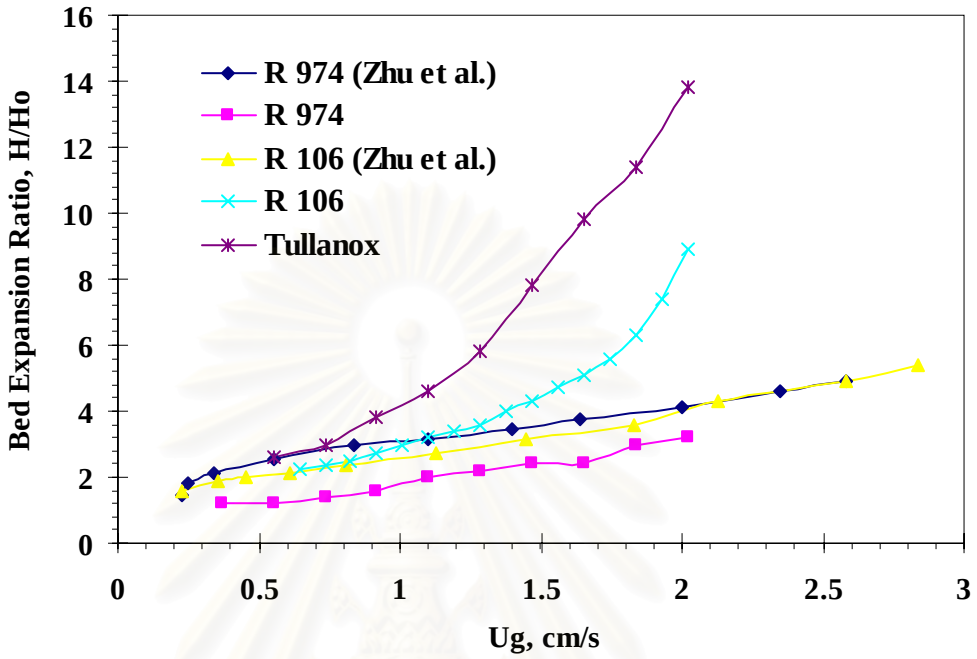

Figure 6.5 Homogeneous Expansion of Nanoparticles

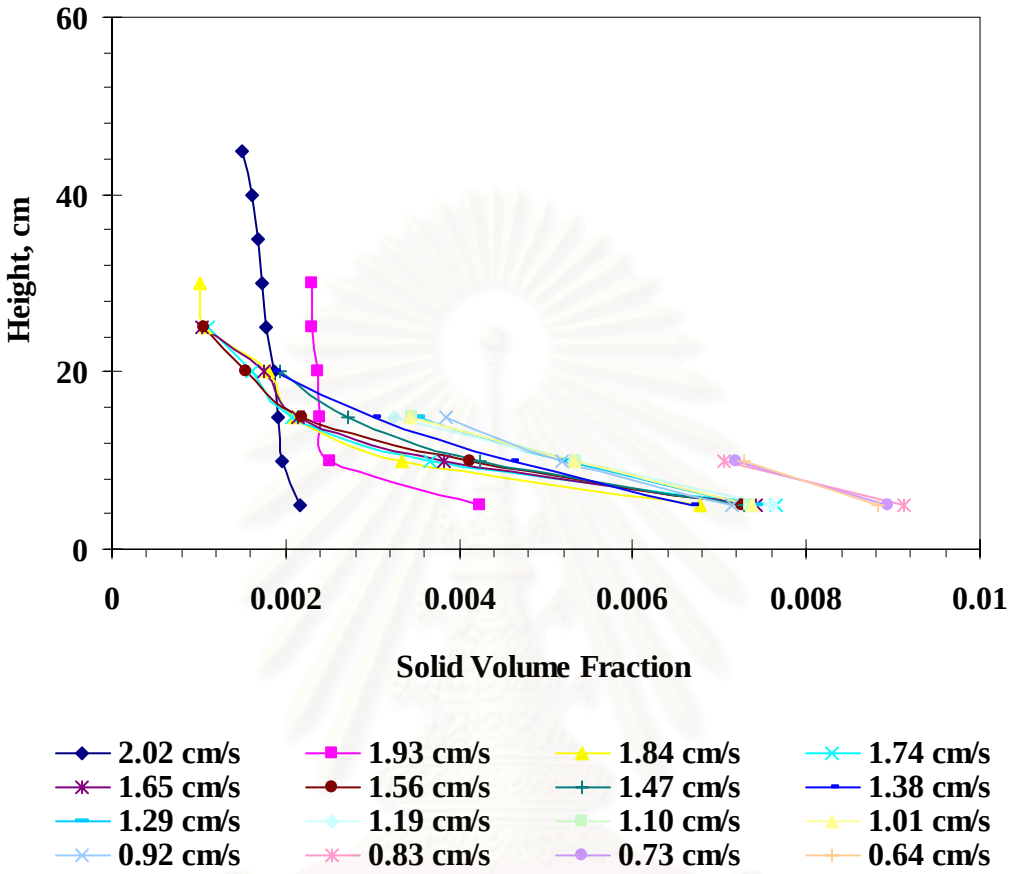

Figure 6.6 Fluidization of R106 Nanoparticles in a 2-D Bed with Various Gas Velocities

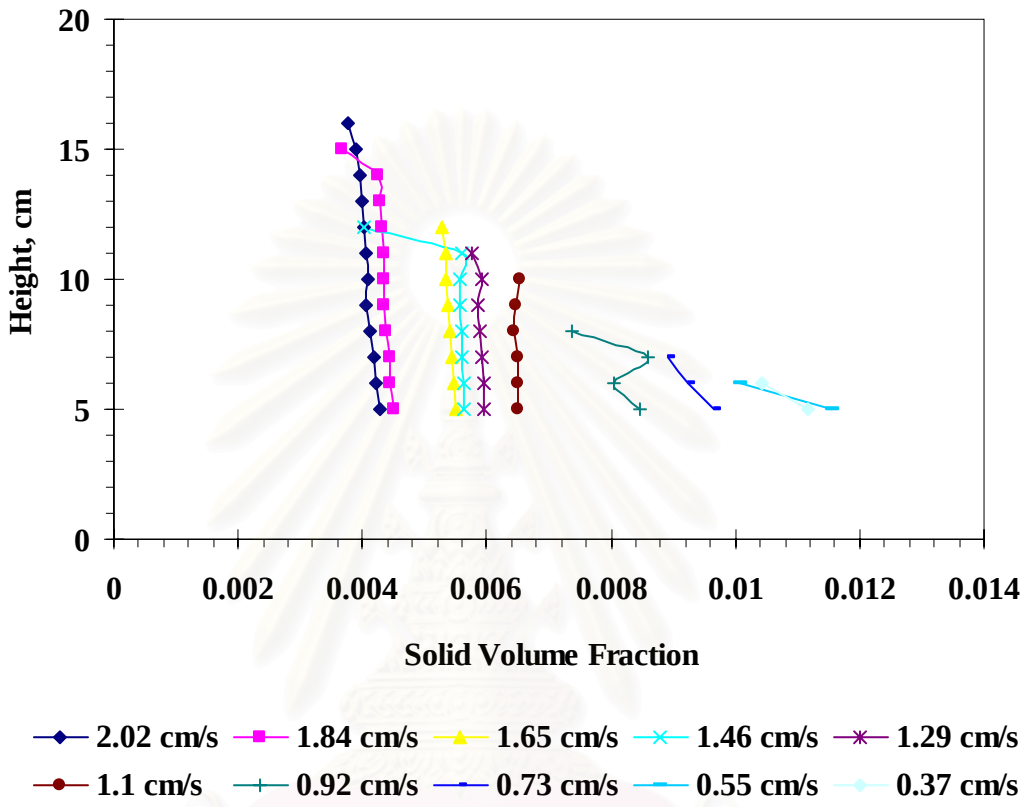

Figure 6.7 Fluidization of R974 Nanoparticles in a 2-D Bed with Various Gas Velocities

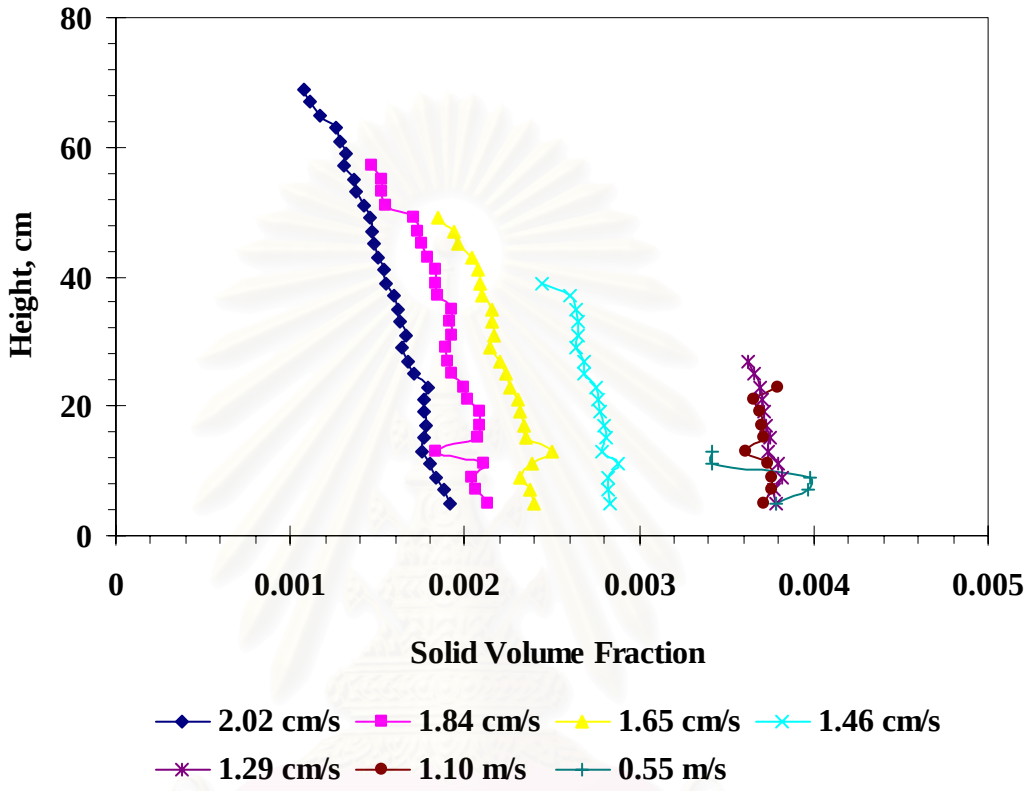

Figure 6.8 Fluidization of Tullanox Nanoparticles in a 2-D Bed with Various Gas Velocities

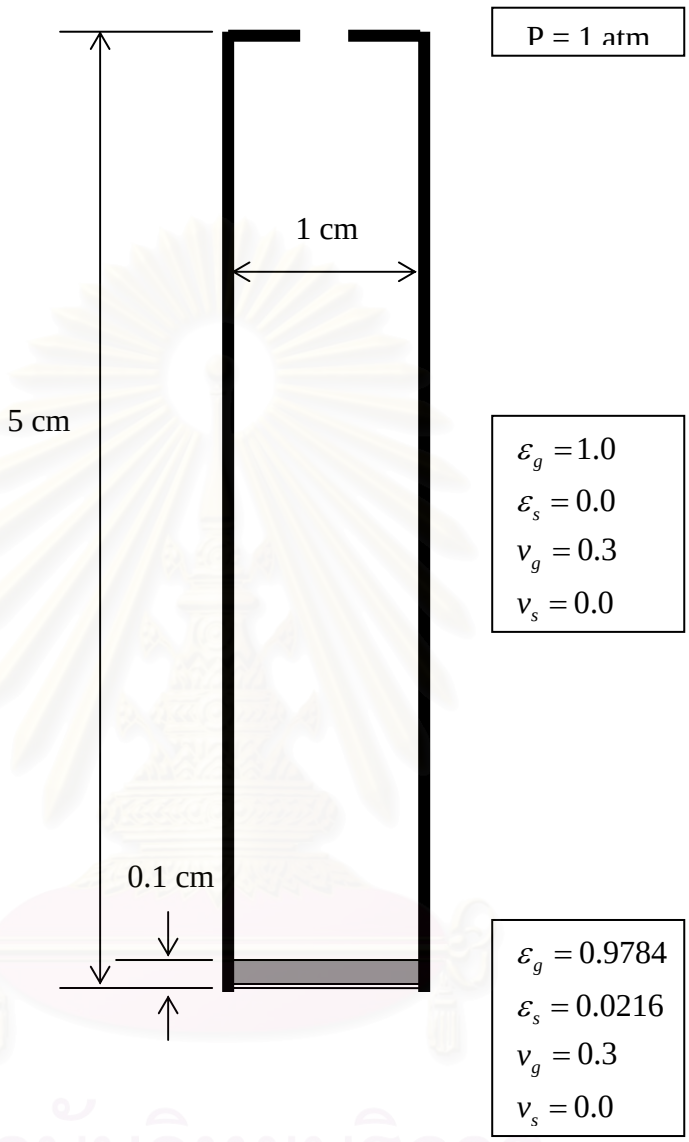

Figure 6.9 Initial condition and configuration for the simulations

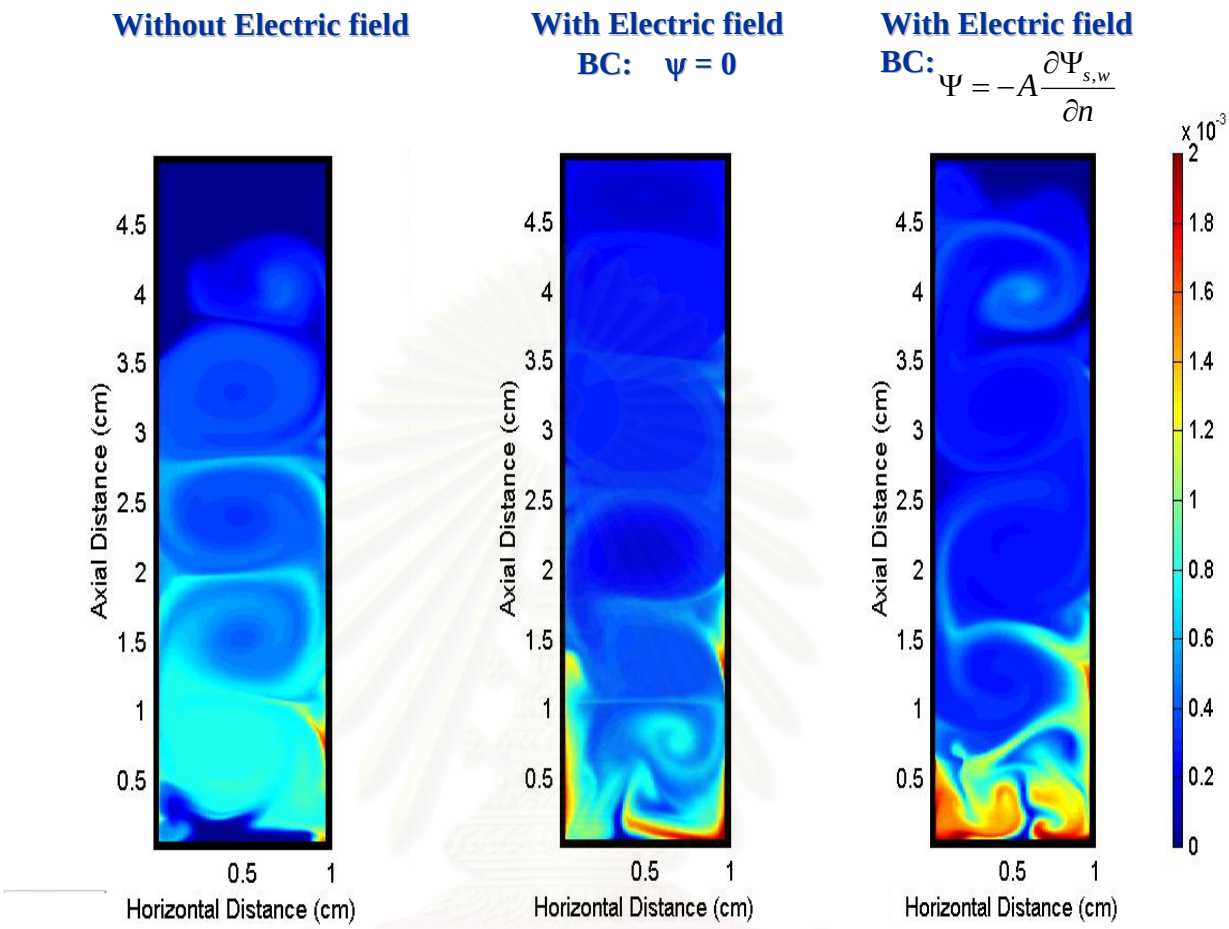

Figure 6.10 Effect of electric field and boundary conditions.
Filled contour plots of the volume fraction of 10 nm silica particles with granular temperature of 1 m^2/s^2 at 0.25 sec
The volume fraction color scale is on the right-hand side.
(a) without electric field (b),(c) with electric field

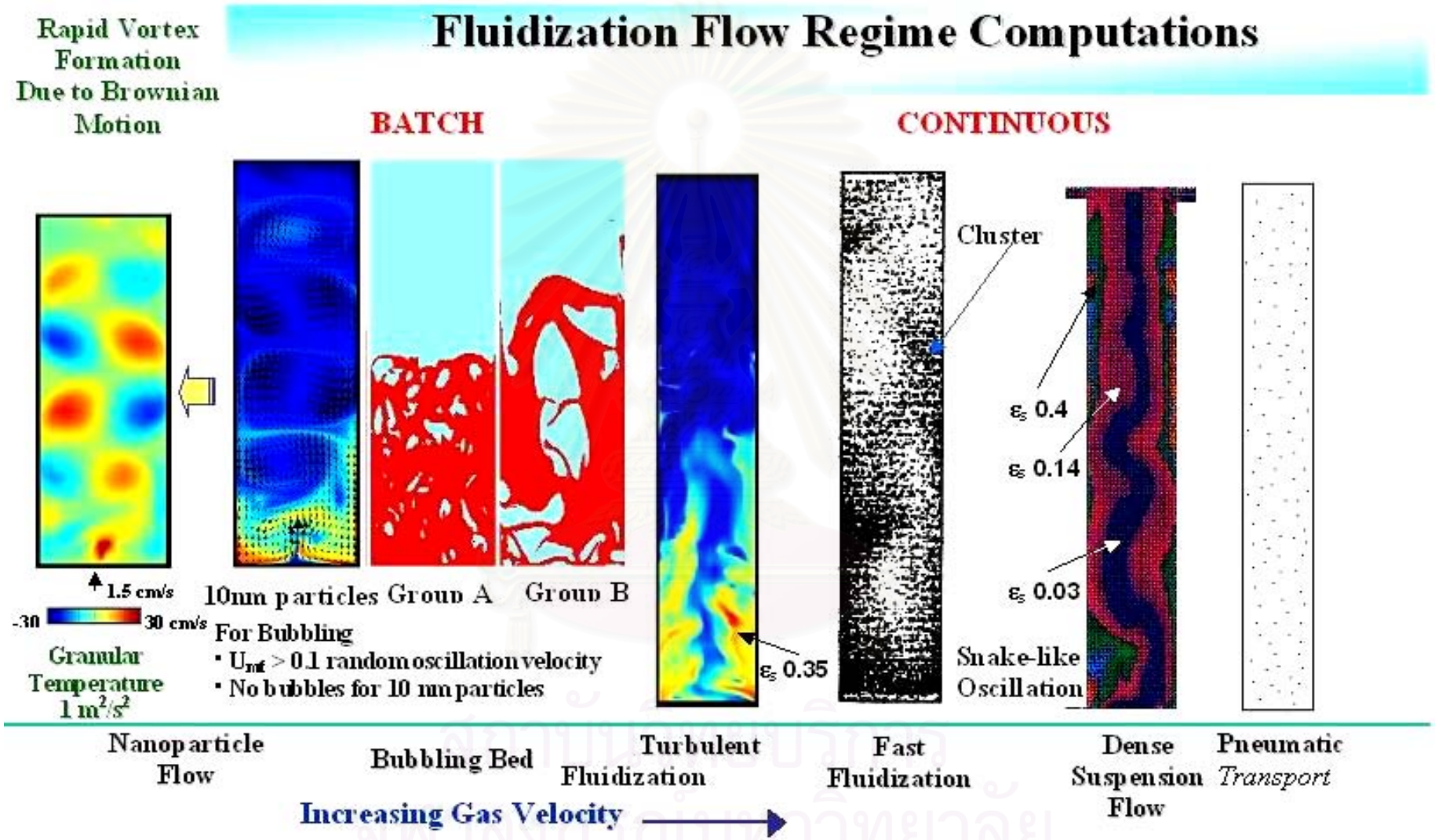

Figure 6.11 Computed fluidization flow regimes. Nanoparticle flow (Jiradilok, et al., 2005); Bubbling bed (Gelderbloom, et al., 2003); Turbulent fluidization: shows the existence of dilute & dense regions (Jiradilok, et al., 2005); Fast fluidization (Neri and Gidaspow, 2000; Tsuo and Gidaspow, 1990; Gidaspow and Mostifi, 2003); Dense suspension flow (Sun and Gidaspow, 1999).

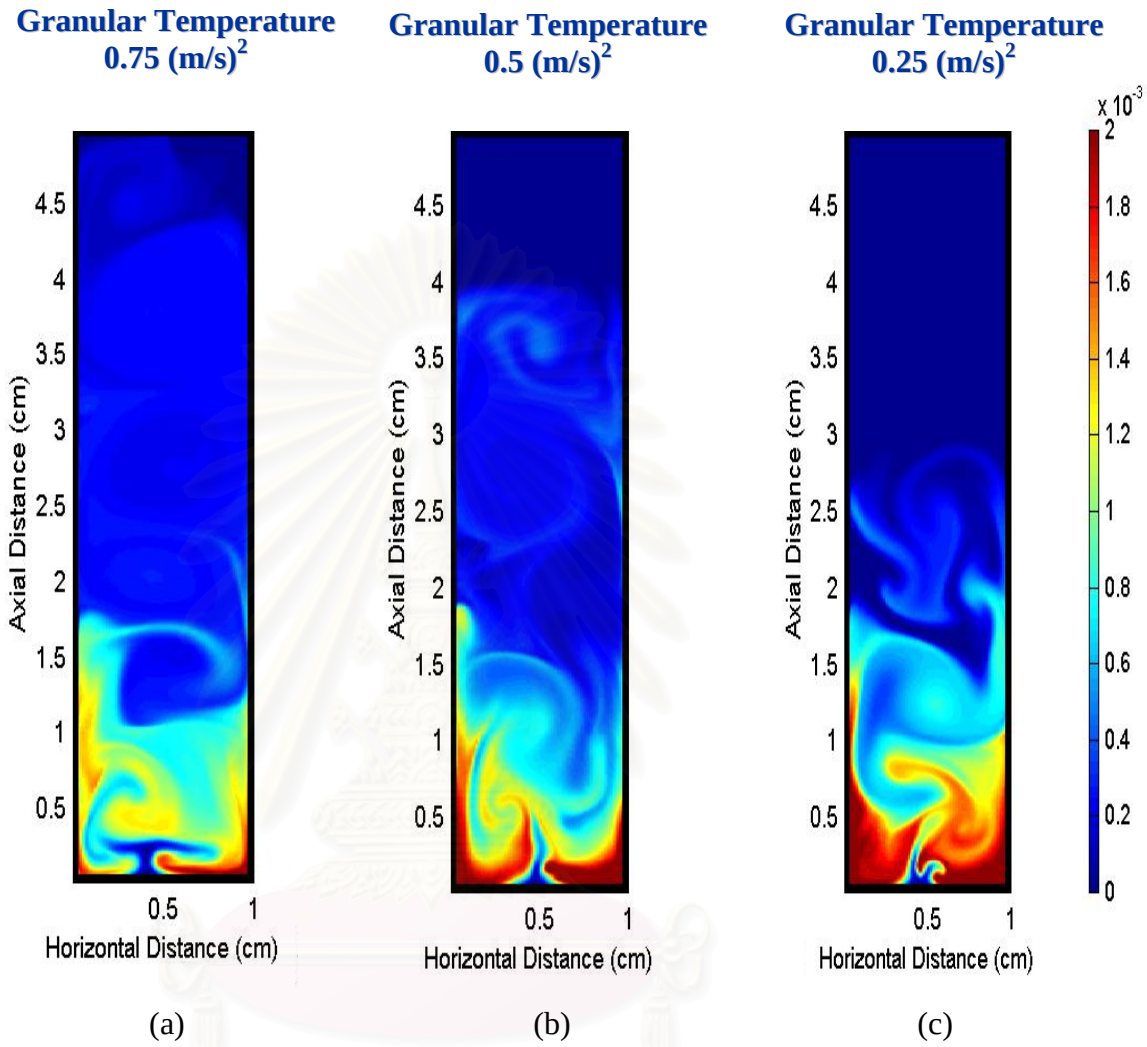

Figure 6.12 Effect of granular temperature
Filled contour plots of the volume fraction of 10 nm silica particles at 0.35 sec, with $\psi = 0$ boundary condition
The volume fraction color scale is on the right-hand side.
(a) 0.75 m^2/s^2 (b) 0.5 m^2/s^2 (c) 0.25 m^2/s^2

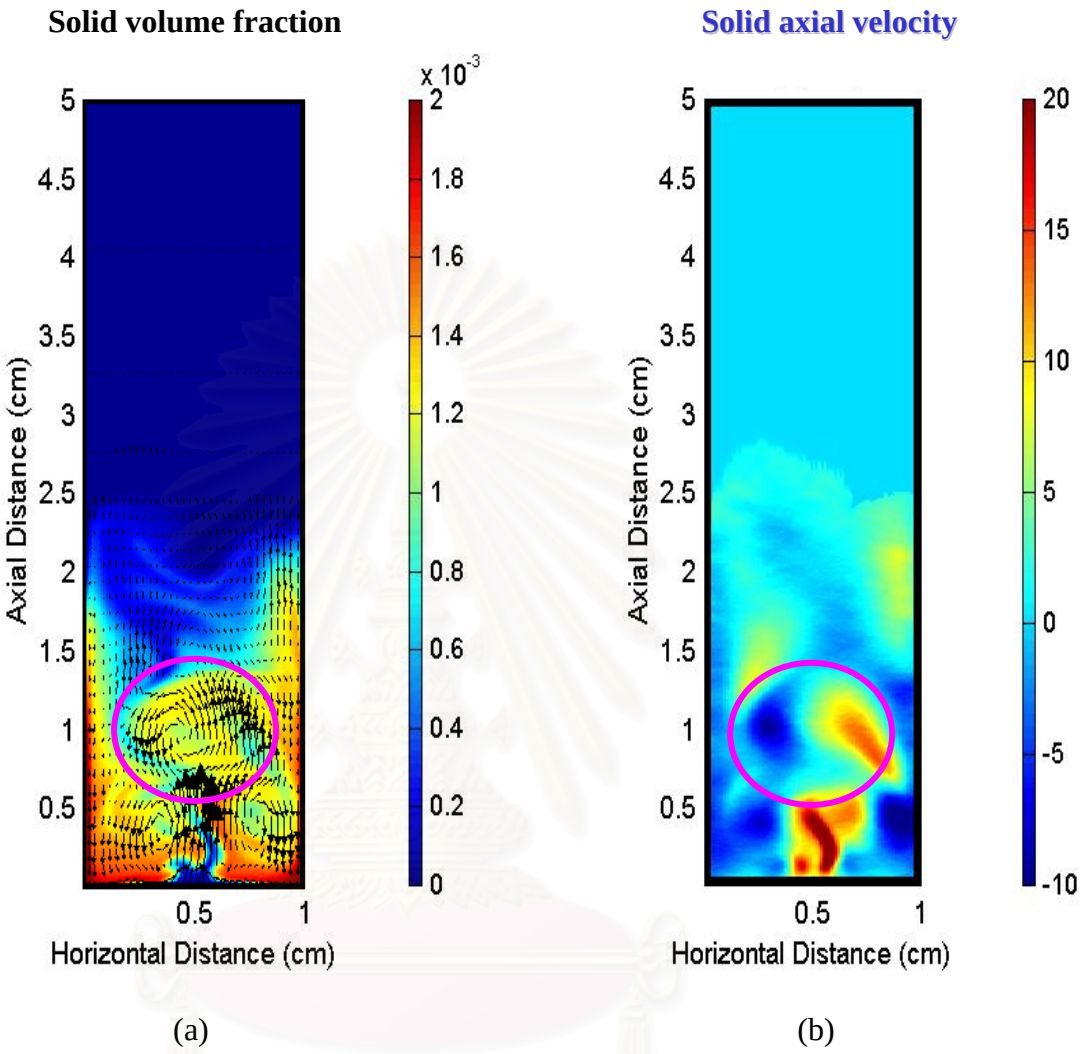

Figure 6.13 Filled contour plots of 10 nm silica particles superimposed with solid velocity vectors
Granular temperature = 0.25 m^2/s^2 at 0.6 sec
with $\Psi = -A\frac{\partial \Psi_{s,w}}{\partial n}$ boundary condition, A = 0.1

The volume fraction and velocity color scales are on the right-hand side.
(a) solids volume fraction (b) solids axial velocity

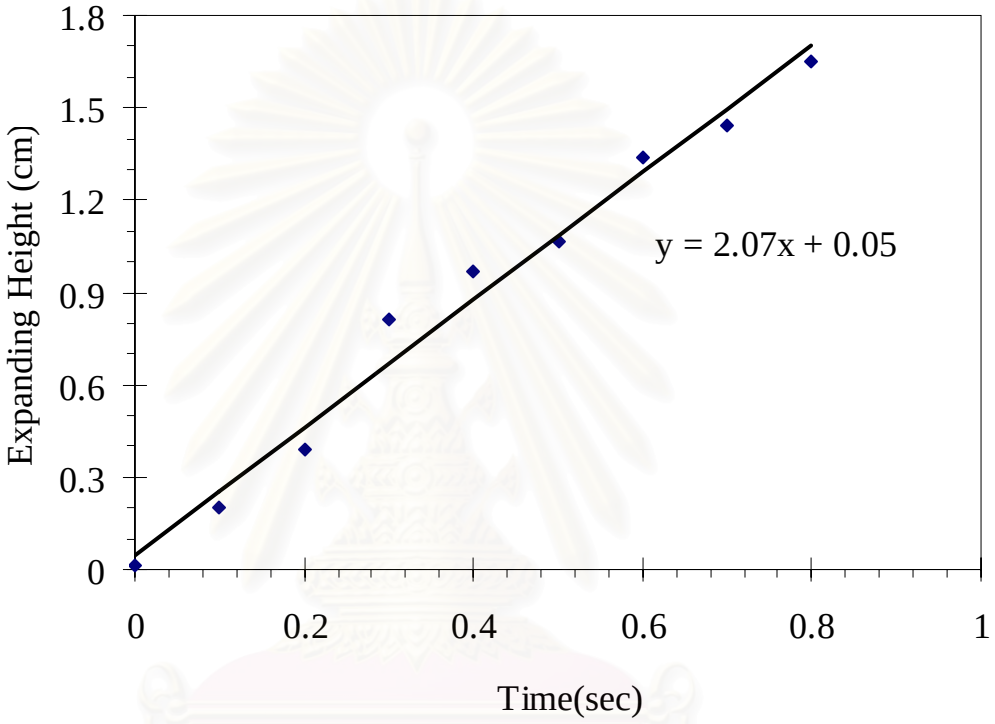

Figure 6.14 Bed expansion with time. Granular temperature = 0.25 m^2/s^2

,with $\Psi = -A\frac{\partial \Psi_{s,w}}{\partial n}$ boundary condition, A = 0.1

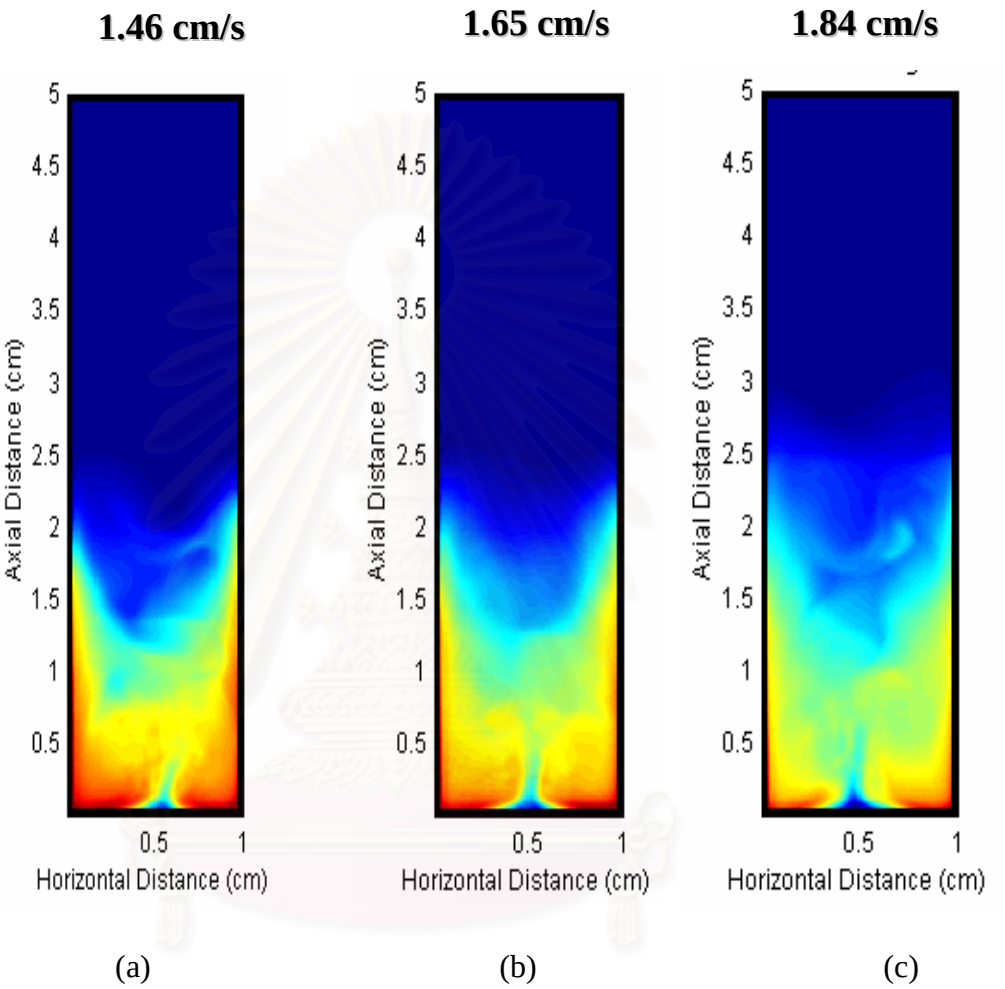

Figure 6.15 Effect of superficial gas velocity
Time averaged of filled contour plots of 10 nm silica particles
Granular temperature = 0.25 m^2/s^2, with $\Psi = -A\frac{\partial \Psi_{s,w}}{\partial n}$ boundary condition, A = 0.1

The volume fraction and velocity color scales are on the right-hand side.
(a) 1.46 cm/s (b) 1.65 cm/s (c) 1.84 cm/s

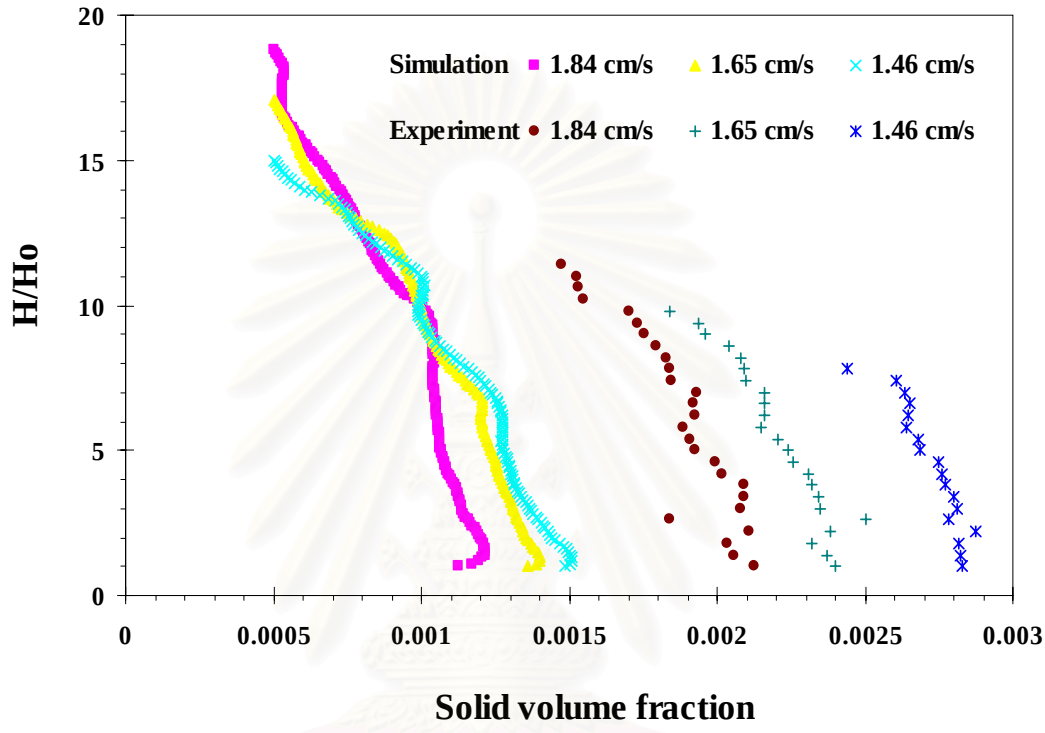

Figure 6.16 Comparison of expansion ratios as a function of superficial gas velocity for experiments and simulations of 10 nm silica particles

Granular temperature = 0.25 m^2/s^2, with $\Psi = -A\frac{\partial \Psi_{s,w}}{\partial n}$ boundary condition, A = 0.1

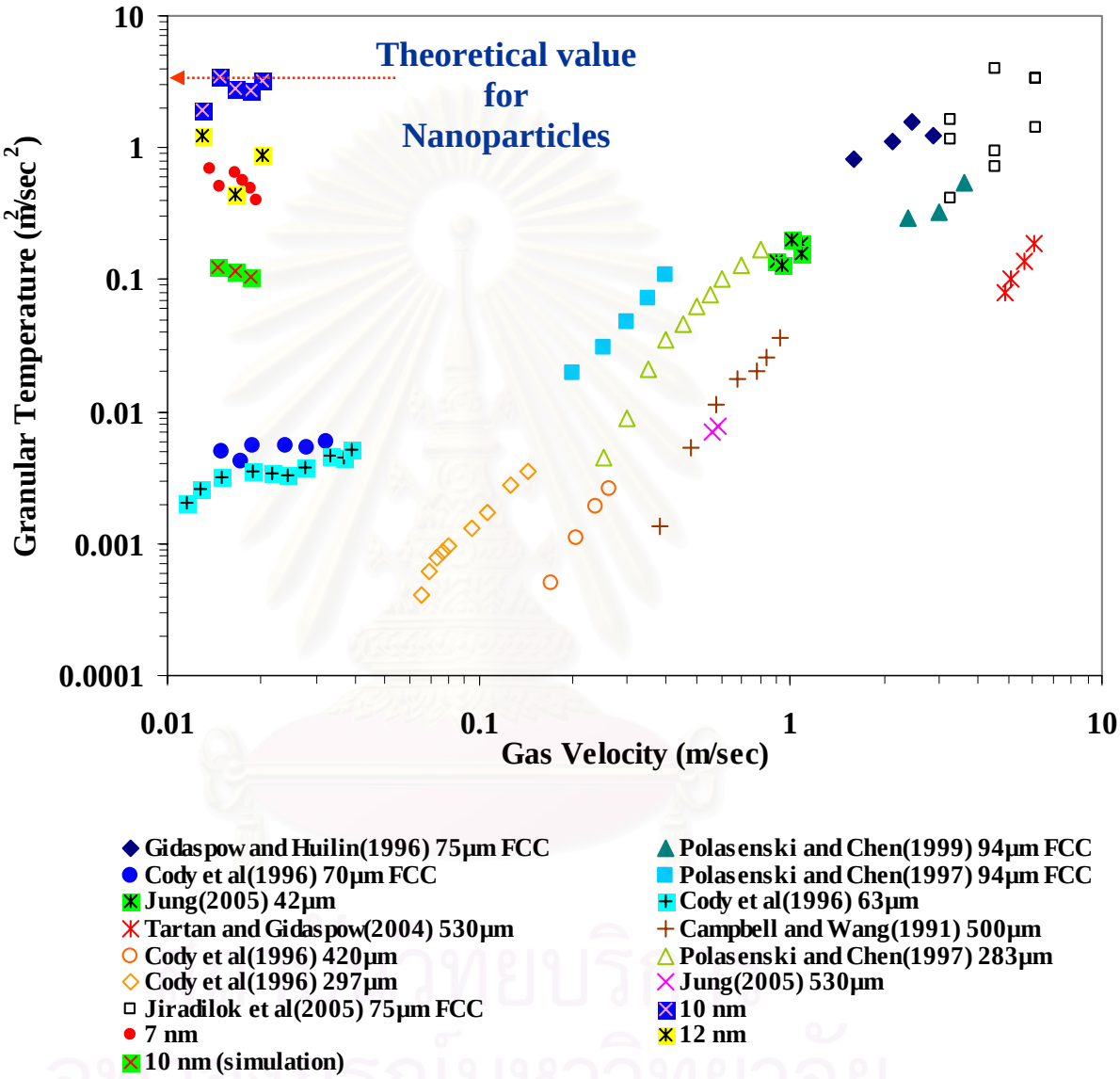

Figure 6.17 Effect of gas velocity on granular temperature of Geldart type A, B and nanoparticles

CHAPTER VII

EXPERIMENTAL STUDY OF TWO KINDS OF GRUNULAR PARTICLES IN BUBBING AND TURBULENT FLUIDIZED BED

7.1 Introduction

Gas-solids circulating fluidized beds (CFBs) have been widely used in the oil, chemical, electric power industries and many process industries for example, fluid catalytic cracking (FCC). Quantitative understanding of the hydrodynamics of fluidization is needed for the design and scale-up of efficient new reactors.

In the fluidization bed reactors, we use the kinetic theory of granular flow for describing the hydrodynamics of the granular particles. The motions of fluidized particles are composed of a mean component and a fluctuating component. There are two possible mechanisms inducing the fluctuations of particle velocity: particle-particle collisions and particle-fluid interaction. (Gidaspow and Huilin, 2003). Savage (1981) used the term of granular temperature defined as the average of the sum of the squares of the three fluctuating velocity. The granular temperature can be obtained from the variances of the instantaneous particle velocities measured by using a CCD camera (Gidaspow and Huilin, 1996;1998a).

We can identify two types of granular temperatures, due to particle oscillations, “laminar” and due to cluster or bubble, “turbulent”. These two kinds of turbulence give rise to two kinds of mixing, mixing on the level of a particle and mixing on the level of cluster or bubble.

In order to understand the hydrodynamics of particles, we measured two kinds of granular temperatures, the particle granular temperature and bubble-like granular temperature, in bubbling and turbulent regimes.

7.2 Experimental Setup and Procedure

The IIT experimental apparatus for gas-solid flows is two-dimensional fluidized bed as shown in Figure 7.1. In order to prevent the particles from sticking to the wall and to facilitate good visual observation, a column was constructed from glass sheets. The height of column was 58.5 cm and the cross-section was 15.4 cm by 2.2 cm. The distributor obtains from 165 x 1400 mesh 304L stainless steel wire (Newark Wire Cloth Company). The fluidizing gas is air dried in a silica filter drier before entering the fluidized bed. Gas flows are measured with a rotameter.

The material used, as the solids were glass beads with an average particle diameter of 530 μm and density of 2500 kg/m^3 as Geldart group B. The superficial gas velocity was 1.51 m/s, which was 6.5 times higher than the minimum fluidized velocity of particles. In this experiment, the solids were charged into the bubbling fluidized bed to give a static bed height of 14 cm for experiment. The particle velocities were measured from three different fluidized bed heights in the center region; 26 cm., 24 cm. and 22 cm.

7.2.1 Particle Velocity

Particle image velocimetry technique is capable to measure particles instantaneous velocity as non-intrusive measurement by means of the color video camera using a charge-coupled device (CCD, Sony DVC-151A). The principle of this technique is that particles scatter light into a photographic zoom lens (Navitar), 18-108 mm, located at 90° to the field of view. Images are formed on a video array detector, and the images are subsequently transferred to a computer. A micro-imaging board is used for capturing and digitizing the images. They are analyzed the particle velocity by Image pro plus software.

For a good visualization of microscopic movement of particle, the system must have the correct position of a light. When a fiber-optic light projects into the glass bead, it composed of the reflected light and the refracted light. The backlight helps to improve the quality of the images. We should adjust the angle of the light beam until the reflected light has the correct position, so we can get a good image measured the length of a streak line. The transparency sheet is used to consider the flow direction of particles, upward and downward which can be considered by the arrangement of color of the streak line, yellow, green and red.

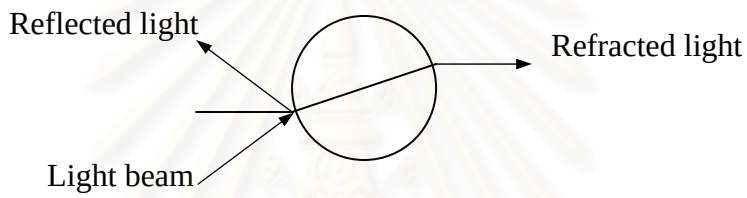

Figure 7.2 shows typical particle streak images captured by a CCD camera. The particle velocity was measured by dividing a length of a streak line by exposure time corresponding the shutter speech of the camera. Radial and axial velocity was calculated as,

$$c_x(r,t) = \frac{\Delta L}{t}\cos\alpha \tag{7.1}$$

$$c_y(r,t) = \frac{\Delta L}{t}\sin\alpha \tag{7.2}$$

Where ΔL is the distance traveled, α is the angle from vertical line, t is the time of shutter time(or 1/shutter speed), c_x and c_y are the instantaneous axial and radial velocity, respectively

7.3 Results and Discussion

7.3.1 Particle velocity

Figure 7.3 shows the histogram of radial and axial particle velocity fluctuation over all frames by using the CCD camera technique of 530 μm glass beads in the center region at a measuring height 22 cm, the superficial inlet velocity is 1.51 m/sec and exposure time is 1/1000 sec. The particle velocity fluctuation is defined as the instantaneous particle velocity minus the hydrodynamics particle velocity, which was calculated as,

$$v_i(r,t) = \frac{1}{n}\sum_{k=1}^{n} c_{ik}(r,t) \qquad (7.3)$$

Where n is the number of particles per unit volume

c is instantaneous particle velocity in i-direction

v is hydrodynamic velocity in i-direction

r is any positions

i is x, y and z direction

The standard deviation of the radial particle velocity fluctuation is less than of the axial particle velocity fluctuation.

Figure 7.4 shows oscillation of hydrodynamics velocity, averaging the mean particle velocity in each frame) of axial and radial direction obtain by CCD camera techniques in the center region and the superficial gas velocity of 1.51 m/s at a measuring height 26 cm. A characteristic feature of the flow is the oscillating motion of particles. The hydrodynamic velocity is an irregularly oscillating function. Variation of velocity as shown in this figure permits the determination of Reynolds stresses. Most of the axial particle velocities are the positive values; it means that the particles flow up in the center of fluidized bed. The radial particle velocities have both, the positive and the negative

values because the particles move right and left side. The mean particle axial particle velocity is 61.45 cm/sec, which is higher than the mean particle radial particle velocity. The mean radial velocity almost equals zero due to measurement at the central of bed.

Figures 7.5 and 7.6 show the mean particle velocity in axial and radial direction of 530 μm glass beads in the central region at a static bed height of 14 cm., superficial inlet velocity is 1.51 m/s. The axial velocity of particle at 26 cm is the highest value because most of the particles move in the bubble phase, but the radial velocity is the least value. It indicates that the particles in bubble phase move in the vertical direction. The values of the axial velocity of particle at 22 cm and at 24 cm almost have the same value. At a measuring height of 22 cm, the particle move in the horizontal direction more than at 24 cm; it can be considered from the radial velocity which has the higher value. Therefore at both heights, the particles move in the emulsion phase. This shows that the axial velocity of particles in the bubble phase is higher than in the emulsion phase but the radial particle velocity in the bubble phase is lower than in the emulsion phase.

7.3.2 Particle stresses

The stresses are particularly useful in describing the forces exerted by the fluid on solid surface. Variation of the solid velocity leads to the determination of 2 main types of stresses.

1. Normal Stresses
    - 1.1 Laminar Particle Stresses
    - 1.2 Reynolds type Normal Particle Stress
2. Shear Stress
    - 2.1 Shear Particle Stresses
    - 2.2 Reynolds type Shear Particle Stress

These quantities have two subscripts associated with the coordinate directions.

Laminar Particle Stresses were calculated from the variances of fluctuating velocity of particle in axial, radial and tangential direction. The fluctuating velocity, also called as peculiar velocity, is defined as instantaneous particle velocity minus hydrodynamic velocity

$$< C_i C_i > (r,t) = \frac{1}{n}\sum_{k=1}^{n}(c_{ik}(r,t) - v_i(r,t))(c_{ik}(r.t) - v_i(r,t)) \tag{7.4}$$

$$v_i(r,t) = \frac{1}{n}\sum_{k=1}^{n} c_{ik}(r,t) \tag{7.5}$$

The bubble-like granular temperature were calculated from particle normal Reynolds stresses

$$\theta_{bubble-like}(r,t) = \frac{1}{3}\left[< V_x V_x > + < V_y V_y > + < V_z V_Z >\right] \tag{7.6}$$

In the two dimensional bed, the bubble-like granular temperature can be calculated

$$\theta_{bubble-like}(r,t) = \frac{1}{3}\left[< V_x V_x > +2 < V_y V_y >\right] \tag{7.7}$$

Shear Particle Stresses

$$< C_x C_y >= \frac{1}{n}\sum_{k=1}^{n}(c_{xk} - v_x)(c_{yk} - v_y) \tag{7.8}$$

Figures 7.7 and 7.8 show the normal stresses in x and y direction at three measuring height. At a measuring height 26 cm., the laminar normal stress in x direction $(C_x C_x)$ has a lot of high peaks. These peaks show that the velocity of particle at that time differs from the hydrodynamic velocity. It indicates that the movement of the particle in the bubble phase can be observed from these peaks; therefore, the variance of the fluctuating velocity of the particle has the high value when the particles move in the bubble phase. The mean value of the normal stress in y direction has the same trend as in x direction.

Figure 7.9 shows times average normal particle stresses in the centre region. The axial normal stresses of about 138 cm^2/sec^2 were 220 times higher than the radial normal stresses. The shear normal stresses were very low, close to zero at three measuring heights.

<u>Reynolds type Normal Particle Stress</u> The normal Reynolds stresses were calculated from that the variance of the hydrodynamic velocity of the particle. Turbulent part of the normal stresses evaluated from the time-smoothed velocity $\bar{v}_i(r)$ are given as follows:

$$< V_i V_i > (r) = \frac{1}{m}\sum_{k=1}^{m}(v_{ik}(r,t) - \bar{v}_i(r))(v_{ik}(r,t) - \bar{v}_i(r)) \qquad (7.9)$$

$$\bar{v}_i(r) = \frac{1}{m}\sum_{k=1}^{m} v_{ik}(r,t) \qquad (7.10)$$

Where m is the total number of frames over a given time period

$\bar{v}_i$ is the mean particle velocity

<u>Reynolds type Shear Particle Stress</u>

$$< V_x V_y > (r) = \frac{1}{m}\sum_{k=1}^{m}(v_{xk} - \bar{v}_x)(v_{yk} - \bar{v}_y) \qquad (7.11)$$

Figure 7.10 shows times average shear particle stresses in the centre region. The axial Reynolds normal stresses of about 1079 cm^2/sec^2 were 383 times higher than the radial Reynolds normal stresses. The Reynolds shear stresses were very low of about 8.3 cm^2/sec^2.

7.3.3 Comparison of particle and bubble –like temperatures

The granular temperature can be introduced as a measure for the energy of the fluctuating velocity of the particles, which is related to the particle normal stresses.

$$\theta_{particle}(r,t) = \frac{1}{3}\left[< C_x C_x > + < C_y C_y > + < C_z C_Z >\right] \qquad (7.12)$$

In the two dimensional bed, it can be defined assuming the velocity fluctuations in y direction and in z direction to be equal.

$$\theta_{particle}(r,t) \cong \frac{1}{3}\left[< C_x C_x > +2 < C_y C_y >\right] \tag{7.13}$$

The bubble-like granular temperature were calculated from particle normal Reynolds stresses

$$\theta_{bubble-like}(r,t) = \frac{1}{3}\left[< V_x V_x > + < V_y V_y > + < V_z V_Z >\right] \tag{7.14}$$

The bubble-like granular temperature can be defined assuming the tangential and radial velocity fluctuations to be equal in the two dimensional bed,

$$\theta_{bubble-like}(r,t) = \frac{1}{3}\left[< V_x V_x > +2 < V_y V_y >\right] \tag{7.15}$$

Figure 7.11 shows a comparison of measured particle granular temperature and bubble-like granular temperature of 530 μm glass beads at 1.51 m/s. The mean particle granular temperature over a given time is 46 cm^2/sec^2 and the bubble-like granular temperature is 362 cm^2/sec^2. The bubble-like granular temperature due to the formation of bubble is much high than the particle oscillations. In this study, the particle plus bubble-like granular temperature is 408 cm^2/sec^2.

Jung et al. (2003) measured the particle and bubble-like granular temperature of 530 μm glass beads using a CCD camera technique in the bubbling fluidization. The superficial gas velocity is 2.5 times the minimum fluidization velocity of particles. The granular temperatures were shown in table 7.1.

Table 7.1 The comparison of two kinds of granular temperature between this work and Jung (2003)

	U_o/U_{mf}	Granular Temperature $(cm/sec)^2$	Bubble-Like Granular Temperature $(cm/sec)^2$
Jung (2003)	2.5	30	200
This Experiment	6.5	46	362

Figure 7.12 shows a comparison of the particle and bubble-like granular temperature between this work and Jung's data. It can be indicated that at the high velocity, the granular temperature will be correspondingly high. It agrees well with the value of Turbulent Intensity

Figure 7.13 gives the summary of the granular temperature from the literature and from this work of Geldart A and B particles. In this work, the granular temperature of Geldart B particles 530 μm glass bead is included two terms, the particle and bubble-like granular temperature. It shows a reasonably good agreement with the experimental values from the literature.

7.3.4 Turbulent Intensity

In developed flow, the particles were assumed as elastic particle. The balance of the granular temperature (Gidaspow, 1994; Jackson, 2000) is related between conduction and generation. The system is considered as the cylindrical coordinates and it is as follows for a constant conductivity, κ and particle viscosity, μ_s.

$$\frac{k}{r}\frac{d}{dr}\left(r\frac{d\theta}{dr}\right) = -\mu_s\left(\frac{\partial v_s}{\partial r}\right)^2 \tag{7.16}$$

Then simplifier the equation,

$$\theta_{\max} = \left(\frac{\mu}{\kappa}\right)\bar{v}_s^2 \tag{7.17}$$

Equation 7.17 shows that the granular temperature is of the order of the particle velocity squared. In the dilute limit the ratio of viscosity and conductivity is 4/15 (Gidaspow, 1994). In the term of the dimensionless, Turbulent Intensity is defined as the square root of the average granular temperature scaled with the average particle axial velocity $(\sqrt{\theta_{ave}}/\bar{v}_s)$. In the dilute kinetic theory, the turbulent intensity scaled the particle granular temperature was of order of 0.5. In this experiment, the value is 0.388 which estimates form the total granular temperature, 408 cm^2/s^2 and the average the particle velocity, 52 cm/s. Therefore the turbulent intensity value in the bubbling and turbulent regime is lower than in the dilute kinetic theory.

7.4 Conclusion

Two kinds of granular temperatures in bubbling and turbulent regimes are obtained in the experimental work. The fluctuations of particle velocity are caused by bubble motion and particle oscillations. In agreement with the experimental data of Jung et al. (2003) the granular temperature can be defined 2 terms, the particle granular temperature and the bubble-like granular temperature. It has the same trends which is the granular temperature due to bubble motion was much higher than due to particle oscillations in the bubbling and turbulent regimes. This experiment correctly shows that at the high superficial gas velocity the motion of particle in the fluid is turbulent, so the granular temperature is high. It agrees with a review of the literature. The turbulent intensity value in the bubbling and turbulent regime is 0.388. Similar value was observed in the riser (Tartan and Gidaspow, 2004).

สถาบันวิทยบริการ
จุฬาลงกรณ์มหาวิทยาลัย

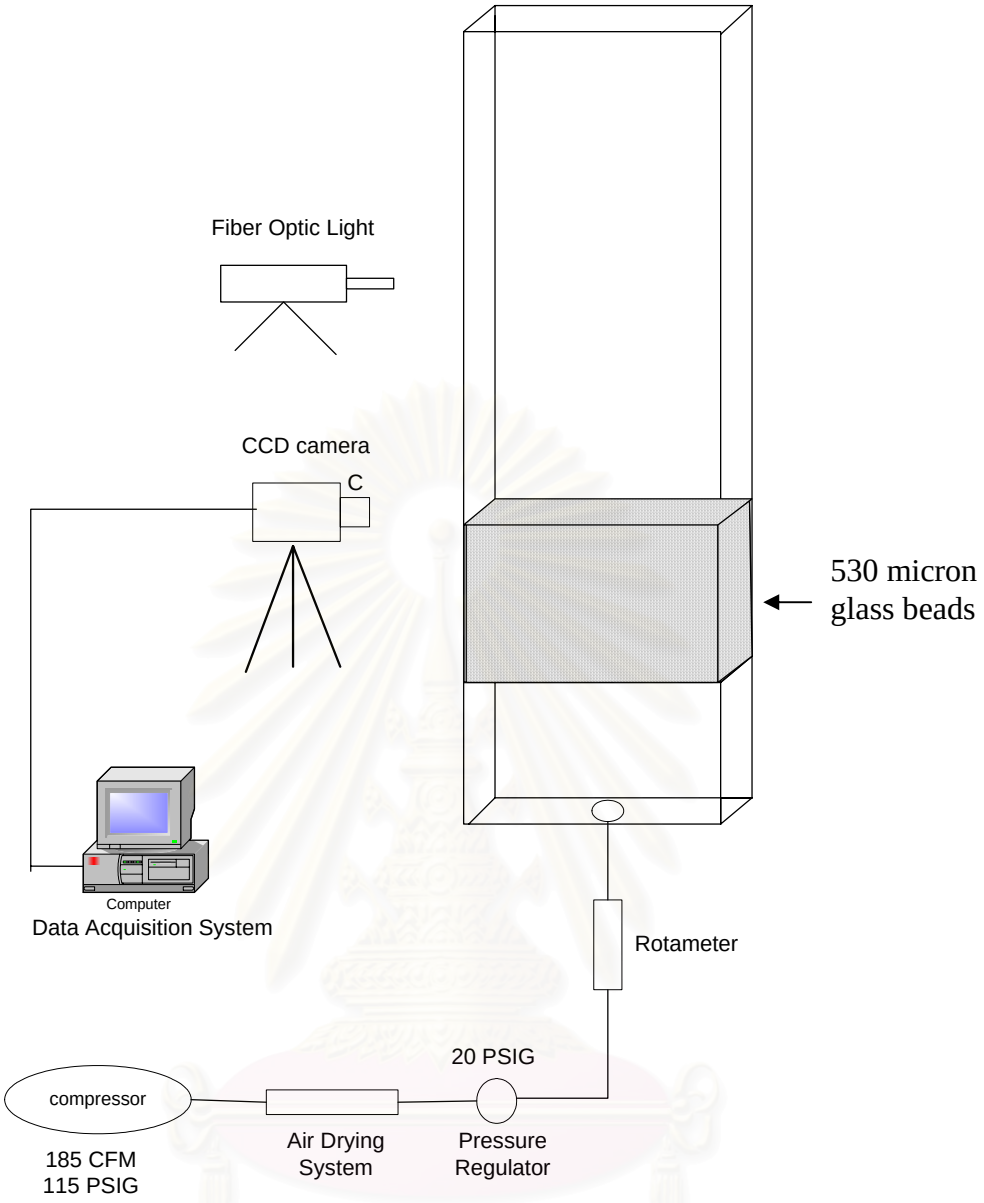

Figure 7.1 Experimental Schematic Diagram for Two-Dimensional Rectangular Fluidized Bed [0.154 m (Width) x 0.022 m (Depth) x 0.58 m (Height)]

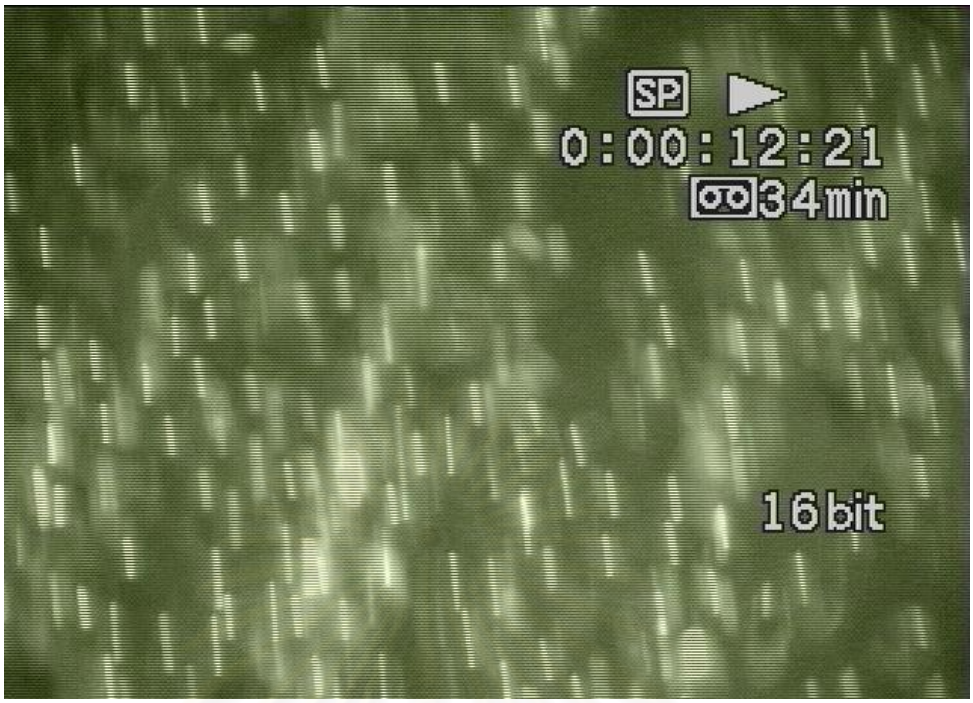

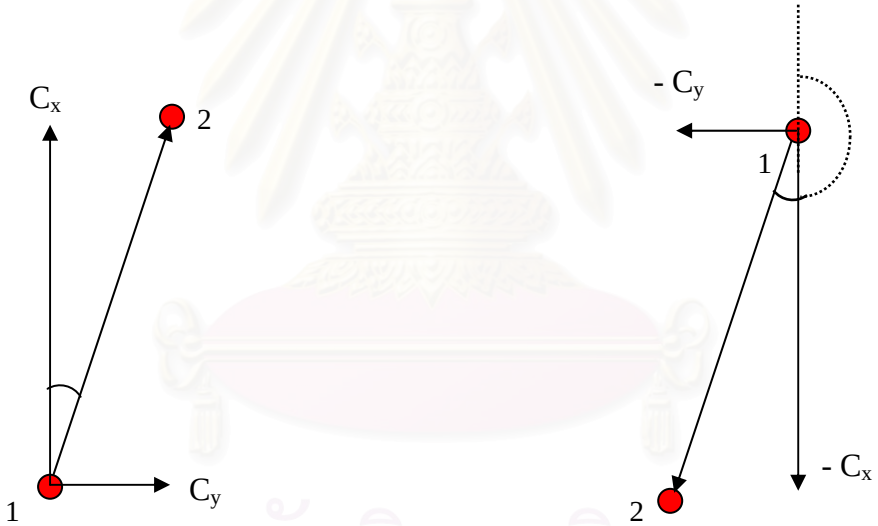

Figure 7.2 Particle Streak Images Captured by using a CCD camera of 530 micron. Superficial Inlet Velocity is 1.51 m/sec. Exposure time is 1/1000 sec.

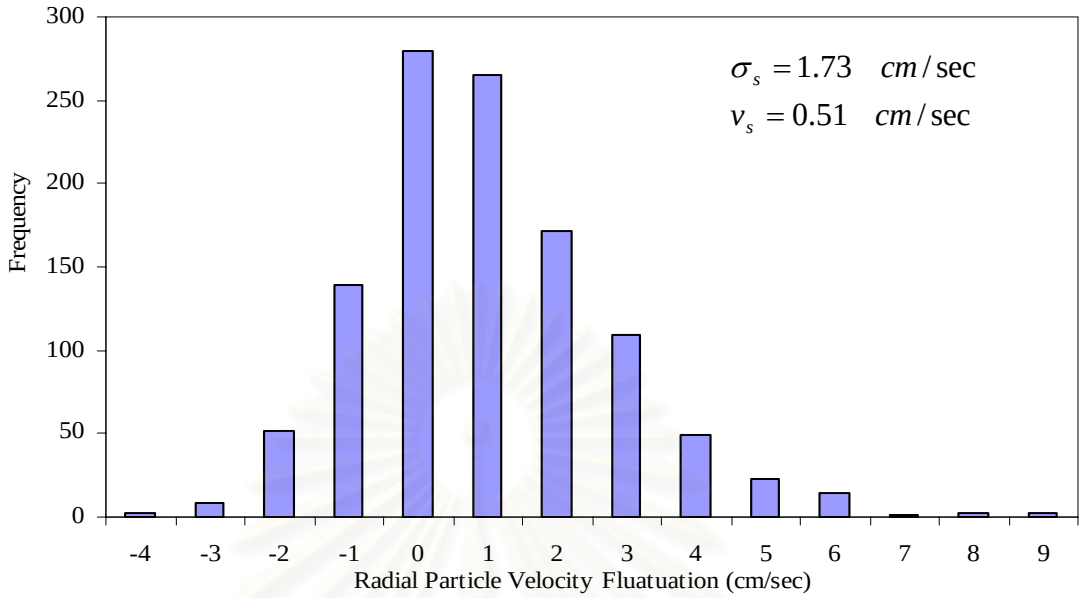

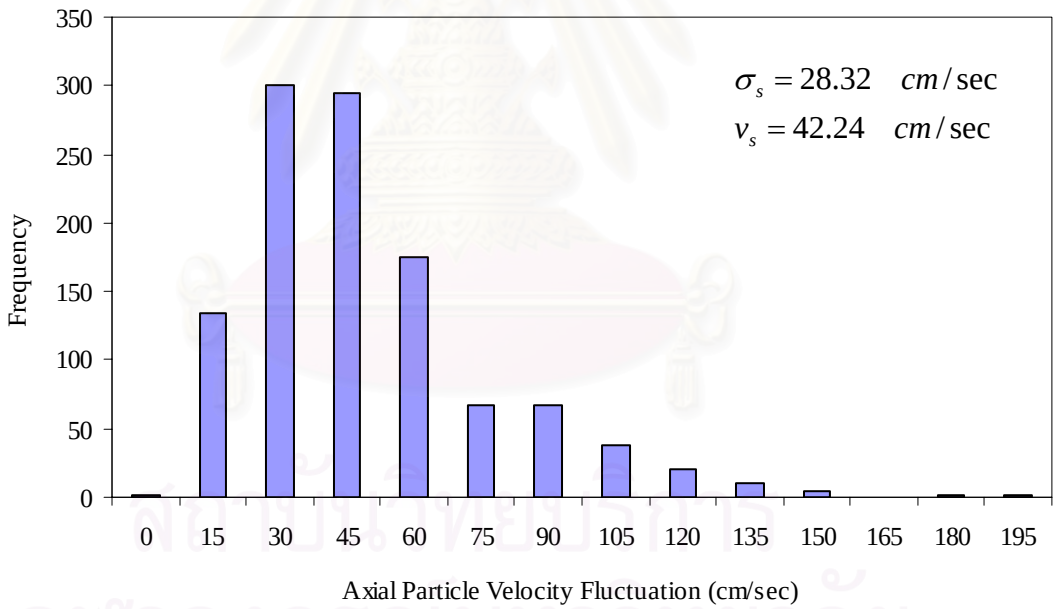

Figure 7.3 Histogram of Radial and Axial Particle Velocity Fluctuation over All Frames of 530 micron in the Center Region at a Measuring Height 22 cm. Superficial Inlet Velocity is 1.51 m/sec. Exposure time is 1/1000 sec.

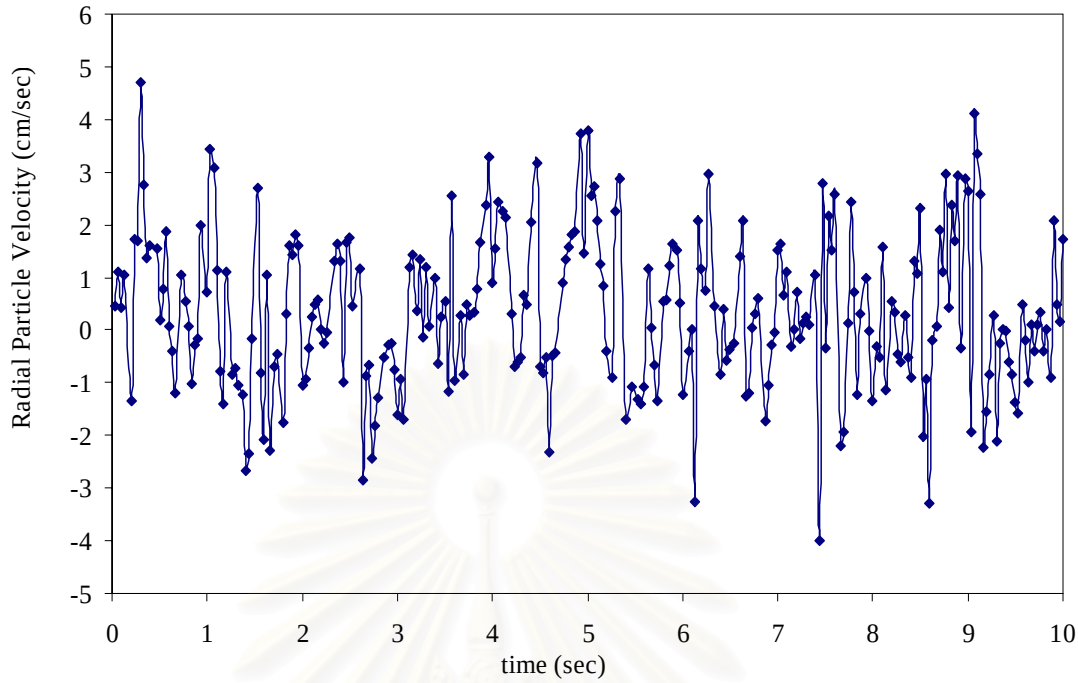

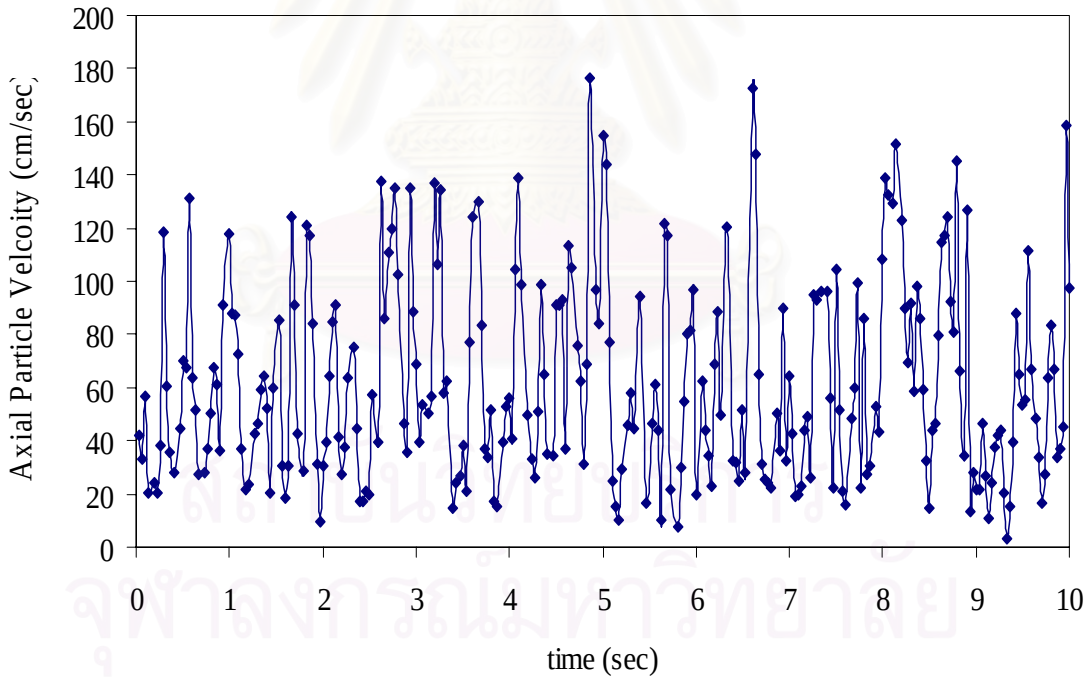

Figure 7.4 Oscillation of hydrodynamic velocity (averaging the mean particle velocity in each frame) of radial and axial directions obtained by CCD camera technique in the centre region at a measuring height 26 cm

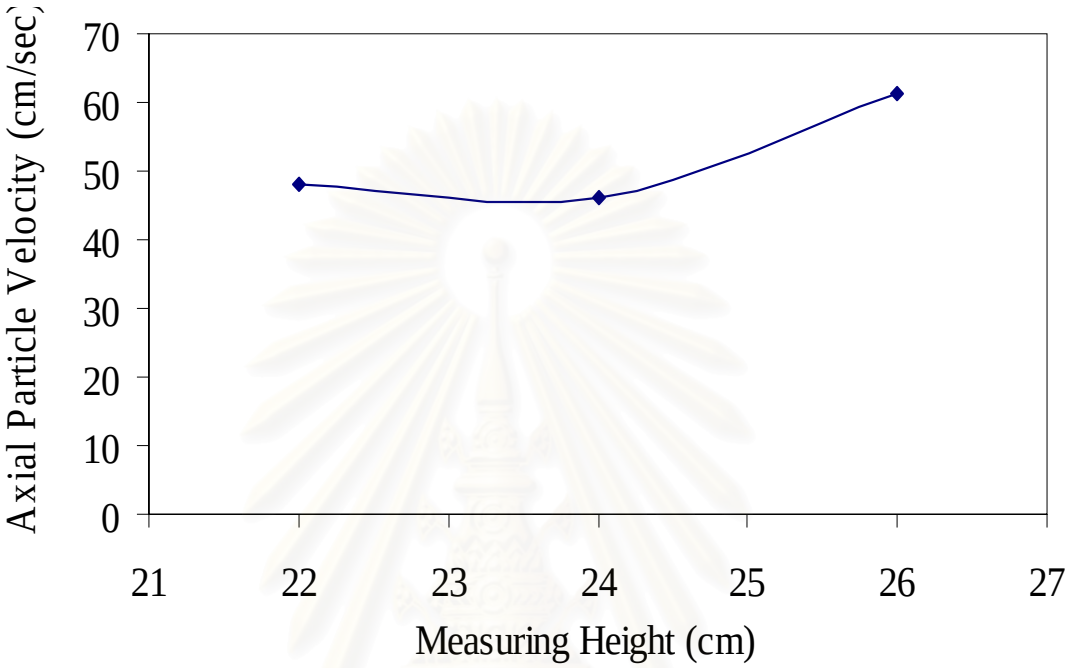

Figure 7.5 Axial velocity of 530 micron in the central region at a bed height of 14 cm, superficial inlet velocity is 1.51 m/s, exposure time is 1/1000 sec.

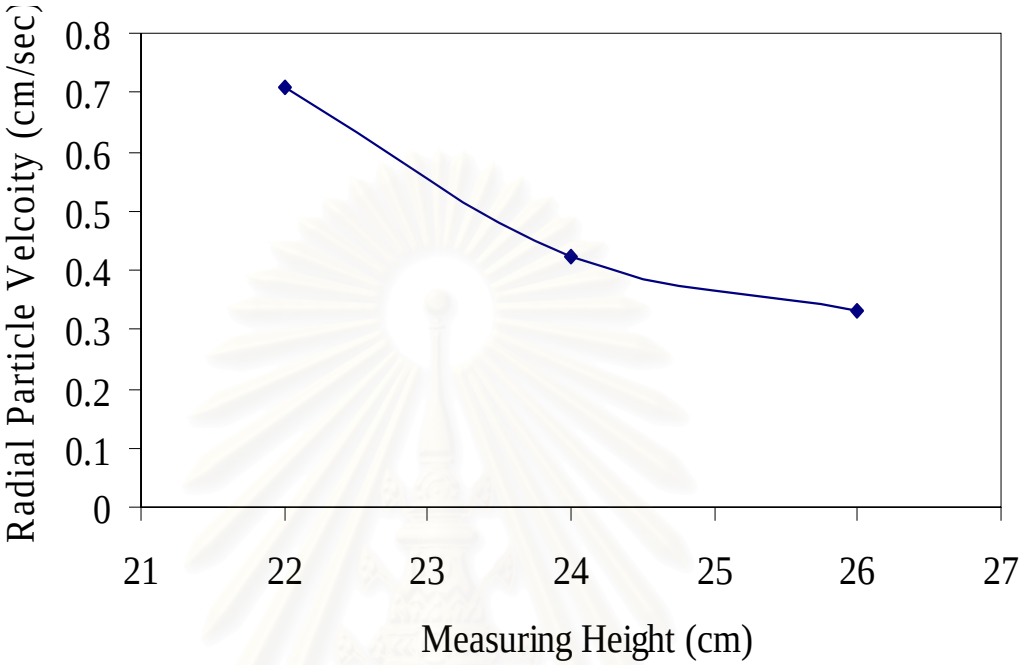

Figure 7.6 Radial velocity of 530 μm glass beads in the central region at a bed height of 14 cm, superficial inlet velocity is 1.51 m/s, exposure time is 1/1000 sec.

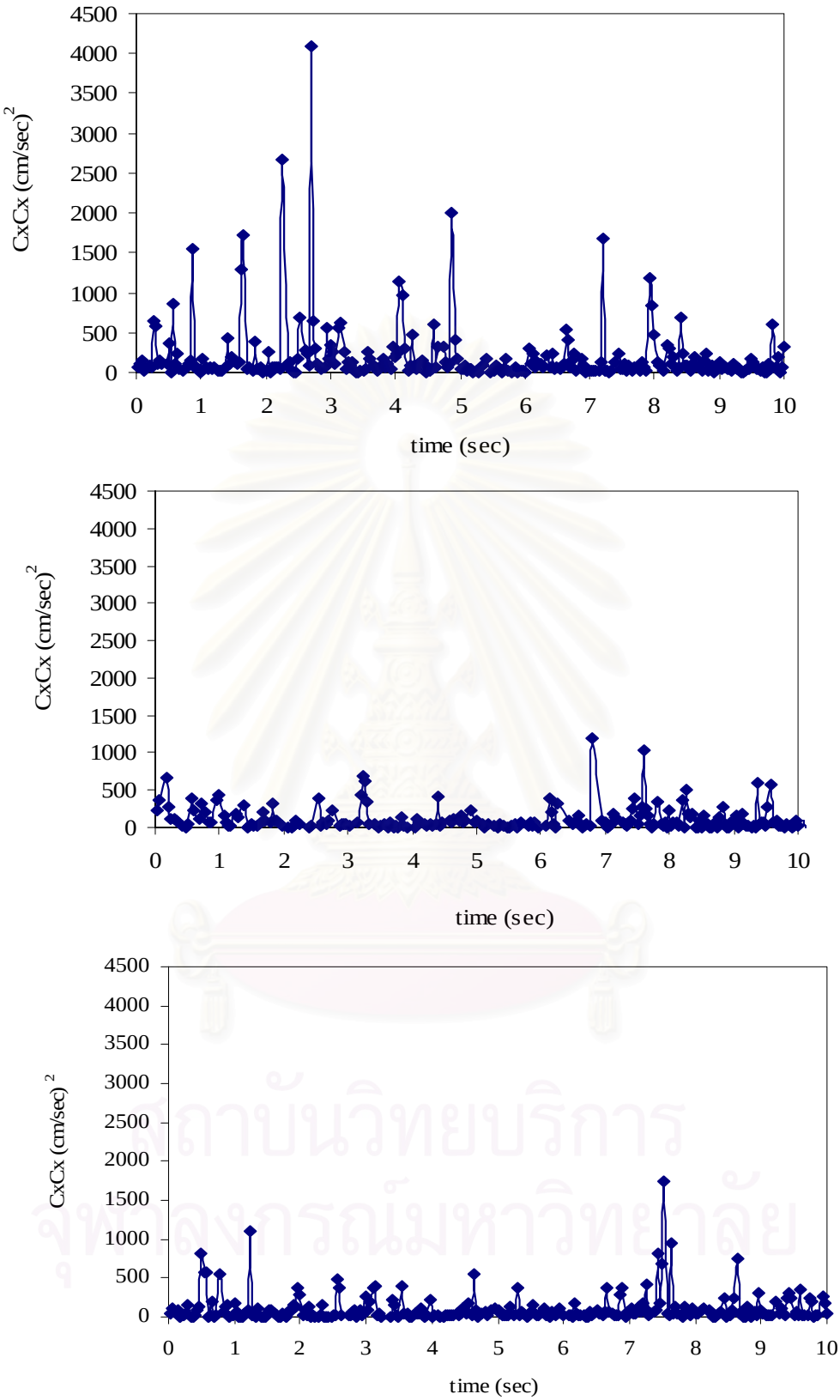

Figure 7.7 The Normal Stress in x direction at Measuring Height at a) 26 cm b) 24 cm and c) 22 cm

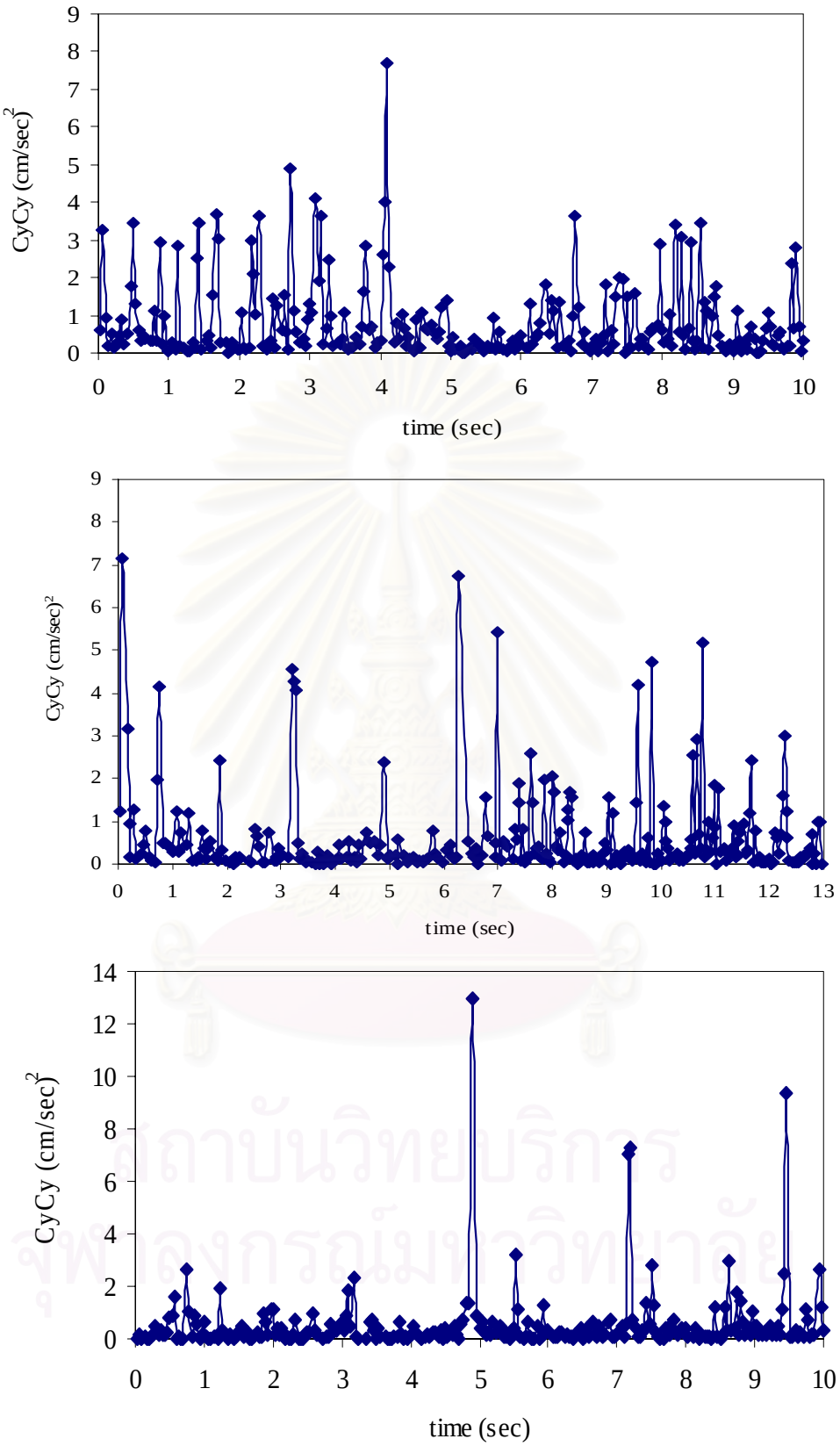

Figure 7.8 The normal stress in y direction at Measuring Height at a) 26 cm b) 24 cm and c) 22 cm

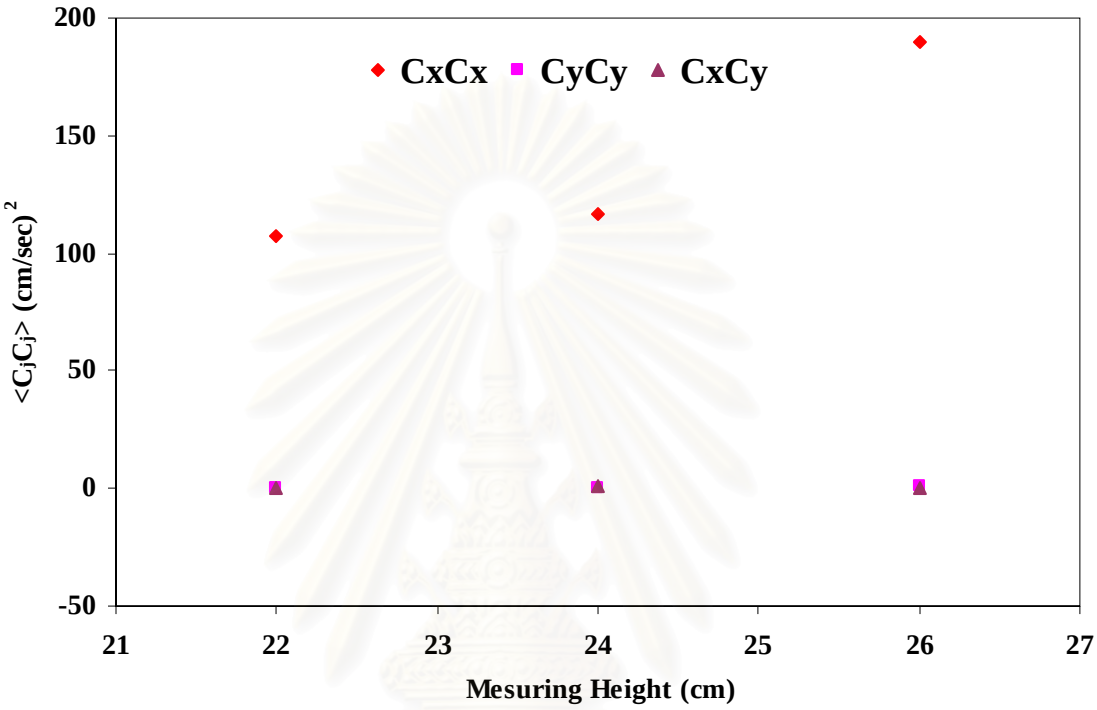

Figure 7.9 Time Average Particle Stresses Measured by CCD Camera Technique in the Center Region at U_o/U_{mf} = 6.5

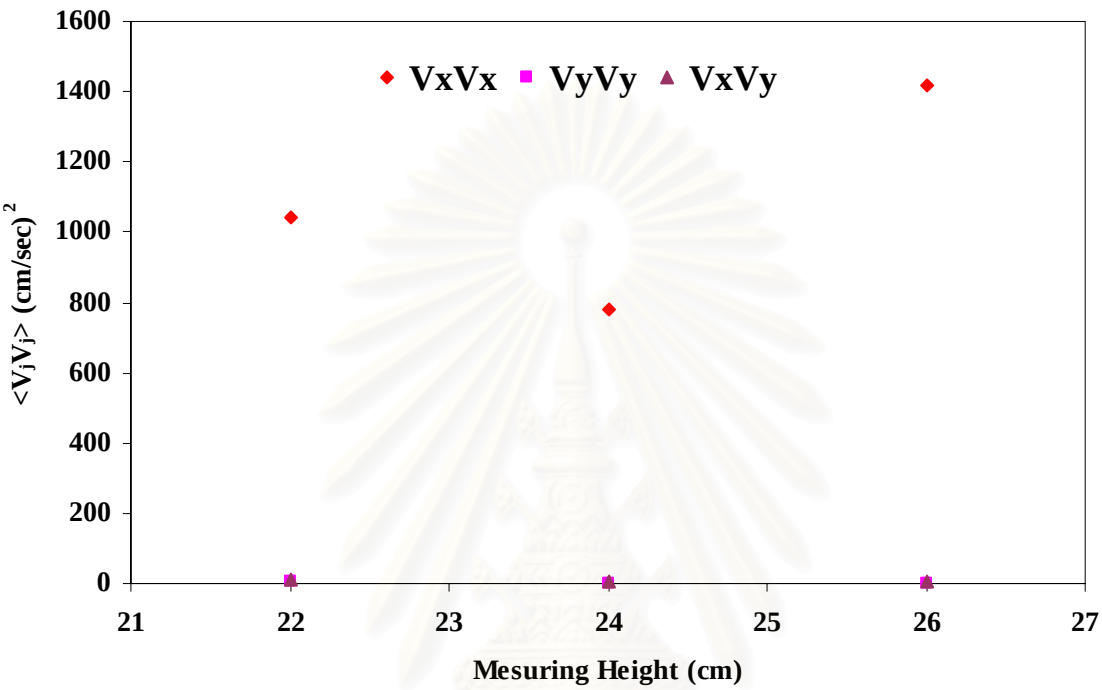

Figure 7.10 Time Average Particle Reynolds Stresses Measured by CCD Camera Technique in the Center Region at U_o/U_{mf} = 6.5

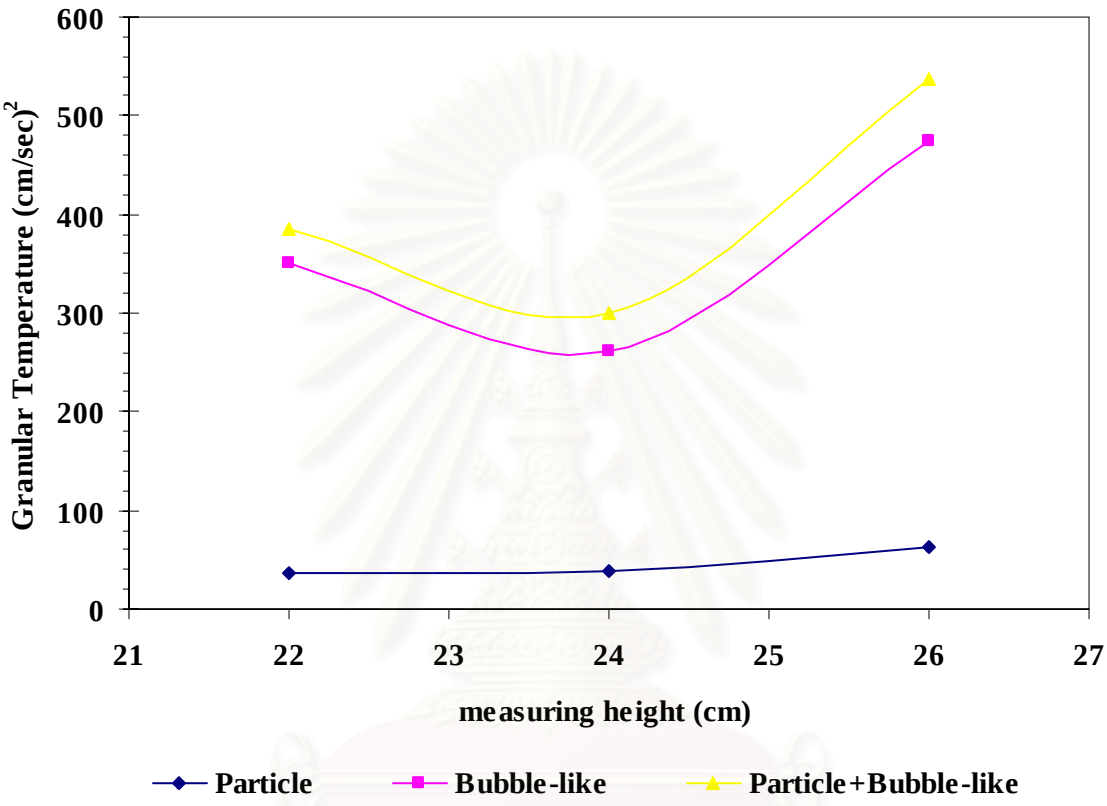

Figure 7.11 A Comparison of Measured Particle, Bubble-like and Particle+Bubble Granular Temperature of 530 μm glass beads at U_o/U_{mf} = 6.5

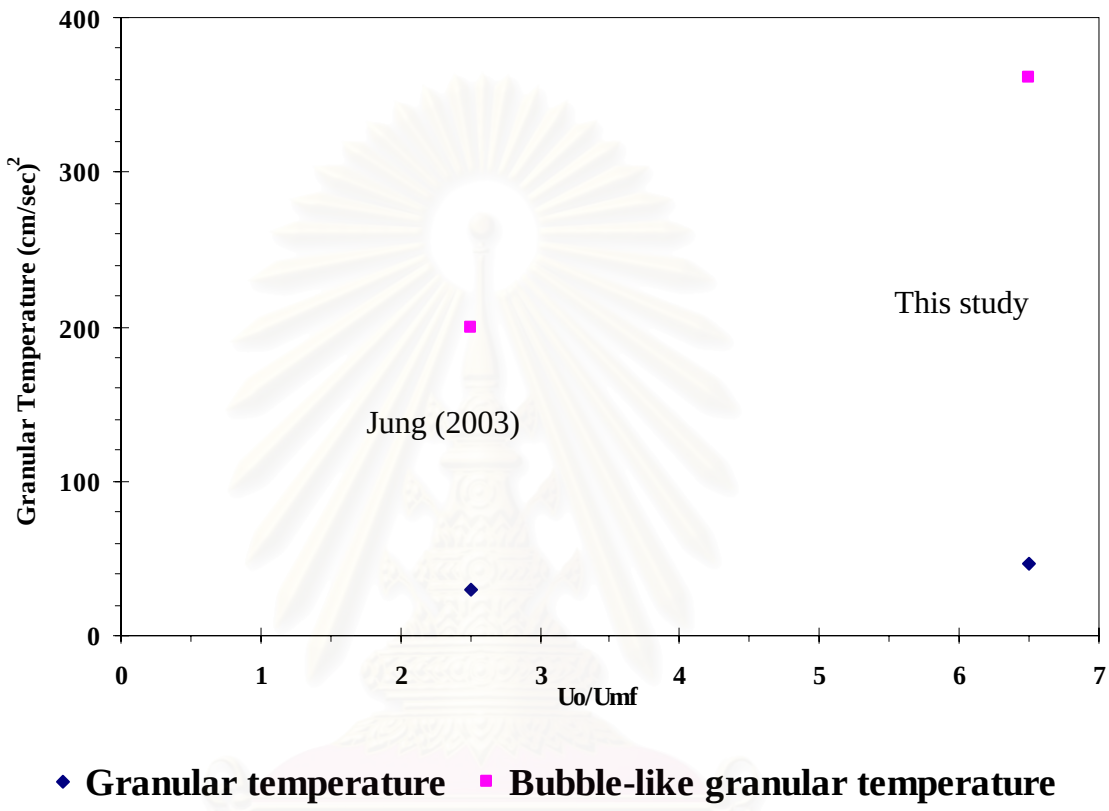

Figure 7.12 A Comparison of Measured Particle and Bubble-like Granular Temperature of 530 μm glass beads between This Experiment and Jung's Data (2003)

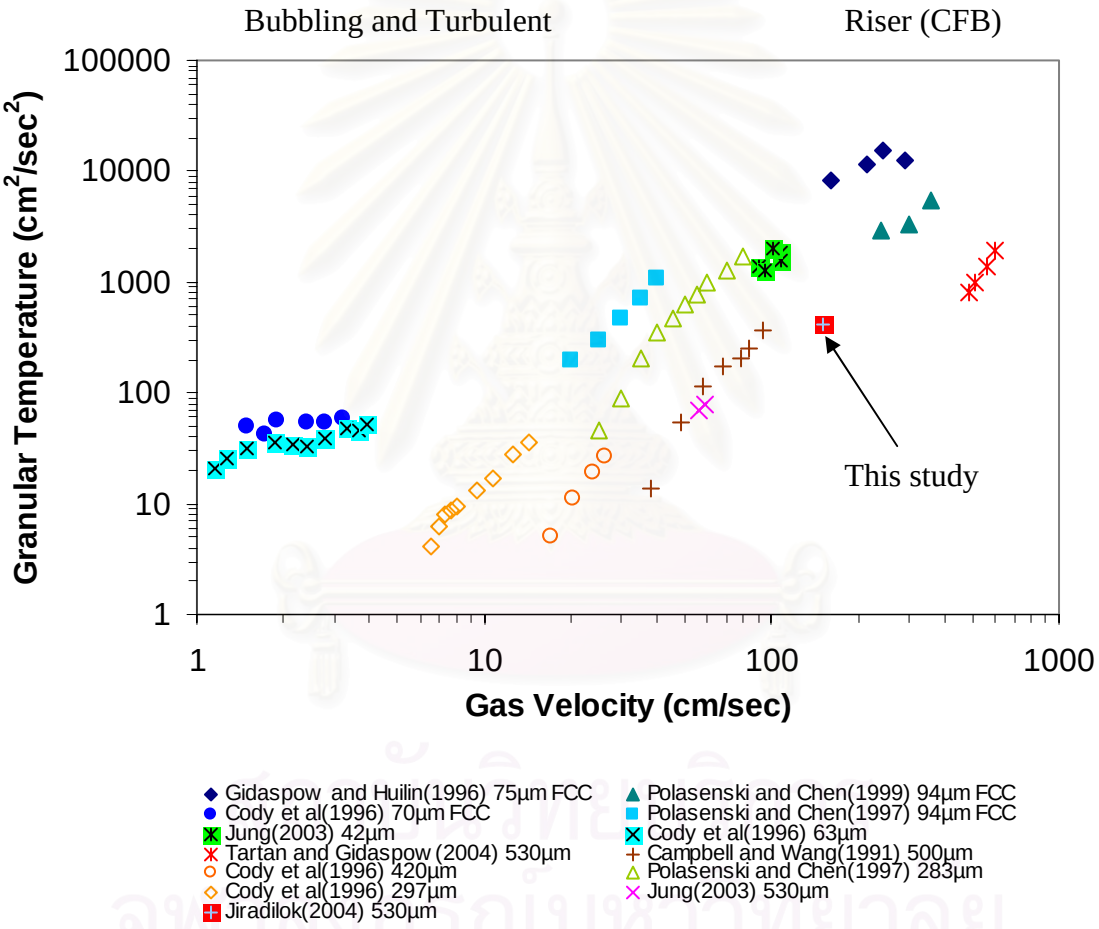

Figure 7.13 Granular temperature of Geldart type A and B particles

CHAPTER VIII

CONCLUSIONS AND RECOMMENDATIONS

Computational fluid dynamics was used to resolve some of the issues of the flow of FCC particles in the turbulent fluidization regime, explosive dissemination of 10nm silica particles and the flow of 10nm silica particles in a 2-dimensional fluidized bed.

Simulation of turbulent fluidization of FCC particles in a riser based kinetic theory model can be concluded as follow;

8. We have shown that the standard kinetic theory based CFD model with a modified drag as suggested by Jinghai Li group, is capable of correctly describing the coexistence of the dense and dilute regimes for flow of FCC particles in a riser in the turbulent regime.

9. The CFD simulations compare well with the high density riser experiment of Wei, et al. (1998) for three high solid fluxes of commercial interest. The computed void fractions agree within about 10% with the experiment at three different heights. For the three fluxes, we computed the observed core-annular regime at the bottom of the riser. However the computed ratio of particle to gas velocity at the center of the riser was considerably lower than that reported for the measurement of Wei, et al. (1998) similar to that computed by Jinghai Li group. The computed solids and gas velocity were close to each other, as expected for Geldart group A particles. The developed slip velocity was, however, almost two times higher than the terminal velocity of FCC particles, reflecting the Li group drag correction.

10. In the dense portion of the riser, the power spectrum of solid volume fraction is almost flat, in agreement with measurements reported in the literature (e.g.

Gidaspow, et al. 2001). However, in the dilute phase of the riser, there was a distinct peak at a frequency of about 0.28 Hz. This is an indication of a distinct core-annular structure.

11. Frequency analysis reveals the famous –5/3 Kolmogorov power law at the higher frequencies, similar to many single-phase flows.

12. The turbulent kinetic energy, essentially the total granular temperature, of the FCC particles agreed with the measurements of the granular temperature of Gidaspow and Huilin (1996) determined in the dense-annular region of the riser, where clusters were observed. The computed solids pressure also agreed with the measurements done with a special transducer. The computed solid viscosity, again, agreed with the measurements in the riser done with the three different instruments: PIV meter, Brookfiled viscometer and pressure drop minus weight of the bed measurements. Near 5% the computed solids viscosity compares well with the correlation for FCC particles of Gidaspow and Huilin (1998), but is about 30% lower at 25% solids holdup.

13. The CFD code also computed the turbulent characteristics of flow, of importance for the dispersion of particles. In the literature (e.g. Du, et al. 2002) it is well known that the radial dispersion coefficient is much smaller than the dispersion coefficient in the direction of the flow. Dispersion coefficients were computed as a function of radial and axial position. The computed dispersion coefficients are similar to the measurements reported in the literature.

14. The computed dispersion coefficients and the normal stresses allow the computation of characteristic lengths of clusters. The length and width agree with snapshot of volume fraction of solids.

Conclusions of explosive dissemination and flow of nanoparticles are as follow;

1. The particulate viscosity of 10 nm silica nanoparticles flowing in a pilot plant of circulating fluidized bed was estimated to be almost half of that of liquid water. This estimate was obtained from measurements of pressure drops, particle fluxes and particle concentrations using the technique developed by Miller and Gidaspow (1992). This value of viscosity agrees with an estimate obtained from elementary kinetic theory, assuming that the Brownian type nanoparticle oscillations are caused by the rapid random motion of the air molecules.

2. The measured nanoparticle viscosity was used in a CFD code developed earlier for explosive dissemination of micron size particles into an atmosphere, such as the pyroplastic flow of dust and the covering of ground by hot particles during eruption of volcanoes. This study shows that nanoparticle flow together with 5 micron particles, modeled earlier, without appreciable segregation. The computed ground concentrations allow a comparison to be made to observations. Eulerian-Lagrangian models found in FLUENT cannot compute such ground concentrations due to the diluteness assumption.

3. The new nanoparticle flow model allows further exploration of some unusual flow behavior of nanoparticles, such as bubbleless fluidization and multiple vortex formation (V. Jiradilok, 2006) during bed expansion, Fig 5.2. In such computations, the nanoparticle viscosity reported here plays a major role.

4. In this study we also show how to use CFD to design an explosive dissemination device that will prevent the overheating of the particles to be disseminated.

Recommendations

For the flow of FCC particles in the turbulent fluidization regime, we computed dense and dilute regimes and turbulence. This was done using the modified drag. This drag relation must be tested experimentally.

Dispersion coefficients for flow of FCC particles should be measured experimentally in the turbulent fluidization regime. Chapter 4 has already developed a theory for the computation of dispersion coefficients for FCC particles. The key assumption in the theory to be tested is the formation of clusters and hence the need for drag modification.

We should measure instantaneous particle velocities for flow of FCC particles using the particle image velocity (PIV) method (See Chapter VII). Using the measured instantaneous particle velocities, the particle and Reynolds stresses are computed for the FCC particles as described in Chapter VII and Tartan and Gidaspow (2004). This will show the fractions of random oscillations and mixing due to particles and clusters. Using the similar theories in Chapter 4, the dispersion coefficients due to two kind of mixing can be estimated.

For the unique flow of nanoparticles, we must to understand the interparticle forces and the mechanism of agglomeration of nanoparticles. A combination of various interparticle forces such as van der Waals, electrostatics interactions, and liquid bridging may occur in a fluidized bed. In the CFD code with the correct interparticle forces, the characteristics of the unique flow of nanoparticles should be predicted.

REFERENCES

Agrawal, K., P.N. Loezos, M. Syamlal, and S. Sundareasan. The Role of Meso-Scale Structures in Rapid Gas-Solid Flows. J. Fluid Mech. 445 (2001): 151-185.

Adel-Al, M.F., D.A. Saville, and S. Sundaresan. The Effect of Static Electrification on Gas-Solid Flows in Vertical Risers. Ind. Eng. Chem. Res. 41 (2002): 6224-6234.

Andreux, R., T. Gauthier, J. Chaouki, and O. Simonin. New Description of Fluidization Regimes. AIChE J. 51 (2005): 1125-1130.

Avidan, A.A. and J., Yerushalmi. Bed Expansion in High Velocity Fluidization. Powder Technology 32(2) (1982): 223-232.

Avidan, A., and J. Yerushalmi. Solids Mixing in an Expanded Top Fluid Bed. AIChE J. 31 (1985): 835-841.

Benyahia, S., H. Arastoopour, T.M. Knowlton, and H. Massah. Simulation of Particles and Gas Flow Behavior in the Riser Section of a Circulating Fluidized Bed using the Kinetic Theory Approach for the Particulate Phase. Powder Technology 112 (2000): 24-33.

Berruti, F., J. Chaouki, L. Godfroy, T.S. Pugsley, and G.S. Patience. Hydrodynamics of Circulating Fluidized Bed Risers: A Review. Canadian J. Chem. Eng. 73 (1995): 579.

Bi, H.T., and J.R. Grace. Effects of Measurement Method on Velocities used to Demarcate Transition to Turbulent Fluidization. Chemical Engineering Science 57 (1995): 261.

Bi, H.T., N. Ellis, I.A. Abba, and J.R. Grace. A State-of-the-Art Review of Gas-Solid Turbulent Fluidization. Chemical Engineering Science 57 (2000): 4789-4825.

Bouillard, J.X., R.W. Lyczkowski, and D. Gidaspow. Porosity Distributions in a Fluidized Bed with an Immersed Obstacle. AIChE J. 35(6) (1989): 908-922.

Bryan, A., Kashiwa B., and B.VanderHeyden. An Extended K-Epsilon Turbulence Model for Multiphase Flow. University of Florida, Gainesville, FL: Thirteenth U.S. National Congress of Applied Mechanics, 1998.

Campbell, C.S., and D.G. Wang. Particle Pressures in Gas Fluidized Beds. J. Fluid Mech. 227 (1991): 495-508.

Chapman, S. and T.G. Cowling. The Mathematical Theory of Non-Uniform Gases. Third edition. New York: Cambridge University Press, 1970.

Cody, G.D., D.J. Goldfarb, G.V. Storch Jr., and A.N. Norris. Particle Granular Temperature in Gas Fluidized Beds. Powder Technology 87 (1996): 211-232.

Ding, J. and D. Gidaspow. A Bubbling Fluidization Model using Kinetic Theory of Granular Flow. AIChE J. 36 (1990): 523-538.

Ding, J., and D. Gidaspow. A Semi-Empirical Model for Fluidization of Fine Particles. Indian Chem. Engr. 36(4) (1994): 139-150.

Du, B., W. Warsito, and L.S. Fan. Bed Nonhomogeneity in Turbulent Gas-Solid Fluidization. AIChE J. 49 (2003): 1109-1126.

Du, B., L.S. Fan, F. Wei, and W. Warsito. Gas and Solids Mixing in a Turbulent Fluidized Bed. AIChE J. 48 (2002): 1896-1909.

Frankel N.A., A. Acrivos. On the Viscosity of a Concentrated Suspension of Solid Spheres. Chemical Engineering Science 22 (1967): 847-853.

Gelderbloom, S.J., D. Gidaspow, and R.W. Lyczkowski. CFD Simulations of Bubbling/Collapsing Fluidized Beds for Three Geldart Groups. AIChE J. 49 (2003): 844-858.

Gidaspow, D. and B. Ettehadieh. Fluidization in Two Dimensional Beds with a Jet. Part II. Hydrodynamic Modeling. I&EC Fundamentals 22 (1983): 193-201.

Gidaspow, D., M. Syamlal, J.L. Austing, A.J. Tulis, W.K. Samida and W. Comeyne. The Large-Scale Detonation of a Particulate Pyrotechnic in a Computer Modeled Dispersed State. Proceedings of the Ninth Pyrotechnics Symposium, IIT Research Institute (Aug. 1984): 193-226.

Gidaspow, D., Y.P. Tsuo, J.L. Austing, A.J. Tulis and W. Comeyne. Simulation of Pyrotechnic Powder Distributions Using a Hydrodynamic Multiparticle-Size Computer Model. Proceedings of the Eleventh International Pyrotechnics Seminar, IIT Research Institute (1986): 227-242.

Gidaspow, D., M. Syamlal, J.L. Austing, A.J. Tulis, E. Buhrmaster and D.L. Heberlein. The Explosive Dissemination of Particulate Pyrotechnic and Explosive Powders. Thirteenth International Pyrotechnics Seminar, IIT Research Institute (1988): 347-373.

Gidaspow, D. and D.F. Aldis. Hydrodynamics of Dispersed Particulate Detonation in Combustion and Detonation Phenomena. 19th International Annual Conference of ICT, Fraunhofer-Institut Fur Chemische Technologie, Karlsruhe, Germany (1988): 33-14.

Gidaspow, D. Multiphase Flow and Fluidization: Continuum and Kinetic Theory Descriptions. California: Academic Press, 1994.

Gidaspow, D., and L. Huilin. Collisional Viscosity of FCC Particles in a CFB. AlChE J. 42 (1996): 2503-2510.

Gidaspow, D., L. Huilin. A Comparison of Gas-Solid and Liquid-Solid Fluidization using Kinetic Theory and Statistical Mechanics. Fluidization IX (1998): 661.

Gidaspow, D., and L. Huilin. Equation of State and Radial Distribution Functions of FCC Particles in a CFB. AIChE J. 44 (1998): 279-293.

Gidaspow, D., L. Huilin and R. Mostofi. Large Scale Oscillations or Gravity Waves in a Riser and Bubbling Beds. Fluidization X (2001): 317-323.

Gidaspow, D., and R. Mostofi. Maximum Carrying Capacity and Granular Temperature of A, B and C Particles. AIChE J. 49 (2003): 831-843.

Gidaspow, D., and L. Huilin. Hydrodynamics of Binary Fluidization in a Riser: CFD Simulation using Two Granular Temperatures. Chemical Engineering Science 58 (2003): 3777.

Gidaspow, D., J. Jung and R.K. Singh. Hydrodynamics of Fluidization using Kinetic Theory: an Emerging Paradigm 2002 Flour-Daniel Lecture. Powder Technology 148 (2004): 123-141.

Gidapow, D., H. Arastroopour, R. Pfeffer, V.N. Vasishta, R.J. Singh, and J. Jung. Fluidization of Nanoparticle. NSF Nanoscale Science and Engineering Grantee Conference (13-15 December 2004): 274.

Gidaspow D. and V. Jiradilok. Explosive Dissemination of Particles. Orlando, Florida: Tutorial at Obscurants, 2005.

Goldschmidt, M.J.V., J.A.M. Kuipers and W.P.M. van Swaaij. Hydrodynamic Modelling of Dense Gas-Fluidized Beds using the Kinetic Theory of

Granular Flow: Effect of Restitution Coefficient on Bed Dynamics. Chemical Engineering Science 56 (2001): 571-578.

Grace, J. R. Reflections on Turbulent Fluidization and Dense Suspension Upflow. Powder Technology 113 (2000): 242-248.

Guo Y. and D. Gidaspow. 75 μm FCC Particle Surface Charge in the CFB at IIT. Illinois Institute of Technology: Revised Report, 1997.

Hakim, L.F., J.L. Portman, M.D. Casper, A.W. Weimer. Aggregation Behavior of Nanoparticles in Fluidized Beds. Powder Technology 160 (2005): 149 – 160.

Hinze, H. O. Turbulence. New York: McGraw-Hill, 1965.

Hrenya, C.M., and J.L. Sinclair. Effects of Particle-Phase Turbulence in Gas-Solid Flows. AIChE J. 43 (1997): 853-869.

Huilin, L., D.Gidaspow, J. Bouillard and L. Wentie. Hydrodynamic Simulation of Gas–Solid Flow in a Riser using Kinetic Theory of Granular Flow. Chemical Engineering Journal 95 (2003): 1–13.

Jackson, R. Hydrodynamic Stability of Fluid-Particle System. J.F. Davidson, R. Cliff and D. Harrison, Fluidization, 47-72. New York: Academic Press, 1985.

Jackson, R. The Dynamics of Fluidized Particles. New York: Cambridge University Press, 2000.

Jenkins, J.T. and S.B. Savage. A Theory for the Rapid Flow of Identical, Smooth, Nearly Elastic, Spherical Particles. J. Fluid Mech.130 (1983): 187 – 202.

Jayaswal, U.K., D. Gidaspow, J.L. Austing and A.J. Tulis. Hydrodynamics of Particulate Dissemination from a Disseminator into a Bag. Proceedings of

the 15th International Pyrotechnics Seminar, IIT Research Institute (1990): 493-514.

Jayaswal, U.K. Hydrodynamics of Multiphase Flows: Seperartioc, Dissemination and Fluidization. Doctoral dissertation, Department of Chemical and Environmental Engineering, Faculty of Engineering, Illinois Institute of Technology, 1991.

Jiradilok, V., D. Gidaspow, S. Damronglerd, W. J. Koves, R. Mostofi, and S. Nitivattananon. Kinetic Theory Based CFD Simulation of Turbulent Fluidization of FCC Particles in a Riser. Cincinnati, OH: AIChE annual Meeting, 31 October 2005.

Jiradilok, V. Hydrodynamics of Fluidization of FCC and Nanoparticles. Doctoral dissertation, Department of Chemical Technology, Faculty of Science Chulalongkorn University, 2005.

Johnson, P.C. and R. Jackson. Frictional-Collisional Constitutive Relations for Granular Materials, with Application to Plane Shearing. J. Fluid Mech. 176 (1987): 67-93.

Jung J. and D. Gidaspow. Fluidization of Nano-Size Particles. Journal of Nanoparticle Research 4 (2002): 483-497.

Jung, J., D.Gidaspow, and I. K. Gamwo. Measurement of Two Kinds of Granular Temperatures, Stresses, and Dispersion in Bubbling Beds. Ind. Eng. Chem. Res. 44 (2005): 1329-1341.

Jung, J., D.Gidaspow, and I. K. Gamwo. Bubble Computation, Granular Temperatures and Reynolds Stresses. Chem. Eng. Commun. (2005): in review.

Kalra, J. Fluidization of Silica Nano-Size Particles in Circulating and Two Dimensional Fluidized Beds, Master thesis, Department of Chemical and Environmental Engineering, Faculty of Engineering, Illinois Institute of Technology, 2005.

Kim, J., P. Moin, and R. Moser. Turbulence Statistics in Fully Developed Channel Flow at Low Reynolds Number. J. Fluid Mech. 177 (1987): 133-166.

Kitoh, O. Experimental Study of Turbulent Swirling Flow in a Straight Pipe. J. Fluid Mech. 225 (1991): 445-479.

Koenigsdorff, R., and J., Werther. Gas and Solid Mixing in and Flow Structure Modeling of the Upper Dilute Zone of a Circulating Fluidized Bed. Powder Technology 82 (1995): 317-329.

Kunii, D. and O. Levenspiel. Fluidization Engineering Second edition. Boston: Butterworth-Heinemann, 1991.

Longmire, E.K., and J.K. Eaton. Structure of a Particle-Laden Round Jet. J. Fluid Mech. 236 (1992): 217 – 257.

Lun, C.K.K., S.B. Savage, D.J. Jeffrey, and N. Chepurniy. Kinetic Theories for Granular Flows: Inelastic Particles in Couette Flow and Singly In elastic Particles in a General Flow Field. J. Fluid Mech. 140 (1984): 223-256.

Lyczkowski, R.W., D. Gidaspow, C.W. Solibrig and E.C.Hudhes. Characteristics and Stability Analysis of Transient One-dimensional Two-Phase Flow Equations and their Finite Difference Approximations. Nuclear Science and Eng. 66 (1978): 378-396.

Makkawi, Y. T. and P.C. Wright. Fluidization Regimes in a Conventional Fluidized Bed Characterized by means of Electrical Capacitance Tomography. Chemical Engineering Science 57 (2002): 2411.

Mansour, N. N., J. Kim and P. Moin. Reynolds-Stress and Dissipation-Rate Budgets in a Turbulent Channel Flow. J. Fluid Mech. 194 (1988): 15-44.

Mathiesen, V., T. Solberg and B.H. Hjertager. An Experimental and Computational Study of Multiphase Flow Behavior in a Circulating Fluidized Bed. Int. J. Multiphase Flow 26 (2000): 387.

Matonis, D., D. Gidaspow and M. Bahary. CFD Simulation of Flow and Turbulence in a Slurry Bubble Column. AIChE J. 48 (2002): 1413-1429.

Matsen, J. M. Mechanisms of Choking and Entrainment. Powder Technology 32 (1982): 21.

Miller A., and D. Gidaspow. Dense Vertical Gas-Solid Flow in a Pipe. AlChE J. 38**,** (1992): 1801-1815.

Mori, S., O. Hashimoto, T. Haruta, I. Yamada, M. Kuwa, Y. Saito. Fundamentals of Turbulent Fluidized Catalytic Reactor. Fluidization VI (1989): 49.

Mudde, R.F., D.J. Lee, J. Reese, and L.S. Fan. Role of Coherent Structures on Reynolds Stresses in a 2-D Bubble Column. AIChE J. 43 (1997): 913-926.

Mukherjee, A. Characterization and Separation of Charged Particles. Doctoral dissertation, Department of Chemical and Environmental Engineering, Faculty of Engineering, Illinois Institute of Technology, 1987.

Nakamura , K. and C.E. Capes. Vertical Pneumatic Conveying of Binary Particle Mixtures. Fluidization Technology. Vol. II. New York: 1976.

Neri, A. and D. Gidaspow. Riser Hydrodynamics: Simulation Using Kinetic Theory. AIChE J. 46 (2000): 52-67.

Neri, A., T.E. Ongaro, G. Macedonio and D. Gidaspow. Multiparticle Simulation of Collapsing Volcanic Columns and Pyroclastic Flow. J. Geophys. Res. 108 (2003): (B4), 2202, doi:10.1029/2001JB000508

Pan, Y., M.P. Dudukovic, and M. Chang. Numerical Investigation of Gas-Driven Flow in 2-D Bubble Columns. AIChE J. 46 (2000): 434-449.

Pape, R., and D. Gidaspow. Numerical Simulation of Intense Reaction Propagation in Multiphase Systems. AIChE J. 44(2) (1998): 294-309.

Polashenski, W., and J. C. Chen. Normal Solid Stress in Fluidized Beds. Powder Technology 90 (1997): 13-27.

Polashenski, W., and J. C. Chen. Measurement of Particle Phase Stresses in Fast Fluidized Beds. Ind. Eng. Chem. Res. 38 (1999): 705-713.

Potter, O. E. Fluidization. Academic Press, 1971.

Ranade V.V. Computational Flow Modeling for Chemical Reactor Engineering. San Diego, Calif.; London: Academic Press, 2002.

Rowe, P.H. Experimental Properties of Bubbles. J.F. Davidson and D. Harrison, Fluidization. Chapter 4. New York: Academic Press, 1971.

Roy, S., A. Kemoun, M.H. Al-Dahhan, and M.P. Dudukovic. Experimental Investigation of Hydrodynamics in a liquid-solid riser. AlChE J. 51 (2005): 802-835.

Rhodes M. What is Turbulent Fluidization. Powder Technology 88 (1996): 3.

Savage, S. B. Granular Flows at High Shear Rates. Meyer, R. E, In Theory of Dispersed Multiphase Flow, 339. New York: Academic Press, 1983.

Savage, S.B. Streaming Motions in a Bed of Vibrationally Fluidized Dry Granular Material. J. Fluid Mech. 194 (1988): 457 – 478.

Simonin, O. Modeling and Simulation of Industrial Gas-Solid Flows: from Dilute to Dense Particle Laden Flows. 4th ASME/ JSME Joint Fluids Engineering Conference, 6 – 10 July 2003.

Sinclair, J. L. and R. Jackson. Gas-Particle Flow in a Vertical Pipe with Particle-Particle Interactions. AIChE J. **35** (1989): 1473-148.

Soo, S.L. Fluid Dynamics of Multiphase Systems. Waltham: Blaisdell Publ. Co., 1967.

Strumendo, M. Method of Moments for Gas-Solids Flows. Doctoral dissertation, University of Padova, 2003.

Strumendo, M., D. Gidaspow and P. Canu. Method of Moments for Gas-Solids: Application to the Riser. China: 8th Circulating Fluidized Bed Conference, 2005.

Sun B., D. Gidaspow, R. Pape and W. Comeyne. The Numerical Modeling of an Explosive Dissemination System. Proceedings of the Twentieth International Pyrotechnics Seminar, IIT Research Institute (1994): 1061-1080.

Sun, B. and D. Gidaspow. Computation of Circulating Fluidized-Bed Riser Flow for the Fluidization VIII Benchmark Test. Ind. Eng. Chem. Res. 38 (1999): 787-792.

Syamlal, M., and D. Gidaspow. Hydrodynamics of Fluidization: Prediction of Wall-to-Bed Heat Transfer Coefficients. AIChE J. 31 (1985):127-135.

Syamlal, M., W. Rogers, and T.J. O'Brien. MFIX Documentation Theory Guide DOE/METC-94/1004, NTIS/DE94000087 Morgantown: 1993.

Syamlal, M. MFIX Documentation - Numerical Technique, DOE/MC31346-5824, DE98002029 Morgantown: 1998.

Syamlal, M. Multiphase Hydrodynamics of Gas-Solid Flow. Doctoral dissertation, Department of Chemical and Environmental Engineering, Faculty of Engineering, Illinois Institute of Technology, 1985.

Tartan, M.and D.Gidaspow. Measurement of Granular Temperature and Stresses in Risers. AIChE J. 50 (2004): 1760-1775.

Taylor, G. I. Diffusion by Continuous Movements. Proc. London Math. Soc. 20 (1921): 196.

Tennekes, H., and J. L. Lumley. A First Course in Turbulence. Cambridge, MA: MIT Press, 1972.

Therdthianwong, A., P. Pantaraks and S. Therdthianwong. Modeling and Simulation of Circulating Fluidized Bed Reactor with Catalytic Ozone Decomposition Reaction. Powder Technology 133 (2003): 1-14.

Thiel, W. J., and O. E. Potter. The Mixing of Solids in Slugging Gas Fluidized Beds. AIChE J. 24 (1978): 561-569.

Tolstoy, I., Wave Propagation, McGraw-Hill, New York (1973).

Tsinontides, S.C. and R. Jackson. The Mechanics of Gas Fluidized Beds with an Interval of Stable Fluidization. J. Fluid Mech. 255 (1993): 237-274.

Tsukada, M., D. Nakanishi and M. Horio. The Effect of Pressure on the Phase Transition from Bubbling to Turbulent Fluidization. International Journal of Multiphase Flow 19 (1993): 27.

Tsukada, M., D. Nakanishi and M. Horio. Effect of Pressure on Transport Velocity in a Circulating Fluidized Bed. Circulating Fluidized Bed Technology IV (1994): 209.

Tuso, Y. P. and D. Gidaspow. Compuatation of Flow Patterns in Circulating Fluidzed Beds. AIChE J. 36 (1990): 885-896.

Valentine, G.A., and K.H. Wohletz. Numerical Models of Plinian Eruption Columns and Pyroclastic flows. J. Geophys. Res. 94(B2) 10.1029/88JB03773 (1989): 1867-1887.

Vasishta, V.N. Hydrodynamics of Fluidization and Settling of Silica Nanoparticles. Master thesis, Department of Chemical and Environmental Engineering, Faculty of Engineering, Illinois Institute of Technology, 2004.

Wei, F., W. Chen, Y. Jin, and Z. Q. Yu. Lateral and Axial Mixing of the Dispersed Particles in CFB. J. Chem. Eng. Jpn. 28 (1995): 506.

Wei, F., Y.Cheng, Y. Jin, and Z. Q. Yu. Axial and Lateral Dispersion of Fined Particles in a Binary-Solid Riser. Can. J. of Chem. Eng. 76 (1998): 19.

Wei, F., H. Lin, Y. Cheng, Z. Wang, and Y. Jin. Profiles of Particle Velocity and Solids Fraction in a High-Density Riser. Powder Technology 100 (1998): 183-189.

Wohletz, K.H., T.R. McGeetchin, M.T. Sandford II, and E.M. Jones. Hydrodynamic aspects of Caldera-Forming Eruption: Numerical Models. J. Geophys. Res. 89 (1984): 8269-8285.

Yang, N., W. Wang, W. Ge, L. Wang, and J. Li. Simulation of Heterogeneous Structure in a Circulating Fluidized-Bed Riser by Combining the Two-Fluid Model with EMMS Approach. Ind. Eng. Chem. Res. 43 (2004): 5548-5561.

Yang W.C., D.C. Chitester, R.M. Kornosky, D.L. Keairns. A Generalized Methodology for Estimating Minimum Fluidization Velocity at Elevated Pressure and Temperature. AIChE J. 31(7) (1985): 1086-1092.

Yu, Q., R.N. Dave, C. Zhu, J.A. Quevedo, R. Pfeffer. Enhanced Fluidization of Nanoparticles in an Oscillating Magnetic Field. AIChE J. 51(7) (2005): 1971-1979.

Zhu C., Q. Yu, R.N. Dave, R. Pfeffer. Gas Fluidization Characteristics of Nanoparticle Agglomerates. AIChE J. 51(2) (2005): 426-439.

สถาบันวิทยบริการ
จุฬาลงกรณ์มหาวิทยาลัย

APPENDICES

สถาบันวิทยบริการ
จุฬาลงกรณ์มหาวิทยาลัย

APPENDIX A

NUMERICAL TECHNIQUE OF HYDRODYNAMIC MODEL B

สถาบันวิทยบริการ
จุฬาลงกรณ์มหาวิทยาลัย

The Finite Difference Equations

The solution produce uses the implicit Multi Field (IMF) numerical technique. The computations are carried out using a two-dimensional Eulerian mesh of non-uniform size finite-difference computational cells. In Cartesian coordinates (x, y) these cells are rectangles with dimensions δx_i and δy_j; in cylindrical coordinates (r, z), these cells are toroids about the z-axis with rectangular cross-sections and dimensions of δr_i and δz_j. A typical computational cell (i, j), in Cartesian coordinates is shown in Figure A 1. The indexes i and j (or I and J) that label cell (i, j) count cell centers in the –x or –r direction and the –y or –z direction, respectively, and assume only positive integer values. The half-integer indexes denote cell edge positions. The scalar variables $(\varepsilon_k, \rho_k, P_k, T_k, H_k)$ are located at the cell center and the vector variables $(v_k, [\tau_k])$ at the cell boundaries.

The finite difference approximations to the hydrodynamic equations form a system of nonlinear algebraic equations quantities at time $t = (n+1)\delta t$, where n is zero or a position integer and δt is the time increment by which these quantities advance each computational cycle.

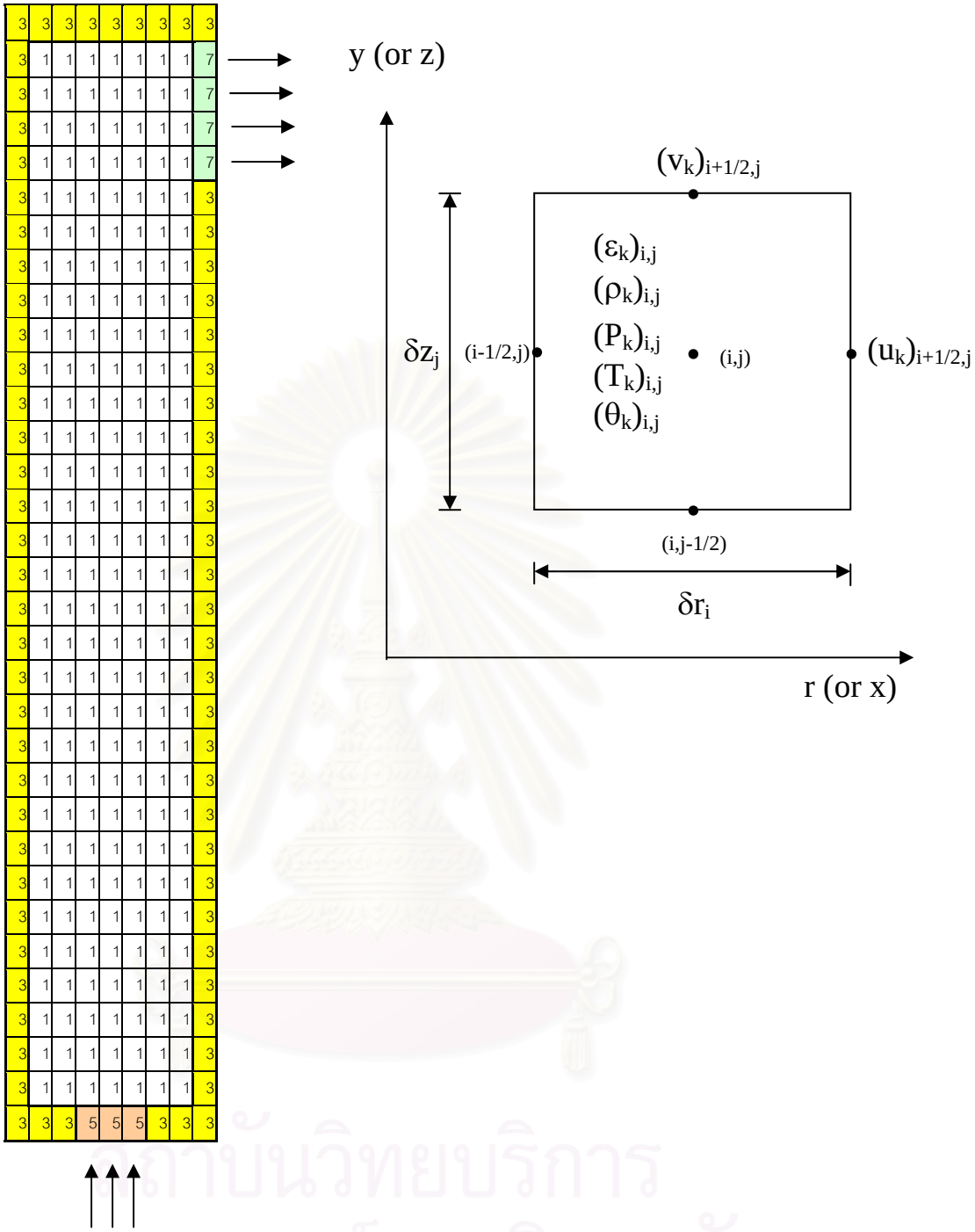

Figure A.1 The computational mesh

1. **Averaging Process.** Quantities in the finite difference equations required at spatial locations other than where they are defined are obtained by weighted averaging

a) Cell centered Quantities

The cell centered properties Ψ are defined at the cell center at (i, j). At other locations averaging is used as follows,

$$\Psi_{i+\frac{1}{2},j} = \frac{1}{2\delta r_{i+\frac{1}{2}}}\left(\delta r_{i+1}\Psi_{i,j} + \delta r_i \Psi_{i+1,j}\right) \tag{A.1}$$

$$\Psi_{i,j+\frac{1}{2}} = \frac{1}{2\delta z_{j+\frac{1}{2}}}\left(\delta z_{i+1}\Psi_{i,j} + \delta z_i \Psi_{i,j+1}\right) \tag{A.2}$$

$$\Psi_{i+\frac{1}{2},j+\frac{1}{2}} = \frac{1}{4\delta r_{i+\frac{1}{2}}\delta z_{j+\frac{1}{2}}}\left(\delta r_{i+1} z_{J+1}\Psi_{i,j}\right.$$

$$\left. + \delta r_i \delta z_{j+1}\Psi_{i+1,j} + \delta r_{i+1}\delta z_j \Psi_{i,j+1} + \delta r_i \delta z_j \Psi_{i+1,j+1}\right) \tag{A.3}$$

b) Boundary Centered Quantities

The boundary centered quantities in –x direction is u which is defined at $i, j+\frac{1}{2}$. The averaging is as follows,

$$u_{i,j} = \frac{1}{2}\left[u_{i+\frac{1}{2},j} + u_{i+\frac{1}{2},j}\right] \tag{A.4}$$

$$u_{i+\frac{1}{2},j+\frac{1}{2}} = \frac{1}{2\delta z_{j+\frac{1}{2}}}\left[\delta z_{j+1} u_{i+\frac{1}{2},j} + \delta z_j u_{i+\frac{1}{2},j+1}\right] \tag{A.5}$$

$$u_{i,j+\frac{1}{2}} = \frac{1}{4\delta z_{j+\frac{1}{2}}}\left[\delta z_{j+1}\left(u_{i-\frac{1}{2},j} + u_{i+\frac{1}{2},j}\right) + \delta z_j\left(u_{i-\frac{1}{2},j+1} + u_{i+\frac{1}{2},j+1}\right)\right] \tag{A.6}$$

The boundary centered quantities in –y direction is v which is defined at $i+\frac{1}{2}, j$. The averaging is as follows,

$$v_{i,j} = \frac{1}{2}\left[v_{i+\frac{1}{2},j} + v_{i+\frac{1}{2},j} \right] \tag{A.7}$$

$$v_{i+\frac{1}{2},j+\frac{1}{2}} = \frac{1}{2\delta r_{j+\frac{1}{2}}}\left[\delta r_{j+1} v_{i+\frac{1}{2},j} + \delta r_j v_{i+\frac{1}{2},j+1} \right] \tag{A.8}$$

$$v_{i,j+\frac{1}{2}} = \frac{1}{4\delta r_{j+\frac{1}{2}}}\left[\delta r_{j+1}\left(v_{i-\frac{1}{2},j} + v_{i+\frac{1}{2},j} \right) + \delta r_j \left(v_{i-\frac{1}{2},j+1} + v_{i+\frac{1}{2},j+1} \right) \right] \tag{A.9}$$

These finite difference equations are written in cylindrical coordinate (r,z) for generality. Some coordinate system dependent terms will now be defined. For Cartesian coordinates,

$$R_i = R_{j+\frac{1}{2}} = 1 \tag{A.10}$$

and, for cylindrical coordinate

$$R_1 = R_{st} - \frac{1}{2}\delta r_1 \tag{A.11}$$

$$R_i = R_1 + \sum_{m=1}^{i-1} \delta r_{m+\frac{1}{2}} \quad i = 2,3,\ldots,i_{\max} \tag{A.12}$$

$$R_{\frac{3}{2}} = R_{st} \tag{A.13}$$

$$R_{i+\frac{1}{2}} = R_{\frac{3}{2}} + \sum_{m=2}^{i} \delta r_m \quad i = 2,3,\ldots,i_{\max} \tag{A.14}$$

$$\left(\frac{\delta R}{\delta r}\right)_m = \frac{R_{m+\frac{1}{2}} - R_{m-\frac{1}{2}}}{\delta r_m} = \begin{cases} 0 & Cartesian \quad Coordinates \\ 1 & Cylindrical \quad Coordinates \end{cases} \tag{A.15}$$

Geometrically, in cylindrical coordinate, R_i is the r coordinate of the center of cell (i, j) and $R_{i+\frac{1}{2}}$ is the r coordinate of points on the right edge of this cell, where r is measured from the left edge of the i =2 column of cells.

2. **Continuity Equations.** The continuity equations is differenced fully implicitly as follows,

$$(\varepsilon_k \rho_k)_{i,j}^{n+1} = (\varepsilon_k \rho_k)_{i,j}^{n} - \frac{\delta t}{R_i \delta r_i} \langle R(\varepsilon_k \rho_k) u_k \rangle_{i,j}^{n+1} - \frac{\delta t}{\delta z_j} \langle (\varepsilon_k \rho_k) v_k \rangle_{i,j}^{n+1} \qquad \text{(A.16)}$$

The donor cell differencing aids computational stability without the introduction of explicit artificial viscosity.

3. **Momentum Equations.** The momentum equations are differenced over a staggered mesh (Figure 4) using a scheme in which the convection terms are treated explicitly and all other terms are treated implicitly. The difference equations are,

$$\begin{aligned}(\varepsilon_k \rho_k u_k)_{i+\frac{1}{2},j}^{n+1} &= \left(\overline{\varepsilon_k \rho_k u_k}\right)_{i+\frac{1}{2},j} - \frac{\delta t}{\delta r_{i+\frac{1}{2}}} \left((p_k)_{i+1,j}^{n+1} - (p_k)_{i,j}^{n+1}\right) \\ &\quad - (w_k)_{i+\frac{1}{2},j}^{n+1} g_r \delta t + \delta t \sum_{\substack{l=f,1 \\ l \neq k}}^{N} (\beta_{lk})_{i+\frac{1}{2},j}^{n} \left((u_l)_{i+\frac{1}{2},j}^{n+1} - (u_k)_{i+\frac{1}{2},j}^{n+1} \right) \\ &\quad + \frac{\delta t}{\delta r_{i+\frac{1}{2}}} \left((\tau_{ck})_{i+1,j}^{n+1} - (\tau_{ck})_{i,j}^{n+1}\right) \qquad \text{(A.17)}\end{aligned}$$

$$\begin{aligned}(\varepsilon_k \rho_k v_k)_{i,j+\frac{1}{2}}^{n+1} &= \left(\overline{\varepsilon_k \rho_k v_k}\right)_{i,j+\frac{1}{2}} - \frac{\delta t}{\delta z_{j+\frac{1}{2}}} \left((p_k)_{i+1,j}^{n+1} - (p_k)_{i,j}^{n+1}\right) \\ &\quad - (w_k)_{i,j+\frac{1}{2}}^{n+1} g_z \delta t + \delta t \sum_{\substack{l=f,1 \\ l \neq k}}^{N} (\beta_{lk})_{i,j+\frac{1}{2}}^{n} \left((v_l)_{i,j+\frac{1}{2}}^{n+1} - (v_k)_{i,j+\frac{1}{2}}^{n+1} \right) \\ &\quad + \frac{\delta t}{\delta z_{j+\frac{1}{2}}} \left((\tau_{ck})_{i,j+1}^{n+1} - (\tau_{ck})_{i,j}^{n+1}\right) \qquad \text{(A.18)}\end{aligned}$$

where for fluid phase $w_f = \rho_f$ and $\tau_{cf} = 0$, and for particulate phases (k=1,…,N),

$$w_k = \frac{\varepsilon_k}{\varepsilon_f}\left(\rho_k - \sum_{l=f,1}^{N} \varepsilon_l \rho_l\right) \tag{A.19}$$

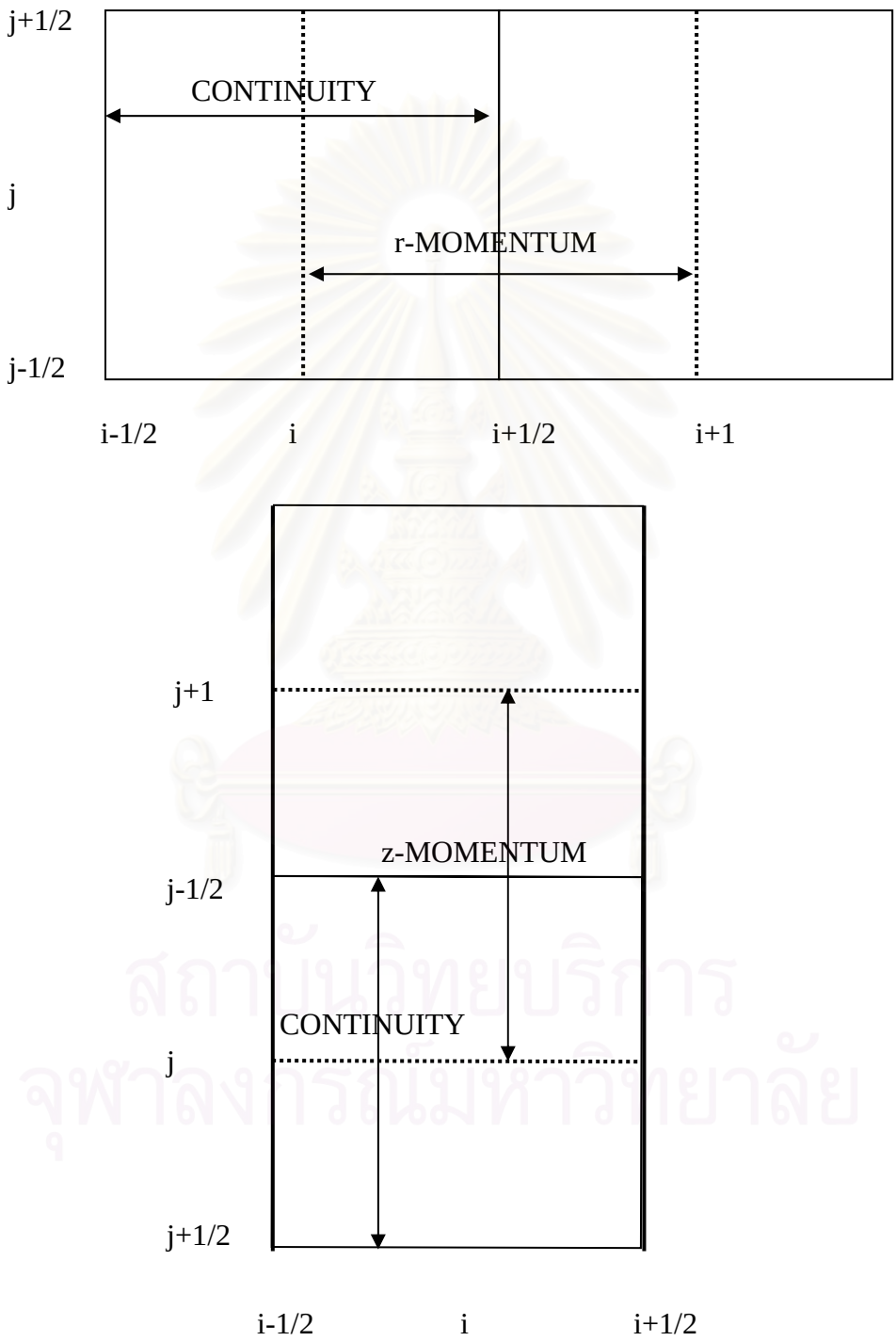

Figure A.2 The staggered computational mesh for momentum equations

All the explicit terms are lumped into subroutine “TILDE” quantities as shown below,

$$\left(\overline{\varepsilon_k \rho_k u_k}\right)_{i+\frac{1}{2},j} = \left(\varepsilon_k \rho_k u_k\right)^n_{i+\frac{1}{2},j} - \frac{\delta t}{R_{i+\frac{1}{2}} \delta r_{i+\frac{1}{2}}} \left\langle R\left(\varepsilon_k \rho_k u_k\right) u_k \right\rangle^n_{i+\frac{1}{2},j} - \frac{\delta t}{\delta z_j} \left\langle \left(\varepsilon_k \rho_k u_k\right) v_k \right\rangle^n_{i+\frac{1}{2},j}$$

$$+ \frac{\delta t}{R_{i+\frac{1}{2}} \delta r_{i+\frac{1}{2}}} \left[R_{i+1} \left(\tau_{krr}\right)^n_{i+1} - R_i \left(\tau_{krr}\right)^n_{i,j} \right]$$

$$+ \frac{\delta t}{\delta z_j} \left[\left(\tau_{krz}\right)^n_{i+\frac{1}{2},j+\frac{1}{2}} - \left(\tau_{krz}\right)^n_{i+\frac{1}{2},j-\frac{1}{2}} \right] - \frac{\delta t}{R_{i+\frac{1}{2}}} \left(\tau_{ko}\right)^n_{i+\frac{1}{2},j} \left(\frac{\delta R}{\delta r}\right)_{i+\frac{1}{2},j} \qquad \text{(A.20)}$$

$$\left(\overline{\varepsilon_k \rho_k v_k}\right)_{i,j+\frac{1}{2}} = \left(\varepsilon_k \rho_k v_k\right)^n_{i,j+\frac{1}{2}} - \frac{\delta t}{R_i \delta r_i} \left\langle R\left(\varepsilon_k \rho_k v_k\right) u_k \right\rangle^n_{i,j+\frac{1}{2}} - \frac{\delta t}{\delta z_{j+\frac{1}{2}}} \left\langle \left(\varepsilon_k \rho_k v_k\right) v_k \right\rangle^n_{i,j+\frac{1}{2}}$$

$$+ \frac{\delta t}{R_i \delta r_i} \left[R_{i+\frac{1}{2}} \left(\tau_{krz}\right)^n_{i+\frac{1}{2},j+\frac{1}{2}} - R_{i-\frac{1}{2}} \left(\tau_{krz}\right)^n_{i-\frac{1}{2},j+\frac{1}{2}} \right]$$

$$+ \frac{\delta t}{\delta z_{j+\frac{1}{2}}} \left[\left(\tau_{kzz}\right)^n_{i,j+1} - \left(\tau_{kzz}\right)^n_{i,j} \right] \qquad \text{(A.21)}$$

4. Energy Equations

(a) Fluid Phase:

$$\left(\varepsilon_f \rho_f H_f\right)^{n+1}_{i,j} = \left(\varepsilon_f \rho_f H_f\right)^n_{i,j} + \left(\overline{\varepsilon_f \rho_f H_f}\right)_{i,j} + \delta t \sum_{k=1}^{N} \left(h_{vk}\right)^n_{i,j} \left(T_k - T_f\right)^{n+1}_{i,j}$$

$$+ \delta t \sum_{k=1}^{N} \left(\beta_{kf}\right)^n_{i,j} \left[\left(\left(u_k\right)^n_{i,j} - \left(u_f\right)^n_{i,j}\right)^2 + \left(\left(v_k\right)^n_{i,j} - \left(v_f\right)^n_{i,j}\right)^2 \right] \qquad \text{(A.22)}$$

(b) Solids Phase:

$$\left(\varepsilon_k \rho_k H_k\right)^{n+1}_{i,j} = \left(\varepsilon_k \rho_k H_k\right)^n_{i,j} + \left(\overline{\varepsilon_k \rho_k H_k}\right)_{i,j} + \delta t \left(h_{vk}\right)^n_{i,j} \left(T_f - T_k\right)^{n+1}_{i,j} \qquad \text{(A.23)}$$

“TILDE” quantities are given by,

$$\left(\overline{\varepsilon_f \rho_f H_f}\right)_{i,j} = -\frac{\delta t}{R_i \delta r_i} \left\langle R\left(\varepsilon_f \rho_f\right)^{n+1} \overline{H}_f \left(u_f\right)^{n+1} \right\rangle_{i,j} - \frac{\delta t}{\delta z_j} \left\langle \left(\varepsilon_f \rho_f\right)^{n+1} \overline{H}_f \left(v_f\right)^{n+1} \right\rangle_{i,j}$$

$$+\left(\left(p_f\right)_{i,j}^{n+1}-\left(p_f\right)_{i,j}^{n}\right)+\frac{\delta t}{R_i\delta r_i}\left(u_f\right)_{i,j}^{n+1}\left(R_{i+\frac{1}{2}}\left(p_f\right)_{i+\frac{1}{2},j}^{n+1}-R_{i-\frac{1}{2}}\left(p_f\right)_{i-\frac{1}{2},j}^{n+1}\right)$$

$$+\frac{\delta t}{\delta z_j}\left(v_f\right)_{i,j}^{n+1}\left(\left(p_f\right)_{i,j+\frac{1}{2}}^{n+1}-\left(p_f\right)_{i,j-\frac{1}{2}}^{n+1}\right)$$

$$+\frac{\delta t}{R_i\delta r_i}\left[R_{i+\frac{1}{2}}\left(K_f\right)_{i+\frac{1}{2},j}^{n}\frac{\left(\overline{T}_f\right)_{i+1,j}-\left(\overline{T}_f\right)_{i,j}}{\delta r_{i+\frac{1}{2}}}-R_{i-\frac{1}{2}}\left(K_f\right)_{i-\frac{1}{2},j}^{n}\frac{\left(\overline{T}_f\right)_{i,j}-\left(\overline{T}_f\right)_{i-1,j}}{\delta r_{i-\frac{1}{2}}}\right]$$

$$+\frac{\delta t}{\delta z_j}\left[\left(K_f\right)_{i,j+\frac{1}{2}}^{n}\frac{\left(\overline{T}_f\right)_{i,j+1}-\left(\overline{T}_f\right)_{i,j}}{\delta z_{j+\frac{1}{2}}}-\left(K_f\right)_{i,j-\frac{1}{2}}^{n}\frac{\left(\overline{T}_f\right)_{i,j}-\left(\overline{T}_f\right)_{i,j-1}}{\delta z_{j-\frac{1}{2}}}\right]+\delta t\left(\Phi_f\right)_{i,j}^{n}$$

(A.24)

$$\left(\overline{\varepsilon_k\rho_k H_k}\right)_{i,j}=-\frac{\delta t}{R_i\delta r_i}\left\langle R\left(\varepsilon_k\rho_k\right)^{n+1}\overline{H}_k\left(u_k\right)^{n+1}\right\rangle_{i,j}-\frac{\delta t}{\delta z_j}\left\langle\left(\varepsilon_k\rho_k\right)^{n+1}\overline{H}_k\left(v_k\right)^{n+1}\right\rangle_{i,j}$$

$$+\frac{\delta t}{R_i\delta r_i}\left[R_{i+\frac{1}{2}}\left(K_k\right)_{i+\frac{1}{2},j}^{n}\frac{\left(\overline{T}_k\right)_{i+1,j}-\left(\overline{T}_k\right)_{i,j}}{\delta r_{i+\frac{1}{2}}}-R_{i-\frac{1}{2}}\left(K_k\right)_{i-\frac{1}{2},j}^{n}\frac{\left(\overline{T}_k\right)_{i,j}-\left(\overline{T}_k\right)_{i-1,j}}{\delta r_{i-\frac{1}{2}}}\right]$$

$$+\frac{\delta t}{\delta z_j}\left[\left(K_k\right)_{i,j+\frac{1}{2}}^{n}\frac{\left(\overline{T}_k\right)_{i,j+1}-\left(\overline{T}_k\right)_{i,j}}{\delta z_{j+\frac{1}{2}}}-\left(K_k\right)_{i,j-\frac{1}{2}}^{n}\frac{\left(\overline{T}_k\right)_{i,j}-\left(\overline{T}_k\right)_{i,j-1}}{\delta z_{j-\frac{1}{2}}}\right]+\delta t\left(\Phi_k\right)_{i,j}^{n}$$

(A.25)

As mentioned before, the flux quantities denoted by $\langle R\Psi u_k\rangle$ and $\langle\Psi v_k\rangle$ are calculated using donor-cell differencing, where Ψ refers to $(\varepsilon_k\rho_k)$, $(\varepsilon_k\rho_k u_k)$, $(\varepsilon_k\rho_k v_k)$, or $(\varepsilon_k\rho_k\overline{H}_k)$ quantities. The angular brackets represent donor cell differenced quatities as shown below,

$$\left(\Phi_k\right)_{i,j}^{n}=\left(\tau_{krr}\right)_{i,j}^{n}\frac{\left(u_k\right)_{i+\frac{1}{2},j}^{n+1}-\left(u_k\right)_{i-\frac{1}{2},j}^{n+1}}{\delta r_i}+\left(\tau_{kzz}\right)_{i,j}^{n}\frac{\left(v_k\right)_{i,j+\frac{1}{2}}^{n+1}-\left(v_k\right)_{i,j-\frac{1}{2}}^{n+1}}{\delta z_j}$$

$$+\frac{\left(\left(\tau_{krz}\right)_{i,j}^{n}\right)^{2}}{2\left(\mu_{k}\right)_{i,j}^{n}}+\left(\tau_{ko}\right)_{i,j}^{n}\frac{\left(u_{k}\right)_{i,j}^{n+1}}{R_{i}}\left(\frac{\delta R}{\delta r}\right)_{i} \tag{A.26}$$

$$\left\langle R\Psi u_{k}\right\rangle_{m,p}=R_{m+\frac{1}{2}}\left(u_{k}\right)_{m+\frac{1}{2},p}\begin{cases}\left(\Psi\right)_{m,p} & if\left(u_{k}\right)_{m+\frac{1}{2},p}\geq 0\\ \left(\Psi\right)_{m+1,p} & if\left(u_{k}\right)_{m+\frac{1}{2},p}<0\end{cases}$$

$$-R_{m-\frac{1}{2}}\left(u_{k}\right)_{m-\frac{1}{2},p}\begin{cases}\left(\Psi\right)_{m-1,p} & if\left(u_{k}\right)_{m-\frac{1}{2},p}\geq 0\\ \left(\Psi\right)_{m,p} & if\left(u_{k}\right)_{m-\frac{1}{2},p}<0\end{cases} \tag{A.27}$$

$$\left\langle R\Psi v_{k}\right\rangle_{m,p}=\left(v_{k}\right)_{m,p+\frac{1}{2}}\begin{cases}\left(\Psi\right)_{m,p} & if\left(v_{k}\right)_{m,p+\frac{1}{2}}\geq 0\\ \left(\Psi\right)_{m,p+1} & if\left(v_{k}\right)_{m,p+\frac{1}{2}}<0\end{cases}$$

$$-\left(v_{k}\right)_{m,p-\frac{1}{2}}\begin{cases}\left(\Psi\right)_{m,p-1} & if\left(v_{k}\right)_{m,p-\frac{1}{2}}\geq 0\\ \left(\Psi\right)_{m,p} & if\left(v_{k}\right)_{m,p-\frac{1}{2}}<0\end{cases} \tag{A.28}$$

The viscous stress components are calculated with standard differencing, i.e.,

$$\left(\nabla\cdot v_{k}\right)_{i,j}=\frac{R_{i+\frac{1}{2}}\left(u_{k}\right)_{i+\frac{1}{2},j}-R_{i-\frac{1}{2}}\left(u_{k}\right)_{i-\frac{1}{2},j}}{R_{i}\delta r_{i}}+\frac{\left(v_{k}\right)_{i,j+\frac{1}{2}}-\left(v_{k}\right)_{i,j-\frac{1}{2}}}{\delta z_{j}} \tag{A.29}$$

$$\left(\tau_{krr}\right)_{i,j}=2\left(\mu_{k}\right)_{i,j}\left(\frac{\left(u_{k}\right)_{i+\frac{1}{2},j}-\left(u_{k}\right)_{i-\frac{1}{2},j}}{\delta r_{i}}\right)+\left(\xi_{k}-\frac{2}{3}\mu_{k}\right)_{i,j}\left(\nabla\cdot v_{k}\right)_{i,j} \tag{A.30}$$

$$\left(\tau_{kzz}\right)_{i,j}=2\left(\mu_{k}\right)_{i,j}\left(\frac{\left(v_{k}\right)_{i,j+\frac{1}{2}}-\left(v_{k}\right)_{i,j-\frac{1}{2}}}{\delta z_{j}}\right)+\left(\xi_{k}-\frac{2}{3}\mu_{k}\right)_{i,j}\left(\nabla\cdot v_{k}\right)_{i,j} \tag{A.31}$$

$$\left(\tau_{krz}\right)_{i,j}=2\left(\mu_{k}\right)_{i,j}\left(\frac{\left(u_{k}\right)_{i,j+1}-\left(u_{k}\right)_{i,j-1}}{\delta z_{j-\frac{1}{2}}+\delta z_{j+\frac{1}{2}}}+\frac{\left(v_{k}\right)_{i+1,j}-\left(v_{k}\right)_{i-1,j-1}}{\delta r_{i-\frac{1}{2}}+\delta r_{i+\frac{1}{2}}}\right) \tag{A.32}$$

$$\left(\tau_{krz}\right)_{i,j}=2\left(\mu_{k}\right)_{i,j}\left(\frac{\left(u_{k}\right)_{i,j+1}-\left(u_{k}\right)_{i,j-1}}{\delta z_{j-\frac{1}{2}}+\delta z_{j+\frac{1}{2}}}+\frac{\left(v_{k}\right)_{i+1,j}-\left(v_{k}\right)_{i-1,j-1}}{\delta r_{i-\frac{1}{2}}+\delta r_{i+\frac{1}{2}}}\right) \tag{A.33}$$

$$\left(\tau_{krz}\right)_{i+\frac{1}{2},j+\frac{1}{2}} = 2\left(\mu_k\right)_{i+\frac{1}{2},j+\frac{1}{2}}\left(\frac{\left(u_k\right)_{i+\frac{1}{2},j+1}-\left(u_k\right)_{i+\frac{1}{2},j}}{\delta z_{j+\frac{1}{2}}}+\frac{\left(v_k\right)_{i+1,j+\frac{1}{2}}-\left(v_k\right)_{i,j-\frac{1}{2}}}{\delta r_{i+\frac{1}{2}}}\right)$$

(A.34)

$$\left(\tau_{ko}\right)_{i+\frac{1}{2},j} = 2\left(\mu_k\right)_{i+\frac{1}{2},j}\frac{\left(u_k\right)_{i+\frac{1}{2},j}}{R_{i+\frac{1}{2}}}+\left(\xi_k-\frac{2}{3}\mu_k\right)_{i+\frac{1}{2},j}$$

$$\cdot\left(\frac{R_{i+\frac{3}{2}}\left(u_k\right)^n_{i+\frac{3}{2},j}-R_{i-\frac{1}{2}}\left(u_k\right)^n_{i-\frac{1}{2},j}}{2R_{i+\frac{1}{2}}\delta r_{i+\frac{1}{2}}}+\frac{\left(v_k\right)^n_{i+\frac{1}{2},j+\frac{1}{2}}-\left(v_k\right)^n_{i+\frac{1}{2},j-\frac{1}{2}}}{\delta z_j}\right) \qquad \text{(A.35)}$$

$$\left(\tau_{ko}\right)_{i,j} = 2\left(\mu_k\right)_{i+\frac{1}{2},j}\frac{\left(u_k\right)_{i,j}}{R_i}+\left(\xi_k-\frac{2}{3}\mu_k\right)_{i,j}\left(\nabla\cdot v_k\right)_{i,j} \qquad \text{(A.36)}$$

For the fluid phase μ_k is replaced by $\varepsilon_f\mu_f$ and $\left(\xi_k-\frac{2}{3}\mu_k\right)$ is replaced by $-\frac{2}{3}\varepsilon_f\mu_f$.

5.Fluctuating Energy Equation.

$$\frac{3}{2}\left(\varepsilon_k\rho_k\theta\right)^{n+1}_{i,j} = \frac{3}{2}\left(\varepsilon_k\rho_k\theta\right)^{n}_{i,j}+\left(\overline{\varepsilon_k\rho_k\theta}\right)_{i,j}-\delta t\left(p_k\right)^{n+1}_{i,j}\left(\nabla\cdot v_k\right)^{n+1}_{i,j}$$

$$+\delta t\left(\Phi_k\right)^{n+1}_{i,j}-\delta t\left(\gamma_k\right)^{n+1}_{i,j}-3\delta t\left(\beta_{fk}\right)^{n}_{i,j}\left(\theta\right)^{n+1}_{i,j} \qquad \text{(A.37)}$$

“TILDE” quantities are given by,

$$\left(\overline{\varepsilon_k\rho_k\theta}\right)_{i,j} = -\frac{3}{2}\frac{\delta t}{R_i\delta r_i}\left\langle R\left(\varepsilon_k\rho_k\right)^{n+1}\left(\theta\right)^n\left(u_k\right)^{n+1}\right\rangle_{i,j}$$

$$-\frac{3}{2}\frac{\delta t}{\delta z_j}\left\langle\left(\varepsilon_k\rho_k\right)^{n+1}\left(\theta\right)^n\left(v_k\right)^{n+1}\right\rangle_{i,j}$$

$$+\frac{\delta t}{R_i\delta r_i}\left[R_{i+\frac{1}{2}}\left(\kappa_k\right)^n_{i+\frac{1}{2},j}\frac{\left(\theta\right)^n_{i+1,j}-\left(\theta\right)^n_{i,j}}{\delta r_{i+\frac{1}{2}}}-R_{i-\frac{1}{2}}\left(\kappa_k\right)^n_{i-\frac{1}{2},j}\frac{\left(\theta\right)^n_{i,j}-\left(\theta\right)^n_{i-1,j}}{\delta r_{i-\frac{1}{2}}}\right]$$

$$+\frac{\delta t}{\delta z_j}\left[\left(\kappa_k\right)^n_{i,j+\frac{1}{2}}\frac{\left(\theta\right)^n_{i,j+1}-\left(\theta\right)^n_{i,j}}{\delta z_{j+\frac{1}{2}}}-\left(\kappa_k\right)^n_{i,j-\frac{1}{2}}\frac{\left(\theta\right)^n_{i,j}-\left(\theta\right)^n_{i,j-1}}{\delta z_{j-\frac{1}{2}}}\right] \quad \text{(A.38)}$$

Solution Technique for Finite-Difference Equations

An iterative technique is used to solve the finite difference equations given in the previous section.

Solution of the Momentum Equations. To facilitate the particular method of solution the equations are recast in the following form. The momentum equation in –r direction could be collected together in a matrix form.

$$\left(A\right)_{i+\frac{1}{2},j}\left(U\right)^n_{i+\frac{1}{2},j}=\left(B_u\right)_{i+\frac{1}{2},j} \quad \text{(A.39)}$$

$$A=\begin{pmatrix} A_{ff} & A_{f1} & A_{f3} & \cdots & A_{fN} \\ A_{1f} & A_{11} & A_{12} & \cdots & A_{1N} \\ \vdots & \vdots & \ddots & \ddots & \vdots \\ A_{Nf} & A_{N1} & A_{N2} & \cdots & A_{NN} \end{pmatrix} \quad \text{(A.40)}$$

where

$$A_{kk}=\left(\varepsilon_k\rho_k\right)^{n+1}+\delta t\sum_{\substack{l=f,l\\ l\neq k}}^{N}\left(\beta_{lk}\right)^n \quad \text{(A.41)}$$

$$A_{kl}=A_{lk}=-\delta t\left(\beta_{lk}\right)^n \quad \text{(A.42)}$$

$$A_{i+\frac{1}{2},j}\cdot\begin{pmatrix} u_f \\ u_1 \\ \vdots \\ u_N \end{pmatrix}=\begin{pmatrix} \left(\overline{\varepsilon_f\rho_f u_f}\right)-\frac{\delta t}{\delta r_{i+\frac{1}{2}}}\left(\left(p_f\right)^{n+1}_{i+1,j}-\left(p_f\right)^{n+1}_{i,j}\right)-\left(\varepsilon_f\rho_f\right)g_r\delta t \\ \left(\overline{\varepsilon_1\rho_1 u_1}\right)-\frac{\delta t}{\delta r_{i+\frac{1}{2}}}\left(\left(p_1\right)^{n+1}_{i+1,j}-\left(p_1\right)^{n+1}_{i,j}\right)-\left(\varepsilon_1\rho_1\right)g_r\delta t \\ \vdots \\ \left(\overline{\varepsilon_N\rho_N u_N}\right)-\frac{\delta t}{\delta r_{i+\frac{1}{2}}}\left(\left(p_N\right)^{n+1}_{i+1,j}-\left(p_N\right)^{n+1}_{i,j}\right)-\left(\varepsilon_N\rho_N\right)g_r\delta t \end{pmatrix} \quad \text{(A.43)}$$

are similarly, momentum equation in z-direction can be written as,

$$(A)_{i,j+\frac{1}{2}}(V)^{n}_{i,j+\frac{1}{2}} = (B_V)_{i,j+\frac{1}{2}} \tag{A.44}$$

$$A_{i,j+\frac{1}{2}} \cdot \begin{pmatrix} v_f \\ v_1 \\ \vdots \\ v_N \end{pmatrix} = \begin{pmatrix} \left(\overline{\varepsilon_f \rho_f v_f}\right) - \frac{\delta t}{\delta z_{j+\frac{1}{2}}}\left((p_f)^{n+1}_{i,j+1} - (p_f)^{n+1}_{i,j}\right) - (\varepsilon_f \rho_f) g_z \delta t \\ \left(\overline{\varepsilon_1 \rho_1 v_1}\right) - \frac{\delta t}{\delta z_{j+\frac{1}{2}}}\left((p_1)^{n+1}_{i,j+1} - (p_1)^{n+1}_{i,j}\right) - (\varepsilon_1 \rho_1) g_z \delta t \\ \vdots \\ \left(\overline{\varepsilon_N \rho_N v_N}\right) - \frac{\delta t}{\delta z_{j+\frac{1}{2}}}\left((p_N)^{n+1}_{i,j+1} - (p_N)^{n+1}_{i,j}\right) - (\varepsilon_N \rho_N) g_z \delta t \end{pmatrix} \tag{A.45}$$

2. Convergence on Fluid Continuity Equation. The solution process is carried out in two major steps. First of all, the continuity equations, the momentum equations, and a part of energy equation are solved simultaneously to establish the pressure and the velocity fields. In this step only the interphase heat transfer part of the energy equation is considered. Secondly, the remaining parts of the energy equations are solved to establish the temperature profiles. The solution procedure of computation sweep is illustrated in Figure A.3

The first step proceeds as follows:

$$\varepsilon_f = 1 - \sum_{k=1}^{N} \varepsilon_k \tag{A.46}$$

$$D_{i,j} = -(\varepsilon_f \rho_f)^{n+1}_{i,j} + (\varepsilon_f \rho_f)^{n}_{i,j} - \frac{\delta t}{R_i \delta r_i}\left\langle R(\varepsilon_f \rho_f) u_f \right\rangle^{n+1}_{i,j} - \frac{\delta t}{\delta z_j}\left\langle (\varepsilon_f \rho_f) v_f \right\rangle^{n+1}_{i,j} \tag{A.47}$$

$$D_{i,j} \le CONV^{n+1}_{i,j} = EPSG(\varepsilon_f \rho_f)^{n}_{i,j} \tag{A.48}$$

3. Pressure Iteration. When $D_{i,j}$ fails to meet the convergence criterion in any cell, the pressure is adjusted using a combination of Newton's method and secant method. The initial adjustment of pressure uses Newton's method.

$$(p_f)^{m+1} = (p_f)^{m} - \omega \frac{D^m}{\partial D / \partial (p_f)^m} \tag{A.49}$$

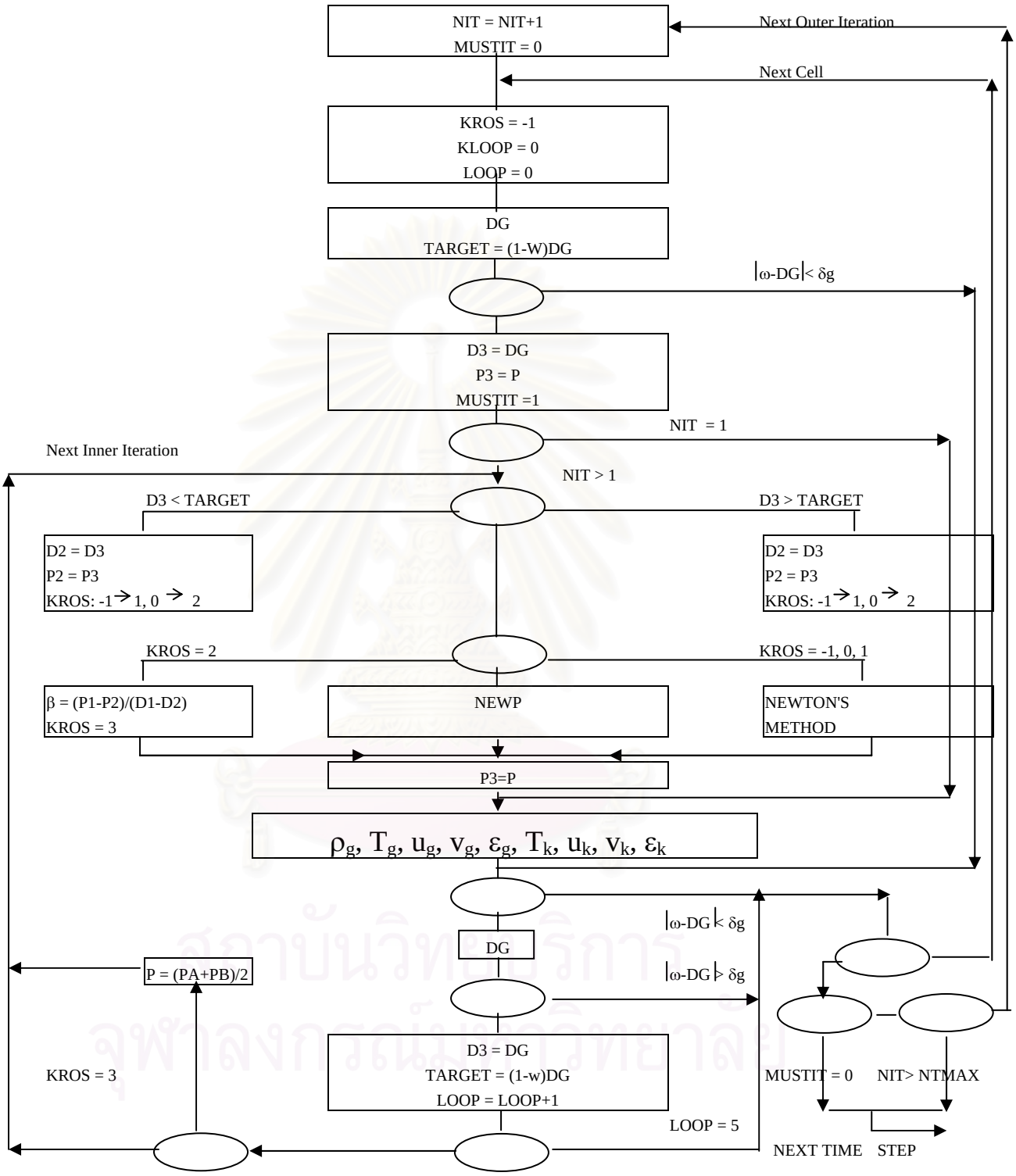

Figure A.3 The computational sweep

where the indices i, j and n have been omitted. The index, m, indicates the iteration level. This is equivalent to using Newton's method for each cell, where ω is a relaxation parameter near unity, and $\overline{\beta}$ is computed as,

$$\frac{1}{\overline{\beta}_{i,j}} = \frac{\partial D_{i,j}}{\partial (p_f)_{i,j}} = \frac{\varepsilon_f}{C_{i,j}^2} + \frac{1}{R_i}\left(\frac{\delta t}{\delta r_i}\right)^2 \left(R_{i+\frac{1}{2}} (\varepsilon_f)_{i+\frac{1}{2},j} + R_{i-\frac{1}{2}} (\varepsilon_f)_{i-\frac{1}{2},j} \right)$$

$$+ \left(\frac{\delta t}{\delta z_j}\right)^2 \left((\varepsilon_f)_{i,j+\frac{1}{2}} + (\varepsilon_f)_{i,j-\frac{1}{2}} \right) \tag{A.50}$$

once every time step. The sound speed $C_{i,j}$ is given by,

$$C_{i,j}^2 = \left(\frac{\partial p_f}{\partial \rho_f}\right)_{i,j} \tag{A.51}$$

where $(\partial p_f / \partial \rho_f)$ can be determined from the equation of state.

This formation is only approximate. Hence, subsequent use the secant method:

$$(p_f)^{m+1} = (p_f)^m - \omega \left(\frac{(p_f)^{m-1} - (p_f)^m}{D^{m-1} - D^m} \right) D^m \tag{A.52}$$

The use of secant method is combined until $D_{i,j}$ changes sign. Thereafter a combination of the secant method and a bisection method is used. The method is illustrated in the Figure A 4.

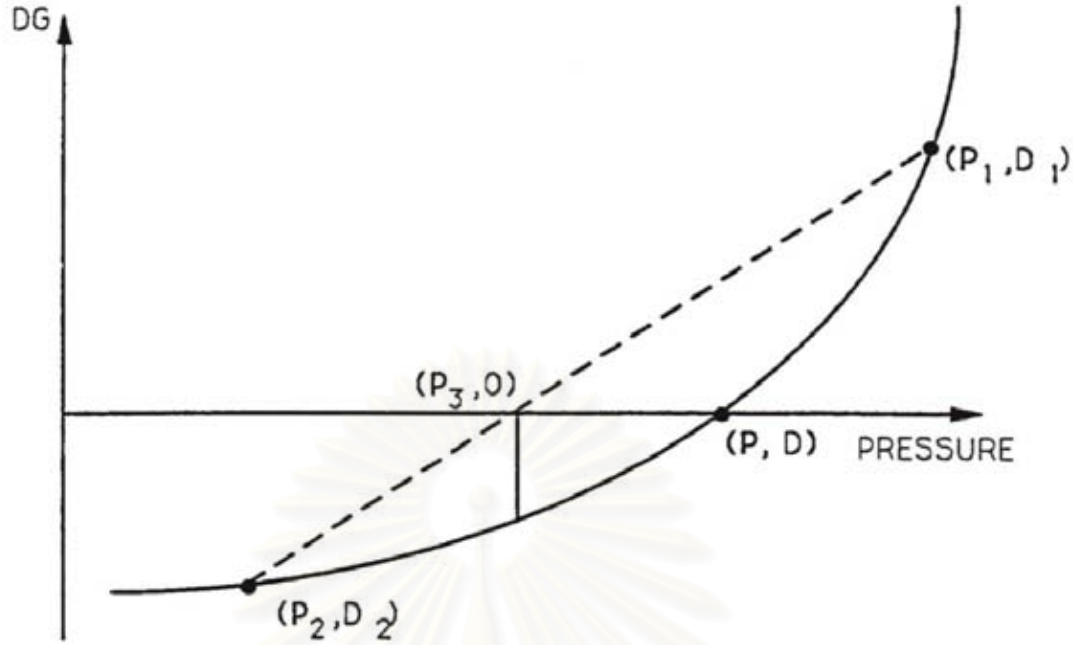

(a) Newton ‘s Method

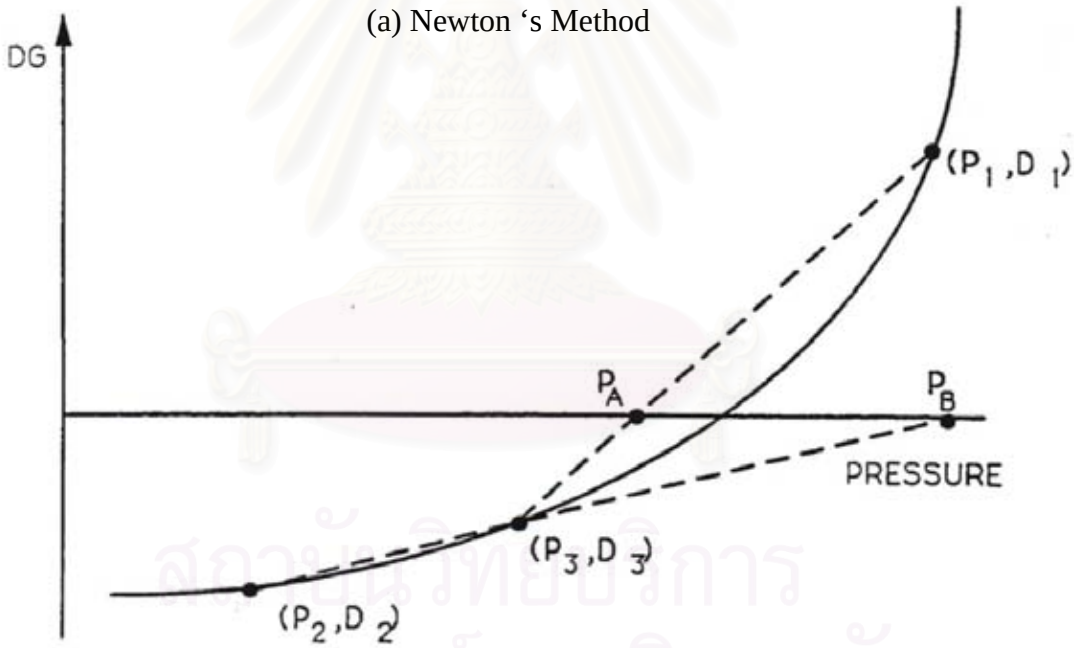

(a) Secant ‘s Method

Figure A.4 The methods for pressure iteration

Given the three pressure p_1, p_2 and p_3 of which p_1 and p_2 bracket the desired pressure and p_3 lies between them and the respective mass residuals D_1, D_2 and D_3 do not satisfy the convergence criterion in cell (i, j), D_1>0, and D_2<0. With three pressures and their mass residuals obtained as described, or otherwise a constrained two-sides secant technique is used to obtain further pressure adjustment. Form these pressures and their mass residuals, the pressure p_A and p_B are determined by straight line extrapolation and interpolation, respectively, as follow,

$$p_A = \begin{cases} (p_3 D_1 - p_1 D_3)/(D_1 - D_3) & for \quad D_1 \neq D_3 \\ (p_2 + p_3)/2 & for \quad D_1 = D_3 \end{cases} \tag{A.53}$$

and

$$p_B = \begin{cases} (p_3 D_2 - p_2 D_3)/(D_2 - D_3) & for \quad D_2 \neq D_3 \\ (p_1 + p_3)/2 & for \quad D_2 = D_3 \end{cases} \tag{A.54}$$

The new estimate of the advanced time pressure is then computed as,

$$(p_f)^{m+1} = \frac{1}{2}(p_A + p_B) \tag{A.55}$$

If the pressure, p_A should lie outside the interval p_1 to p_3, it is given the valve $\frac{1}{2}(p_A + p_B)$. After $(p_f)^{m+1}$ is estimated, point 2 is discarded add points 1 and 3 are retained as improved bounds for the next pressure estimate. When $D_{i,j}$ changes sign, the valve of $\overline{\beta}$ is also updated for future iteration as,

$$\overline{\beta} = \frac{p_1 - p_2}{D_1 - D_2} \tag{A.56}$$

4. Solution of the Energy Equations. The specific enthalpies $\overline{H}_k$ are calculated in subroutine IGIL accounting for the mass, momentum and energy exchange rates. For

the iterative part of the solution, a simplified set of energy equations is used, which is differenced as follows,

$$\left(\varepsilon_f \rho_f\right)_{i,j}^{n+1}\left(\overline{H}_f\right)_{i,j} = \left(\varepsilon_f \rho_f\right)_{i,j}^{n+1}\left(H_f\right)_{i,j}^{n} + \frac{\delta t}{2}\sum_{k=1}^{N}\left(h_{vk}\right)_{i,j}^{n}\left(\overline{T}_k - \overline{T}_f\right)$$

$$+ \delta t \sum_{k=1}^{N}\left(\beta_{kf}\right)_{i,j}^{n}\left[\left(\left(u_k\right)_{i,j}^{n} - \left(u_f\right)_{i,j}^{n}\right)^2 + \left(\left(v_k\right)_{i,j}^{n} - \left(v_f\right)_{i,j}^{n}\right)^2\right]$$

$$\left(\varepsilon_k \rho_k\right)_{i,j}^{n+1}\left(\overline{H}_k\right)_{i,j} = \left(\varepsilon_k \rho_k\right)_{i,j}^{n+1}\left(H_k\right)_{i,j}^{n} + \frac{\delta t}{2}\left(h_{vk}\right)_{i,j}^{n}\left(\overline{T}_f - \overline{T}_k\right)$$

(A.57)

Note that only half the effect of the interphase heat transfer is considered here. Thus $\overline{H}$ is some intermediate valve between H^n and H^{n+1} defined as,

$$\overline{H}_k = H^n + \left(\overline{T}_k - T_f^n\right)c_k \qquad \text{(A.58)}$$

where, c_k is the specific heat of the fluid or the particulate phases. Rearranging, we get,

$$\overline{T}_k = \frac{\overline{H}_k - H_k^n}{c_k} + T_k^n \qquad \text{(A.59)}$$

Thus we get,

$$\left(\varepsilon_f \rho_f\right)_{i,j}^{n+1}\left(\overline{H}_f\right)_{i,j} = \left(\varepsilon_f \rho_f\right)_{i,j}^{n+1}\left(H_f\right)_{i,j}^{n} + \frac{\delta t}{2}\sum_{k=1}^{N}\left(h_{vk}\right)_{i,j}^{n}$$

$$\left(\frac{\left(\overline{H}_k\right)_{i,j} - \left(H_k\right)_{i,j}^{n}}{c_k} + \left(T_k\right)_{i,j}^{n} - \frac{\left(\overline{H}_f\right)_{i,j} - \left(H_f\right)_{i,j}^{n}}{c_f} - \left(T_f\right)_{i,j}^{n}\right)$$

$$+ \delta t \sum_{k=1}^{N}\left(\beta_{kf}\right)_{i,j}^{n}\left[\left(\left(u_k\right)_{i,j}^{n} - \left(u_f\right)_{i,j}^{n}\right)^2 + \left(\left(v_k\right)_{i,j}^{n} - \left(v_f\right)_{i,j}^{n}\right)^2\right]$$

(A.60)

$$\left(\varepsilon_k \rho_k\right)_{i,j}^{n+1}\left(\overline{H}_k\right)_{i,j} = \left(\varepsilon_k \rho_k\right)_{i,j}^{n+1}\left(H_k\right)_{i,j}^{n} + \frac{\delta t}{2}\left(h_{vk}\right)_{i,j}^{n}$$

$$\left(\frac{\left(\overline{H}_f\right)_{i,j} - \left(H_f\right)_{i,j}^{n}}{c_f} + \left(T_f\right)_{i,j}^{n} - \frac{\left(\overline{H}_k\right)_{i,j} - \left(H_k\right)_{i,j}^{n}}{c_k} - \left(T_k\right)_{i,j}^{n}\right)$$

(A.61)

In matrix form,

$$\left(A_h\right)_{i,j}\left(\overline{H}\right)_{i,j}^{n} = \left(B_h\right)_{i,j} \tag{A.62}$$

Note that $\left(\varepsilon_k \rho_k\right)$,k=1,f,…,N are evaluated at time $\left(n+1\right)$and H_k, T_k, h_{vk} are evaluated at time n.

$$\begin{pmatrix} \varepsilon_f \rho_f + \frac{\delta t}{2c_f}\sum_{k=1}^{N} h_{vk} & -\frac{\delta t h_{v1}}{2c_1} & -\frac{\delta t h_{v2}}{2c_2} & \cdots & -\frac{\delta t h_{vN}}{2c_N} \\ -\frac{\delta t h_{v1}}{2c_f} & \varepsilon_1 \rho_1 + \frac{\delta t h_{v1}}{2c_1} & 0 & \cdots & 0 \\ -\frac{\delta t h_{v2}}{2c_f} & 0 & \varepsilon_2 \rho_2 + \frac{\delta t h_{v2}}{2c_2} & \cdots & 0 \\ \vdots & \vdots & \vdots & \ddots & \vdots \\ -\frac{\delta t h_{vN}}{2c_f} & 0 & 0 & \cdots & \varepsilon_N \rho_N + \frac{\delta t h_{vN}}{2c_N} \end{pmatrix}$$

$$\bullet \begin{pmatrix} \overline{H}_f \\ \overline{H}_1 \\ \overline{H}_2 \\ \vdots \\ \overline{H}_N \end{pmatrix} = \begin{pmatrix} \left(\varepsilon_f \rho_f\right)H_f + \frac{\delta t}{2}\sum_{k=1}^{N} h_{vk}\left(\frac{H_f}{c_f} - \frac{H_k}{c_k} + T_k - T_f\right) + \delta t \sum_{k=1}^{N} \beta_{kf}\left[\left(u_k - u_f\right)^2 + \left(v_k - v_f\right)^2\right] \\ \left(\varepsilon_1 \rho_1\right)H_1 + \frac{\delta t}{2} h_{v1}\left(\frac{H_1}{c_f} - \frac{H_f}{c_f} + T_f - T_1\right) \\ \left(\varepsilon_2 \rho_2\right)H_2 + \frac{\delta t}{2} h_{v2}\left(\frac{H_2}{c_f} - \frac{H_f}{c_f} + T_f - T_2\right) \\ \vdots \\ \left(\varepsilon_N \rho_N\right)H_N + \frac{\delta t}{2} h_{vN}\left(\frac{H_N}{c_f} - \frac{H_f}{c_f} + T_f - T_N\right) \end{pmatrix}$$

(A.63)

After the converged solution is obtained for the continuity and momentum equations, the solution of the energy equation is completed. The part of the energy equation solved during the iterative solution of the momentum and continuity

equations is subtracted from the complete energy equations. Assuming that $\left(\overline{T}_f - \overline{T}_k\right) \approx \left(T_f - T_k\right)^{n+1}$, we get,

$$T_k^{n+1} = \frac{H_k^{n+1} - \overline{H}_k}{c_k} + \overline{T}_k \tag{A.64}$$

$$\begin{aligned}\left(\varepsilon_f \rho_f\right)_{i,j}^{n+1}\left(H_f\right)_{i,j}^{n+1} &= \left(\varepsilon_f \rho_f\right)_{i,j}^{n+1}\left[\left(\overline{H}_f\right)_{i,j} - \left(H_f\right)_{i,j}^{n}\right] + \left(\varepsilon_f \rho_f\right)_{i,j}^{n}\left(H_f\right)_{i,j}^{n} \\ &+ \left(\overline{\varepsilon_f \rho_f H_f}\right)_{i,j} + \frac{\delta t}{2}\sum_{k=1}^{N}\left(h_{vk}\right)_{i,j}^{n}\left(\frac{\left(H_k\right)_{i,j}^{n+1} - \left(\overline{H}_k\right)_{i,j}}{c_k}\right. \\ &\left. + \left(\overline{T}_k\right)_{i,j} - \frac{\left(H_f\right)_{i,j}^{n+1} - \left(\overline{H}_f\right)_{i,j}}{c_f} - \left(\overline{T}_f\right)_{i,j}^{n}\right)\end{aligned} \tag{A.65}$$

$$\begin{aligned}\left(\varepsilon_k \rho_k\right)_{i,j}^{n+1}\left(H_k\right)_{i,j}^{n+1} &= \left(\varepsilon_k \rho_k\right)_{i,j}^{n+1}\left[\left(\overline{H}_k\right)_{i,j} - \left(H_k\right)_{i,j}^{n}\right] + \left(\varepsilon_k \rho_k\right)_{i,j}^{n}\left(H_k\right)_{i,j}^{n} \\ &+ \left(\overline{\varepsilon_k \rho_k H_k}\right)_{i,j} + \frac{\delta t}{2}\left(h_{vk}\right)_{i,j}^{n}\left(\frac{\left(H_f\right)_{i,j}^{n+1} - \left(\overline{H}_f\right)^{n}{}_{i,j}}{c_f}\right. \\ &\left. + \left(\overline{T}_f\right)_{i,j} - \frac{\left(H_k\right)_{i,j}^{n+1} - \left(\overline{H}_k\right)^{n}{}_{i,j}}{c_k} - \left(\overline{T}_k\right)_{i,j}^{n}\right)\end{aligned} \tag{A.66}$$

Solution procedure is same as the one discuss above.

Boundary Conditions

The rectangular region in which calculations are to preformed is partitioned into cells of sizes dx_i (or dr_i) in x (or r)-direction and dy_i (or dz_i) in y (or z)-direction. A perimeter of fictitious (dummy) boundary cells surrounding the computing mesh is used to enforce boundary conditions. Several boundary conditions around the computing mesh perimeter are programmed in the code. The cell flag types are indicated by IFL(I,J).

Flag	Cell Type
1	Fluid cell
2	No-slip rigid walls
3	Partial-slip rigid walls for solid phases
4	Continuous outflow
5	Prescribed inflow rate
6	Prescribed pressure inflow
7	Prescribed pressure outflow with particulate outflow
8	Prescribed pressure outflow with no particulate outflow

The free and no slip boundary conditions are shown in figure A 5.

Free – slip wall No – slip wall

Figure A.5 Free and no slip conditions

The no-slip condition cannot always be applied to solids motion, because the particulate diameter is usually larger than the length scale of surface roughness of the rigid wall. The solids tangential velocity v_{kt} at the wall can be taken to be proportional to its gradient at the wall.

$$v_{kt} = -\lambda_k \left. \frac{\partial v_{kt}}{\partial x_n} \right|_{\omega} \tag{A.67}$$

where the x_n direction is normal to the wall. The slip parameter is defined as,

$$\lambda_k = d_k / \varepsilon_k^{1/3} \tag{A.68}$$

Note that for small particle diameter the boundary condition is close to the no-slip condition.

In the bottom row and left column of boundary cells, any number of inflow opening can be specified using flag types 5 and 6. Similarly, in the top row and right column of boundary cells, any number of outflow opening can be specified using flag types 4, 7 and 8. Flag types 2 and 3 may be prescribed on any of the four boundaries to represent rigid (solid) cell. Obstacles blocks within the computing mesh are built from rigid cells, flag types (IFL =2 or 3).

The position of all blocks must coincide with rectangular cells within the computing mesh. Calculations are not performed in the obstacle cells, only in the remaining fluid cells within the computing mesh. Cell flag type (IFL=1) is a computational cell.

1. Rigid Cells Three types of boundary conditions may be specified for a rigid cell: free-slip, no-slip and partial slip (IFL = 2 or 3). In two dimensions, a free-slip boundary represents line of symmetry and a non-adhering boundary that exerts no drag on the fluid; a no-slip boundary represents a viscous boundary that exerts a drag on the fluid.

Consider cell (i, j), which is a fluid cell, an inflow boundary cell, or an outflow boundary cell. An adiabatic rigid cell is said to be a corner cell if and only if it has at least two adjacent edged, each of which is shared with afluid cell, an inflow boundary cell, or an outflow boundary cell.

If right cell $(i+1, j)$ or left cell $(i-1, j)$, is a rigid cell, then for all time levels n,

$$(u_k)^{n+1}_{i\pm\frac{1}{2}, j} = 0 \tag{A.69}$$

$$(v_k)^{n+1}_{i\pm1,j+\frac{1}{2}} = \begin{cases} (v_k)^n_{i,j+\frac{1}{2}} & for(IFL=2) \\ -\delta r_{i\pm1}(v_k)^n_{i,j+\frac{1}{2}} / \delta r_i & for(IFL=3), k \neq solid \\ \left(\dfrac{2\lambda_{i,j} - \delta r_{i\pm1}}{2\lambda_{i,j} - \delta r_i}\right)(v_k)_{i,j+\frac{1}{2}} & for(IFL=3), k = solid \end{cases} \quad \text{(A.70)}$$

Similarly, if top cell $(i, j+1)$ or bottom cell $(i, j-1)$, is a rigid cell and if free-slip boundary conditions (IFL = 2) or no-slip boundary conditions (IFL = 3) are imposed, then for all n,

$$(u_k)^{n+1}_{i+\frac{1}{2},j\pm1} = \begin{cases} (u_k)^n_{i+\frac{1}{2},j} & for(IFL=2) \\ -\delta z_{j\pm1}(u_k)^n_{i+\frac{1}{2},j} / \delta z_j & for(IFL=3), k \neq solid \\ \left(\dfrac{2\lambda_{i,j} - \delta z_{j\pm1}}{2\lambda_{i,j} - \delta z_j}\right)(u_k)_{i+\frac{1}{2},j} & for(IFL=3), k = solid \end{cases} \quad \text{(A.71)}$$

$$(v_k)^{n+1}_{i,j\pm\frac{1}{2}} = 0 \quad \text{(A.72)}$$

If any one of the cells $(i+1, j), (i-1, j), (i, j+1)$, or $(i, j-1)$ is both a rigid cell and a corner cell, then, for all free-slip, no-slip and particle-slip boundary condition, all its velocity components located at the center are set equal to zero

2. Inflow Boundary Cells. For each inflow opening a fluid pressure, p_f, velocities u_k and v_k, and solid volume fraction, ε_k, temperature, T_k for all phases (k = f,1,…,N), and solid granular temperature θ must be specified in the input data, as necessary.

The pressure data is required for both (IFL = 5) and (IFL = 6). For the mass fluxes, the solid volume fraction and solid velocity have to be defined, as follow,

$$W_s = \varepsilon_s \rho_s v_s \quad \text{(A.73)}$$

3. Outflow Boundary Cells. For each outflow opening, a pressure, p_f, is specified at the beginning of each computation cycle. The types od outflow boundary conditions used are: pressure prescribed outflow with particulates outflow (IFL = 7), or no particulates outflow (IFL = 8), or continuative outflow (IFL = 4)

For outflow boundary conditions, the volume fractions, for a given cell of an outflow opening, is obtaining by reflection. The tangential component of the velocities are set to zero. A numerical screen is used to keep particulate phases form leaving the fluidized bed for (IFL = 8)

Therefore, at the top outflow boundary, where (i, j)=(I,JB2); $\left(i+\frac{1}{2}, j\right)$=(I,JB2); $\left(i, j+\frac{1}{2}\right)$=(I,JB2); $(i, j-1)$=(I,JB1) and $\left(i, j-\frac{1}{2}\right)$=(I,JB1), we have,

$$(p_f)_{i,j}^{n+1} = \begin{cases} p_o & for(IFL = 7or8) \\ (p_f)_{i,j-1}^{n} & for(IFL = 4) \end{cases} \tag{A.74}$$

$$(\varepsilon_k)_{i,j}^{n+1} = \begin{cases} (\varepsilon_k)_{i,j-1}^{n} & for(IFL = 4or7) \\ \begin{cases} 1 & k = f \\ 0 & k \neq f \end{cases} & for(IFL = 8) \end{cases} \tag{A.75}$$

$$(u_k)_{i+\frac{1}{2},j}^{n+1} = 0 \tag{A.76}$$

$$(v_f)_{i,j+\frac{1}{2}}^{n+1} = (\varepsilon_f \rho_f)_{i,j-1}^{n+1} (v_f)_{i,j-\frac{1}{2}}^{n+1} / (\varepsilon_f \rho_f)_{i,j}^{n+1} \tag{A.77}$$

$$(v_k)_{i,j+\frac{1}{2}}^{n+1} = \begin{cases} (\varepsilon_k \rho_k)_{i,j-1}^{n+1} (v_k)_{i,j-\frac{1}{2}}^{n+1} / (\varepsilon_k \rho_k)_{i,j}^{n+1} & for(IFL = 4or7) \\ 0 & for(IFL = 8) \end{cases} \tag{A.78}$$

At the right outflow boundary, where (i, j)=(IB2,J); $\left(i+\frac{1}{2}, j\right)$=(IB2,J); $(i+1, j)$=(IB1,J), $\left(i-\frac{1}{2}, j\right)$=(IB1,J), $(i-1, j)$=(IB1,J), and we have,

$$\left(p_f\right)_{i,j}^{n+1} = \begin{cases} p_o & for(IFL = 7or8) \\ \left(p_f\right)_{i-1,j}^{n} & for(IFL = 4) \end{cases} \tag{A.79}$$

$$\left(\varepsilon_k\right)_{i,j}^{n+1} = \begin{cases} \left(\varepsilon_k\right)_{i-1,j}^{n} & for(IFL = 4or7) \\ \begin{cases} 1 & k = f \\ 0 & k \neq f \end{cases} & for(IFL = 8) \end{cases} \tag{A.80}$$

$$\left(u_f\right)_{i+\frac{1}{2},j}^{n+1} = r_{i-\frac{1}{2}}\left(\varepsilon_f \rho_f\right)_{i-1,j}^{n+1}\left(u_f\right)_{i-\frac{1}{2},j}^{n+1} / \left[r_{i+\frac{1}{2}}\left(\varepsilon_f \rho_f\right)_{i,j}^{n+1}\right] \tag{A.81}$$

$$\left(u_k\right)_{i+\frac{1}{2},j}^{n+1} = \begin{cases} r_{i-\frac{1}{2}}\left(\varepsilon_k \rho_k\right)_{i-1,j}^{n+1}\left(u_k\right)_{i-\frac{1}{2},j}^{n+1} / \left[r_{i+\frac{1}{2}}\left(\varepsilon_k \rho_k\right)_{i,j}^{n+1}\right] & for(IFL = 4or7) \\ 0 & for(IFL = 8) \end{cases} \tag{A.82}$$

Initial Conditions

At the beginning if the simulation the distribution of all field variables given by the initial conditions. Uniform and simple non-uniform initial conditions can be specified using the input data. Fluid cell (IFL = 1) with the filed variables have to be specified.

APPENDIX B

ORGANIZATION AND USER MENU

สถาบันวิทยบริการ
จุฬาลงกรณ์มหาวิทยาลัย

Program Organization

A flow chart of the program CFB1_2S.f with the various subroutines is given in Figure B 1. An alphabetical listing of the various subroutines and their functions are as follows:

BDRY	Set the boundary conditions – reflects cell centered quantities
BETAS	Calculates the reciprocal derivatives of the mass residuals with respect to pressure $\overline{\beta}_{i,j} = \left(\partial D / \partial P_g\right)_{i,j}$ for iteration procedure.
FEFLUX	Calculates composition for each phase
FLIC	Set cell flags based on input data
GRNVIS	Calculates new granular temperature and particulate properties using kinetic theory of granular solids
GRPROP	Initializes particulate properties using kinetic theory of granular solids
GRTEMF	Calculates granular temperature fluxes of kinetic theory
HEATCG	Calculates the heat flux for the gas phase, using the phase conductivities
HEATCL	Calculates the heat flux for the solid phase, using the phase conductivities
ICONV	Updates the specific energies to account for the effects of convection, viscous and pressure work, and conduction
IGIL	Updates the specific energies to account for the effects of mass momentum and energy exchange
IINV	Calculates inverse of matrix with non-zero first column, first row and diagonal column
INDX	Calculates indices for array quantities

ITER	Performs the iterative solution of the difference equation of mass momentum and energy equations
KDRAGG	Calculates gas-solid drag coefficients
KDRAGS	Calculates gas-solid drag for low or high solid concentration
MASFG	Calculates mass fluxes for the gas phase
MASFK	Calculates mass fluxes for the solid phases
MATS	Calculates the matrix component for velocity calculations
MULTI	Calculates particle to particle interaction
NEWP	Calculates a new estimate of advanced time pressure from three (pressure residual) points
PROD	Calculates the mass flux at inlet and outlet for gas phase
PROG	Controls the program flow and output
QESOL	Solves quadratic equation
QFLUX	Calculates heat generations due to reactions
RHEATS	Calculates the value of interface heat transfer coefficient
RRATE	Defines the rates of reactions and heat generations
SETUP	Defines the initial values of field variables in the fluid, inflow and outflow boundary cells, using the input data
SIEGF	Calculates fluxes of specific energy for the gas phase
SIELF	Calculates fluxes of specific energy for the solid phase
SOLUTION	Identifies rate control step (reaction or mass transfer)
TAPERD	Reads the restart file for initial conditions
TAPEWR	Write to a restart file
THRCON	Calculates the thermal conductivities for the phases

TILDE	Calculate momenta due to convection, gravity, viscous stress, solids pressure and cohesive stress (tilde quantities)
UGMOMF	Calculates fluxes of radial momentum for the gas phase
UGVS	Calculates stress tensor terms for the gas phase in radial direction
ULMOMF	Calculates fluxes of radial momentum for the particulate phases
ULVS	Calculates stress tensor terms for the particulate phases in radial direction
VELINV	Uses Gauss-Dolittle method for symmetric matrix inversion
VELSK	Calculates velocities on the four boundaries of the cell
VGMOMF	Calculate fluxes of axial momentum for the gas phase
VGVS	Calculates stress tensor term for the gas phase in axial direction
VLMOMF	Calculate fluxes of axial momentum for the particulate phases
VLVS	Calculates stress tensor term for the particulate phases in axial direction
VWORKL	Calculates the viscous work for the phase specific energy equation

สถาบันวิทยบริการ
จุฬาลงกรณ์มหาวิทยาลัย

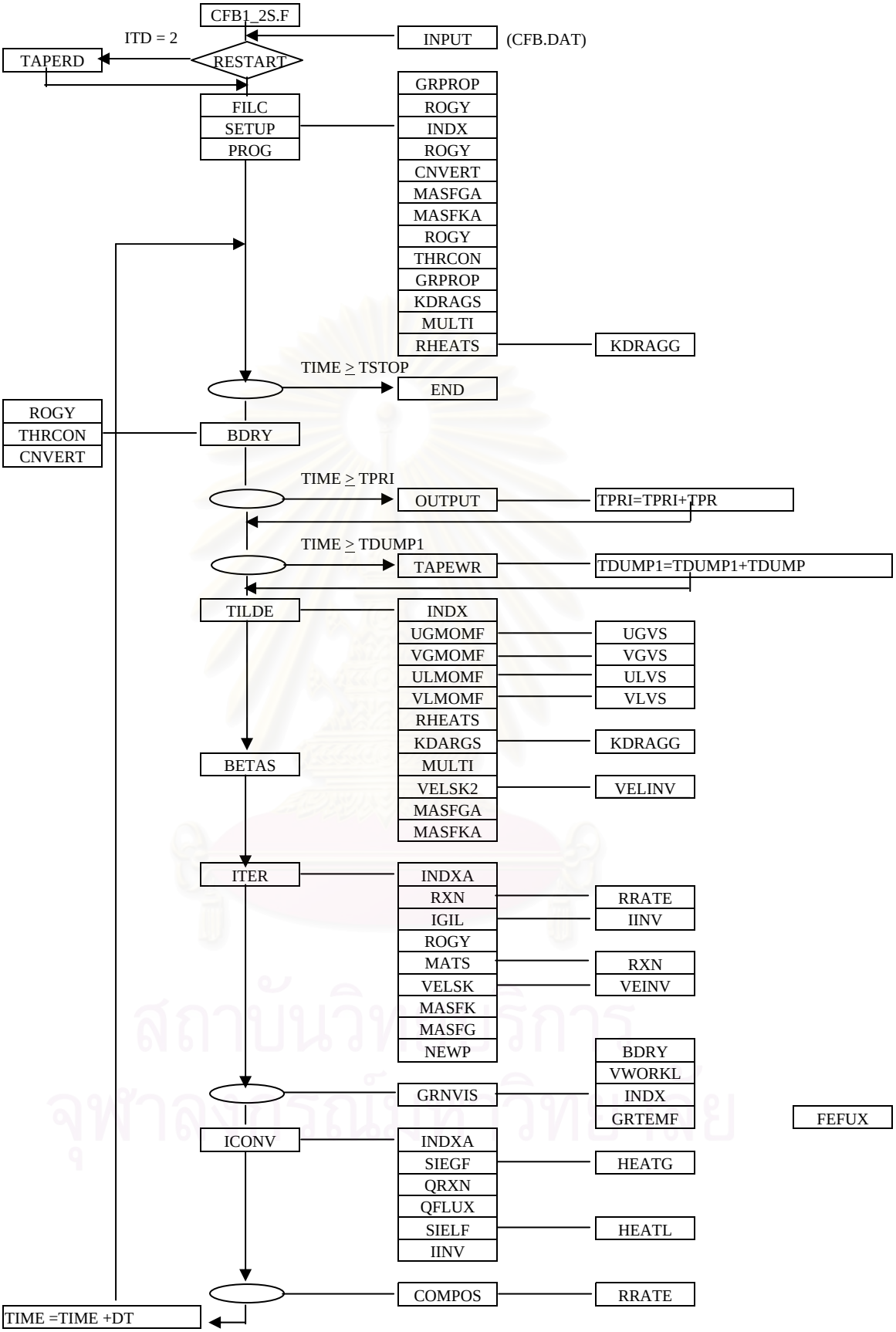

Figure B.1 The program flow chart

INPUT DATA (Explosive dissemination of nanoparticle & Al particles): cfb1.dat

```
TEST_ENERGY (dissemination step)
1*1     1*2.2          1*5.5          50*19.85       1*1
1*1     43*1.99        10*2.91        43*1.99        1*1
3 3 3 3
1   0   2   3   2   44
1   0   2   2   45 54
1   0   3   3   45 54
1   0   2   3   55 97
1   0   4   53  2  97
4   0   54 54  2  97
1e-6            5e-4
1.0             1.0
2.2             2.7
1.5d7           1.5D7
0.              0.0
0.08    0.999   0.96    0.02    0.0
0       1.E-3
0       1.E-3
0.              0.0     1.01325D6       1.0     300.0
0.              0.0                     0.0     300.0   0.0
0.              0.0                     0.0     300.0   0.0
1.206e3         0.0     2.65e6          0.989   761.0
0.0             0.0                     0.0     300.0   0.0
1.283e3         0.0                     0.011   695.0   0.0
3.684e3         0.0     2.59e6          0.894   319.0
3.684e3         0.0                     0.025   318.0   0.0
3.661e3         0.0                     0.081   319.0   0.0
0.              0.0     1.01325D6       1.0     300.0
0.              0.0                     0.0     300.0   0.0
0.              0.0                     0.0     300.0   0.0
0.              0.0     1.01325D6       1.0     300.0
0.              0.0                     0.0     300.0   0.0
0.              0.0                     0.0     300.0   0.0
0.              0.0     1.01325D6       1.0     300.0
0.              0.0                     0.0     300.0   0.0
0.              0.0                     0.0     300.0   0.0
28.9
0
1.0
0.0
0.0
1.0
0.0
0.0
1.0
0.0
0.0
1.0
```

0.0
0.0
1.0
0.0
0.0
1.0
0.0
0.0
0
0. 30d-2 1.D-5
1d-3 1D-3
0. -981.

สถาบันวิทยบริการ
จุฬาลงกรณ์มหาวิทยาลัย

INPUT DATA : cfb1.dat
A description of the input data file is given below.

LINE 1:	NAME :case identifier
LINE 2:	(NUMBER OF CELL*DR(I), I=1, IB2)
LINE 3:	(NUMBER OF CELL*DZ(J), J=1, JB2)
LINE 4:	(NSL(M), M=1,4) To indicate the boundary condition of four wall, bottom, top, left, and right. The free-slip and no slip boundary condition is used, 2 and 3 respectively. These values are ignored across inflow and outflow opening.
LINE 5-10:	The type of cell, ITHMF(0), position of cell at the begin in x direction, position of cell at the end in x direction, position of cell at the begin in y direction, position of cell at the end in y direction
LINE 11:	DK(NPHASE) particle diameter
LINE 12:	PHI(NPHASE) sphericity of particle
LINE 13:	RL(NPHASE) density
LINE 14:	CL(NPHASE) specific heat
LINE 15:	VISS(NPHASE) =0 because the viscosity is defined in the code
LINE 16:	THMIN,CRES,CRESW,PHIW,BETAC THMIN - minimum of void = maximum packing of solid CRES - restitution coefficient CRESW - restitution coefficient at wall PHIW - sphericity at wall
LINE 17-18:	(KIN(K), RLKMIN(K), K=1, NPHASE): KIN(K)=1, 0 for kinetic theory and viscosity model RLKMIN(K) is used only in kinetic theory model, when solid concentration is should more than RLKMIN(K)
LINE 19:	UIO(1), VIO(1), PIO(1), THIO(1), TEMIO(1): velocities in x-direction, y-direction, pressure, volume fraction and temperature of the **first** block **for gas phase**.
LINE 20-21:	UIO(K,1), VIO(K,1), PIO(K,1), THIO(K,1), TEMIO(K,1): velocities in x-direction, y-direction, pressure, volume fraction and temperature of the **first** block **for solid phase 1,2**.
LINE 22:	UIO(2), VIO(2), PIO(2), THIO(2), TEMIO(2): velocities in x-direction, y-direction, pressure, volume fraction and temperature of the **second** block **for gas phase**.
LINE 23-24 :	UIO(K,2), VIO(K,2), PIO(K,2), THIO(K,2), TEMIO(K,2): velocities in x-direction, y-direction, pressure, volume fraction and temperature of the **second** block **for solid phase 1,2**.
LINE :	UIO(NO), VIO(NO), PIO(NO), THIO(NO), TEMIO(NO): velocities in x-direction, y-direction, pressure, volume fraction and temperature of the **NO-th** block **for gas phase**.
LINE :	UIO(K,NO), VIO(K,NO), PIO(K,NO), THIO(K,NO), TEMIO(K,NO): velocities in x-direction, y-direction, pressure, volume fraction and temperature of the **NO-th** block **for solid phase 1,2**.
LINE 37 :	(WM(JX),JX=1,JXN) The molecular weight of fluid phase
LINE 38:	IRXN (reaction)

LNE 39-56: IRXN = 0 turn off of reaction / IRXN = 1 turn on of reaction

LINE 57: ITD

ITD = 0 no restart / ITD = 2 read the initial data from a restart file

LINE 58: TIME,TSTOP,DT

TIME – initial time of the problem

TSTOP – the time at which the calculation is to step

DT – the time increment

LINE 59: TPR,TDUMP

TPR – the time interval fpr printing data on the output file

TDUMP – the time interval for output to a disk file which may be used as a restart file

LINE 60: GRAVX,GRAVY

GRAVX – gravity in x – direction

GRAVY – gravity in y – direction

สถาบันวิทยบริการ
จุฬาลงกรณ์มหาวิทยาลัย

INPUT DATA (Turbulent fluidization of FCC particles): cfb1.dat

```
flux 9.88 g/cm2.s U 325 cm/s PHIW (wei_case)
42*0.465
300*2.68
3 3 3 3
1       0       2       41      2       299
5       0       12      17      1       1
5       0       18      25      1       1
5       0       26      31      1       1
4       0       42      42      284     298
0.006
1.0
1.4
4.9D7
0.
0.36    0.90    0.6     0.6     0.0
1  1.E-5
0.      0.      1.01325D6       0.99    298.15
0.      0.                      0.01    298.15          0.0
0       100     1.1856D6        0.9     298.15
0.      50                      0.1     298.15          100.0
0       752     1.1856D6        0.9     298.15
0.      278                     0.1     298.15          100.0
0       100     1.1856D6        0.9     298.15
0.      50                      0.1     298.15          100.0
0.      0.      1.01325D6       1.0     298.15
0.      0.                      0.0     298.15  0.0
28.9
0
1.0
0.0
1.0
0.0
1.0
0.0
1.0
0.0
1.0
0.0
0
0. 10.D+1 5.D-5
1.D-1 1.D-1
0. -981.
```

```
C*************************************************************
C                                                            *
C    COMMON FILE CFB1.COM OF THE PROGRAM CFB1_2S.F           *
C        (Explosive dissemination of nanoparticle & Al particles)  *
C*************************************************************

C
      IMPLICIT DOUBLE PRECISION(A-H,O-Z)
C
      PARAMETER(IB2=54,JB2=98,NPHASE=2,NPHS1=NPHASE+1,LT=NPHS1)
      PARAMETER(NIN=0,NOUT=1,NFL=5,NOBS=0,JXN=1,THICK=40.8127)
      PARAMETER(ITC=0,IPRE=0,RST=0.)
C
      PARAMETER(IB=IB2-2,IB1=IB2-1,JB=JB2-2,JB1=JB2-1)
      PARAMETER(IB3=IB2+1,IB4=IB2+2,IB2JB2=IB2*JB2)
      PARAMETER(IB2JB1=IB2JB2-IB2,IB1JB2=IB2JB2-1,
     $        IB2JB0=JB*IB2+1)
      PARAMETER(NO=NIN+NOUT+NFL,NT=NO+NOBS)
      PARAMETER(NH=NPHASE,NC=IB2JB2,NI=IB2,NJ=JB2,
     $        NP=NPHS1,NF=NP*(NP+1)/2)
      PARAMETER(CG=1.8D7,VISF=1.82D-4,FAC=3.0)
      PARAMETER(C1=300.,C2=300.)
      PARAMETER(C17=8.314e7,C18=0.0,c19=0.037155)
      PARAMETER(PI=3.14159265359)
      COMMON / PARAM0 /
     $ THMIN,CRES,CRESW,PHIW,BETAC
      COMMON / PARAM1 /
     $ DT,KIN(NH),IRXN,VISS(NH),
     $ DG,D1,D2,D3,P1,P2,P3,GRAVX,GRAVY,NIT,
     $ TIME,TDUMP,TPR,TSTOP,TARRAY(2),TTIM
      COMMON / PARAM2 /
     $ ITHMF(NT),QF(NC),
     $ AYM(JXN,JB2),AYMOL(JXN,JB2),AYMOL1(JXN,JB2),YMOL(JXN,NC),
     $ FLUX(JB2),AMIX(20),
     $ TG(NC), TL(NH,NC), TGN(NC), TLN(NH,NC),
     $ SIEG(NC), SIEGN(NC), AKG(NC),
     $ SIEL(NH,NC), SIELN(NH,NC), AKL(NH,NC),
     $ CL(NH), RHEAT(NH,NC),
     $ UGFL,  UGFR,  UGFT,  UGFB(NI),
     $ ULFL(NH),  ULFR(NH), ULFT(NH), ULFB(NH,NI),
     $ VGFL,  VGFR,  VGFT,  VGFB(NI),
     $ VLFL(NH), VLFR(NH), VLFT(NH), VLFB(NH,NI),
     $ THFL,  THFR,  THFT,  THFB(NI),
     $ EGFL,  EGFR,  EGFT,  EGFB(NI),
     $ HFGL,  HFGR,  HFGT,  HFGB,
     $ ELFL(NH), ELFR(NH), ELFT(NH), ELFB(NH,NI),
     $ HFLL(NH), HFLR(NH), HFLT(NH), HFLB(NH,NI),
     $ OMTFL(NH), OMTFR(NH), OMTFT(NH), OMTFB(NH,NI),
     $ SUGL,  SUGR,  SUGT,  SUGB,  SUGC,
```

```
     $ SULL(NH), SULR(NH),SULT(NH), SULB(NH), SULC(NH),
     1 SVGL,  SVGR,  SVGT,  SVGB,
     $ SVLL(NH), SVLR(NH),SVLT(NH), SVLB(NH)
      COMMON / PARAM3 /
     $ IOB(4,NT), ARL(NH), DK(NH), GTH(0:1000), DKF(NH,NH),
     $ C(16), RL(NH),VISSD(NH),IFL(NC),INDS(NC,5), PHI(NH),
     $ CPHI(NH), PHILIM(NH,NH), EPSL(NH,NH), EPSU(NH,NH),
     $ R(NI), RB(NI),  RRB(NI),COHF(0:1000),
     $ DR(NI), DZ(NJ),  DRP(NI), DZP(NJ),
     $ RDR(NI), RDZ(NJ), RDRP(NI), RDZP(NJ),
     $ AR(NI), BR(NI),  AZ(NJ),  BZ(NJ),
     $ DTODR(NI), DTODZ(NJ), DTODRP(NI), DTODZP(NJ),
     $ RRIDR(NI), RRIDRP(NI), DTOBDR(NI), DTORDR(NI)
      COMMON / PARAMI /
     $ I, IJ, IJB, IJBR, IJL, IJM, IJP, IJR, IMJM,
     $ IJRR, IJT, IJTL, IJTR, IJTT, IMJ, IMJP, IPJ,
     $ IPJM, IPJP, ITD, J, K, NSL(4), NSO(NT)
      COMMON/AREA1/
     $ ABETA(NC), CONV(NC), P(NC), PN(NC), TH(NC), THN(NC),
     $ RGFR(NC), RGFT(NC), RGFL(NC),RGP(NC),RGPN(NC), ROG(NC),
     $ RGFRY(NC),RGFTY(NC),
     $ APP(NF,NC), RUG(NC), RVG(NC),
     $ AU1(NP,NP), AV1(NP,NP), AU(NP,NP), AV(NP,NP),
     $ BU1(NP), BV1(NP), BU(NP),  BV(NP)
      COMMON/AREA2/
     $ RLFRK(NH,NC), RLFLK(NH,NC),RLFTK(NH,NC), RKPG(NH,NC),
     $ RLFRKY(NH,NC),RLFTKY(NH,NC),
     $ RUK(NH,NC), RVK(NH,NC), RLK(NH,NC), RLKN(NH,NC),
     $ UG(NC), VG(NC),  UK(NH,NC), VK(NH,NC)
       COMMON/INPUT/
     $ UIO(NO), VIO(NO),    PIO(NO), THIO(NO), TEMIO(NO),
     $ UPIO(NH,NO), VPIO(NH,NO),  THPIO(NH,NO), TEMPIO(NH,NO),
     $ WM(JXN),Q(NC),DOTM(LT),DOTMJ(LT,JXN),YIO(LT,JXN,NO),
     $ QGEN(LT),QFLOW(LT),IHO(LT),IHE(LT),HHO(LT,5),
     $ HHE(LT,5),AHO(LT,5,JXN),AHE(LT,5,JXN),Y(LT,JXN,NC),
     $ RHO(LT,5),RHE(LT,5),TOB(NC),YN(LT,JXN,NC),
     $ KEY(4),AHK(LT,5,JXN),DGG(NC),QQ(NT),TOBB(NT),COEK(NT),
     $ COE(NC),
     $ RLKMIN(NH),TSKIO(NH,NO),TSK(NH,NC),VISBL(NH,NC),
     $ VISCL(NH,NC),VISDIL(NH),PS(NH,NC),TSKN(NH,NC),
     $ SILM(NH,NC),VWLM(NH,NC),VWLS(NH,NC),GCON(NH,NC),
     $ GAMMA(NH,NC),TSKCB(NH),TSKFB(NH,NI),THL(NH,NC),
     $ TSKCL(NH),TSKCT(NH),TSKCR(NH),
     $ TSKFL(NH),TSKFT(NH),TSKFR(NH),
C-----------------------------------------
     $ APAR1(NC),APAR2(NC),APAR3(NC),APAR4(NC),APAR5(NC),APAR6(NC)
C-----------------------------------------
```

APPENDIX C

SOURCE FORTRAN CODE OF CFB1_2S.F

สถาบันวิทยบริการ
จุฬาลงกรณ์มหาวิทยาลัย

```
C*****************************************************************
C                                                                 *
C       PROGRAM CFB1.F                                            *
C       (preliminary restricted version)                          *
C                                                                 *
C       Common file: CFB1.COM                                     *
C       Input file: CFB1.DAT                                      *
C                                                                 *
C       Simulation of two-phase gas-solid flows along the riser   *
C       of a Circulating Fluidized Beds using kinetic theory      *
C                                                                 *
C       The program is a modified version of the program          *
C       MLTENR.F used for the modeling of methanol synthesys.     *
C                                                                 *
C       Augusto Neri, IIT Chicago, 9/4/1998                       *
C                                                                 *
C*****************************************************************
C       PROCRAM CFB1_2S.F                                         *
C       This program is modified in order to simulate             *
C       the flow of nanopartilces & micro size particles          *

C                                                                 *
C       It can use from viscosity and kinetic theory model        *

C                                                                 *
C       The energy equation & kinetic theory model is modified    *
C                                                                 *
C       Veeraya Jiradilok, IIT Chicago, 1/1/2006                  *
C*****************************************************************

        PROGRAM CFB1_2S
C
        INCLUDE 'cfb1.com'

        CHARACTER*80 NAME
C
        OPEN(UNIT=5,FILE='cfb1.dat')
        OPEN(UNIT=6,FILE='cfb1.out',STATUS='UNKNOWN')
        OPEN(UNIT=9,FILE='cfb1.r',FORM='UNFORMATTED')
        OPEN(UNIT=3,FILE='dxdat.sam',STATUS='UNKNOWN')
        OPEN(UNIT=4,FILE='dydat.sam',STATUS='UNKNOWN')

C*********************************************
C*******add For sample.f
        open(21,file='time.out',status='unknown')
        open(22,file='glsfp0.out',status='unknown')
        open(23,file='glsfth0.out',status='unknown')
        open(24,file='glsfv0.out',status='unknown')
        open(25,file='glsfu0.out',status='unknown')
        open(30,file='glsfgt1.out',status='unknown')
```

```
      open(27,file='glsfth1.out',status='unknown')
      open(28,file='glsfv1.out',status='unknown')
      open(29,file='glsfu1.out',status='unknown')
      open(31,file='Tsolid1.out',status='unknown')
      open(32,file='Tgas1.out',status='unknown')
c     for SOLID PHASE 2
      open(33,file='glsfth2.out',status='unknown')
      open(34,file='glsfv2.out',status='unknown')
      open(35,file='glsfu2.out',status='unknown')
      open(36,file='Tsolid2.out',status='unknown')

      READ(5,100) NAME
      WRITE(6,200) NAME
 100  FORMAT(A80)
 200  FORMAT(1X,'Simulation ID:',A80)
C
C     READ INPUT DATA FOR CFB1.DAT
      READ(5,*) (DR(I),I=1,IB2)
      READ(5,*) (DZ(J),J=1,JB2)
C
      WRITE(6,210) ITC,IB2,JB2,DR(1),DZ(1)
      WRITE(6,215) (DR(I),I=1,IB2)
      WRITE(6,216) (DZ(J),J=1,JB2)

      WRITE(3,668) (DR(I),I=1,IB2)
      WRITE(4,668) (DZ(J),J=1,JB2)

      READ(5,*) (NSL(M),M=1,4)
C
      WRITE(6,220) (NSL(M),M=1,4)
      WRITE(6,230) NIN,NOUT,NFL,NOBS
      WRITE(6,240)
C
      DO 5 N=1,NT
      READ(5,*) NSO(N),ITHMF(N),(IOB(M,N),M=1,4)
      WRITE(6,245) NSO(N),(IOB(M,N),M=1,4)
      IF(ITHMF(N).EQ.1) THEN
      READ(5,*) QQ(N),TOBB(N),COEK(N)
      ENDIF
  5   CONTINUE
C
      READ(5,*) (DK(K),K=1,NPHASE)
      READ(5,*) (PHI(K),K=1,NPHASE)
      READ(5,*) (RL(K),K=1,NPHASE)
      READ(5,*) (CL(K),K=1,NPHASE)
      READ(5,*) (VISS(K),K=1,NPHASE)
      READ(5,*) THMIN,CRES,CRESW,PHIW,BETAC
      READ(5,*) (KIN(K),RLKMIN(K),K=1,NPHASE)
C
      WRITE(6,250)
```

```
      WRITE(6,255) (DK(K),RL(K),CL(K),PHI(K),VISS(K),K=1,NPHASE)
C
      READ(5,*) UIO(1),VIO(1),PIO(1),THIO(1),TEMIO(1)
      READ(5,*) (UPIO(K,1),VPIO(K,1),THPIO(K,1),TEMPIO(K,1),
     $ TSKIO(K,1),K=1,NPHASE)
C
      WRITE(6,260)
      WRITE(6,265) UIO(1),VIO(1),PIO(1),THIO(1),TEMIO(1)
      WRITE(6,270)
      WRITE(6,275) (K,UPIO(K,1),VPIO(K,1),THPIO(K,1),TEMPIO(K,1),K=1,
     $ NPHASE)
      WRITE(6,280)
C
      DO 10 N=2,NO
      READ(5,*) UIO(N),VIO(N),PIO(N),THIO(N),TEMIO(N)
      READ(5,*) (UPIO(K,N),VPIO(K,N),THPIO(K,N),TEMPIO(K,N),
     $ TSKIO(K,N),K=1,NPHASE)
      WRITE(6,285) UIO(N),VIO(N),PIO(N),THIO(N),TEMIO(N)
 10   CONTINUE
      WRITE(6,290)
      DO 15 N=2,NO
      WRITE(6,295) (K,UPIO(K,N),VPIO(K,N),THPIO(K,N),TEMPIO(K,N),
     $  K=1,NPHASE)
 15   CONTINUE
C
      READ(5,*) (WM(JX),JX=1,JXN)
C
      WRITE(6,*)
      WRITE(6,*)'WM=',(WM(JX),JX=1,JXN)
      WRITE(6,*)
C
      READ(5,*) IRXN
      IF(IRXN.EQ.1)THEN
      WRITE(6,*)'RXN HEAT & STOICHIOMETRIC COEFF.'
      WRITE(6,*)
C
      DO 16 K=1,NPHASE+1
      READ(5,*)IHO(K),IHE(K)
      WRITE(6,*)'K=',K,'IHO=',IHO(K),'IHE=',IHE(K)
      IF(IHO(K).NE.0) THEN
      DO 17 IX=1,IHO(K)
      READ(5,*) HHO(K,IX),(AHO(K,IX,JX),JX=1,JXN)
      WRITE(6,*) HHO(K,IX),(AHO(K,IX,JX),JX=1,JXN)
17    CONTINUE
      ENDIF
      IF(IHE(K).NE.0) THEN
      DO 21 IX=1,IHE(K)
      READ(5,*) HHE(K,IX),(AHE(K,IX,JX),JX=1,JXN)
      READ(5,*) HHE(K,IX),(AHK(K,IX,JX),JX=1,JXN)
      WRITE(6,*) HHE(K,IX),(AHE(K,IX,JX),JX=1,JXN)
```

```
      WRITE(6,*) HHE(K,IX),(AHK(K,IX,JX),JX=1,JXN)
21    CONTINUE
      ENDIF
16    CONTINUE
      ENDIF
C
      WRITE(6,*)
      WRITE(6,*)'COMPOSITIONS'
      WRITE(6,*)
      DO 19 N=1,NO
      DO 19 K=1,NPHASE+1
      READ(5,*) (YIO(K,JX,N),JX=1,JXN)
      WRITE(6,*) (YIO(K,JX,N),JX=1,JXN)
19    CONTINUE
C
      READ(5,*) ITD
      READ(5,*) TIME,TSTOP,DT
      READ(5,*) TPR,TDUMP
      WRITE(6,300) ITD,TIME,TSTOP,DT,TPR,TDUMP
      READ(5,*) GRAVX,GRAVY
      WRITE(6,310) GRAVY,GRAVX
C
      WRITE(6,*)
      DO 30 J=1,JB2
      DO 30 I=1,IB2
      IJ=I+(J-1)*IB2
      TOB(IJ)=0.0
      COE(IJ)=0.0
      QF(IJ)=0.0
 30   CONTINUE
      DO 22 N=1,NT
      IF(ITHMF(N).NE.1) GOTO 22
      DO 23 J=IOB(3,N),IOB(4,N)
      DO 23 I=IOB(1,N),IOB(2,N)
      IJ=I+(J-1)*IB2
      TOB(IJ)=TOBB(N)
      COE(IJ)=COEK(N)
      QF(IJ)=QQ(N)
 23   CONTINUE
 22   CONTINUE
      DO 27 N=1,NT
      IF(ITHMF(N).NE.1) GOTO 27
      DO 24 J=1,JB2
      DO 24 I=1,IB2
      IJ=I+(J-1)*IB2
      Q(IJ)=QF(IJ)+TOB(IJ)
 24   CONTINUE
 25   FORMAT(6(1X,G12.4))
      GOTO 29
 27   CONTINUE
```

```
 29     CONTINUE
        REWIND(9)
C-------------------------------------------------------
        DO 18 K=1,NPHASE
        VISSD(K)=VISS(K)
        VISDIL(K)=5.0*SQRT(PI)/96.0*RL(K)*DK(K)
 18     CONTINUE
C-------------------------------------------------------
        TTIM=0.0
        IF(ITD.EQ.2) CALL TAPERD
        DO 20 K=1,NPHASE
        ARL(K)=1./RL(K)
 20     CONTINUE
C
        CALL FLIC
        CALL SETUP
        CALL PROG
        STOP
C
 210    FORMAT(/' 1. GEOMETRY'/'   A. COORDINATES
   $    (CART=0, CYLIND=1, SPHER=2)
   $    =',I3/'   B. MESH SIZE,    IB2=',I3,6X,'JB2=',I3/'
   $    C. CELL SIZE'
   $   ,',    DR=',1PE12.4,'   DZ=',1PE12.4)
 215    FORMAT(7X,'DR='/8(2X,F6.3))
 216    FORMAT(7X,'DZ='/8(2X,F6.3))
 220    FORMAT(/' 2. CELL FLAGS'/'   A. BOUNDARIES (FREE-SLIP=2
   $    NO-SLIP=3)'
   $    /7X,'BOTTOM=',I3,'   LEFT=',I3,'   TOP=',I3,'  RIGHT=',I3)
 230    FORMAT('   B. INLETS =',I3,' OUTLETS =',I3,' FLUIDS =', I3,
   $   ' OBSTACLES =',I3)
 240    FORMAT('     SLIP',10X,'------COORDINATES------')
 245    FORMAT(5X,I3,4(4X,I5))
 250    FORMAT(/' 3. PARTICULATE PHASE DATA'/7X,'DIAMETER
   $    MACROSCOPIC',
   $   ' DENSITY',4X,'PARTICLE HEAT CAPACITY',4X,'SPHERICITY',
   $    4X,'VISCOSITY')
 255    FORMAT((2(6X,G10.3),13X,G10.3,7X,G10.3,7X,G10.3))
 260    FORMAT(/' 4. INITIAL AND BOUNDARY DATA'/'   A. INITIAL DATA',
   $   ' (FLUID)'/11X,'UO',13X,'VO',13X,'PO',12X,'THO',11X,'TEMGO')
 265    FORMAT((2X,5(4X,1PE11.4)))
 270    FORMAT('   B. INITIAL DATA  (SOLID)'/8X,'PHASE',9X,
   $   'UKO',11X,'VKO',10X,'THKO',9X,'TEMKO')
 275    FORMAT((8X,I3,3X,4(3X,1PE11.4)))
 280    FORMAT('   C. INFLOW - OUTFLOW DATA  (FLUID)'/10X,'UIO',12X,
   $   'VIO',12X,'PIO',12X,'THIO',11X,'TEMIO')
 285    FORMAT((2X,5(4X,1PE11.4)))
 290    FORMAT('   D. INFLOW - OUTFLOW DATA  (SOLID)'/8X,'PHASE',9X,
   $   'UPIO',11X,'VPIO',10X,'THPIO',9X,'TEMPIO')
 295    FORMAT((8X,I3,3X,4(4X,1PE11.4)))
```

```
 300    FORMAT(/' 5. CONTROL'/ 3X,'A. DUMP AND RESTART,    ITD='
   $    ,I3/3X,
   $    'B. TIME   TSTART=',1PE11.4,'  TSTOP=',1PE11.4,' DT=',
   $    1PE11.4/
   $    '   C. PRINTING AND PLOTTING,   TPR=',1PE11.4,' TDUMP=',
   $    1PE11.4)
 310    FORMAT(/' 6. GRAVITY'/'   A. GRAVY=',1PE15.7,'   GRAVX='
   $    ,1PE15.7)
C
668     FORMAT(F9.5)
        END
C
C*****************************************************************
**
C
        SUBROUTINE BDRY
C
        INCLUDE 'cfb1.com'
C
        DO 200 J=2,JB1
        DO 200 I=2,IB1
        IJ=I+(J-1)*IB2
        IF(IFL(IJ).EQ.1) THEN
        RGPN(IJ)=RGP(IJ)
        THN(IJ)=TH(IJ)
        SIEGN(IJ)=SIEG(IJ)
        TG(IJ)=C1+SIEG(IJ)/CG
        CALL ROGY(IJ)
        AKG(IJ)=8.67D5*(TG(IJ)/1400.0)**1.786
        DO 9 K=1,NPHASE
        SIELN(K,IJ)=SIEL(K,IJ)
        IF(RLK(K,IJ).EQ.0.0) THEN
        TL(K,IJ)=0.0
        ELSE
        TL(K,IJ)=C2+SIEL(K,IJ)/CL(K)
        ENDIF
        CALL THRCON
        TSKN(K,IJ)=TSK(K,IJ)
        RLKN(K,IJ)=RLK(K,IJ)
  9     CONTINUE
C
        IPJ=IJ+1
        IJP=IJ+IB2
        IMJ=IJ-1
        IJM=IJ-IB2
        IPJP=IJP+1
        IMJP=IJP-1
        IPJM=IJM+1
        NFLR=IFL(IPJ)
        NFLTR=IFL(IPJP)
```

```
      NFLT=IFL(IJP)
c************ ADD FOR LEFT OUTLET
      NFLL=IFL(IMJ)
      NFLTL=IFL(IMJP)
C ****************************
C
C     RIGHT OUTLET

      IF(NFLR.EQ.4.OR.NFLR.GE.7) THEN
      N1=IJ
      N2=IPJ
      IF(NFLR.EQ.4.OR.UG(N1).GT.0.)THEN
      RGFR(N2)=RGFR(N1)
      RGP(N2)=RGP(N1)
      RUG(N2)=RUG(N1)
      TH(N2)=TH(N1)
c     add ****3 feb calculate the solid volume fravtion at BC.
      Do 10 K=1,NPHASE
      THL(K,N2)=THL(K,N1)
 10   CONTINUE
C  ***********************************************************
      TG(N2)=TG(N1)
      DO 14 JX=1,JXN
      YN(1,JX,N2)=YN(1,JX,N1)
      Y(1,JX,N2)=Y(1,JX,N1)
 14   CONTINUE
      DO 15 K=1,NPHASE
      RLFRK(K,N2)=RLFRK(K,N1)
      RLK(K,N2)=RLK(K,N1)
      TSK(K,N2)=TSK(K,N1)
      TSKN(K,N2)=TSK(K,N1)
      RUK(K,N2)=RUK(K,N1)
      DO 13 JX=1,JXN
      YN(K+1,JX,N2)=YN(K+1,JX,N1)
      Y(K+1,JX,N2)=Y(K+1,JX,N1)
 13   CONTINUE
      TL(K,N2)=TL(K,N1)
 15   CONTINUE
      IF(NFLR.GE.7)THEN
      IJ=N2
      CALL CNVERT
      IJ=N1
      ELSE
      P(N2)=P(N1)
      ENDIF
      ENDIF
      IF(NFLTR.GE.4)THEN
      VG(N2)=VG(N1)
      DO 17 K=1,NPHASE
      VK(K,N2)=VK(K,N1)
```

```
 17     CONTINUE
        ENDIF
        DO 18 K=1,NPHASE
        UK(K,N2)=UK(K,N1)
 18     CONTINUE
        UG(N2)=UG(N1)
C---------------------------------------------
        IF(NFLR.EQ.8)THEN
        DO 20 K=1,NPHASE
        UK(K,N1)=0.0
        RLFRK(K,N1)=0.0
        UK(K,N2)=0.0
        VK(K,N2)=0.0
 20     CONTINUE
        ENDIF
C---------------------------------------------
        ENDIF
C
C       TOP OUTLET
        IF(NFLT.EQ.4.OR.NFLT.GE.7) THEN
        N1=IJ
        N2=IJP
        IF(NFLT.EQ.4.OR.VG(N1).GT.0.)THEN
        RGFT(N2)=RGFT(N1)
        RGP(N2)=RGP(N1)
        RVG(N2)=RVG(N1)
        TH(N2)=TH(N1)
c       add ****3 feb calculate the solid volume fravtion at BC.
        Do 100 K=1,NPHASE
        THL(K,N2)=THL(K,N1)
100      CONTINUE
C  ***********************************************************
        TG(N2)=TG(N1)
        DO 24 JX=1,JXN
        YN(1,JX,N2)=YN(1,JX,N1)
        Y(1,JX,N2)=Y(1,JX,N1)
 24     CONTINUE
        DO 25 K=1,NPHASE
        RLFTK(K,N2)=RLFTK(K,N1)
        TSK(K,N2)=TSK(K,N1)
        TSKN(K,N2)=TSK(K,N1)
        RLK(K,N2)=RLK(K,N1)
        RVK(K,N2)=RVK(K,N1)
        DO 23 JX=1,JXN
        YN(K+1,JX,N2)=YN(K+1,JX,N1)
        Y(K+1,JX,N2)=Y(K+1,JX,N1)
 23     CONTINUE
        TL(K,N2)=TL(K,N1)
 25     CONTINUE
        IF(NFLT.GE.7)THEN
```

```
      IJ=N2
      CALL CNVERT
      IJ=N1
      ELSE
      P(N2)=P(N1)
      ENDIF
      ENDIF
      IF(NFLTR.GE.4) THEN
      UG(N2)=0.0
      DO 27 K=1,NPHASE
      UK(K,N2)=0.0
 27   CONTINUE
      ENDIF
      RGP(N2)=RGP(N1)
      VG(N2)=VG(N1)
      DO 28 K=1,NPHASE
      VK(K,N2)=VK(K,N1)
 28   CONTINUE
      IF(NFLT.EQ.8)THEN
      DO 30 K=1,NPHASE
      UK(K,N2)=0.0
      VK(K,N2)=0.0
 30   CONTINUE
      ENDIF
      ENDIF
C
C     ADD 3 FEB 05
C     LELT OUTLET
      IF(NFLL.EQ.4.OR.NFLL.GE.7) THEN
      N1=IJ
      N2=IMJ
      IF(NFLL.EQ.4.OR.UG(N1).GT.0.)THEN
      RGFL(N2)=RGFL(N1)
      RGP(N2)=RGP(N1)
      RUG(N2)=RUG(N1)
      TH(N2)=TH(N1)
c     add ****3 feb calculate the solid volume fravtion at BC.
      Do 31 K=1,NPHASE
      THL(K,N2)=THL(K,N1)
31    CONTINUE
C ***********************************************************
      TG(N2)=TG(N1)
      DO 34 JX=1,JXN
      YN(1,JX,N2)=YN(1,JX,N1)
      Y(1,JX,N2)=Y(1,JX,N1)
 34   CONTINUE
      DO 35 K=1,NPHASE
      RLFLK(K,N2)=RLFLK(K,N1)
      RLK(K,N2)=RLK(K,N1)
      TSK(K,N2)=TSK(K,N1)
```

```
      TSKN(K,N2)=TSK(K,N1)
      RUK(K,N2)=RUK(K,N1)
      DO 33 JX=1,JXN
      YN(K+1,JX,N2)=YN(K+1,JX,N1)
      Y(K+1,JX,N2)=Y(K+1,JX,N1)
 33   CONTINUE
      TL(K,N2)=TL(K,N1)
 35   CONTINUE
      IF(NFLL.GE.7)THEN
      IJ=N2
      CALL CNVERT
      IJ=N1
      ELSE
      P(N2)=P(N1)
      ENDIF
      ENDIF
      IF(NFLTL.GE.4)THEN
      VG(N2)=VG(N1)
      DO 37 K=1,NPHASE
      VK(K,N2)=VK(K,N1)
 37   CONTINUE
      ENDIF
      DO 38 K=1,NPHASE
      UK(K,N2)=UK(K,N1)
 38   CONTINUE
      UG(N2)=UG(N1)
C---------------------------------------------
      IF(NFLL.EQ.8)THEN
      DO 40 K=1,NPHASE
      UK(K,N1)=0.0
      RLFLK(K,N1)=0.0
      UK(K,N2)=0.0
      VK(K,N2)=0.0
 40   CONTINUE
      ENDIF
C---------------------------------------------
      ENDIF
C     OBSTACLES
C
      IF(IFL(IJ).EQ.1) THEN
      IF(NFLR.EQ.2) THEN
      VG(IPJ)=VG(IJ)
      DO 91 K=1,NPHASE
      TSKN(K,IPJ)=TSKN(K,IJ)
      VK(K,IPJ)=VK(K,IJ)
 91   CONTINUE
      ELSEIF (NFLR.EQ.3) THEN
      VG(IPJ)=-VG(IJ)
      DO 92 K=1,NPHASE
C-------------------------------------------------------
```

```
      IF(RLK(K,IJ).GT.RLKMIN(K)) THEN
      IF(KIN(K).EQ.1.AND.TSKN(K,IJ).GT.0.0) THEN
      THL(K,IJ)=ARL(K)*RLK(K,IJ)
      G0=1.0/(1.0-(THL(K,IJ)/(1.0-THMIN))**(1./3.))
      PLP=(6.0*VISCL(K,IJ)*(1.0-THMIN))
     $ /(PI*SQRT(3.)*PHIW*RLK(K,IJ)*G0*SQRT(TSKN(K,IJ)))
      ELSE
      PLP=DK(K)*(RL(K)/RLK(K,IJ))**(1./3.)
      ENDIF
      ELSE
      PLP=0.0
      ENDIF
      VK(K,IPJ)=VK(K,IJ)*(2.*PLP-DR(I+1))/(2.*PLP+DR(I))
      IF(RLK(K,IJ).GT.RLKMIN(K).AND.KIN(K).EQ.1) THEN
      THL(K,IJ)=ARL(K)*RLK(K,IJ)
      G0=1.0/(1.0-(THL(K,IJ)/(1.0-THMIN))**(1./3.))
      CS1=(1.0+CRES)*THL(K,IJ)*G0
      CS4=2.*VISDIL(K)/((1.+CRES)*G0)
      GCOND=3.75*CS4*(1.+1.2*CS1)**2
     $ +2.*RLK(K,IJ)*DK(K)*CS1/PI**0.5
      GAM=SQRT(3.)*PI*RLK(K,IJ)*(1.-CRESW**2)*G0
     $  /(4.*(1.0-THMIN))
      PGR1=GCOND/GAM
C
      VW=VK(K,IJ)+(VK(K,IPJ)-VK(K,IJ))
     $ *DR(I)/(DR(I)+DR(I+1))
      PGR2=PI*SQRT(3.)*PHIW*RLK(K,IJ)*VW*VW*G0
     $ /(6.0*(1.0-THMIN))/GAM
      TSKN(K,IPJ)=(TSKN(K,IJ)*(2.*PGR1-DR(I+1))
     $ +PGR2*(DR(I)+DR(I+1)))/(2.*PGR1+DR(I))
      ENDIF
C-----------------------------------------------------------
 92   CONTINUE
      ENDIF
C
      IF(NFLT.EQ.2) THEN
      UG(IJP)=UG(IJ)
      DO 93 K=1,NPHASE
      TSKN(K,IJP)=TSKN(K,IJ)
      UK(K,IJP)=UK(K,IJ)
 93   CONTINUE
      ELSEIF(NFLT.EQ.3) THEN
      UG(IJP)=-UG(IJ)
      VG(IJP)=-VG(IJ)
      DO 94 K=1,NPHASE
      VK(K,IJP)=-VK(K,IJ)
C-----------------------------------------------------------
      IF(RLK(K,IJ).GT.RLKMIN(K)) THEN
      IF(KIN(K).EQ.1.AND.TSKN(K,IJ).GT.0.0) THEN
      THL(K,IJ)=ARL(K)*RLK(K,IJ)
```

```
      G0=1.0/(1.0-(THL(K,IJ)/(1.0-THMIN))**(1./3.))
      PLP=(6.0*VISCL(K,IJ)*(1.0-THMIN))
     $ /(PI*SQRT(3.)*PHIW*RLK(K,IJ)*G0*SQRT(TSKN(K,IJ)))
      ELSE
      PLP=DK(K)*(RL(K)/RLK(K,IJ))**(1./3.)
      ENDIF
      ELSE
      PLP=0.0
      ENDIF
      UK(K,IJP)=UK(K,IJ)*(2.*PLP-DZ(J+1))/(2.*PLP+DZ(J))
      IF(RLK(K,IJ).GT.RLKMIN(K).AND.KIN(K).EQ.1) THEN
      THL(K,IJ)=ARL(K)*RLK(K,IJ)
      G0=1.0/(1.0-(THL(K,IJ)/(1.0-THMIN))**(1./3.))
      CS1=(1.0+CRES)*THL(K,IJ)*G0
      CS4=2.*VISDIL(K)/((1.+CRES)*G0)
      GCOND=3.75*CS4*(1.+1.2*CS1)**2
     $ +2.*RLK(K,IJ)*DK(K)*CS1/PI**0.5
      GAM=SQRT(3.)*PI*RLK(K,IJ)*(1.-CRESW**2)*G0
     $ /(4.*(1.0-THMIN))
      PGR1=GCOND/GAM
C
      VW=UK(K,IJ)+(UK(K,IJP)-UK(K,IJ))
     $ *DZ(J)/(DZ(J)+DZ(J+1))
      PGR2=PI*SQRT(3.)*PHIW*RLK(K,IJ)*VW*VW*G0
     $ /(6.0*(1.0-THMIN))/GAM
      TSKN(K,IJP)=(TSKN(K,IJ)*(2.*PGR1-DZ(J+1))
     $ +PGR2*(DZ(J)+DZ(J+1)))/(2.*PGR1+DZ(J))
      ENDIF
C-----------------------------------------------------------
 94   CONTINUE
      ENDIF
C
      NFLL=IFL(IMJ)
      NFLTL=IFL(IMJP)
C
      IF(NFLL.EQ.2) THEN
      VG(IMJ)=VG(IJ)
      UG(IMJ)=UG(IJ)
      DO 95 K=1,NPHASE
      TSKN(K,IMJ)=TSKN(K,IJ)
      VK(K,IMJ)=VK(K,IJ)
      UK(K,IMJ)=UK(K,IJ)
 95   CONTINUE
      ELSEIF(NFLL.EQ.3) THEN
      VG(IMJ)=-VG(IJ)
      DO 96 K=1,NPHASE
C-----------------------------------------------------------
      IF(RLK(K,IJ).GT.RLKMIN(K)) THEN
      IF(KIN(K).EQ.1.AND.TSKN(K,IJ).GT.0.0) THEN
      THL(K,IJ)=ARL(K)*RLK(K,IJ)
```

```
      G0=1.0/(1.0-(THL(K,IJ)/(1.0-THMIN))**(1./3.))
      PLP=(6.0*VISCL(K,IJ)*(1.0-THMIN))
     $ /(PI*SQRT(3.)*PHIW*RLK(K,IJ)*G0*SQRT(TSKN(K,IJ)))
      ELSE
      PLP=DK(K)*(RL(K)/RLK(K,IJ))**(1./3.)
      ENDIF
      ELSE
      PLP=0.0
      ENDIF
      VK(K,IMJ)=VK(K,IJ)*(2.*PLP-DR(I-1))/(2.*PLP+DR(I))
      IF(RLK(K,IJ).GT.RLKMIN(K).AND.KIN(K).EQ.1) THEN
      THL(K,IJ)=ARL(K)*RLK(K,IJ)
      G0=1.0/(1.0-(THL(K,IJ)/(1.0-THMIN))**(1./3.))
      CS1=(1.0+CRES)*THL(K,IJ)*G0
      CS4=2.*VISDIL(K)/((1.+CRES)*G0)
      GCOND=3.75*CS4*(1.+1.2*CS1)**2
     $ +2.*RLK(K,IJ)*DK(K)*CS1/PI**0.5
      GAM=SQRT(3.)*PI*RLK(K,IJ)*(1.-CRESW**2)*G0
     $ /(4.*(1.0-THMIN))
      PGR1=GCOND/GAM
C
      VW=VK(K,IJ)+(VK(K,IMJ)-VK(K,IJ))
     $ *DR(I)/(DR(I)+DR(I-1))
      PGR2=PI*SQRT(3.)*PHIW*RLK(K,IJ)*VW*VW*G0
     $ /(6.0*(1.0-THMIN))/GAM
      TSKN(K,IMJ)=(TSKN(K,IJ)*(2.*PGR1-DR(I-1))
     $ +PGR2*(DR(I)+DR(I-1)))/(2.*PGR1+DR(I))
      ENDIF
C-----------------------------------------------------------
 96   CONTINUE
      ENDIF
C
      NFLB=IFL(IJM)
      NFLBR=IFL(IPJM)
C
      IF(NFLB.EQ.2) THEN
      UG(IJM)=UG(IJ)
      DO 97 K=1,NPHASE
      TSKN(K,IJM)=TSKN(K,IJ)
      UK(K,IJM)=UK(K,IJ)
 97   CONTINUE
      ELSEIF(NFLB.EQ.3) THEN
      UG(IJM)=-UG(IJ)
      VG(IJM)=-VG(IJ)
      DO 98 K=1,NPHASE
      VK(K,IJM)=-VK(K,IJ)
      IF(RLK(K,IJ).GT.RLKMIN(K)) THEN
      IF(KIN(K).EQ.1.AND.TSKN(K,IJ).GT.0.0) THEN
      THL(K,IJ)=ARL(K)*RLK(K,IJ)
      G0=1.0/(1.0-(THL(K,IJ)/(1.0-THMIN))**(1./3.))
```

```
      PLP=(6.0*VISCL(K,IJ)*(1.0-THMIN))
     $ /(PI*SQRT(3.)*PHIW*RLK(K,IJ)*G0*SQRT(TSKN(K,IJ)))
      ELSE
      PLP=DK(K)*(RL(K)/RLK(K,IJ))**(1./3.)
      ENDIF
      ELSE
      PLP=0.0
      ENDIF
      UK(K,IJM)=UK(K,IJ)*(2.*PLP-DZ(J-1))/(2.*PLP+DZ(J))
C
      IF(RLK(K,IJ).GT.RLKMIN(K).AND.KIN(K).EQ.1) THEN
      THL(K,IJ)=ARL(K)*RLK(K,IJ)
      G0=1.0/(1.0-(THL(K,IJ)/(1.0-THMIN))**(1./3.))
      CS1=(1.0+CRES)*THL(K,IJ)*G0
      CS4=2.*VISDIL(K)/((1.+CRES)*G0)
      GCOND=3.75*CS4*(1.+1.2*CS1)**2
     $ +2.*RLK(K,IJ)*DK(K)*CS1/PI**0.5
      GAM=SQRT(3.)*PI*RLK(K,IJ)*(1.-CRESW**2)*G0
     $ /(4.*(1.0-THMIN))
      PGR1=GCOND/GAM
C
      VW=UK(K,IJ)+(UK(K,IJM)-UK(K,IJ))
     $ *DZ(J)/(DZ(J)+DZ(J-1))
      PGR2=PI*SQRT(3.)*PHIW*RLK(K,IJ)*VW*VW*G0
     $ /(6.0*(1.0-THMIN))/GAM
      TSKN(K,IJM)=(TSKN(K,IJ)*(2.*PGR1-DZ(J-1))
     $ +PGR2*(DZ(J)+DZ(J-1)))/(2.*PGR1+DZ(J))
      ENDIF
C-----------------------------------------------------------
 98   CONTINUE
      ELSEIF(NFLB.EQ.5) THEN
      DO 99 K=1,NPHASE
      TSKN(K,IJM)=TSKN(K,IJM)
 99   CONTINUE
      ENDIF
      ENDIF
      ENDIF
 200  CONTINUE
C
      RETURN
      END
C
C*****************************************************************
**
C
      SUBROUTINE BETAS
C
      INCLUDE 'cfb1.com'
C      convergence criteria to 1 exp-4
      PARAMETER (EPSG=1.0D-4)
```

```
C
      DO 10 J=2,JB1
      DO 10 I=2,IB1
      IJ=I+(J-1)*IB2
      IF(IFL(IJ).NE.1) GOTO 10
C
      CALL INDXA
      IF(IFL(IPJ).EQ.1.OR.IFL(IPJ).EQ.4.OR.IFL(IPJ).GE.7)THEN
      RIG=RB(I)*(AR(I)*TH(IJ)+BR(I)*TH(IJR))
      ELSE
      RIG=0.
      ENDIF
      IF(IFL(IMJ).NE.2.AND.IFL(IMJ).NE.3.AND.IFL(IMJ).NE.5)THEN
      EFL=RB(I-1)*(BR(I-1)*TH(IJ)+AR(I-1)*TH(IJL))
      ELSE
      EFL=0.
      ENDIF
      IF(IFL(IJP).EQ.1.OR.IFL(IJP).EQ.4.OR.IFL(IJP).GE.7)THEN
      TOP=AZ(J)*TH(IJ)+BZ(J)*TH(IJT)
      ELSE
      TOP=0.
      ENDIF
      IF(IFL(IJM).EQ.1.OR.IFL(IJM).EQ.4.OR.IFL(IJM).EQ.6)THEN
      BOT=BZ(J-1)*TH(IJ)+AZ(J-1)*TH(IJB)
      ELSE
      BOT=0.
      ENDIF
C
      CONV(IJ)=EPSG*RGP(IJ)
      RBETA=TH(IJ)*ROG(IJ)/P(IJ)+DTODZ(J)*DTODZ(J)*(TOP+BOT)+
   $  DTORDR(I)*DTODR(I)*(RIG+EFL)
      ABETA(IJ)=1./RBETA
 10   CONTINUE
C
      RETURN
      END
C
C*****************************************************************
**
C
      SUBROUTINE CNVERT
C
      INCLUDE 'cfb1.com'
C
      CALL ROGY(IJ)
      RGP(IJ)=ROG(IJ)*TH(IJ)
      RGPN(IJ)=RGP(IJ)
      SIEG(IJ)=(TG(IJ)-C1)*CG
      SIEGN(IJ)=SIEG(IJ)
      AKG(IJ)=8.67D5*(TG(IJ)/1400.0)**1.786
```

```
      DO 10 K=1,NPHASE
      TSKN(K,IJ)=TSK(K,IJ)
      RLKN(K,IJ)=RLK(K,IJ)
      SIEL(K,IJ)=(TL(K,IJ)-C2)*CL(K)
      SIELN(K,IJ)=SIEL(K,IJ)
 10   CONTINUE
C
      RETURN
      END
C
C*****************************************************************
**
C
      SUBROUTINE FLIC
C
      INCLUDE 'cfb1.com'
C
      IJ=0
      DO 150 J=1,JB2
      DO 150 I=1,IB2
      IJ=IJ+1
      IFL(IJ)=1
      IF (J.EQ.JB2) THEN
      IFL(IJ)=NSL(3)
      ELSEIF(J.EQ.1) THEN
      IFL(IJ)=NSL(1)
      ENDIF
      IF(I.EQ.1) THEN
      IFL(IJ)=NSL(2)
      ELSEIF (I.EQ.IB2) THEN
      IFL(IJ)=NSL(4)
      ENDIF
150   CONTINUE
      DO 300 N=1,NT
      DO 300 I=IOB(1,N),IOB(2,N)
      DO 300 J=IOB(3,N),IOB(4,N)
      IJ=I+(J-1)*IB2
      IFL(IJ)=NSO(N)
300   CONTINUE
      IF(IFL(IB1JB2).EQ.4.AND.IFL(IB2JB1).EQ.4)IFL(IB2JB2)=4
      IF(IFL(IB1JB2).EQ.7.AND.IFL(IB2JB1).EQ.7)IFL(IB2JB2)=7
C
      RETURN
      END
C
C*****************************************************************
**
C
      SUBROUTINE HEATCG
C
```

```
      INCLUDE 'cfb1.com'
C
C     CALCULATES THE  HEAT FLUXES FROM GAS CONDUCTIVITY
C
      HFGB=(BZ(J-1)*AKG(IJ)+AZ(J-1)*AKG(IJB))*
     $ (BZ(J-1)*TH(IJ)+AZ(J-1)*TH(IJB))*
     $ (TG(IJ)-TG(IJB))*RDZP(J-1)
C
      ENTRY HEATGA
      HFGL=RB(I-1)*(BR(I-1)*AKG(IJ)+AR(I-1)*AKG(IJL))
     $ *(BR(I-1)*TH(IJ)+AR(I-1)*TH(IJL))*
     $ (TG(IJ)-TG(IJL))*RDRP(I-1)
C
      ENTRY HEATGB
      HFGR=RB(I)*(AR(I)*AKG(IJ)+BR(I)*AKG(IJR))
     $ *(AR(I)*TH(IJ)+BR(I)*TH(IJR))*
     $ (TG(IJR)-TG(IJ))*RDRP(I)
      HFGT=(AZ(J)*AKG(IJ)+BZ(J)*AKG(IJT))
     $ *(AZ(J)*TH(IJ)+BZ(J)*TH(IJT))*
     $ (TG(IJT)-TG(IJ))*RDZP(J)
C
      RETURN
      END
C
C*********************************************************************
**
C
      SUBROUTINE HEATCL
C
      INCLUDE 'cfb1.com'
C
C     CALCULATES THE  HEAT FLUXES FROM SOLIDS CONDUCTIVITY
C
      HFLB(K,I)=(BZ(J-1)*AKL(K,IJ)+AZ(J-1)*AKL(K,IJB))
     $ *(BZ(J-1)*RLK(K,IJ)+AZ(J-1)*RLK(K,IJB))
     $ * (TL(K,IJ)-TL(K,IJB))*ARL(K)*RDZP(J-1)
C
      ENTRY HEATLA
      HFLL(K)=RB(I-1)*(BR(I-1)*AKL(K,IJ)+AR(I-1)*AKL(K,IJL))
     $ * (BR(I-1)*RLK(K,IJ)+AR(I-1)*RLK(K,IJL))
     $ *(TL(K,IJ)-TL(K,IJL))*ARL(K)*RDRP(I-1)
C
      ENTRY HEATLB
      HFLR(K)=RB(I)*(AR(I)*AKL(K,IJ)+BR(I)*AKL(K,IJR))
     $ * (AR(I)*RLK(K,IJ)+BR(I)*RLK(K,IJR))
     $ *(TL(K,IJR)-TL(K,IJ))*ARL(K)*RDRP(I)
      HFLT(K)=(AZ(J)*AKL(K,IJ)+BZ(J)*AKL(K,IJT))
     $ * (AZ(J)*RLK(K,IJ)+BZ(J)*RLK(K,IJT))
     $ *(TL(K,IJT)-TL(K,IJ))*ARL(K)*RDZP(J)
C
```

```
      RETURN
      END
C
C*****************************************************************
**
C
      SUBROUTINE ICONV
C
      INCLUDE 'cfb1.com'
      DIMENSION AI(NP,NP),BI(NP)
C
C     FINAL UPDATING OF THE SPECIFIC ENERGIES ( ENTHALPIES )
C
      DO 100 J=2,JB1
      DO 100 I=2,IB1
      IJ=I+(J-1)*IB2
      IF(IFL(IJ).EQ.1) THEN
      CALL INDXA
      CALL SIEGF
      CALL QRXN
      CALL QFLUX
C ******************************** ADDING
      DPZ=(AZ(J)-BZ(J-1))*P(IJ)+BZ(J)*p(IJT)-AZ(J-1)*P(IJB)
      DPR=RB(I)*(BR(I)*P(IJR)+AR(I)*P(IJ))
      1-RB(I-1)*(BR(I-1)*P(IJ)+AR(I-1)*P(IJL))

      BI(1)=RGP(IJ)*(P(IJ)-PN(IJ)+0.5*(DTODZ(J)*DPZ
      1*(VG(IJ)+VG(IJM))+DTORDR(I)*DPR
      1*(RB(I)*UG(IJ)+RB(I-1)*UG(IMJ))/R(I)))
C
      AI(1,1)=RGP(IJ)
      BI(1)=BI(1)+RGP(IJ)*SIEG(IJ)-SIEGN(IJ)*(RGP(IJ)-RGPN(IJ))-
     $ DTODZ(J)*(EGFT-EGFB(I))-DTORDR(I)*(EGFR-EGFL)

      DO 10 K=1,NPHASE
      CALL SIELF
      KP=K+1
      RHT=-0.5*DT*RHEAT(K,IJ)
      AI(1,KP)=RHT/CL(K)
      AI(KP,1)=RHT/CG
      AI(1,1)=AI(1,1)-AI(KP,1)
      AI(KP,KP)=RLK(K,IJ)-AI(1,KP)
      RIT=(SIEG(IJ)/CG-SIEL(K,IJ)/CL(K)+TL(K,IJ)-TG(IJ))*RHT
      BI(1)=BI(1)-RIT
      BI(KP)=RLK(K,IJ)*SIEL(K,IJ)-SIELN(K,IJ)*(RLK(K,IJ)-
     $ RLKN(K,IJ))+
     $ RIT-DTODZ(J)*(ELFT(K)-ELFB(K,I))-DTORDR(I)*(ELFR(K)
     $ -ELFL(K))+VISCL(K,IJ)*VWLS(K,IJ)
     $ +(VISBL(K,IJ)-(2./3.)*VISCL(K,IJ))*VWLM(K,IJ)
      BI(KP)=BI(KP)+DT*(QGEN(KP)+QFLOW(KP))
```

```
 10     CONTINUE
        CALL IINV(NPHS1,AI,BI)
        SIEG(IJ)=BI(1)
        DO 20 K=1,NPHASE
        SIEL(K,IJ)=BI(K+1)
        ELFL(K)=ELFR(K)
        ELFB(K,I)=ELFT(K)
 20     CONTINUE
        EGFB(I)=EGFT
        EGFL=EGFR
        ENDIF
 100    CONTINUE
C
        RETURN
        END
C*****************************************************************
**
C
        SUBROUTINE IGIL
C
        INCLUDE 'cfb1.com'
        DIMENSION AI(NP,NP),BI(NP)
C
        CALL QRXN
        CALL QFLUX
        AI(1,1)=RGP(IJ)
        BI(1)=RGP(IJ)*SIEGN(IJ)
        BI(1)=BI(1)+DT*(QGEN(1)+QFLOW(1))
        DO 10 K=1,NPHASE
        KP=K+1
        RHT=-0.5*DT*RHEAT(K,IJ)
        AI(1,KP)=RHT/CL(K)
        AI(KP,1)=RHT/CG
        AI(1,1)=AI(1,1)-AI(KP,1)
        AI(KP,KP)=RLK(K,IJ)-AI(1,KP)
        RIT=(SIEGN(IJ)/CG-SIELN(K,IJ)/CL(K)+TLN(K,IJ)-TGN(IJ))*RHT
        BI(1)=BI(1)-RIT
        BI(KP)=RLK(K,IJ)*SIELN(K,IJ)+RIT
        BI(KP)=BI(KP)+DT*(QGEN(KP)+QFLOW(KP))
 10     CONTINUE
        CALL IINV(NPHS1,AI,BI)
        SIEG(IJ)=BI(1)
        DO 100 K=1,NPHASE
        SIEL(K,IJ)=BI(K+1)
 100    CONTINUE
C
        RETURN
        END
C
```

```
C*****************************************************************
**
C
      SUBROUTINE IINV(NP,A,B)
C
      IMPLICIT REAL*8(A-H,O-Z)
      DIMENSION A(NP,NP),B(NP)
C
C     INVERSE OF MATRIX WITH NON-ZERO FIRST COLUMN,
C     FIRST ROW & DIAGONAL COLUMN
C
      DO 10 K=NP,2,-1
      IF(ABS(A(K,K)).LE.1.D-6) THEN
      A(1,K)=0.0
      A(K,1)=0.0
      B(K)=0.0
      ELSE
      DIV=1./A(K,K)
      A(K,1)=A(K,1)*DIV
      B(K)=B(K)*DIV
      B(1)=B(1)-A(1,K)*B(K)
      A(1,1)=A(1,1)-A(1,K)*A(K,1)
      ENDIF
 10   CONTINUE
      B(1)=B(1)/A(1,1)
      DO 20 K=2,NP
      B(K)=B(K)-A(K,1)*B(1)
 20   CONTINUE
C
      RETURN
      END
C
C*****************************************************************
**
C
      SUBROUTINE INDX
C
      INCLUDE 'cfb1.com'
C
      IMJP=IJ-1+IB2
      IJTL=IMJP
      IF((IFL(IMJP).EQ.2).OR.(IFL(IMJP).EQ.3)) IJTL=IJ+IB2
      IPJM=IJ+1-IB2
      IJBR=IPJM
      IF((IFL(IPJM).EQ.2).OR.(IFL(IPJM).EQ.3)) IJBR=IJ+1
      IJRR=IJ+2
      IF(I.EQ.IB1) IJRR=IJ+1
      IF((IFL(IJRR).EQ.2).OR.(IFL(IJRR).EQ.3)) IJRR=IJ+1
      IJTT=IJ+IB2+IB2
      IF(J.EQ.JB1) IJTT=IJ+IB2
```

```
      IF((IFL(IJTT).EQ.2).OR.(IFL(IJTT).EQ.3)) IJTT=IJ+IB2
C
      ENTRY INDXA
      IPJ=IJ+1
      IJP=IJ+IB2
      IMJ=IJ-1
      IJM=IJ-IB2
      IPJP=IJP+1
      IMJM=IJM-1
      IJR=INDS(IJ,1)
      IJL=INDS(IJ,2)
      IJT=INDS(IJ,3)
      IJB=INDS(IJ,4)
      IJTR=INDS(IJ,5)
C
      RETURN
      END
C
C*****************************************************************
**
C
      SUBROUTINE ITER
C
      INCLUDE 'cfb1.com'
      LOGICAL MUSTIT
      PARAMETER (LMAX=5,OMEGA=1.05)
C
      DO 5 IJ=1,IB2JB2
      PN(IJ)=P(IJ)
      TGN(IJ)=C1+SIEGN(IJ)/CG
      DO 5 K=1,NPHASE
      IF(RLK(K,IJ).EQ.0.0) THEN
      TLN(K,IJ)=0.0
      ELSE
      TLN(K,IJ)=C2+SIELN(K,IJ)/CL(K)
      ENDIF
 5    CONTINUE
      MUSTIT=.FALSE.
      DO 200 NIT=1,2000
      DO 100 J=2,JB1
      DO 100 I=2,IB1
      IJ=I+(J-1)*IB2
      IF(IFL(IJ).NE.1) GOTO 100
      LOOP=0
      KROS=-1
      CALL INDXA
      CALL RXN
      DG=RGP(IJ)-RGPN(IJ)+DTORDR(I)*(RGFR(IJ)-RGFR(IMJ))
   $  +DTODZ(J)*(RGFT(IJ)-RGFT(IJM))
      DG=DG-DT*DOTM(1)
```

```
      ADG=ABS(DG)
      DGORIG=ADG
      IF(ADG.LE.CONV(IJ)) GOTO 78
      MUSTIT=.FALSE.
      D3=DG
      P3=P(IJ)
      IF(NIT.EQ.1) GOTO 55
10    IF(D3.GT.0.0) GOTO 11
      D2=D3
      P2=P3
      IF(KROS.EQ.-1) KROS=1
      IF(KROS.EQ.0) KROS=2
      GOTO 12
11    D1=D3
      P1=P3
      IF(KROS.EQ.-1) KROS=0
      IF(KROS.EQ.1) KROS=2
12    IF(KROS.EQ.3) GOTO 54
      IF(KROS.EQ.2) GOTO 13
      DSN=SIGN(1.D0,D3)
      DP=-D3*ABETA(IJ)
      IF(-DP*DSN.GT.0.25*P3) DP=-0.25*DSN*P3
      P(IJ)=P(IJ)+DP
      GOTO 54
13    P(IJ)=(D1*P2-D2*P1)/(D1-D2)
      ABETA(IJ)=(P1-P2)/(D1-D2)
      KROS=3
54    P3=P(IJ)
55    CONTINUE
      CALL IGIL
      TG(IJ)=C1+SIEG(IJ)/CG
      CALL ROGY(IJ)
      DO 83 K=1,NPHASE
      IF(RLK(K,IJ).EQ.0.0) THEN
      TL(K,IJ)=0.0
      ELSE
      TL(K,IJ)=C2+SIEL(K,IJ)/CL(K)
      ENDIF
83    CONTINUE
      RGP(IJ)=TH(IJ)*ROG(IJ)
      CALL MATS
      CALL VELSK
      CALL MASFK
      CALL RXN
78    THX=0.0
      DO 79 K=1,NPHASE
      RLK(K,IJ)=RLKN(K,IJ)-DTORDR(I)*(RLFRK(K,IJ)-RLFRK(K,IMJ))
     $-DTODZ(J)*(RLFTK(K,IJ)-RLFTK(K,IJM))
      RLK(K,IJ)=RLK(K,IJ)+DT*DOTM(K+1)
      IF(RLK(K,IJ).LT.1.D-27) RLK(K,IJ)=0.0
```

```
 79     THX=THX+RLK(K,IJ)*ARL(K)
        TH(IJ)=1.-THX
        DO 80 K=1,NPHASE
80      THL(K,IJ)=RLK(K,IJ)/RL(K)
        RGP(IJ)=ROG(IJ)*TH(IJ)
        IF(ADG.LE.CONV(IJ)) GOTO 99
        CALL MASFG
        CALL RXN
        DG=RGP(IJ)-RGPN(IJ)+DTORDR(I)*(RGFR(IJ)-RGFR(IMJ))+DTODZ(J)*
    $   (RGFT(IJ)-RGFT(IJM))
        DG=DG-DT*DOTM(1)
        ADG=ABS(DG)
        IF((ADG.LE.CONV(IJ)).AND.(ADG.LT.DGORIG)) GOTO 99
        IF((NIT.EQ.1).AND.(LOOP.EQ.0)) DGORIG=ADG
        D3=DG
        LOOP=LOOP+1
        IF((KROS.LT.2).AND.(LOOP.EQ.LMAX))
    $   ABETA(IJ)=.5*LMAX*ABETA(IJ)
        IF(LOOP.EQ.LMAX) GOTO 99
        IF(KROS.EQ.3) CALL NEWP
        GOTO 10
 99     DGG(IJ)=DG
 100    CONTINUE
        IF(MUSTIT) RETURN
        MUSTIT=.TRUE.
C
        IF(NIT.EQ.2000) THEN
        WRITE(6,*)'MAX ITERATION AT TIME = ',TIME
        STOP
        ENDIF
C
 200    CONTINUE
C
        RETURN
        END
C
C*************************************************************
**
C
        SUBROUTINE KDRAGG(DRAG,VREL)
C
        INCLUDE 'cfb1.com'
C
        DRCOE=0.44
        REYN=TH(IJ)*ROG(IJ)*DK(K)*VREL*PHI(K)/VISF
        IF(REYN.LT.0.001) REYN=0.001
        IF(REYN.LE.1000.0) DRCOE=(24.0/REYN)*(1.0+0.15*REYN**0.687)
        DRDVTH=DRCOE*VREL/TH(IJ)**2.65
        IF(DRDVTH.LE.1.0D30) THEN
        DRAG=0.75*RLK(K,IJ)*DRDVTH*ROG(IJ)*ARL(K)/(DK(K)*PHI(K))
```

```
      ELSE
      DRAG=1.0D30
      ENDIF
C
      RETURN
      END
C
C*****************************************************************
**
C
      SUBROUTINE KDRAGS
C
      INCLUDE 'cfb1.com'
C
      DO 130 K=1,NPHASE
      DV=(VG(IJ)-VK(K,IJ)+VG(IJM)-VK(K,IJM))*0.5
      DU=(UG(IJ)-UK(K,IJ)+UG(IMJ)-UK(K,IMJ))*0.5
      VREL=(DU*DU+DV*DV)**0.5
      IF(TH(IJ).GE.0.8) THEN
      CALL KDRAGG(DRAG,VREL)
      ELSE
      DENOM=DK(K)*PHI(K)*TH(IJ)
      DRAG=(150.0*(1.0-TH(IJ))*VISF/DENOM+1.75*ROG(IJ)*VREL)
     $ *RLK(K,IJ)/(RL(K)*DENOM)
      ENDIF
      RKPG(K,IJ)=DRAG*RL(K)/(RL(K)-ROG(IJ))
 130  CONTINUE
C
      RETURN
      END
C
C*****************************************************************
**
C
      SUBROUTINE MASFG
C
      INCLUDE 'cfb1.com'
C
      IF(UG(IMJ).GE.0.)THEN
      RGFR(IMJ)=UG(IMJ)*RGP(IJL)*RB(I-1)
      ELSE
      RGFR(IMJ)=UG(IMJ)*RGP(IJ)*RB(I-1)
      ENDIF
      IF(VG(IJM).GE.0.)THEN
      RGFT(IJM)=VG(IJM)*RGP(IJB)
      ELSE
      RGFT(IJM)=VG(IJM)*RGP(IJ)
      ENDIF
C
      ENTRY MASFGA
```

```
      IF(UG(IJ).GE.0.)THEN
      RGFR(IJ)=UG(IJ)*RGP(IJ)*RB(I)
      ELSE
      RGFR(IJ)=UG(IJ)*RGP(IJR)*RB(I)
      ENDIF
      IF(VG(IJ).GE.0.)THEN
      RGFT(IJ)=VG(IJ)*RGP(IJ)
      ELSE
      RGFT(IJ)=VG(IJ)*RGP(IJT)
      ENDIF
C
      RETURN
      END
C
C*****************************************************************
**
C
      SUBROUTINE MASFK
C
      INCLUDE 'cfb1.com'
C
      DO 10 K=1,NPHASE
      IF(UK(K,IMJ).GE.0.)THEN
      RLFRK(K,IMJ)=UK(K,IMJ)*RLK(K,IJL)*RB(I-1)
      ELSE
      RLFRK(K,IMJ)=UK(K,IMJ)*RLK(K,IJ)*RB(I-1)
      ENDIF
      IF(VK(K,IJM).GE.0.)THEN
      RLFTK(K,IJM)=VK(K,IJM)*RLK(K,IJB)
      ELSE
      RLFTK(K,IJM)=VK(K,IJM)*RLK(K,IJ)
      ENDIF
 10   CONTINUE
C
      ENTRY MASFKA
      DO 20 K=1,NPHASE
      IF(UK(K,IJ).GE.0.)THEN
      RLFRK(K,IJ)=UK(K,IJ)*RLK(K,IJ)*RB(I)
      ELSE
      RLFRK(K,IJ)=UK(K,IJ)*RLK(K,IJR)*RB(I)
      ENDIF
      IF(VK(K,IJ).GE.0.)THEN
      RLFTK(K,IJ)=VK(K,IJ)*RLK(K,IJ)
      ELSE
      RLFTK(K,IJ)=VK(K,IJ)*RLK(K,IJT)
      ENDIF
 20   CONTINUE
C
      RETURN
      END
```

```
C
C*****************************************************************
**
C
      SUBROUTINE MATS
C
      INCLUDE 'cfb1.com'
C
      CALL RXN
      BU1(1)=RUG(IMJ)-DTODRP(I-1)*(P(IJ)-P(IJL))
      BV1(1)=RVG(IJM)-DTODZP(J-1)*(P(IJ)-P(IJB))
      AU1(1,1)=AR(I-1)*(APP(1,IJL)+RGP(IJL))
     $ +BR(I-1)*(APP(1,IJ)+RGP(IJ))
      AV1(1,1)=AZ(J-1)*(APP(1,IJB)+RGP(IJB))
     $ +BZ(J-1)*(APP(1,IJ)+RGP(IJ))
      AU1(1,1)=AU1(1,1)-DT*DOTM(1)
      AV1(1,1)=AV1(1,1)-DT*DOTM(1)
      DO 130 K=2,NPHS1
      KM1=K-1
      BU1(K)=RUK(KM1,IMJ)
      BV1(K)=RVK(KM1,IJM)
      DO 110 KK=1,KM1
      KS=K*KM1/2+KK
      AU1(K,KK)=AR(I-1)*APP(KS,IJL)+BR(I-1)*APP(KS,IJ)
      AU1(KK,K)=AU1(K,KK)
      AV1(K,KK)=AZ(J-1)*APP(KS,IJB)+BZ(J-1)*APP(KS,IJ)
      AV1(KK,K)=AV1(K,KK)
110   CONTINUE
      KS=K*(K+1)/2
      AU1(K,K)=AR(I-1)*(APP(KS,IJL)+RLK(KM1,IJL))
     $ +BR(I-1)*(APP(KS,IJ)+RLK(KM1,IJ))
      AV1(K,K)=AZ(J-1)*(APP(KS,IJB)+RLK(KM1,IJB))
     $ +BZ(J-1)*(APP(KS,IJ)+RLK(KM1,IJ))
      AU1(K,K)=AU1(K,K)-DT*DOTM(K)
      AV1(K,K)=AV1(K,K)-DT*DOTM(K)
130   CONTINUE
C
      ENTRY MATSA
      CALL RXN
      BU(1)=RUG(IJ)-DTODRP(I)*(P(IJR)-P(IJ))
      BV(1)=RVG(IJ)-DTODZP(J)*(P(IJT)-P(IJ))
      AU(1,1)=AR(I)*(APP(1,IJ)+RGP(IJ))+BR(I)*(APP(1,IJR)+RGP(IJR))
      AV(1,1)=AZ(J)*(APP(1,IJ)+RGP(IJ))+BZ(J)*(APP(1,IJT)+RGP(IJT))
      AU(1,1)=AU(1,1)-DT*DOTM(1)
      AV(1,1)=AV(1,1)-DT*DOTM(1)
      DO 230 K=2,NPHS1
      KM1=K-1
      BU(K)=RUK(KM1,IJ)
      BV(K)=RVK(KM1,IJ)
      DO 210 KK=1,KM1
```

```
      KS=K*KM1/2+KK
      AU(K,KK)=AR(I)*APP(KS,IJ)+BR(I)*APP(KS,IJR)
      AU(KK,K)=AU(K,KK)
      AV(K,KK)=AZ(J)*APP(KS,IJ)+BZ(J)*APP(KS,IJT)
      AV(KK,K)=AV(K,KK)
210   CONTINUE
      KS=K*(K+1)/2
      AU(K,K)=AR(I)*(APP(KS,IJ)+RLK(KM1,IJ))
   $  +BR(I)*(APP(KS,IJR)+RLK(KM1,IJR))
      AV(K,K)=AZ(J)*(APP(KS,IJ)+RLK(KM1,IJ))
   $  +BZ(J)*(APP(KS,IJT)+RLK(KM1,IJT))
      AU(K,K)=AU(K,K)-DT*DOTM(K)
      AV(K,K)=AV(K,K)-DT*DOTM(K)
230   CONTINUE
C
      RETURN
      END
C
C*****************************************************************
**
C
      SUBROUTINE MULTI
C
      INCLUDE 'cfb1.com'
C
      KS=1
      DO 100 K=1,NPHASE
      KS=KS+1
      APP(KS,IJ)=-RKPG(K,IJ)*DT
      DO 98 KK=1,K-1
      KS=KS+1
      DV=(VK(K,IJ)-VK(KK,IJ)+VK(K,IJM)-VK(KK,IJM))*0.5
      DU=(UK(K,IJ)-UK(KK,IJ)+UK(K,IMJ)-UK(KK,IMJ))*0.5
      VREL=(DU*DU+DV*DV)**0.5
      APP(KS,IJ)=-RLK(K,IJ)*RLK(KK,IJ)*DKF(K,KK)*VREL
 98   CONTINUE
      KS=KS+1
 100  CONTINUE
      DO 105 K=1,NPHS1
      SUM=0.0
      DO 101 KK=1,K-1
      KS=K*(K-1)/2+KK
      SUM=SUM+APP(KS,IJ)
 101  CONTINUE
      DO 102 KK=K+1,NPHS1
      KS=KK*(KK-1)/2+K
      SUM=SUM+APP(KS,IJ)
 102   CONTINUE
      KS=K*(K+1)/2
      APP(KS,IJ)=-SUM
```

```
 105    CONTINUE
C
        RETURN
        END
C
C*****************************************************************
**
C
        SUBROUTINE NEWP
C
        INCLUDE 'cfb1.com'
C
        IF(D1.NE.D3) THEN
        PA=(D1*P3-D3*P1)/(D1-D3)
        ELSE
        PA=0.5*(P2+P3)
        ENDIF
        IF(D2.NE.D3) THEN
        PB=(D2*P3-D3*P2)/(D2-D3)
        ELSE
        PB=0.5*(P1+P3)
        ENDIF
        IF(D1*D3.GT.0.) THEN
        IF(PA.LT.P2.OR.PA.GT.P3)PA=0.5*(P2+P3)
        IF(PB.LT.P3.OR.PB.GT.P1)PB=0.5*(P1+P3)
        ENDIF
        P(IJ)=0.5*(PA+PB)
C
        RETURN
        END
C
C*****************************************************************
**
C
        SUBROUTINE PROG
C
        INCLUDE 'cfb1.com'
C
        TDUMP1=TIME
        TPRI=TIME
1       CONTINUE
        CALL BDRY
        TPDT=TIME+0.1*DT
        IF(TPDT.GE.TPRI) THEN
        TPRI=TPRI+TPR
        IF(TIME.GE.0.0)THEN
        CAll OUTP
        ENDIF
        ENDIF
        IF(TPDT.GT.TSTOP.OR.TPDT.GT.TDUMP1) THEN
```

```
      CALL TAPEWR
      REWIND(9)
      TDUMP1=TDUMP1+TDUMP
      ENDIF
      IF(TPDT.LT.TSTOP) THEN
      TIME=TIME+DT
      CALL TILDE
      CALL BETAS
      CALL ITER
      DO 11 KNN=1,NPHASE
      IF(KIN(KNN).EQ.1) CALL GRNVIS
11    CONTINUE
      DO 20 J=2,JB1
      DO 20 I=2,IB1
      IJ=I+(J-1)*IB2
      DO 12 K=1,NPHASE
      IF(KIN(K).eq.0) THEN
      if (k.eq.2)then
      VISBL(K,IJ)=0.0
      VISCL(K,IJ)=5*THL(K,IJ)
      PS(K,IJ)=0.0
      else
C     for nano particle, we use the correlation vis=0.011*(svf^(1/3))go
c     for nano particle. maximun packing =0.08
      G0=1.0/(1.0-(THL(K,IJ)/(0.08))**(1./3.))
      VISBL(K,IJ)=0.0
      VISCL(K,IJ)=0.011*(THL(K,IJ)**(1./3.))*G0
      PS(K,IJ)=0.0
      endif
      ENDIF
12    CONTINUE
20    CONTINUE
      CALL ICONV
      CALL COMPOS
      GOTO 1
      ENDIF
C
      RETURN
      END
C
C*************************************************************** PROD
C
      SUBROUTINE PROD
C
      INCLUDE 'cfb1.com'
C
      TMASSG=0.0
      TMASSS=0.0
      DO 10 J=1,JB2
      KI=0
```

```
      DO 9 JX=1,JXN
      AYM(JX,J)=0.0
      AYMOL(JX,J)=0.0
9     CONTINUE
      FLUX(J)=0.0
      DO 20 I=2,IB2-1
      IJ=I+(J-1)*IB2
      IF(IFL(IJ).EQ.3) GOTO 20
      CALL ROGY(IJ)
      WMO=0.0
      DO 7 JX=1,JXN
      WMO=WMO+Y(1,JX,IJ)/WM(JX)
7     CONTINUE
      DO 8 JX1=1,JXN
      AYM(JX1,J)=AYM(JX1,J)+TH(IJ)*ROG(IJ)*VG(IJ)
  $   *Y(1,JX1,IJ)*DR(I)*THICK
      YMOL(JX1,IJ)=Y(1,JX1,IJ)/WM(JX1)/WMO
      AYMOL(JX1,J)=AYMOL(JX1,J)+YMOL(JX1,IJ)
8     CONTINUE
      KI=KI+1
      FLUX(J)=FLUX(J)+TH(IJ)*ROG(IJ)*VG(IJ)*DR(I)*THICK
      IF(J.EQ.1.OR.J.EQ.JB2) GOTO 20
      TMASSG=TMASSG+TH(IJ)*ROG(IJ)*DR(I)*DZ(J)*THICK
      TMASSS=TMASSS+RLK(1,IJ)*DR(I)*DZ(J)*THICK
20    CONTINUE
      DO 11 JX=1,JXN
      AYM(JX,J)=AYM(JX,J)/KI
      AYMOL(JX,J)=AYMOL(JX,J)/KI
11    CONTINUE
      WMO=0.0
      DO 12 JX=1,JXN
      WMO=WMO+AYM(JX,J)/WM(JX)
12    CONTINUE
      DO 13 JX=1,JXN
      IF(WMO.EQ.0.0)THEN
      AYMOL1(JX,J)=AYMOL(JX,J)
      ELSE
      AYMOL1(JX,J)=AYM(JX,J)/WM(JX)/WMO
      ENDIF
13    CONTINUE
10    CONTINUE
      AMIX(1)=TMASSG
      AMIX(2)=TMASSS
      AMIX(3)=FLUX(1)
      AMIX(4)=FLUX(JB2)
      DO 15 JX=1,JXN
      AMIX(4+JX)=AYMOL(JX,JB2)
15    CONTINUE
      DO 16 JX=1,JXN
      AMIX(10+JX)=AYMOL1(JX,JB2)
```

```
 16     CONTINUE
        AMIX(17)=TIME
C
        RETURN
        END
C
C*****************************************************************
**
C
        SUBROUTINE RHEATS
        INCLUDE 'cfb1.com'
C
C       INTERPASE HEAT TRANSFER COEFFICIENT
C
        DO 10 K=1,NPHASE
        SP=RLK(K,IJ)*(6./DK(K))*ARL(K)
        DV=(VG(IJ)-VK(K,IJ)+VG(IJM)-VK(K,IJM))*0.5
        DU=(UG(IJ)-UK(K,IJ)+UG(IMJ)-UK(K,IMJ))*0.5
        VREL=SQRT(DU*DU+DV*DV)
        REYN=DK(K)*VREL*ROG(IJ)/VISF
         PR=CG*VISF/AKG(IJ)

        CRPR=PR**(1./3.)
        IF(TH(IJ).GE.0.8) THEN
        IF(REYN.LE.200.)THEN
        PNU=(2.+1.1*REYN**.6*CRPR)*SP
        ELSEIF(REYN.LE.2000.)THEN
        PNU=.123*(4.*REYN/DK(K))**.83*SP**.17
        ELSE
        PNU=.61*REYN**.67*SP
        ENDIF
        ELSE
        IF(REYN.LE.200.)THEN
        PNU=(2.+0.16*REYN**0.67)*SP
        ELSEIF(REYN.LE.1000.)THEN
        PNU=8.2*REYN**0.6*SP
        ELSE
        PNU=1.06*REYN**0.457*SP
        ENDIF
        ENDIF
        RHEAT(K,IJ)=PNU*AKG(IJ)/DK(K)
 10     CONTINUE
C
        RETURN
        END
C
C*****************************************************************
**
C
        SUBROUTINE SETUP
```

```
C
      INCLUDE 'cfb1.com'
C     DIMENSION RLX(NH)
C
      WRITE(6,660)
      DO 1 I=1,IB1
      DRP(I)=0.5*(DR(I)+DR(I+1))
      RDR(I)=1.0/DR(I)
      RDRP(I)=2.0/(DR(I)+DR(I+1))
      AR(I)=0.5*DR(I+1)*RDRP(I)
      BR(I)=1.0-AR(I)
 1    CONTINUE
      DRP(IB2)=DR(IB2)
      RDR(IB2)=1.0/DR(IB2)
      RDRP(IB2)=RDR(IB2)
      AR(IB2)=0.5
      BR(IB2)=0.5
      DO 2 J=1,JB1
      DZP(J)=0.5*(DZ(J)+DZ(J+1))
      RDZ(J)=1.0/DZ(J)
      RDZP(J)=2.0/(DZ(J)+DZ(J+1))
      AZ(J)=0.5*DZ(J+1)*RDZP(J)
      BZ(J)=1.0-AZ(J)
 2    CONTINUE
      DZP(JB2)=DZ(JB2)
      RDZ(JB2)=1.0/DZ(JB2)
      RDZP(JB2)=RDZ(JB2)
      AZ(JB2)=0.5
      BZ(JB2)=0.5
C
      IF(ITC.EQ.0) GOTO 5
      RTC=RST-0.5*DR(1)
      RTB=RST
      R(1)=RTC**ITC
      RB(1)=RTB**ITC
      IF((RTC.LE.0.).AND.(ITC.EQ.2))R(1)=-R(1)
      IF(RB(1).LT.1.D-8) THEN
      RRB(1)=0.0
      ELSE
      RRB(1)=1.0/RB(1)
      ENDIF
      DO 3 I=2,IB2
      RTC=RTB+0.5*DR(I)
      RTB=RTB+DR(I)
      R(I)=RTC**ITC
      RB(I)=RTB**ITC
      RRB(I)=1./RB(I)
 3    CONTINUE
      GOTO 10
 5    CONTINUE
```

```
      DO 8 I=1,IB2
      R(I)=1.
      RB(I)=1.
      RRB(I)=1.
 8    CONTINUE
 10   CONTINUE
      DO 11 I=1,IB2
      RRIDR(I)=RDR(I)/R(I)
      RRIDRP(I)=RRB(I)*RDRP(I)
      DTODR(I)=DT*RDR(I)
      DTODRP(I)=DT*RDRP(I)
      DTORDR(I)=DT*RRIDR(I)
      DTOBDR(I)=DT*RRIDRP(I)
 11   CONTINUE
      DO 12 J=1,JB2
      DTODZ(J)=DT*RDZ(J)
      DTODZP(J)=DT*RDZP(J)
 12   CONTINUE
      DO 15 IJ2=IB2JB2,IB2,-IB2
      IJ1=IJ2-IB1
      WRITE(6,650)(IFL(IKPR),IKPR=IJ1,IJ2)
 15   CONTINUE
      WRITE(6,660)
C
      DO 20 I=0,1000
      THX=I/1000.
      COHF(I)=0.0
C-----------------------------------------------
c     COHF(I)=10.**(-10.6*THX+5.5)
C-----------------------------------------------
C     GTH(I)=0.0
C-----------------------------------------------
C     GTH(I)=10.**(-8.686*THX+8.577)
C
C     FOR NANOPARTICLE
      GTH(I)=10.**(-14.926*THX+18.667)
c     GTH(I)=10.**(-8.76*THX+7.8)
C-----------------------------------------------
 20   CONTINUE
C
      DO 30 J=2,JB1
      DO 30 I=2,IB1
      IJ=I+(J-1)*IB2
      IPJ=IJ+1
      IJR=IPJ
      IJP=IJ+IB2
      IJT=IJP
      IMJ=IJ-1
      IJL=IMJ
      IJM=IJ-IB2
```

```
      IJB=IJM
      IPJP=IJP+1
      IJTR=IPJP
      IF((IFL(IPJ).EQ.2).OR.(IFL(IPJ).EQ.3)) IJR=IJ
      IF((IFL(IMJ).EQ.2).OR.(IFL(IMJ).EQ.3)) IJL=IJ
      IF((IFL(IJP).EQ.2).OR.(IFL(IJP).EQ.3)) IJT=IJ
      IF((IFL(IJM).EQ.2).OR.(IFL(IJM).EQ.3)) IJB=IJ
      IF(IJ .EQ. (IB2JB1-1))IJTR=IJ
      GOTO (29,21,21,29,29,29,29),IFL(IPJP)
 21   GOTO (22,24,24,22,22,22,22),IFL(IJP)
 22   GOTO (25,26,26,25,25,25,25),IFL(IPJ)
 24   GOTO (28,25,25,28,28,28,28),IFL(IPJ)
 25   IJTR=IJ
      GOTO 29
 26   IJTR=IJP
      GOTO 29
 28   IJTR=IPJ
 29   CONTINUE
      INDS(IJ,1)=IJR
      INDS(IJ,2)=IJL
      INDS(IJ,3)=IJT
      INDS(IJ,4)=IJB
      INDS(IJ,5)=IJTR
 30   CONTINUE
C
      DO 40 K=1,NPHASE
      DO 40 KK=1,K-1
      DKF(K,KK)=FAC*DT*(DK(K)+DK(KK))**2/(RL(K)*
     $ DK(K)**3+RL(KK)*DK(KK)**3)
 40   CONTINUE
C
      IF(ITD.NE.2)THEN
      DO 60 N=1,NO
      DO 60 J=IOB(3,N),IOB(4,N)
      JJ=(J-1)*IB2
      DO 60 I=IOB(1,N),IOB(2,N)
      IJ=I+JJ
      IF((IFL(IJ).EQ.2).OR.(IFL(IJ).EQ.3))GOTO 60
      P(IJ)=PIO(N)
      TG(IJ)=TEMIO(N)
      TH(IJ)=THIO(N)
       THN(IJ)=TH(IJ)
      UG(IJ)=UIO(N)
      VG(IJ)=VIO(N)
      DO 56 K=1,NPHASE
      TL(K,IJ)=TEMPIO(K,N)
      UK(K,IJ)=UPIO(K,N)
      VK(K,IJ)=VPIO(K,N)
      THL(K,IJ)=THPIO(K,N)
      RLK(K,IJ)=RL(K)*THPIO(K,N)
```

```
      RLKN(K,IJ)=RLK(K,IJ)
C-----------------------------------------------
      IF(KIN(K).EQ.1) THEN
      CALL GRPROP
      ELSE
       if (k.eq.2)then
      VISBL(K,IJ)=0.0
      VISCL(K,IJ)=5*THL(K,IJ)
      PS(K,IJ)=0.0
      else
C     for nano particle, we usr the correlation vis=0.011*(svf^(1/3))go
c     for nano particle. maximun packing =0.08
      G0=1.0/(1.0-(THL(K,IJ)/(0.08))**(1./3.))
      VISBL(K,IJ)=0.0
      VISCL(K,IJ)=0.011*(THL(K,IJ)**(1./3.))*G0
      PS(K,IJ)=0.0
      endif
      ENDIF

C-----------------------------------------------
 56   CONTINUE
      DO 55 K=1,LT
      DO 55 JX=1,JXN
      YN(K,JX,IJ)=YIO(K,JX,N)
      Y(K,JX,IJ)=YIO(K,JX,N)
 55   CONTINUE
      CALL ROGY(IJ)
      RGP(IJ)=ROG(IJ)*TH(IJ)
 60   CONTINUE
      ENDIF
C
      DO 65 J=2,JB1
      DO 65 I=2,IB1
      IJ=I+(J-1)*IB2
      IF((IFL(IJ).EQ.2).OR.(IFL(IJ).EQ.3))GOTO 65
      CALL INDXA
C     INITIAL BED PRESSURE
      IF(ITD.NE.2)THEN
      IF(IPRE.NE.0)THEN
      IF(IJ.EQ.IJB)THEN
       IF(IJ.NE.IJL)THEN
      CALL ROGY(IJL)
      CC=ROG(IJL)
      RLXSUM=TH(IJL)*CC
      DO 61 K=1,NPHASE
      RLXSUM=RLXSUM+RLK(K,IJL)
 61   CONTINUE
      P(IJ)=P(IJL)+GRAVX*DR(I)*RLXSUM
      ENDIF
      ELSE
```

```
      CALL ROGY(IJB)
      CC=ROG(IJB)
      RLXSUM=TH(IJB)*CC
      DO 62 K=1,NPHASE
      RLXSUM=RLXSUM+RLK(K,IJB)
 62   CONTINUE
      P(IJ)=P(IJB)+GRAVY*DZ(J)*RLXSUM
      ENDIF
      ENDIF
      ENDIF
C
      CALL CNVERT
      CALL MASFGA
      CALL MASFKA
      THN(IJ)=TH(IJ)
      TG(IJ)=C1+SIEG(IJ)/CG
      CALL ROGY(IJ)
      DO 63 K=1,NPHASE
      IF(RLK(K,IJ).EQ.0.0) THEN
      TL(K,IJ)=0.0
      ELSE
      TL(K,IJ)=C2+SIEL(K,IJ)/CL(K)
      ENDIF
      CALL THRCON
      TSKN(K,IJ)=TSK(K,IJ)
      IF(KIN(K).EQ.1) THEN
      CALL GRPROP
      ELSE
      if (k.eq.2)then
      VISBL(K,IJ)=0.0
      VISCL(K,IJ)=5*THL(K,IJ)
      PS(K,IJ)=0.0
      else
C     for nano particle, we usr the correlation vis=0.011*(svf^(1/3))go
c     for nano particle. maximun packing =0.08
      G0=1.0/(1.0-(THL(K,IJ)/(0.08))**(1./3.))
      VISBL(K,IJ)=0.0
      VISCL(K,IJ)=0.011*(THL(K,IJ)**(1./3.))*G0
      PS(K,IJ)=0.0
      endif
      ENDIF
      RLKN(K,IJ)=RLK(K,IJ)
 63   CONTINUE
      CALL KDRAGS
      CALL MULTI
      CALL RHEATS
 65   CONTINUE
C
 650  FORMAT(1X,100I1)
 660  FORMAT(//)
```

```
C
      RETURN
      END
C
C*****************************************************************
**
C
      SUBROUTINE SIEGF
C
      INCLUDE 'cfb1.com'
C
C     CALCULATES THE FLUXES OF SPECIFIC INTERNAL
c     ENERGY DENSITY FOR GAS
C
      IF(UG(IJ).GE.0.) THEN
      EGFR=RGP(IJ)*SIEGN(IJ)*UG(IJ)*RB(I)
      ELSE
      EGFR=RGP(IJR)*SIEGN(IJR)*UG(IJ)*RB(I)
      ENDIF
      IF(VG(IJ).GE.0.) THEN
      EGFT=RGP(IJ)*SIEGN(IJ)*VG(IJ)
      ELSE
      EGFT=RGP(IJT)*SIEGN(IJT)*VG(IJ)
      ENDIF
      IF(IFL(IMJ).NE.1) GOTO 1
      IF(IFL(IJM).NE.1) GOTO 2
      CALL HEATGB
      GOTO 4
C
 1    IF(UG(IMJ).GE.0.) THEN
      EGFL=RGP(IJL)*SIEGN(IJL)*UG(IMJ)*RB(I-1)
      ELSE
      EGFL=RGP(IJ)*SIEGN(IJ)*UG(IMJ)*RB(I-1)
      ENDIF
      IF(IFL(IJM).NE.1) GOTO 2
      CALL HEATGA
      GOTO 3
C
 2    IF(VG(IJM).GE.0.) THEN
      EGFB(I)=RGP(IJB)*SIEGN(IJB)*VG(IJM)
      ELSE
      EGFB(I)=RGP(IJ)*SIEGN(IJ)*VG(IJM)
      ENDIF
C
      CALL HEATCG
      EGFB(I)=EGFB(I)-HFGB
      IF(IFL(IMJ).EQ.1) GOTO 4
 3    EGFL=EGFL-HFGL
 4    EGFT=EGFT-HFGT
      EGFR=EGFR-HFGR
```

```
C
      RETURN
      END
C
C*****************************************************************
**
C
      SUBROUTINE SIELF
C
      INCLUDE 'cfb1.com'
C
C     CALCULATES FLUXES OF SPECIFIC INTERNAL
c     ENERGY DENSITY OF THE LIQ.
C
      IF(UK(K,IJ).GE.0.) THEN
      ELFR(K)=RLK(K,IJ)*SIELN(K,IJ)*UK(K,IJ)*RB(I)
      ELSE
      ELFR(K)=RLK(K,IJR)*SIELN(K,IJR)*UK(K,IJ)*RB(I)
      ENDIF
      IF(VK(K,IJ).GE.0.) THEN
      ELFT(K)=RLK(K,IJ)*SIELN(K,IJ)*VK(K,IJ)
      ELSE
       ELFT(K)=RLK(K,IJT)*SIELN(K,IJT)*VK(K,IJ)
      ENDIF
      IF(IFL(IMJ).NE.1) GOTO 1
      IF(IFL(IJM).NE.1) GOTO 2
      CALL HEATLB
      GOTO 4
C
 1    IF(UK(K,IMJ).GE.0.) THEN
      ELFL(K)=RLK(K,IJL)*SIELN(K,IJL)*UK(K,IMJ)*RB(I-1)
      ELSE
      ELFL(K)=RLK(K,IJ)*SIELN(K,IJ)*UK(K,IMJ)*RB(I-1)
      ENDIF
      IF(IFL(IJM).NE.1) GOTO 2
      CALL HEATLA
      GOTO 3
C
 2    IF(VK(K,IJM).GE.0.) THEN
      ELFB(K,I)=RLK(K,IJB)*SIELN(K,IJB)*VK(K,IJM)
      ELSE
      ELFB(K,I)=RLK(K,IJ)*SIELN(K,IJ)*VK(K,IJM)
      ENDIF
C
      CALL HEATCL
      ELFB(K,I)=ELFB(K,I)-HFLB(K,I)
      IF(IFL(IMJ).EQ.1) GOTO 4
 3    ELFL(K)=ELFL(K)-HFLL(K)
 4    ELFT(K)=ELFT(K)-HFLT(K)
      ELFR(K)=ELFR(K)-HFLR(K)
```

```
C
      RETURN
      END
C
C*****************************************************************
**
C
      SUBROUTINE TAPERD
C
      INCLUDE 'cfb1.com'
C
      READ(9) TIME,TTIM
      READ(9) (P(IJ),TH(IJ),UG(IJ),VG(IJ),TG(IJ),IJ=1,IB2JB2)
      READ(9) ((RLK(K,IJ),UK(K,IJ),VK(K,IJ),TL(K,IJ),
   $  TSK(K,IJ),TSKN(K,IJ),K=1,NPHASE),IJ=1,IB2JB2)
      READ(9) (((Y(K,JX,IJ),K=1,LT),JX=1,JXN),IJ=1,IB2JB2)
      READ(9) (((YN(K,JX,IJ),K=1,LT),JX=1,JXN),IJ=1,IB2JB2)
C
      RETURN
      END
C
C*****************************************************************
**
C
      SUBROUTINE TAPEWR
C
      INCLUDE 'cfb1.com'
      REWIND(9)
C
      WRITE(9) TIME,TTIM
      WRITE(9) (P(IJ),TH(IJ),UG(IJ),VG(IJ),TG(IJ),IJ=1,IB2JB2)
      WRITE(9) ((RLK(K,IJ),UK(K,IJ),VK(K,IJ),TL(K,IJ),
   $  TSK(K,IJ),TSKN(K,IJ),K=1,NPHASE),IJ=1,IB2JB2)
      WRITE(9) (((Y(K,JX,IJ),K=1,LT),JX=1,JXN),IJ=1,IB2JB2)
      WRITE(9) (((YN(K,JX,IJ),K=1,LT),JX=1,JXN),IJ=1,IB2JB2)
C
      RETURN
      END
C
C*****************************************************************
**
C
      SUBROUTINE THRCON
C
      INCLUDE 'cfb1.com'
      PARAMETER (PIC=7.26D-3,RKP=0.3289,RKG=0.0269)
      PARAMETER (APIC=1.-PIC,RF=RKP/RKG)
C
C     DAMKOHLER's EQUIVALENT THERMAL CONDUCTIVITY
C
```

```
      IF(TH(IJ).LT.0.99) THEN
      BB=1.25*((1.0-TH(IJ))/TH(IJ))**(10./9.)
      CC=1.0-BB/RF
      RKO=(2./CC)*(BB*(RF-1.)/(CC*CC*RF)*DLOG(RF/BB)-(BB-1.)/CC
     $ -(BB+1.)/2.)
      A3=SQRT(1.0-TH(IJ))
      AKL(K,IJ)=(1.-A3)+A3*(PIC*RF+APIC*RKO)*AKG(IJ)
      ELSEIF (TH(IJ).EQ.1.0) THEN
      AKL(K,IJ)=0.0
      ELSE
      AKL(K,IJ)=AKG(IJ)
      ENDIF
C
      RETURN
      END
C
C*****************************************************************
**
C
      SUBROUTINE TILDE
C
      INCLUDE 'cfb1.com'
C
      DO 10 J=2,JB1
      DO 10 I=2,IB1
      IJ=I+(J-1)*IB2
      IF(IFL(IJ).NE.1) GOTO 10
      CALL INDX
       CALL UGMOMF
       IGKU=(AR(I)*TH(IJ)+BR(I)*TH(IJR))*1000
       IGKV=(AZ(J)*TH(IJ)+BZ(J)*TH(IJT))*1000
       IGJ=TH(IJ)*1000
       IGT=TH(IJT)*1000
       IGR=TH(IJR)*1000
C
       RUG(IJ)=(AR(I)*RGP(IJ)+BR(I)*RGP(IJR))*(UG(IJ)+GRAVX*DT)
     $ -DTOBDR(I)*(UGFR-UGFL)-DTODZ(J)*(UGFT-UGFB(I))-
DT*SUGC*ITC
       UGFL=UGFR
       UGFB(I)=UGFT
       CALL VGMOMF
C
       RVG(IJ)=(AZ(J)*RGP(IJ)+BZ(J)*RGP(IJT))*(VG(IJ)+GRAVY*DT)
     $ -DTORDR(I)*(VGFR-VGFL)-DTODZP(J)*(VGFT-VGFB(I))
       VGFL=VGFR
       VGFB(I)=VGFT
C
      DO 9 K=1,NPHASE
      IF(KIN(K).EQ.1.AND.RLK(K,IJ).NE.0.) THEN
      VISSD(K)=VISCL(K,IJ)*RL(K)/RLK(K,IJ)
```

```
      ELSE
      VISSD(K)=VISCL(K,IJ)
      ENDIF
      CALL ULMOMF

      RUK(K,IJ)=
     $ (AR(I)*RLK(K,IJ)+BR(I)*RLK(K,IJR))*(UK(K,IJ)+GRAVX*DT)
     $ -DTOBDR(I)*(ULFR(K)-ULFL(K))-DTODZ(J)*(ULFT(K)-ULFB(K,I))
     $ -DTODRP(I)*(GTH(IGKU)*(RLK(K,IJR)-RLK(K,IJ))*ARL(K)
     $ -(COHF(IGR)-COHF(IGJ)))
     $ -DT*SULC(K)*ITC
     $ -DTODRP(I)*(PS(K,IJR)-PS(K,IJ))

      ULFL(K)=ULFR(K)
      ULFB(K,I)=ULFT(K)
      CALL VLMOMF

      RVK(K,IJ)=(AZ(J)*RLK(K,IJ)+BZ(J)*RLK(K,IJT))
     $ *(VK(K,IJ)+DT*GRAVY)
     $ -DTORDR(I)*(VLFR(K)-VLFL(K))-DTODZP(J)*(VLFT(K)-VLFB(K,I))
     $ -DTODZP(J)*(GTH(IGKV)*(RLK(K,IJT)-RLK(K,IJ))*ARL(K)
     $ -(COHF(IGT)-COHF(IGJ)))
     $ -DTODZP(J)*(PS(K,IJT)-PS(K,IJ))
C
      VLFL(K)=VLFR(K)
      VLFB(K,I)=VLFT(K)
 9    CONTINUE
      CALL RHEATS
      CALL KDRAGS
      CALL MULTI
 10   CONTINUE
C
      DO 20 J=2,JB1
      DO 20 I=2,IB1
      IJ=I+(J-1)*IB2
      IF(IFL(IJ).NE.1) GOTO 20
      CALL INDXA
      CALL MATSA
      CALL VELSK2
      CALL MASFGA
      CALL MASFKA
 20   CONTINUE
C
      RETURN
      END
C
C*****************************************************************
**
C
      SUBROUTINE UGMOMF
```

```
C
      INCLUDE 'cfb1.com'
C
      CS=0.5*(UG(IJ)+UG(IPJ))
      IF(CS.GE.0.) THEN
      UGFR=(AR(I)*RGP(IJ)+BR(I)*RGP(IJR))*UG(IJ)*CS*R(I+1)
      ELSE
      UGFR=(AR(I+1)*RGP(IJR)+BR(I+1)*RGP(IJRR))*UG(IPJ)*CS*R(I+1)
      ENDIF
      CS=AR(I)*VG(IJ)+BR(I)*VG(IPJ)
      IF(CS.GE.0.) THEN
      UGFT=(AR(I)*RGP(IJ)+BR(I)*RGP(IJR))*UG(IJ)*CS
      ELSE
      UGFT=(AR(I)*RGP(IJT)+BR(I)*RGP(IJTR))*UG(IJP)*CS
      ENDIF
      IF(IFL(IMJ).NE.1) GOTO 1
      IF(IFL(IJM).NE.1) GOTO 2
      CALL UGVSB
      GOTO 4
C
 1    CS=0.5*(UG(IJ)+UG(IMJ))
      IF(CS.GE.0.) THEN
      UGFL=(BR(I-1)*RGP(IJ)+AR(I-1)*RGP(IJL))*UG(IMJ)*CS*R(I)
      ELSE
      UGFL=(AR(I)*RGP(IJ)+BR(I)*RGP(IJR))*UG(IJ)*CS*R(I)
      ENDIF
      IF(IFL(IJM).NE.1) GOTO 2
      CALL UGVSA
      GOTO 3
C
 2    CS=(AR(I)*VG(IJM)+BR(I)*VG(IPJM))
      IF(CS.GE.0.) THEN
      UGFB(I)=(AR(I)*RGP(IJB)+BR(I)*RGP(IJBR))*UG(IJM)*CS
      ELSE
      UGFB(I)=(AR(I)*RGP(IJ)+BR(I)*RGP(IJR))*UG(IJ)*CS
      ENDIF
C
      CALL UGVS
      UGFB(I)=UGFB(I)-SUGB
      IF(IFL(IMJ).EQ.1) GOTO 4
 3    UGFL=UGFL-SUGL
 4    UGFT=UGFT-SUGT
      UGFR=UGFR-SUGR
C
      RETURN
      END
C
C*****************************************************************
**
C
```

```
      SUBROUTINE UGVS
C
      INCLUDE 'cfb1.com'
C
      SUGB=VISF*((VG(IPJM)-VG(IJM))*RDRP(I)+(UG(IJ)-UG(IJM))
     $ *RDZP(J-1))*
     $ (BZ(J-1)*(AR(I)*TH(IJ)+BR(I)*TH(IJR))
     $ +AZ(J-1)*(AR(I)*TH(IJB)+BR(I)*TH(IJBR)))
C
      ENTRY UGVSA
      SUGL=VISF*(2.*(UG(IJ)-UG(IMJ))*RDR(I)-(2./3.)
     $ *(RRIDR(I)*(RB(I)*
     $ UG(IJ)-RB(I-1)*UG(IMJ))+(VG(IJ)-VG(IJM))
     $ *RDZ(J)))*TH(IJ)*R(I)
C
      ENTRY UGVSB
      SUGT=VISF*((VG(IPJ)-VG(IJ))*RDRP(I)+(UG(IJP)-
     $ UG(IJ))*RDZP(J))*
     $ (AZ(J)*(AR(I)*TH(IJ)+BR(I)*TH(IJR))
     $ +BZ(J)*(AR(I)*TH(IJT)+BR(I)*TH(IJTR)))
      SUGR=VISF*(2.*(UG(IPJ)-UG(IJ))*RDR(I+1)-(2./3.)*(RRIDR(I+1)
     $ *(RB(I+1)*
     $ UG(IPJ)-RB(I)*UG(IJ))+(VG(IPJ)-VG(IPJM))*RDZ(J)))
     $ *TH(IJR)*R(I+1)
      SUGC=VISF*(2.*RRB(I)*UG(IJ)-(2./3.)*(0.5*RRIDRP(I)*
     $ (RB(I+1)*UG(IPJ)-RB(I-1)*UG(IMJ))+
     $ (AR(I)*(VG(IJ)-VG(IJM))
     $ +BR(I)*(VG(IPJ)-VG(IPJM)))*RDZ(J)))*RRB(I)
     $ *(AR(I)*TH(IJ)+BR(I)*TH(IJR))
C
      RETURN
      END
C
C*****************************************************************
**
C
      SUBROUTINE ULMOMF
C
      INCLUDE 'cfb1.com'
C
      CS=0.5*(UK(K,IJ)+UK(K,IPJ))
      IF(CS.GE.0.) THEN
      ULFR(K)=(AR(I)*RLK(K,IJ)+BR(I)*RLK(K,IJR))
     $ *UK(K,IJ)*CS*R(I+1)
      ELSE
      ULFR(K)=(AR(I+1)*RLK(K,IJR)+BR(I+1)*RLK(K,IJRR))
     $ *UK(K,IPJ)*CS*R(I+1)
      ENDIF
      CS=AR(I)*VK(K,IJ)+BR(I)*VK(K,IPJ)
      IF(CS.GE.0.) THEN
```

```
      ULFT(K)=(AR(I)*RLK(K,IJ)+BR(I)*RLK(K,IJR))*UK(K,IJ)*CS
      ELSE
      ULFT(K)=(AR(I)*RLK(K,IJT)+BR(I)*RLK(K,IJTR))*UK(K,IJP)*CS
      ENDIF
      IF(IFL(IMJ).NE.1) GOTO 1
      IF(IFL(IJM).NE.1) GOTO 2
      CALL ULVSB
      GOTO 4
C
 1    CS=0.5*(UK(K,IJ)+UK(K,IMJ))
      IF(CS.GE.0.) THEN
      ULFL(K)=(BR(I-1)*RLK(K,IJ)+AR(I-1)*RLK(K,IJL))
   $  *UK(K,IMJ)*CS*R(I)
      ELSE
      ULFL(K)=(AR(I)*RLK(K,IJ)+BR(I)*RLK(K,IJR))*UK(K,IJ)*CS*R(I)
      ENDIF
      IF(IFL(IJM).NE.1) GOTO 2
      CALL ULVSA
      GOTO 3
C
 2    CS=AR(I)*VK(K,IJM)+BR(I)*VK(K,IPJM)
      IF(CS.GE.0.) THEN
      ULFB(K,I)=(AR(I)*RLK(K,IJB)+BR(I)*RLK(K,IJBR))*UK(K,IJM)*CS
      ELSE
      ULFB(K,I)=(AR(I)*RLK(K,IJ)+BR(I)*RLK(K,IJR))*UK(K,IJ)*CS
      ENDIF

      CALL ULVS
      ULFB(K,I)=ULFB(K,I)-SULB(K)

      IF(IFL(IMJ).EQ.1) GOTO 4
 3    ULFL(K)=ULFL(K)-SULL(K)
 4    ULFT(K)=ULFT(K)-SULT(K)
      ULFR(K)=ULFR(K)-SULR(K)
C
      RETURN
      END
C
C*****************************************************************
**
C
      SUBROUTINE ULVS
C
      INCLUDE 'cfb1.com'
C
C
      SULB(K)=((VK(K,IPJM)-VK(K,IJM))*RDRP(I)+(UK(K,IJ)-UK(K,IJM))
   $  *RDZP(J-1))*((BZ(J-1)*(AR(I)*RLK(K,IJ)+BR(I)*RLK(K,IJR))
   $  +AZ(J-1)*(AR(I)*RLK(K,IJB)+BR(I)*RLK(K,IJBR)))
   $  *ARL(K)*VISSD(K))
```

```
      ENTRY ULVSA
      SULL(K)=2.*RLK(K,IJ)*ARL(K)*VISSD(K)*R(I)
     $ *RDR(I)*(UK(K,IJ)-UK(K,IMJ))
     $ +(VISBL(K,IJ)-(2./3.)*RLK(K,IJ)*ARL(K)*VISSD(K))
     $ *R(I)*(RRIDR(I)*(RB(I)*UK(K,IJ)-RB(I-1)*UK(K,IMJ))
     $ +(VK(K,IJ)-VK(K,IJM))*RDZ(J))
      ENTRY ULVSB
      SULT(K)=((VK(K,IPJ)-VK(K,IJ))*RDRP(I)+(UK(K,IJP)-UK(K,IJ))
     $ *RDZP(J))
     $ *((AZ(J)*(AR(I)*RLK(K,IJ)+BR(I)*RLK(K,IJR))
     $ +BZ(J)*(AR(I)*RLK(K,IJT)+BR(I)*RLK(K,IJTR)))*ARL(K)
     $ *VISSD(K))
      SULR(K)=2.*RLK(K,IJR)*ARL(K)*VISSD(K)*R(I+1)
     $ *RDR(I+1)*(UK(K,IPJ)-UK(K,IJ))
     $ +(VISBL(K,IJR)-(2./3.)*RLK(K,IJR)*ARL(K)*VISSD(K))
     $ *R(I+1)*(RRIDR(I+1)*(RB(I+1)*UK(K,IPJ)-RB(I)*UK(K,IJ))
     $ +(VK(K,IPJ)-VK(K,IPJM))*RDZ(J))
      SULC(K)=2.*RRB(I)*UK(K,IJ)
     $ *(AR(I)*RLK(K,IJ)+BR(I)*RLK(K,IJR))*ARL(K)*VISSD(K)
     $ +(VISBL(K,IJ)-(2./3.)
     $ *(AR(I)*RLK(K,IJ)+BR(I)*RLK(K,IJR))*ARL(K)*VISSD(K))*RRB(I)
     $ *(0.5*RRIDRP(I)*(RB(I+1)*UK(K,IPJ)-RB(I-1)*UK(K,IMJ))
     $ +(AR(I)*(VK(K,IJ)-VK(K,IJM))
     $ +BR(I)*(VK(K,IPJ)-VK(K,IPJM)))*RDZ(J))
      RETURN
      END
C
C*****************************************************************
**
C
      SUBROUTINE VELINV(NH,NP,A,B)
C
      IMPLICIT REAL*8(A-H,O-Z)
      DIMENSION A(NP,NP),B(NP)
      RMIN=1.D-6
C
C     USE GAUSS-DOLITTLE METHOD FOR SYMMETRIC MATRIX
INVERSION
C
      DO 136 K=2,NP
      IF(ABS(A(K,K)).GE.RMIN) GOTO 136
      DO 135 KK=1,NP
      A(K,KK)=0.0
      A(KK,K)=0.0
 135  CONTINUE
      B(K)=0.0
 136  CONTINUE
C
      DO 160 K=1,NP
      IF(A(K,K).EQ.0.0) GOTO 160
```

```
      KP1=K+1
      DIV=1./A(K,K)
      DO 140 KJ=KP1,NP
      A(K,KJ)=A(K,KJ)*DIV
 140  CONTINUE
      B(K)=B(K)*DIV
      DO 150 KI=KP1,NP
      AMUL=A(KI,K)
      DO 145 KJ=KP1,NP
      A(KI,KJ)=A(KI,KJ)-AMUL*A(K,KJ)
 145  CONTINUE
      B(KI)=B(KI)-AMUL*B(K)
 150  CONTINUE
 160  CONTINUE
      DO 170 K=NH,1,-1
      KP1=K+1
      DO 170 KI=KP1,NP
      B(K)=B(K)-B(KI)*A(K,KI)
 170  CONTINUE
C
      RETURN
      END
C
C*****************************************************************
**
C
      SUBROUTINE VELSK
C
      INCLUDE 'cfb1.com'
      IFLL=IFL(IMJ)
      IF((IFLL.EQ.2).OR.(IFLL.EQ.3).OR.(IFLL.EQ.5)) GOTO 200
      CALL VELINV(NPHASE,NPHS1,AU1,BU1)
      UG(IMJ)=BU1(1)
      DO 165 K=2,NPHS1
      UK(K-1,IMJ)=BU1(K)
 165  CONTINUE
 200  CONTINUE
C
      IFLB=IFL(IJM)
      IF((IFLB.EQ.2).OR.(IFLB.EQ.3).OR.(IFLB.EQ.5)) GOTO 300
      CALL VELINV(NPHASE,NPHS1,AV1,BV1)
      VG(IJM)=BV1(1)
      DO 265 K=2,NPHS1
      VK(K-1,IJM)=BV1(K)
 265  CONTINUE
      ENTRY VELSK2
 300  CONTINUE
C
      IFLR=IFL(IPJ)
      IF((IFLR.EQ.2).OR.(IFLR.EQ.3).OR.(IFLR.EQ.5)) GOTO 400
```

```
      CALL VELINV(NPHASE,NPHS1,AU,BU)
      UG(IJ)=BU(1)
      DO 365 K=2,NPHS1
      UK(K-1,IJ)=BU(K)
C-----------------------------------------------
      IF(IFLR.EQ.8) THEN
      UK(K-1,IJ)=0.0
      ENDIF
C-----------------------------------------------------
 365  CONTINUE
 400  CONTINUE
C
      IFLT=IFL(IJP)
      IF((IFLT.EQ.2).OR.(IFLT.EQ.3).OR.(IFLT.EQ.5)) RETURN
      CALL VELINV(NPHASE,NPHS1,AV,BV)
      VG(IJ)=BV(1)
      DO 465 K=2,NPHS1
      VK(K-1,IJ)=BV(K)
 465  CONTINUE
C
      RETURN
      END
C
C*****************************************************************
**
C
      SUBROUTINE VGMOMF
C
      INCLUDE 'cfb1.com'
C
      CS=0.5*(VG(IJ)+VG(IJP))
      IF(CS.GE.0.) THEN
      VGFT=(AZ(J)*RGP(IJ)+BZ(J)*RGP(IJT))*VG(IJ)*CS
      ELSE
      VGFT=(AZ(J+1)*RGP(IJT)+BZ(J+1)*RGP(IJTT))*VG(IJP)*CS
      ENDIF
      CS=AZ(J)*UG(IJ)+BZ(J)*UG(IJP)
      IF(CS.GE.0.) THEN
      VGFR=(AZ(J)*RGP(IJ)+BZ(J)*RGP(IJT))*VG(IJ)*CS*RB(I)
      ELSE
      VGFR=(AZ(J)*RGP(IJR)+BZ(J)*RGP(IJTR))*VG(IPJ)*CS*RB(I)
      ENDIF
      IF(IFL(IMJ).NE.1) GOTO 1
      IF(IFL(IJM).NE.1) GOTO 2
      CALL VGVSB
      GOTO 4
C
 1    CS=AZ(J)*UG(IMJ)+BZ(J)*UG(IMJP)
      IF(CS.GE.0.) THEN
      VGFL=(AZ(J)*RGP(IJL)+BZ(J)*RGP(IJTL))*VG(IMJ)*CS*RB(I-1)
```

```
      ELSE
      VGFL=(AZ(J)*RGP(IJ)+BZ(J)*RGP(IJT))*VG(IJ)*CS*RB(I-1)
      ENDIF
      IF(IFL(IJM).NE.1) GOTO2
      CALL VGVSA
      GOTO 3
C
 2    CS=0.5*(VG(IJM)+VG(IJ))
      IF(CS.GE.0.) THEN
      VGFB(I)=(BZ(J-1)*RGP(IJ)+AZ(J-1)*RGP(IJB))*VG(IJM)*CS
      ELSE
      VGFB(I)=(AZ(J)*RGP(IJ)+BZ(J)*RGP(IJT))*VG(IJ)*CS
      ENDIF
C
      CALL VGVS
      VGFB(I)=VGFB(I)-SVGB
      IF(IFL(IMJ).EQ.1) GOTO 4
 3    VGFL=VGFL-SVGL
 4    VGFT=VGFT-SVGT
      VGFR=VGFR-SVGR
C
      RETURN
      END
C
C*********************************************************************
**
C
      SUBROUTINE VGVS
C
      INCLUDE 'cfb1.com'
C
      SVGB=VISF*(2./3.)*(2.*(VG(IJ)-VG(IJM))*RDZ(J)
     $ -RRIDR(I)*(RB(I)
     $ *UG(IJ)-RB(I-1)*UG(IMJ)))*TH(IJ)
C
      ENTRY VGVSA
      SVGL=VISF*((VG(IJ)-VG(IMJ))*RDRP(I-1)+(UG(IMJP)-UG(IMJ))
     $ *RDZP(J))
     $ *RB(I-1)*(AZ(J)*(BR(I-1)*TH(IJ)+AR(I-1)*TH(IJL))
     $ +BZ(J)*(BR(I-1)*TH(IJT)+AR(I-1)*TH(IJTL)))
C
      ENTRY VGVSB
      SVGT=VISF*(2./3.)*(2.*(VG(IJP)-VG(IJ))*RDZ(J+1)-RRIDR(I)
     $ *(RB(I)
     $ *UG(IJP)-RB(I-1)*UG(IMJP)))*TH(IJT)
      SVGR=VISF*((VG(IPJ)-VG(IJ))*RDRP(I)+(UG(IJP)-UG(IJ))
     $ *RDZP(J))
     $ *RB(I)*(AZ(J)*(AR(I)*TH(IJ)+BR(I)*TH(IJR))
     $ +BZ(J)*(AR(I)*TH(IJT)+BR(I)*TH(IJTR)))
C
```

```
      RETURN
      END
C
C*****************************************************************
**
C
      SUBROUTINE VLMOMF
C
      INCLUDE 'cfb1.com'
C
      CS=0.5*(VK(K,IJ)+VK(K,IJP))
      IF(CS.GE.0.) THEN
      VLFT(K)=(AZ(J)*RLK(K,IJ)+BZ(J)*RLK(K,IJT))*VK(K,IJ)*CS
      ELSE
      VLFT(K)=(AZ(J+1)*RLK(K,IJT)+BZ(J+1)*RLK(K,IJTT))
     $ *VK(K,IJP)*CS
      ENDIF
      CS=AZ(J)*UK(K,IJ)+BZ(J)*UK(K,IJP)
      IF(CS.GE.0.) THEN
      VLFR(K)=(AZ(J)*RLK(K,IJ)+BZ(J)*RLK(K,IJT))*VK(K,IJ)*CS*RB(I)
      ELSE
      VLFR(K)=(AZ(J)*RLK(K,IJR)+BZ(J)*RLK(K,IJTR))
     $ *VK(K,IPJ)*CS*RB(I)
      ENDIF
      IF(IFL(IMJ).NE.1) GOTO 1
      IF(IFL(IJM).NE.1) GOTO 2
      CALL VLVSB
      GOTO 4
C
 1    CS=AZ(J)*UK(K,IMJ)+BZ(J)*UK(K,IMJP)
      IF(CS.GE.0.) THEN
      VLFL(K)=(AZ(J)*RLK(K,IJL)+BZ(J)*RLK(K,IJTL))
     $ *VK(K,IMJ)*CS*RB(I-1)
      ELSE
      VLFL(K)=(AZ(J)*RLK(K,IJ)+BZ(J)*RLK(K,IJT))
     $ *VK(K,IJ)*CS*RB(I-1)
      ENDIF
      IF(IFL(IJM).NE.1) GOTO2
      CALL VLVSA
      GOTO 3
C
 2    CS=0.5*(VK(K,IJM)+VK(K,IJ))
      IF(CS.GE.0.) THEN
      VLFB(K,I)=(BZ(J-1)*RLK(K,IJ)+AZ(J-1)*RLK(K,IJB))
     $ *VK(K,IJM)*CS
      ELSE
      VLFB(K,I)=(AZ(J)*RLK(K,IJ)+BZ(J)*RLK(K,IJT))*VK(K,IJ)*CS
      ENDIF
C
      CALL VLVS
```

```
      VLFB(K,I)=VLFB(K,I)-SVLB(K)
      IF(IFL(IMJ).EQ.1) GOTO 4
 3    VLFL(K)=VLFL(K)-SVLL(K)
 4    VLFT(K)=VLFT(K)-SVLT(K)
      VLFR(K)=VLFR(K)-SVLR(K)
C
      RETURN
      END
C
C*****************************************************************
**
C
      SUBROUTINE VLVS
C
      INCLUDE 'cfb1.com'

      SVLB(K)=(2./3.)*(2.*(VK(K,IJ)-VK(K,IJM))*RDZ(J)-RRIDR(I)
     $  *(RB(I)*UK(K,IJ)-RB(I-1)*UK(K,IMJ)))
     $  *(RLK(K,IJ)*ARL(K)*VISSD(K))
     $  +VISBL(K,IJ)*RRIDR(I)*(RB(I)*UK(K,IJ)-RB(I-1)*UK(K,IMJ))
      ENTRY VLVSA
      SVLL(K)=((VK(K,IJ)-VK(K,IMJ))*RDRP(I-1)
     $  +(UK(K,IMJP)-UK(K,IMJ))
     $  *RDZP(J))*RB(I-1)*((AZ(J)*(BR(I-1)*RLK(K,IJ)+AR(I-1)
     $  *RLK(K,IJL))
     $  +BZ(J)*(BR(I-1)*RLK(K,IJT)+AR(I-1)*RLK(K,IJTL)))
     $ *ARL(K)*VISSD(K))
      ENTRY VLVSB
      SVLT(K)=(2./3.)*(2.*(VK(K,IJP)-VK(K,IJ))*RDZ(J+1)-RRIDR(I)
     $ *(RB(I)*UK(K,IJP)-RB(I-1)*UK(K,IMJP)))
     $ *(RLK(K,IJT)*ARL(K)*VISSD(K))
     $ +VISBL(K,IJ)*RRIDR(I)
     $ *(RB(I)*UK(K,IJP)-RB(I-1)*UK(K,IMJP))
      SVLR(K)=((VK(K,IPJ)-VK(K,IJ))*RDRP(I)+(UK(K,IJP)-UK(K,IJ))
     $  *RDZP(J))*RB(I)
     $  *((AZ(J)*(AR(I)*RLK(K,IJ)+BR(I)*RLK(K,IJR))
     $  +BZ(J)*(AR(I)*RLK(K,IJT)+BR(I)*RLK(K,IJTR)))
     $  *ARL(K)*VISSD(K))
C
      RETURN
      END
C
C*****************************************************************
**
C
      SUBROUTINE QFLUX
C
      INCLUDE 'cfb1.com'
C
      DO 5 K=1,LT
```

```
      QFLOW(K)=0.0
 5    CONTINUE
      IF(TG(IJ).LE.398.150) GOTO 20
      QFL=QF(IJM)+QF(IMJ)+QF(IPJ)+QF(IJP)
      IF(TOB(IJM).NE.0.0)QFLOW(1)=(QFL-(COE(IJM)*(TG(IJ)-TOB(IJM))
  $                 /DZ(J)))*TH(IJ)
      IF(TOB(IMJ).NE.0.0)QFLOW(1)=(QFL-(COE(IMJ)*(TG(IJ)-TOB(IMJ))
  $                 /DR(I)))*TH(IJ)
      IF(TOB(IPJ).NE.0.0)QFLOW(1)=(QFL-(COE(IPJ)*(TG(IJ)-TOB(IPJ))
  $                 /DR(I)))*TH(IJ)
      IF(TOB(IJP).NE.0.0)QFLOW(1)=(QFL-(COE(IJP)*(TG(IJ)-TOB(IJP))
  $                 /DZ(J)))*TH(IJ)
      DO 10 K=2,LT
      IF(TOB(IJM).NE.0.0)QFLOW(K)=(QFL-(COE(IJM)*(TL(K-1,IJ)-
TOB(IJM))
  $                 /DZ(J)))*RLK(K-1,IJ)*ARL(K-1)
      IF(TOB(IMJ).NE.0.0)QFLOW(K)=(QFL-(COE(IMJ)*(TL(K-1,IJ)-
TOB(IMJ))
  $                 /DR(I)))*RLK(K-1,IJ)*ARL(K-1)
      IF(TOB(IPJ).NE.0.0)QFLOW(K)=(QFL-(COE(IPJ)*(TL(K-1,IJ)-TOB(IPJ))
  $                 /DR(I)))*RLK(K-1,IJ)*ARL(K-1)
      IF(TOB(IJP).NE.0.0)QFLOW(K)=(QFL-(COE(IJP)*(TL(K-1,IJ)-TOB(IJP))
  $                 /DZ(J)))*RLK(K-1,IJ)*ARL(K-1)
 10   CONTINUE
 20   CONTINUE
C
      RETURN
      END
C
C*****************************************************************
**
C
      SUBROUTINE RRATE
C
      INCLUDE 'cfb1.com'
C
      IF(IRXN.NE.1) RETURN
      DO 20 MK=1,LT
      DO 10 IX=1,IHO(MK)
      RHO(MK,IX)=0.0
 10   CONTINUE
      DO 20 IX=1,IHE(MK)
      RHE(MK,IX)=0.0
 20   CONTINUE
      TMO=0.0
      DO 30 JX=1,JXN
      TMO=TMO+YN(1,JX,IJ)/WM(JX)
 30   CONTINUE
      PATM=P(IJ)*1D-6
      PH2=PATM*YN(1,3,IJ)/WM(3)/TMO
```

```
      PCO=PATM*YN(1,1,IJ)/WM(1)/TMO
      PME=PATM*YN(1,5,IJ)/WM(5)/TMO
      T=TG(IJ)
C-----------------------------------------------
      IF(T.LE.430.) T=430.0
      IF(T.GE.630.) T=630.0
C-----------------------------------------------
      IF(PH2.EQ.0.0.OR.PCO.EQ.0.0) THEN
      RHO(1,1)=0.0
      ELSE
      RK0=8.93D-8*RLK(1,IJ)
C The Chang's Keq Model is corrected by the data from DME report
      RKEQ=6.249/PATM**2
      RHO(1,1)=RK0*PCO**(1.0/3.0)*PH2**(2.0/3.0)
   $  *(1-PME/PCO/PH2**2.0/RKEQ)
      DTO=RGPN(IJ)*TMO
      CCO=RGPN(IJ)*YN(1,1,IJ)/WM(1)
      CH2=RGPN(IJ)*YN(1,3,IJ)/WM(3)
      CME=RGPN(IJ)*YN(1,5,IJ)/WM(5)
C     CALL SOLUTION(RKEQ,DTO,CCO,CH2,CME,RHOX)
c     RHOX=RHOX/DT
      IF(RHO(1,1)*DT.GE.MIN(CCO,2*CH2))
   $  RHO(1,1)=0.1*MIN(CCO,2*CH2)/DT
C
C     RHO(1,1)=1.98D7*EXP(-RT1)*(PH2**0.4)*(PCO**0.13)
C     1-2.15D10*EXP(-RT2)*(PME**0.13)
C     RHO(1,1)=RHO(1,1)*RLK(1,IJ)/3.6D6
C     CLM=YN(3,5,IJ)*0.70025/WM(5)
C     HME=1.49D6*exp(-17235.0/8.314/TG(IJ))
C     CLGM=10.0*PME/HME
C     RHE(3,1)=1.2*(CLGM-CLM)*RLK(2,IJ)/0.70025
C     IF(RHE(3,1).LE.0.0)RHE(3,1)=0.0
C     IF(RHO(1,1).LE.0.0)RHO(1,1)=0.0
C
      ENDIF
      HHO(1,1)=-8.314D8*T*T*(-9143.6/T/T-7.492/T
   $  +4.076D-3-7.161D-8*T*2)
C
      RETURN
      END
C
C*****************************************************************
**
C
      SUBROUTINE SOLUTION(DK,DTO,C1,C2,C3,X)
C
      A=C1
      IF(C1.GE.2*C2) A=C2/2.0
      B=-C3
C     UNDERFLOW
```

```
      COEM=1.0/(C3+A)
      FA=COEM*DK*(C1-A)*(C2-2*A)*(C2-2*A)-
     $COEM*(C3+A)*(DTO-2*A)*(DTO-2*A)
      FB=COEM*DK*(C1-B)*(C2-2*B)*(C2-2*B)-
     $COEM*(C3+B)*(DTO-2*B)*(DTO-2*B)
 1    X=(A+B)/2.0
      FX=COEM*DK*(C1-X)*(C2-2*X)*(C2-2*X)-
     $COEM*(C3+X)*(DTO-2*X)*(DTO-2*X)
      IF(ABS(FX/COEM).LE.1D-20) GOTO 10
      IF(FX.LT.0.0) THEN
      A=X
      ELSE
      B=X
      ENDIF
      GOTO 1
C
 10   RETURN
      END
C
C*****************************************************************
**
C
      SUBROUTINE ROGY(MIJ)
C
      INCLUDE 'cfb1.com'
C
      WMY=0.0
      DO 10 JX=1,JXN
      WMY=WMY+Y(1,JX,MIJ)/WM(JX)
 10   CONTINUE
      WMY=1.0/WMY
      ROG(MIJ)=P(MIJ)/(C19*C17*TG(MIJ)+C18*P(MIJ))
      RETURN
      END
C
C*****************************************************************
**
C
      SUBROUTINE RXN
C
      INCLUDE 'cfb1.com'
C
      IF(IRXN.NE.1) RETURN
      CALL RRATE
      DOTM(1)=0.0
      DO 10 K=2,LT
      DOTM(K)=0.0
      DO 20 JX=1,JXN
      DO 20 IX=1,IHE(K)
      DOTM(K)=DOTM(K)+RHE(K,IX)*WM(JX)*AHK(K,IX,JX)
```

```
 20     CONTINUE
        DOTM(1)=DOTM(1)-DOTM(K)
 10     CONTINUE
C
        RETURN
        END
C
C*****************************************************************
**
C
        SUBROUTINE QRXN
C
        INCLUDE 'cfb1.com'
C
        IF(IRXN.NE.1) RETURN
        CALL RRATE
        DO 10 K=1,LT
        QGEN(K)=0.0
        DO 15 IX=1,IHO(K)
        QGEN(K)=QGEN(K)+RHO(K,IX)*HHO(K,IX)
 15     CONTINUE
        IF(K.NE.1)THEN
        DO 20 IX=1,IHE(K)
        QGEN(K)=QGEN(K)+RHE(K,IX)*HHE(K,IX)
 20     CONTINUE
        ENDIF
 10     CONTINUE
C
        RETURN
        END
C
C*****************************************************************
**
C
        SUBROUTINE COMPOS
C
        INCLUDE 'cfb1.com'
C
        IF(IRXN.NE.1) RETURN
        DO 2 J=2,JB1
        DO 2 I=2,IB1
        IJ=I+(J-1)*IB2
        IF(IFL(IJ).NE.1) GOTO 2
        CALL INDXA
        DO 10 K=1,LT
        K1=K-1
        IF(K.NE.1) GOTO 10
        IF(K.EQ.1) GOTO 6
        IF(RLK(K1,IJ).GT.0.0) GOTO 6
        DO 5 JX=1,JXN
```

```
      Y(K,JX,IJ)=0.0
 5    CONTINUE
      GOTO 10
 6    CALL RRATE
      IF(K.EQ.1) THEN
C     CALL MASFGY
      IF(UG(IMJ).GE.0.)THEN
      RGFRY(IMJ)=UG(IMJ)*RGP(IJL)*RB(I-1)
      KEY(2)=IJL
      ELSE
      RGFRY(IMJ)=UG(IMJ)*RGP(IJ)*RB(I-1)
      KEY(2)=IJ
      ENDIF
      IF(VG(IJM).GE.0.)THEN
      RGFTY(IJM)=VG(IJM)*RGP(IJB)
      KEY(4)=IJB
      ELSE
      RGFTY(IJM)=VG(IJM)*RGP(IJ)
      KEY(4)=IJ
      ENDIF
C     ENTRY MASFGAY
      IF(UG(IJ).GE.0.)THEN
      RGFRY(IJ)=UG(IJ)*RGP(IJ)*RB(I)
      KEY(1)=IJ
      ELSE
      RGFRY(IJ)=UG(IJ)*RGP(IJR)*RB(I)
      KEY(1)=IJR
      ENDIF
      IF(VG(IJ).GE.0.)THEN
      RGFTY(IJ)=VG(IJ)*RGP(IJ)
      KEY(3)=IJ
      ELSE
      RGFTY(IJ)=VG(IJ)*RGP(IJT)
      KEY(3)=IJT
      ENDIF
      ELSE
C     CALL MASFKY
      IF(UK(K1,IMJ).GE.0.)THEN
      RLFRKY(K1,IMJ)=UK(K1,IMJ)*RLK(K1,IJL)*RB(I-1)
      KEY(2)=IJL
      ELSE
      RLFRKY(K1,IMJ)=UK(K1,IMJ)*RLK(K1,IJ)*RB(I-1)
      KEY(2)=IJ
      ENDIF
      IF(VK(K1,IJM).GE.0.)THEN
      RLFTKY(K1,IJM)=VK(K1,IJM)*RLK(K1,IJB)
      KEY(4)=IJB
      ELSE
      RLFTKY(K1,IJM)=VK(K1,IJM)*RLK(K1,IJ)
      KEY(4)=IJ
```

```
      ENDIF
C     ENTRY MASFKAY
      IF(UK(K1,IJ).GE.0.)THEN
      RLFRKY(K1,IJ)=UK(K1,IJ)*RLK(K1,IJ)
      KEY(1)=IJ
      ELSE
      RLFRKY(K1,IJ)=UK(K1,IJ)*RLK(K1,IJR)
      KEY(1)=IJR
      ENDIF
      IF(VK(K1,IJ).GE.0.)THEN
      RLFTKY(K1,IJ)=VK(K1,IJ)*RLK(K1,IJ)
      KEY(3)=IJ
      ELSE
      RLFTKY(K1,IJ)=VK(K1,IJ)*RLK(K1,IJT)
      KEY(3)=IJT
      ENDIF
      ENDIF
      THY=0.0
      DO 25 JX=1,JXN
      DOTMJ(K,JX)=0.0
      DO 30 IX=1,IHO(K)
      DOTMJ(K,JX)=DOTMJ(K,JX)+RHO(K,IX)*AHO(K,IX,JX)
 30   CONTINUE
      IF(K.EQ.1)THEN
      DO 27 K2=2,LT
C     CALL RRATE
      DO 27 IX=1,IHE(K2)
      DOTMJ(K,JX)=DOTMJ(K,JX)+RHE(K2,IX)*AHE(K2,IX,JX)
 27   CONTINUE
      ELSE
      DO 26 IX=1,IHE(K)
      DOTMJ(K,JX)=DOTMJ(K,JX)+RHE(K,IX)*AHK(K,IX,JX)
 26   CONTINUE
      ENDIF
      IF(K.EQ.1)THEN
      SUMN=WM(JX)*DOTMJ(1,JX)*DT+RGPN(IJ)*YN(1,JX,IJ)
    $ +DGG(IJ)*YN(1,JX,IJ)
      SUMD=TH(IJ)*ROG(IJ)
      IF(KEY(1).EQ.IJ)THEN
      SUMD=SUMD+DTORDR(I)*RGFRY(IJ)
      ELSE
      SUMN=SUMN-DTORDR(I)*RGFRY(IJ)*YN(1,JX,IJR)
      ENDIF
      IF(KEY(2).EQ.IJ)THEN
      SUMD=SUMD-DTORDR(I)*RGFRY(IMJ)
      ELSE
      SUMN=SUMN+DTORDR(I)*RGFRY(IMJ)*YN(1,JX,IJL)
      ENDIF
      IF(KEY(3).EQ.IJ)THEN
      SUMD=SUMD+DTODZ(J)*RGFTY(IJ)
```

```
      ELSE
      SUMN=SUMN-DTODZ(J)*RGFTY(IJ)*YN(1,JX,IJT)
      ENDIF
      IF(KEY(4).EQ.IJ)THEN
      SUMD=SUMD-DTODZ(J)*RGFTY(IJM)
      ELSE
      SUMN=SUMN+DTODZ(J)*RGFTY(IJM)*YN(1,JX,IJB)
      ENDIF
      Y(1,JX,IJ)=SUMN/SUMD
      ELSE
      SUMN=WM(JX)*DOTMJ(K,JX)*DT+RLKN(K1,IJ)*YN(K,JX,IJ)
      SUMD=RLK(K1,IJ)
      IF(KEY(1).EQ.IJ)THEN
      SUMD=SUMD+DTORDR(I)*RLFRKY(K1,IJ)
      ELSE
      SUMN=SUMN-DTORDR(I)*RLFRKY(K1,IJ)*YN(K,JX,IJR)
      ENDIF
      IF(KEY(2).EQ.IJ)THEN
      SUMD=SUMD-DTORDR(I)*RLFRKY(K1,IMJ)
      ELSE
      SUMN=SUMN+DTORDR(I)*RLFRKY(K1,IMJ)*YN(K,JX,IJL)
      ENDIF
      IF(KEY(3).EQ.IJ)THEN
      SUMD=SUMD+DTODZ(J)*RLFTKY(K1,IJ)
      ELSE
      SUMN=SUMN-DTODZ(J)*RLFTKY(K1,IJ)*YN(K,JX,IJT)
      ENDIF
      IF(KEY(4).EQ.IJ)THEN
      SUMD=SUMD-DTODZ(J)*RLFTKY(K1,IJM)
      ELSE
      SUMN=SUMN+DTODZ(J)*RLFTKY(K1,IJM)*YN(K,JX,IJB)
      ENDIF
      Y(K,JX,IJ)=SUMN/SUMD
      ENDIF
C
      IF(Y(K,JX,IJ).LE.1D-10) Y(K,JX,IJ)=0.0
      THY=THY+Y(K,JX,IJ)
 25   CONTINUE
      IF(ABS(THY-1.0).LE.1D-10) GOTO 10
      IF(K.EQ.1)THEN
      Y(K,6,IJ)=1.0-(THY-Y(K,6,IJ))
      ELSE
      Y(K,6,IJ)=1.0-(THY-Y(K,6,IJ))
      ENDIF
 10   CONTINUE
 2    CONTINUE
 3    DO 9 IJ=1,IB2JB2
      IF(IFL(IJ).NE.1)GOTO 9
      DO 8 K=1,LT
      DO 8 JX=1,JXN
```

```
      YN(K,JX,IJ)=Y(K,JX,IJ)
 8    CONTINUE
 9    CONTINUE
C
      RETURN
      END
C
C*****************************************************************
**
C
      SUBROUTINE FEFLUX
C
      INCLUDE 'cfb1.com'
C
C     CALCULATE FLUCTUATING ENERGY FLUXES OF KINETIC
THEORY
C
      TSKCB(K)=(TSKN(K,IJ)-TSKN(K,IJM))
   $  *(BZ(J-1)*GCON(K,IJ)+AZ(J-1)*GCON(K,IJB))*RDZP(J-1)
      TSKFB(K,I)=1.5*TSKFB(K,I)-TSKCB(K)
C
      ENTRY FEFLUXA
      IF(IFL(IMJ).NE.1)THEN
      TSKCL(K)=(TSKN(K,IJ)-TSKN(K,IMJ))*RB(I-1)
   $  *(BR(I-1)*GCON(K,IJ)+AR(I-1)*GCON(K,IJL))*RDRP(I-1)
      TSKFL(K)=1.5*TSKFL(K)-TSKCL(K)
      ENDIF
C
      ENTRY FEFLUXB
      TSKCR(K)=(TSKN(K,IPJ)-TSKN(K,IJ))*RB(I)
   $  *(BR(I)*GCON(K,IJR)+AR(I)*GCON(K,IJ))*RDRP(I)
      TSKFR(K)=1.5*TSKFR(K)-TSKCR(K)
C
      TSKCT(K)=(TSKN(K,IJP)-TSKN(K,IJ))
   $  *(BZ(J)*GCON(K,IJT)+AZ(J)*GCON(K,IJ))*RDZP(J)
      TSKFT(K)=1.5*TSKFT(K)-TSKCT(K)

      RETURN
      END
C
C*****************************************************************
**
C
      SUBROUTINE GRNVIS
C
      INCLUDE 'cfb1.com'
C
C     CALCULATE NEW GRANULAR TEMPERATURES AND SOLIDS
      PROPERTIES
C     USING KINETIC THEORY OF GRANULAR SOLIDS
```

```
C
C-----------------------------------
      CALL BDRY
C-----------------------------------
      CALL VWORKL
      DO 10 J=2,JB1
      DO 10 I=2,IB1
      IJ=I+(J-1)*IB2
      IF(IFL(IJ).EQ.1) THEN
      DO 5 K=1,NPHASE
      IF(KIN(K).NE.1) GOTO 5
      IF(RLK(K,IJ).GT.RLKMIN(K)) THEN
      THL(K,IJ)=ARL(K)*RLK(K,IJ)
      TSKS=TSK(K,IJ)**0.5
      G0=1.0/(1.0-(THL(K,IJ)/(1.0-THMIN))**(1./3.))
      CS1=(1.0+CRES)*THL(K,IJ)*G0
      CS2=3.0*(1.0-CRES)*RLK(K,IJ)*CS1
C     CS3=RLK(K,IJ)/(RLK(K,IJ)+DMFP(K))
      CS4=2.*VISDIL(K)/((1.+CRES)*G0)
      RSQRTPI=1.0/SQRT(PI)
      GAMMA(K,IJ)=CS2*(4.0*RSQRTPI/DK(K)*TSKS-SILM(K,IJ))
      PS(K,IJ)=RLK(K,IJ)*(1.0+2.0*CS1)
C
      VISCD=CS4*(1.+.8*CS1)**2
      VISBL(K,IJ)=(4./3.)*RLK(K,IJ)*DK(K)*CS1/PI**0.5
      VISCL(K,IJ)=VISCD+0.6*VISBL(K,IJ)
C
      GCON(K,IJ)=3.75*CS4*(1.+1.2*CS1)**2*TSKS
     $  +1.5*VISBL(K,IJ)*TSKS
      ELSE
      GCON(K,IJ)=0.0
      ENDIF
 5    CONTINUE
      ENDIF
 10   CONTINUE
C
C     FINAL SOLUTION OF GRANULAR TEMPERATURE
C
      DO 100 J=2,JB1
      DO 100 I=2,IB1
      IJ=I+(J-1)*IB2
      IF(IFL(IJ).EQ.1) THEN
      CALL INDX
      DO 20 K=1,NPHASE
      IF(KIN(K).NE.1) GOTO 20
      CALL GRTEMF
      IF(RLK(K,IJ).GT.RLKMIN(K)) THEN
C
C-----------------------------------------
      G0=1.0/(1.0-(THL(K,IJ)/(1.0-THMIN))**(1./3.))
```

```
      FRE=12.*G0*THL(K,IJ)*TSKN(K,IJ)**0.5/(SQRT(PI)*DK(K))
      DISF=4.5*THL(K,IJ)*SQRT(0.5*VISF*ROG(IJ)*FRE)/DK(K)
C--------------------------------------
C
       AP0=-(1.5*RLK(K,IJ)*TSK(K,IJ)-DTODZ(J)*(TSKFT(K)
     $ -TSKFB(K,I))-DTORDR(I)*(TSKFR(K)-TSKFL(K)))
      AP1=-(VISCL(K,IJ)*VWLS(K,IJ)+(VISBL(K,IJ)
     $ -(2./3.)*VISCL(K,IJ))*VWLM(K,IJ))
      AP2=(1.5*RLK(K,IJ)+DT*(3.0*DISF*BETAC
     $ +PS(K,IJ)*SILM(K,IJ)+GAMMA(K,IJ)))
      AA=AP2
      BB=AP0+AP1*TSK(K,IJ)**0.5
      TSK(K,IJ)=-BB/AA
      TSKS=TSK(K,IJ)**0.5
      TSK(K,IJ)=TSKS*TSKS
      VISBL(K,IJ)=VISBL(K,IJ)*TSKS
      VISCL(K,IJ)=VISCL(K,IJ)*TSKS
      PS(K,IJ)=PS(K,IJ)*TSK(K,IJ)
      ELSE
      TSK(K,IJ)=0.0
      VISBL(K,IJ)=0.0
      VISCL(K,IJ)=0.0
      PS(K,IJ)=0.0
      ENDIF
      TSKFL(K)=TSKFR(K)
      TSKFB(K,I)=TSKFT(K)
 20   CONTINUE
      ENDIF
 100  CONTINUE
C
      RETURN
      END
C
C*****************************************************************
**
C
      SUBROUTINE GRPROP
C
      INCLUDE 'cfb1.com'
C
C     INITIALIZE SOLIDS PROPERTIES USING GRANULAR KINETIC
THEORY
C
      IF(RLK(K,IJ).GT.RLKMIN(K)) THEN
      THL(K,IJ)=ARL(K)*RLK(K,IJ)
      TSKS=TSK(K,IJ)**0.5
      G0=1.0/(1.0-(THL(K,IJ)/(1.0-THMIN))**(1./3.))
      CS1=(1.0+CRES)*THL(K,IJ)*G0
      CS2=3.0*(1.0-CRES)*RLK(K,IJ)*CS1
C     CS3=RLK(K,IJ)/(RLK(K,IJ)+DMFP(K))
```

```
      CS4=2.*VISDIL(K)/((1.+CRES)*G0)
      VISCD=CS4*(1.+.8*CS1)**2
      VISBL(K,IJ)=(4./3.)*RLK(K,IJ)*DK(K)*CS1*TSKS/PI**0.5
      VISCL(K,IJ)=VISCD*TSKS+0.6*VISBL(K,IJ)
      PS(K,IJ)=RLK(K,IJ)*(1.0+2.0*CS1)*TSK(K,IJ)
      GCON(K,IJ)=3.75*CS4*(1.+1.2*CS1)**2*TSKS
     $ +1.5*VISBL(K,IJ)
      ELSE
      VISBL(K,IJ)=0.0
      VISCL(K,IJ)=0.0
      PS(K,IJ)=0.0
      GCON(K,IJ)=0.0
      ENDIF
C
      RETURN
      END
C
C*****************************************************************
**
C
      SUBROUTINE GRTEMF
C
      INCLUDE 'cfb1.com'
C
C     CALCULATES GRANULAR TEMPERATURE FLUXES OF KINETIC
THEORY
C
      IF(UK(K,IJ).GE.0.) THEN
      TSKFR(K)=RLFRK(K,IJ)*TSKN(K,IJ)
      ELSE
      TSKFR(K)=RLFRK(K,IJ)*TSKN(K,IPJ)
      ENDIF
      IF(VK(K,IJ).GE.0.) THEN
      TSKFT(K)=RLFTK(K,IJ)*TSKN(K,IJ)
      ELSE
      TSKFT(K)=RLFTK(K,IJ)*TSKN(K,IJP)
      ENDIF
      IF(IFL(IMJ).NE.1) GOTO 1
      IF(IFL(IJM).NE.1) GOTO 2
      CALL FEFLUXB
      RETURN
C
 1    IF(UK(K,IMJ).GE.0.) THEN
      TSKFL(K)=RLFRK(K,IMJ)*TSKN(K,IMJ)
      ELSE
      TSKFL(K)=RLFRK(K,IMJ)*TSKN(K,IJ)
      ENDIF
      IF(IFL(IJM).NE.1) GOTO 2
      CALL FEFLUXA
      RETURN
```

```
C
 2      IF(VK(K,IJM).GE.0.) THEN
        TSKFB(K,I)=RLFTK(K,IJM)*TSKN(K,IJM)
        ELSE
        TSKFB(K,I)=RLFTK(K,IJM)*TSKN(K,IJ)
        ENDIF
        CALL FEFLUX
C
        RETURN
        END
C
C*****************************************************************
**
C
        SUBROUTINE QESOL(AP0,AP1,AP2,XSOL)
C
C       IMPLICIT REAL*8(A-H,O-Z)
        INCLUDE 'cfb1.com'
C
C       SOLVE QUADRATIC EQUATION
C
        AAP0=ABS(AP0)
        AAP1=ABS(AP1)
        AAP2=ABS(AP2)
        APMAX=AAP2
        IF(APMAX.LT.AAP1) APMAX=AAP1
        IF(APMAX.LT.AAP0) APMAX=AAP0
        AP0=AP0/APMAX
        AP1=AP1/APMAX
        AP2=AP2/APMAX
C
        ENTRY QESOL1(AP0,AP1,AP2,XSOL)
        IF(AP0.EQ.0.0) THEN
        IF(AP2.EQ.0.0.OR.AP1.EQ.0.0) THEN
        XSOL=0.0
        ELSE
        XSOL=-AP1/AP2
        IF(XSOL.LT.0.0) THEN
        WRITE(6,*)'+++++++++++++++++++++++++++++++'
        WRITE(6,*)'Warning 1: Negative solution!'
        WRITE(6,*)'time,I,J',TIME,I,J
        WRITE(6,*)'A2,A1,A0',AP2,AP1,AP0
        WRITE(6,*)'XSOL = ', XSOL
        STOP
        ENDIF
        ENDIF
        ELSE
        IF(AP1.EQ.0.0) THEN
        IF(AP2.EQ.0.0) THEN
        WRITE(6,*)'+++++++++++++++++++++++++++++++'
```

```
      WRITE(6,*)'Warning 2: No solutions!'
      WRITE(6,*)'time,I,J',TIME,I,J
      WRITE(6,*)'A2,A1,A0',AP2,AP1,AP0
      STOP
      ELSE
      DISC=-AP0/AP2
      IF(DISC.LE.0.0) THEN
      WRITE(6,*)'++++++++++++++++++++++++++++++++'
      WRITE(6,*)'Warning 3: No real solution!'
      WRITE(6,*)'time,I,J',TIME,I,J
      WRITE(6,*)'A2,A1,A0',AP2,AP1,AP0
      STOP
      ELSE
      XSOL=DISC**0.5
      ENDIF
      ENDIF
      ELSE
      IF(AP2.EQ.0.0) THEN
      XSOL=-AP0/AP1
      IF(XSOL.LT.0.0) THEN
      WRITE(6,*)'++++++++++++++++++++++++++++++++'
      WRITE(6,*)'Warning 4: Negative solution!'
      WRITE(6,*)'time,I,J',TIME,I,J
      WRITE(6,*)'A2,A1,A0',AP2,AP1,AP0
      WRITE(6,*)'XSOL = ', XSOL
      STOP
      ENDIF
      ELSE
      GOTO 10
      ENDIF
      ENDIF
      ENDIF
      RETURN
C
      ENTRY QESOL2(AP0,AP1,AP2,XSOL)
 10   CONTINUE
      SAP1=AP1*AP1
      DISC=SAP1-4.0*AP0*AP2
      IF(DISC.LT.0.0) THEN
      WRITE(6,*)'++++++++++++++++++++++++++++++++'
      WRITE(6,*)'Warning 5: No real solutions!'
      WRITE(6,*)'time,I,J',TIME,I,J
      WRITE(6,*)'A2,A1,A0',AP2,AP1,AP0
      STOP
      ENDIF
      IF(DISC.EQ.0.0) THEN
      XSOL=-AP1/(2*AP2)
      IF(XSOL.LT.0.0) THEN
      WRITE(6,*)'++++++++++++++++++++++++++++++++'
      WRITE(6,*)'Warning 6: Negative solution!'
```

```
      WRITE(6,*)'time,I,J',TIME,I,J
      WRITE(6,*)'A2,A1,A0',AP2,AP1,AP0
      WRITE(6,*)'XSOL = ', XSOL
      STOP
      ENDIF
      ENDIF
      IF(DISC.GT.0.0) THEN
      XSOL1=(-AP1+DISC**0.5)/(2*AP2)
      XSOL2=(-AP1-DISC**0.5)/(2*AP2)
      IF(XSOL1.GT.0.0.AND.XSOL2.GT.0.0) THEN
      WRITE(6,*)'+++++++++++++++++++++++++++++++'
      WRITE(6,*)'Warning 7: Two positive solutions!'
      WRITE(6,*)'time,I,J',TIME,I,J
      WRITE(6,*)'XSOl = XSOL1'
      WRITE(6,*)'A2,A1,A0',AP2,AP1,AP0
      WRITE(6,*)'T1 = ', XSOL1**2,'   T2 = ', XSOL2**2
      XSOL=XSOL1
      ENDIF
      IF(XSOL1.GT.0.0.AND.XSOL2.LE.0.0) THEN
      XSOL=XSOL1
      ENDIF
      IF(XSOL1.LE.0.0.AND.XSOL2.GT.0.0) THEN
      WRITE(6,*)'+++++++++++++++++++++++++++++++'
      WRITE(6,*)'Warning 9: XSOL1 < 0; XSOL2 > 0'
      WRITE(6,*)'time,I,J',TIME,I,J
      WRITE(6,*)'A2,A1,A0',AP2,AP1,AP0
      WRITE(6,*)'T1 = ', XSOL1**2,'   T2 = ', XSOL2**2
      XSOL=XSOL2
      ENDIF
      IF(XSOL1.LT.0.0.AND.XSOL2.LT.0.0) THEN
      WRITE(6,*)'+++++++++++++++++++++++++++++++'
      WRITE(6,*)'Warning 10: Two negative solutions!'
      WRITE(6,*)'time,I,J',TIME,I,J
      WRITE(6,*)'A2,A1,A0',AP2,AP1,AP0
      WRITE(6,*)'XSOL1 = ', XSOL1,'   XSOL2 = ', XSOL2
      STOP
      ENDIF
      ENDIF
      RETURN
      END
C
C*****************************************************************
**
C
      SUBROUTINE VWORKL
C
      INCLUDE 'cfb1.com'
C
C     CALCULATE VISCOUS STRESSES FOR THE WORK TERM IN THE
PHASES
```

```
C       ENERGY EQUATION (NOTE: VISCOSITY IS MULTIPLIED LATER)
C
        DO 100 J=2,JB1
        DO 100 I=2,IB1
        IJ=I+(J-1)*IB2
        IF(IFL(IJ).EQ.1) THEN
        CALL INDX
C
        DO 10 K=1,NPHASE
        IF(KIN(K).NE.1) GOTO 10
        CS1=0.5*((VK(K,IPJ)+VK(K,IPJM)-VK(K,IMJ)-VK(K,IMJM))
   $     /(DRP(I)+DRP(I-1))
   $     +(RB(I)*(UK(K,IJP)-UK(K,IJM))
   $     +RB(I-1)*(UK(K,IMJP)-UK(K,IMJM)))
   $     /(R(I)*(DZP(J)+DZP(J-1))))
        CS2=RDZ(J)*(VK(K,IJ)-VK(K,IJM))
        CS3=RDR(I)*(UK(K,IJ)-UK(K,IMJ))
        CS4=0.5*(RB(I)*UK(K,IJ)+RB(I-1)*UK(K,IMJ))/(R(I)*R(I))
C
        SILM(K,IJ)=RRIDR(I)*(RB(I)*UK(K,IJ)
   $    -RB(I-1)*UK(K,IMJ))+CS2
        SILRZ=CS1
        SILZZ=2.0*CS2
        SILRR=2.0*CS3
        SILPP=2.0*CS4
C
        VWLS(K,IJ)=DT*(SILRZ*CS1+SILZZ*CS2+SILRR*CS3
   $    +SILPP*CS4*ITC)
        VWLM(K,IJ)=DT*SILM(K,IJ)*SILM(K,IJ)
 10     CONTINUE
        ENDIF
 100    CONTINUE
C
        RETURN
        END
C
C*************************************************************
OUTP
        SUBROUTINE OUTP
C
        INCLUDE 'cfb1.com'
C       OUTPUT RESULTS TO DISK FOR FURTHER ANALYSIS
C
c       if(IRXN.EQ.1)then
c       call prod
c       endif

        WRITE(6,547)TIME
        write(21,547)TIME
        write(22,547)TIME
```

```
        write(23,547)TIME
        write(24,547)TIME
        write(25,547)TIME
        write(27,547)TIME
        write(28,547)TIME
        write(29,547)TIME
        write(31,547)TIME
         write(32,547)TIME
c       if(NPHASE.eq.2)then
        write(33,547)TIME
        write(34,547)TIME
        write(35,547)TIME
        write(36,547)TIME
        IF(KIN(K).EQ.1) THEN
        write(30,547)TIME
        endif
        WRITE(22,548)
        DO 325 IJ=IB2JB2,IB2,-IB2
325     WRITE(22,550)(P(IL),IL=IJ-IB1,IJ)
        k=0
        WRITE(23,549) K,K
        DO 228 IJ=IB2JB2,IB2,-IB2
228     WRITE(23,550)(TH(IL),IL=IJ-IB1,IJ)
        WRITE(24,556) K,K
        DO 236 IJ=IB2JB2,IB2,-IB2
236     WRITE(24,550)(VG(IL),IL=IJ-IB1,IJ)
        WRITE(25,557) K,K
        DO 237 IJ=IB2JB2,IB2,-IB2
237     WRITE(25,550)(UG(IL),IL=IJ-IB1,IJ)
        WRITE(32,555) K,K
        DO 238 IJ=IB2JB2,IB2,-IB2
238     WRITE(32,550)(TG(IL),IL=IJ-IB1,IJ)
C
        k=1
        WRITE(27,549) K,K
        DO 328 IJ=IB2JB2,IB2,-IB2
328     WRITE(27,550)(THL(K,IL),IL=IJ-IB1,IJ)
        WRITE(28,556) K,K
        DO 336 IJ=IB2JB2,IB2,-IB2
336     WRITE(28,550)(VK(K,IL),IL=IJ-IB1,IJ)
        WRITE(29,557) K,K
        DO 337 IJ=IB2JB2,IB2,-IB2
337     WRITE(29,550)(UK(K,IL),IL=IJ-IB1,IJ)
        WRITE(31,555) K,K
        DO 338 IJ=IB2JB2,IB2,-IB2
338     WRITE(31,550)(TL(K,IL),IL=IJ-IB1,IJ)

c       if(NPHASE.eq.2)then
        k=2
        WRITE(33,549) K,K
```

```
      DO 428 IJ=IB2JB2,IB2,-IB2
428   WRITE(33,550)(THL(K,IL),IL=IJ-IB1,IJ)
      WRITE(34,556) K,K
      DO 436 IJ=IB2JB2,IB2,-IB2
436   WRITE(34,550)(VK(K,IL),IL=IJ-IB1,IJ)
      WRITE(35,557) K,K
       DO 437 IJ=IB2JB2,IB2,-IB2
437   WRITE(35,550)(UK(K,IL),IL=IJ-IB1,IJ)
      WRITE(36,555) K,K
      DO 438 IJ=IB2JB2,IB2,-IB2
438   WRITE(36,550)(TL(K,IL),IL=IJ-IB1,IJ)
c     endif

      k=1
      IF(KIN(K).EQ.1) THEN
      WRITE(30,558) K,K
       DO 339 IJ=IB2JB2,IB2,-IB2
339   WRITE(30,550)(TSKN(K,IL),IL=IJ-IB1,IJ)
      WRITE(30,559) K,K
      DO 351 IJ=IB2JB2,IB2,-IB2
351   WRITE(30,550)(VISCL(K,IL),IL=IJ-IB1,IJ)
      WRITE(30,565) K,K
      DO 355 IJ=IB2JB2,IB2,-IB2
355   WRITE(30,550)(VISBL(K,IL),IL=IJ-IB1,IJ)
      WRITE(30,566) K,K
      DO 356 IJ=IB2JB2,IB2,-IB2
356   WRITE(30,550)(PS(K,IL),IL=IJ-IB1,IJ)
      endif
      RETURN

547   FORMAT(1X,//,1X,'@ TIME = ',1PE12.5,' secs')
548   FORMAT(1X,/,1X,'FLUID PRESSURE, P (dynes/cm^2)'/)
549   FORMAT(1X,/,1X,'VOLUME FRACTION (PHASE- ',I1
  1 ,'), TH',I1/)
550   FORMAT(1X,100(1X,G10.4))
551   FORMAT(1X,I5,1X,G10.4)
555   FORMAT(1X,/,1X,'TEMPERATURE (PHASE-'
  1 ,I1,'), TL',I1,' (Kelvin)'/)
556    FORMAT(1X,/,1X,'VELOCITY - Z (or Y) component,',
  1 '  (PHASE-',I1,'), VK',I1,' (cm/s)'/)
557   FORMAT(1X,/,1X,'VELOCITY - R (or X) component,',
  1 ' (PHASE-',I1,'), UK',I1,' (cm/s)'/)
558   FORMAT(1X,/,1X,'GRANULAR TEMPERATURE (PHASE-'
  1 ,I1,'), TSK-',I1,' ((cm/s)^2)'/)
559   FORMAT(1X,/,1X,'GRANULAR SHEAR VISCOSITY (PHASE-'
  1 ,I1,'), VISCL-',I1,' (dynes/cm.s)'/)
565   FORMAT(1X,/,1X,'GRANULAR BULK VISCOSITY (PHASE-'
  1 ,I1,'), VISBL-',I1,' (dynes/cm.s)'/)
566   FORMAT(1X,/,1X,'GRANULAR SHEAR STRESS (PHASE-'
  1 ,I1,'), PS-',I1,' (dynes/cm.s)'/)
```

```
560     FORMAT(1X,/,1X,'VELOCITY - THETA (or Z) component,',
    1 ' (PHASE-',I1,'), WK',I1,' (cm/s)'/)
562     FORMAT(1X,/,1X,'WEIGHT PERCENT COMPOSITION,',
    1 ' (PHASE-',I1,'), COMPONENT-',I1,' (cm/s)'/)
563     FORMAT(1X,/,1X,'PRODUCTION OF GAS,',
    1 ' (PHASE-',I1,'), COMPONENT- CH3OH'/)
     END
C*****************************************************************
```

สถาบันวิทยบริการ
จุฬาลงกรณ์มหาวิทยาลัย

BIOGRAPHY

Ms. Veeraya Jiradilok was born in 1980 in Bangkok, Thailand. I obtained Bachelor degree in Chemical Engineering from Department of Chemical Technology, Faculty of Science, Chulalongkorn University in 2002. With the assistance of Thailand Research Fund for the research financial support, I have continued studying Doctor degree at the same Department in 2002. I spent my research works at Illinois Institute of Technology, Chicago, U.S.A. in 2004 -2005.

The conference and publication involving her research works are the following

Gidaspow D. and V. Jiradilok, "Explosive Dissemination of Particles," Tutorial at Obscurants 2005, Orlando, Florida, June 6-9, 2005

Jiradilok, V., D. Gidaspow, S. Damronglerd, W. J. Koves, R. Mostofi, and S. Nitivattananon, "Kinetic Theory Based CFD Simulation of Turbulent Fluidization of FCC Particles in a Riser," AIChE Meeting, 31 October 2005, Cincinnati

Jiradilok, V., D. Gidaspow, S. Damronglerd, W. J. Koves, and R. Mostofi, "Kinetic Theory Based CFD Simulation of Turbulent Fluidization of FCC Particles in a Riser," 2005, in revise process for *Chemical Engineering Science*

Jiradilok, V., D. Gidaspow, J. Kalra, S. Damronglerd, and S. Nitivattananon, "Explosive Dissemination and Flow of Nanoparticles," accepted for publication for *Powder Technology*

สถาบันวิทยบริการ
จุฬาลงกรณ์มหาวิทยาลัย